Gravitational Lensing Constraints on Cosmic Structures

Dissertation

zur

Erlangung der naturwissenschaftlichen Doktorwürde
(Dr. sc. nat.)

vorgelegt der

Mathematisch-naturwissenschaftlichen Fakultät

der

Universität Zürich

von

Marco Miranda

aus

Italien

Promotionskomitee

Prof. Dr. Daniel Wyler (Vorsitz)
Prof. Dr. Philippe Jetzer (Leitung der Dissertation)
Prof. Dr. Giuseppe Longo

Zürich 2007

Die vorliegende Arbeit wurde von der Mathematisch-naturwissenschaftlichen Fakultät der Universität Zürich auf Antrag von Prof. Dr. Philippe Jetzer und Prof. Dr. Ben Moore als Dissertation angenommen.

Contents

Contents **3**

Summary **viii**

Zusammenfassung **xi**

Preface **4**

1 Introduction to Gravitational Lensing **9**

1.1 Historical remarks 10

1.2 Lens equation 11

1.2.1 Point-like lenses 11

1.2.2 Thin lens approximation 12

1.2.3 Lens equation 13

1.2.4 Remarks on the lens equation 15

1.2.5 Lens mapping close to the critical curves 18

1.3 Simple lens models 20

1.3.1 Axially symmetric lenses 20

1.3.2 Einstein radius 21

1.4 Schwarzschild lens 22

1.5 Singular isothermal sphere (SIS) 23

1.6 Singular isothermal ellipsoid (SIE) 24

1.7 Galaxy clusters as lenses 25

1.7.1 Weak lensing 27

1.7.2 Comparison with results from X–ray observations 29

2 Q0045-3337: models including strong lensing by a spiral galaxy **31**

2.1 Introduction 31

2.2 Observational parameters 31

2.3 surface photometry and galaxy subtraction 33

2.4 Single image or multiple images 33

2.5 Multiple images 35

2.5.1 Three images 35

2.5.2 Quasar ellipticity 37

2.5.3 Five images 38

2.5.4 Five images versus three images 38

2.6 Discussion 39

3 Cold Dark Matter models and strong lensing 41

3.1 Success and crisis of CDM 41

3.2 Strong Lensing to probe structures at all scales 41

4 Substructures towards PG1115+080 and B1555+373 43

4.1 Introduction 43

4.2 About PG1115+080 and B1555+375 44

4.3 Analytical treatment 46

4.3.1 Lens Mapping 46

4.3.2 Perturbing the system 47

4.4 Numerical simulations 48

4.4.1 PG1115+080 49

4.4.2 B1555+375 52

4.5 Discussion 52

4.6 Analytic estimates for convergence and shear due to a substructure 56

5 The effect of low mass substructures on the Cusp lensing relation 57

5.1 Introduction 57

5.2 The cusp relation 58

5.3 Lensing Simulations 59

5.3.1 Primary Lens 59

5.3.2 Subhaloes 59

5.3.3 Extrahaloes 60

5.4 Results 61

5.4.1 Testing our model 61

5.4.2 Configuration 1 64

5.4.3 Configuration 2 65

5.4.4 Configuration 3 69

5.5 Fold Relation 70

5.6 Discussion 70

6 Constraining Warm Dark Matter using QSO gravitational lensing 73

6.1 Introduction 73

6.2 Intergalactic haloes mass function 74

6.3 Lensing Formalism 76

6.3.1 The cusp relation 76

6.3.2 The unperturbed lens 77

6.4 Subhaloes along the line of sight: Idea and Procedure 78

6.5 Results 80

6.6 Discussion 83

7 The dynamical state of RX J1347.5-1145 from strong lensing and X-ray analysis 86

7.1 Introduction 86

7.2 Optical data: cluster members and arc candidates 87

7.3 Statistical analysis 87

7.3.1 χ^2 statistic 89

7.4 Fitting analysis 90

7.4.1 One component 91

7.4.2 Bimodal structure: two components 92

7.4.3 Adding complexity 92

7.4.4 Model degeneracies 94

7.5 X-Ray analysis 95

7.5.1 X-ray Spectroscopy 97

7.5.2 Mass Distribution 99

7.5.3 X-ray and SZE face to face 100

7.6 A merger hypothesis 100

7.7 Discussion 101

APPENDIX A: 103

Influence of Orbital Behaviour and Chaos on the Shape of Dark Matter Halos 104

A-1 Numerical Simulations 105

A-1.1 Baryonic core modeling 105

A-2 Numerical Experiments 106

A-3 Discussion and Conclusions 109

References 118

Acknowledgments 124

"...ne' proviamo una stupita emozione per il piccolo focolare che arde nelle nostre case con la sua luce pura, ma davanti piuttosto ai grandi fuochi del cielo, sebbene spesso si oscurino;...Da tutte queste considerazioni, questo possiamo dire: gli uomini hanno a portata di mano cio' che e' utile oppure necessario, tuttavia ammirano sempre cio' che e' straordinario"

Anonimo Del Sublime, XXXV

A Enzo G.

Summary

At the beginning of this new century, astrophysics and cosmology are among the most exciting and promising areas of the physical sciences. One of the main problems in cosmology is to understand the formation and evolution of galaxies, galaxy clusters, and large-scale structure. Whereas the basics of the current Cold Dark Matter (CDM) paradigm for structure formation are widely accepted, some controversial issues for CDM (e.g. cuspiness of dark-matter halos, substructure crisis) still remain. In order to test CDM predictions, one needs to investigate bound objects from the smallest (dwarf galaxies) to the largest (galaxy clusters) scales at different redshifts. In particular, their matter-content, luminous and dark, has to be studied in detail. Gravitational lensing - the attraction of light by matter - displays a number of attractive features as an academic discipline, first of all the ability to draw the dark matter distribution of our Universe. Part of this work addresses this issue by using gravitational lensing. Following a preface and a general introduction to gravitational lensing, the lens properties of imaged systems, we describe the status of the observed lens systems and show some possible image configurations of a recent descovered luminous QSO likely lensed by a spiral galaxy. In the next chapters we focus on the substructures in the lens galaxies. They refer to the signatures of substructures, inside the main galactic halo, on gravitational lensing properties and to a comparison with the observed lensed systems. Then, the concept of the Warm Dark Matter, and its plausible introduction within the cosmological scenario in order to explain the so called missing satellites problem (CDM crisis) is introduced. Finally, on extragalactic scales, I will describe on-going merger processes between cluster of galaxies and I will apply both X-ray and lensing analysis tecniques to a particular cluster of galaxies, RXJ1347-1145, to infer both dark matter and gas distributions, to study the different physical processes and interactions between different matter components, ordinary (baryonic) and dark matter.

During my PhD at the Institute for Theoretical Physics, I had the possibility to start to work with N-body simulations in particular using the tree code PKDGRAV (Stadel 2001). I added a related work at the end of the thesis, althought the topic of the project is not properly associated to the Gravitational Lensing. In the following I give a short summary of the next chapters.

Q0045-3337: a candidate for strong lensing by a spiral galaxy

A disk-like galaxy at ~ 1.2 arcsec from the QSO Q0045-3337 with ESO VLT adaptive optics has been recently discovered. A galaxy Einstein radius (for a point mass) of comparable size has been estimated, thus pointing up the existence of a new, rare, spiral lens candidate, despite no evident image splitting. I discuss the possible lensing effect of the galaxy in some more detail, by verifying if simple mass models, partially constrained by observational data, require unrealistic parameters to produce a still hidden second quasar image. I also evaluated the viability of an instrumental or a lensing origin of the observed QSO deformation. Anyway, existing data are not sufficient to assess the presence of image splitting, nor to constrain the number of images or discriminate between galaxy mass models. Further observations are mandatory to progress in the study of this remarkable system, that could shed more light on the lensing behaviour of spiral galaxies.

Substructures towards PG1115+080 and B1555+373

I study the anomalous flux ratio which is observed in some four-image lens systems, where the source lies close to a fold caustic. In this case two of the images are close to the critical curve and their flux ratio should be equal to unity, instead in several cases the observed value differs significantly. The most plausible solution is to invoke the presence of substructures, as for instance predicted by the Cold Dark Matter scenario, located nearby the two images. In particular, I analyze the two fold lens systems PG1115+080 and B1555+375, for which there are not yet satisfactory models which explain the observed anomalous flux ratios. I add to a smooth lens model, which reproduces well the positions of the images but not the anomalous fluxes, one or two substructures described as singular isothermal spheres. For PG1115+080 I consider a smooth model with the influence of the group of galaxies described by a SIS and a substructure with mass $\sim 10^5\ M_\odot$ as well as a smooth with an external shear and one substructure with mass $\sim 10^8\ M_\odot$. For B1555+375 either a strong external shear or two substructures with mass $\sim 10^7\ M_\odot$ reproduce quite well the data.

The effect of low mass substructures on the cusp lensing relation

In this chapter I investigate the same issue in greater detail focusing on the *cusp* relation which corresponds to images of a source located to the cusp of the inner caustic curve. I use numerical simulations combined with a Monte Carlo approach to study the effects of the expected power law distribution of substructures within ΛCDM haloes on the multiple images. I considered in our analysis a mass range of $10^5 - 10^7 \mathrm{M}_\odot$ for the subhaloes. I also demonstrate that including the effects of the surrounding mass distribution, such as other galaxies close to the primary lens, does not change the results. The main conclusion is that triple images of lensed QSOs do not show any direct evidence for cold dark matter substructures such as dark dwarf galaxies.

Constraining Warm Dark Matter using QSO gravitational lensing

Warm Dark Matter (WDM) has been invoked to resolve apparent conflicts of Cold Dark Matter (CDM) models with observations on subgalactic scales. In this chapter I provide a new and independent lower limit for the WDM particle mass (e.g. sterile neutrino) through the analysis of image fluxes in gravitational lensed QSO. Starting from a theoretical unperturbed cusp configuration I analyze the effects of intergalactic halos (halos along the line of sight) in modifying the fluxes of QSO multiple images, giving rise to the so-called anomalous flux ratio. I found that the global effect of such haloes strongly depends on their mass/abundance ratio and it is maximum for haloes in the mass range $10^6 - 10^8 \mathrm{M}_\odot$. This result opens a new possibility to constrain the CDM predictions on small scales and test different warm candidates, since free streaming of warm dark matter particles can dampen considerably the matter power spectrum in this mass range. As a consequence while a (Λ)CDM model is able to produce flux anomalies at a level similar to those that are observed, a WDM model, with a too light particle, fails in reproducing the observational evidences. I found a lower limit $m_\nu > 10$ keV for the mass of warm dark matter candidates in the form of a sterile neutrino, in good agreement with previous results coming from Lyman-α forest and Cosmic Microwave Background analysis.

The dynamical state of RX J1347.5-1145 from strong lensing and X-ray analysis

The object of this chapter is a combined X-ray and strong lensing analysis of RX J1347.5-1145, one of the most luminous galaxy clusters at X-ray wavelengths. I perform multi-color data analysis of recent archival deep VLT/FORS observations. The results provide constraints on a multiple image system which allows to carry on a detailed strong lensing study. The analysis is done thoroughly in the image plane, taking into account image positions and both the arc shapes and orientations. Our best fitted model is a bimodal mass distribution, composed of two massive dark matter components located in the cluster inner regions, yielding a total cluster mass of $M_{tot} = (9.9 \pm 0.3) \times 10^{14} M_\odot$, within a radius of $520kpc$. The presence of such double structure could be a signature of a recent major merger. The merging scenario is further supported by X-ray data. A temperature map of the cluster, based on deep Chandra observations, reveals a hot front located between the first main component and an X-ray emitting sub-clump, present in the South Eastern region of the cluster. The temperature map also unveils a filament of cold gas in the innermost regions of the cluster,

most probably a cooling wake caused by the motion of the cD inside the cool core region. A merger scenario in the plane of the sky between two dark matter sub-clumps is consistent with both our lensing and X-ray analyses, and can explain previous discrepancies with mass estimates based on the virial theorem.

Influence of Orbital Behaviour and Chaos on the Shape of Dark Matter Halos

In this appendix we perform a detailed analysis of particle orbits in a simulated cosmological dark matter halos to understand *how* and *why* baryons alter its shape. It has been shown that the dissipative gas infall during galaxy formation has the capability to modify the shape of dark matter halos. We show a series of numerical experiments where we grow a baryonic core inside a dark matter halo extracted from a cosmological simulation. We follow the orbits of more than 300 particles with more that 50000 timesteps. Our results clearly show that the dissipational component is responsible for repeatedly deflecting orbits which visit often the center of the system. Moreover, the gravitational potential time dependence associated with the growth of the baryonic mass, shifts the frequencies of the orbits, making them extremely chaotic. This randomization makes the orbits explore a large phase space. When this effect takes place for a significant number of orbits it will be manifested in the density distribution as an approach to a rounder configuration. As a consequence, the influence of the central mass on the shape of the phase space decreases with increasing distance from the center. We discuss the importance of future analysis of controlled experiments (i.e. using analythic potentials instead of live DM halos) to better decipher the dynamics of this phenomenon.

Zusammenfassung

Am Anfang dieses Jahrhunderts stellen Astrophysik und Kosmologie zwei der spannendsten und erwartungsvollsten Bereiche der modernen Physik dar. Eines der Hauptprobleme der Kosmologie besteht im Verständnis der Entstehung und der Entwicklung von Galaxien, von Galaxienhaufen und grossen Strukturen. Wenn auch die Grundlagen des aktuellen kalte dunkle Materie-Paradigmas (CDM) zur Bildung von Strukturen weithin akzeptiert werden, bleiben doch noch einige Kontroversen offen (u.a. die spitzen Profile der Halos dunkler Materie und das Problem der Substrukturen). Um die Voraussetzungen des CDM überprüfen zu können, muss man durch die Gravitationskraft gebundene Objekte von der kleinsten (Zwerggalaxie) bis zur grössten (Galaxienhaufen) Skala, die sich auf unterschiedlichen Distanzen befinden, untersuchen. Besonders wichtig ist dabei eine detaillierte Analyse des leuchtenden und dunklen Materieinhaltes dieser Objekte. Die Ablenkung des Lichtes durch die Gravitationskraft der Materie (auch als Gravitationslinsen bezeichnet) ist eine vielversprechende Methode. Sie ermöglicht insbesondere eine Abbildung der Verteilung der dunklen Materie in unserem Universum. Im ersten Teil dieser Arbeit verwende ich die Gravitationslinsenmethode zur Untersuchung der CDM Problematiken. Nach der Einleitung und einem Überblick über die Gravitationslinsenmethode und die Linseneigenschaften der abgebildeten Systeme, wird der aktuelle Wissensstand der bisher beobachteten Linsensysteme kurz beschrieben. Danach werden einige mögliche Bildkonfigurationen, eines kürzlich entdeckten leuchtenden QSO (Quasi Stellar Object), diskutiert. Die als Linse wirkende Galaxie ist eine Spiralgalaxie. Das darauf folgende Kapitel beschäftigt sich mit Substrukturen in den Linsengalaxien. Dabei geht es um die Wirkung der Substrukturen auf die Gravitationslinseneigenschaften innerhalb des Halos der Hauptgalaxie, als auch um einen Vergleich mit beobachteten Linsensystemen. Anschliessend wird das Konzept der 'warmen dunklen Materie' eingeführt und gezeigt wieweit die Einführung dieses Konzepts in den kosmologischen Modellen zur Lösung des sogenannten Problem der fehlenden Satelliten (CDM Krise) plausibel ist. Zum Schluss will ich den andauerden Kollisionsprozess zwischen Galaxiehaufen auf einer extragalaktischen Skala beschreiben und beide X-ray und Linsen-Analysenmethode auf einen besonderen Galaxienhaufen (bezeichnet als RXJ1347-1145) anwenden. Das Ziel dabei ist es die Verteilung der dunklen Materie und des Gases abzuleiten und die verschiedenen physikalischen Prozesse und Wechselwirkungen der unterschiedlichen Komponenten der Materie, gewöhnliche (baryonische) und dunkle Materie, zu untersuchen. Während meines Doktorats am Institut für Theoretische Physik hatte ich zudem die Gelegenheit mit N-Körpersimulationen zu arbeiten. Ich benutzte vor allem den Tree-Kode PKDGRAV (Stadel 2001). Als Resultat dieser Untersuchungen ist eine Arbeit entstanden, die am Ende dieser Dissertation angehängt ist, obwohl das Thema dieses Projektes nicht direkt mit den vorherigen Arbeiten, die auf der Gravitationslinsenmethoden beruhen, verbunden ist. Im Folgenden gebe ich eine kurze Zusammenfassung der verschiedenen Kapitel.

Q0045-3337: ein Kandidat für starkes "lensing" bei einer Spiralgalaxie

Vor kurzer Zeit wurde eine Spiralgalaxie in einem Abstand von nur ~ 1.2 Bogensekunden von den QSO Q0045-3337, mit dem ESO VLT Teleskop ausgerüstet mit adaptiver Optik, entdeckt. Obwohl nur ein Bild des QSO aufgedeckt wurde, ergibt eine Abschätzung des Einsteinradius der Galaxie (letztere als Punktmasse angenommen) einen Wert der mit dem Abstand QSO-Galaxie vergleichbar

ist. Diese Tatsache legt die Vermutung nahe, dass es sich um ein seltenes Gravitationslinsensystem handelt. Ich betrachte verschiedene Gravitationslinsenmodelle der Galaxie, indem ich (zum Teil von den Beobachtungsdaten nahegelegt) nachprüfe, ob die einfachen Massenmodelle unrealistische Parameter erfordern, um ein noch verstecktes zweites Quasarbild zu ergeben. Ich diskutiere dabei auch die jeweilige Möglichkeit einer entweder instrumentellen oder durch die Gravitationlinse Herkunft der beobachteten QSO-Verformung. Jedoch sind die existierenden Daten weder genügend um die Präsenz von Zersplitterungen der Abbildungen festzulegen, noch helfen sie ihre Zahl zu beschränken oder die verschiedenen verwendeten Massenmodelle der Galaxie zu unterscheiden. Weitere Beobachtungen sind nötig, wenn man beim Studium von diesem bemerkenswerten System vorankommen will. Das könnte ein neues Licht auf das Linsenverhalten von Spiralgalaxien werfen.

Substrukturen innerhalb PG1115+080 und B1555+373

In diesem Kapitel untersuche ich den ungewöhnlichen Flussanteil, der bei einigen Linsensystemen mit vier Bildern zu beobachten ist und deren Quelle nahe einer "fold" kaustik liegt. Bei einem solchen Fall liegen zwei der Abbildungen nahe der kritischen Kurve und das Verhältnis ihrer Flussanteile sollte gleich eins sein. Stattdessen kann man in verschiedenen Fällen feststellen, dass der beobachtete Messwert von diesem Wert stark abweicht. Die plausibelste Erklärung ist das Vorhandensein von Substrukturen, die neben den zwei Bildern sich befinden sollten, so wie es beim 'kalten dunklen Materie-Szenario' vorausgesagt wird. Ich widme mich vor allem der Analyse der zwei Linsensystemen PG1115+080 und B1555+375, für welche es noch keine befriedigenden Modelle gibt, die den beobachteten anomalen Flussanteil erklären könnten. Da ein glattes Linsenmodell die Position der Bilder gut reproduziert, nicht aber die anomalen Flussanteile, füge ich ein oder zwei Substrukturen hinzu, die als isothermische Sphären beschrieben werden. Für PG1115+080 betrachte ich zwei glatte Modelle. Das eine Modell wird von der Galaxiengruppe beeinflusst, und beinhaltet eine Substruktur der Masse $\sim 10^5 M_\odot$. Das zweite Modell enthält einen schärungsterm und eine Substruktur der Masse $\sim 10^8 M_\odot$. Auch im Fall des Linsensystems B1555+375 können entweder ein starker Schärungsterm oder zwei Substrukturen mit Masse $\sim 10^7 M_\odot$ die Daten ziemlich gut reproduzieren.

Die Wirkung von Substrukturen kleiner Masse auf die "cusp-lensing" Beziehungen

In diesem Teil wird diesselbe Problematik wie vorher untersucht, jedoch mit besonderem Augenmerk auf die "cusp" Beziehung. Diese entspricht Abbildungen einer Quelle, die sich auf der "cusp" der inneren kaustik curve befindet. Um die Auswirkung der Verteilungen (nach einem Potenzgesetz) von Substrukturen in Λ CDM Halos auf Multiplerbilder zu erforschen, benutze ich numerische Simulationen zusammen mit einem Monte Carlo Ansatz. In unserer Analyse betrachten wir Subhalos im Massbereich von $10^5 - 10^7 M_\odot$. Weiter beweisen wir, dass die Resultate sich nicht verändern, wenn man Auswirkungen der benachtbarten Massverteilung wie weitere Galaxien, die sich in der nähe der Galaxie die als Linse fungiert, berücksichtigt. Die Hauptschlussfolgerung ist, dass dreifach Bilder von QSO Linsen keinen direkten Nachweis für kalte dunkle Materie Substrukturen, wie dunkle Zwerggalaxien, liefern.

Einschränkung der warmen dunklen Materie durch QSO Gravitationlinsen

Wir haben uns auf warme dunkle Materie berufen, um die deutlichen Widersprüche des kalten dunklen Materiemodells mit den Beobachtungen auf subgalaktischer Skala zu lösen. In diesem Kapitel gebe ich, durch die Analyse von Bilderflüssen von gelinsten QSO, eine neue und unabhängige untere Schranke der WDM-Teilchenmasse (z.B. steriles Neutrino).

Mein Ausgangspunkt ist eine theoretisch ungestörte "cusp"-Konfiguration. Ich analysiere Auswirkungen der intergalaktischen Halos (Halos, die sich entlang der Sichtrichtung befinden) durch die Abänderung des Flusses der multiplen QSO-Bilder, was die anomale Flussanteile bewirkt. Was wir daraus schlussfolgern können, ist, dass die umfassende Wirkung von solchen Halos stark von ihrer Masse abhängt, und dass das Maximum bei Halos der Masse $10^6 - 10^8 M_\odot$ erreicht wird. Dieses Resultat eröffnet eine neue Möglichkeit, um die Voraussagen der CDM auf kleine Skalen einzuschränken und unterschiedliche warme Kandidaten testen zu können. In der Tat dämpfen freie Strömungen warmer dunkler Materie die Spektraldichtefunktion der Materie beträchtlich. Mann kann daher folgern: während ein Λ CDM-Modell Flussanomalien ähnlich den beobachteten erzeugen

kann, gelingt dies in einem WDM Modell mit einem zu leichten Teilchen nicht.

Ich habe eine untere Schranke von $m_\nu > 10$keV für die Masse der warmen dunklen Materie Kandidaten in Form eines sterilen Neutrinos gefunden, was mit den vorherigen Ergebnissen aus dem "Lyman-α forest" und der Kosmischen Hintergrundsstrahlungsanalyse gut übereinstimmt. **Der dynamische Zustand von RX J1347.5-1145 durch starkes linsen und Röntgenanalyse**

Gegenstand dieses Kapitels ist die kombinierte Röntgen- und starke linsen-analyse von RXJ1347.5-1145, einer der leuchtstärksten Galaxienhaufen in den Röntgenwellenlängen. Ich führe eine mehrfarbige Analyse der letzten tiefe VLT/FORS-Beobachtungen durch. Das Ergebnis ergibt Einschränkungen eines multiplen Systems, was es uns ermöglicht, eine detaillierte starke Linsenstudie durchzuführen. Die Analyse wird auf der Bildebene durchgeführt, wobei man die Bildposition und seine Bogenform und Orientierung betrachtet. Das Beste von uns gefundene Modell ist eine bimodale Massenverteilung, welche aus zwei massiven dunklen Materiekomponenten besteht, die sich im Innenbereich des Galaxienhaufens befinden. Die massiven dunkle Materie -Komponenten enthalten eine Gesamtmasse von $M_{tot} = (9.9 \pm 0.3) \times 10^{14} \mathrm{M}_\odot$, innerhalb einem Radius von $520 kpc$. Die Präsenz einer solchen Doppelstruktur könnte ein Hinweis auf eine vor kurzem begonnene Kollision sein. Das Kollisionsszenario ist weiterhin von X-ray Daten bekräftigt. Eine auf tiefe Chandra-Beobachtungen bezogene Temperaturkarte des Galaxienhaufens belegt eine heisse Front in der Mitte der ersten Hauptkomponente und eine röntgenstrahlenden Substruktur in der süd-östlichen Region des Galaxienhaufens. Die Temperaturkarte enthüllt auch einen Streifen aus kaltem Gas in der innersten Region des Galaxienhaufens, was sehr wahrscheinlich ein kühlender Strom ist, der von der Bewegung der zentralen Galaxie (cD). innerhalb der kühlen Kernregion bewirkt wird. Ein Kollisionsszenario in der Ebene des Himmels zwischen den zwei dunklen Materien (sub-clumps) stimmt mit unseren beiden linsen- und Röntgenanalysen überein und erklärt vorherige Diskrepanzen in der Massenabschätzung, die auf dem Virialtheorem basierten.

Der Einfluss von Kreisförmigen Bahnverhalten und Chaos auf die Form der dunklen Materiehalos

In diesem Anhang führe ich eine detaillierte Analyse der Bahnen von Teilchen in einem simulierten kosmologischen dunklen Materiehalo durch, um verstehen zu können, 'wie' und 'warum' Baryonen die Form des Halos verändern können. Es wurde gezeigt, dass das Gas die Fähigkeit besitzt, während der dissipativen Bildungsphase von Galaxien die Form der dunklen Materiehalos zu ändern. Dabei benütze ich eine Reihe von numerischen Berechnungen, in denen ich einen baryonischen Kern vergrössere, welcher sich in einem dunklen Materiehalo befindet, der aus einer kosmologischen Simulation gewonnen wurde. Ich folge den Bahnen von über dreihundert Teilchen in mehr als fünfzigtausend Zeitschritten. Das Ergebnis zeigt deutlich, dass die dissipativen Komponenten verantwortlich für wiederholt abgelenkte Bahnen sind, die oft das Zentrum des Systems durchqueren. Ausserdem verschiebt sich, aufgrund der Zeitabhängigkeit des Gravitationspotentials verbunden mit dem Anwachsen der (baryonischen) Masse, die Frequenzen der Bahnen, so dass sie äusserst chaotisch werden. Auf Grund dieser "Randomisierung" (was zB in der Zwerggalaxie Leo gefunden wurde) durchqueren die Bahnen einen grösseren Phasenraum. Wenn dies für eine bedeutende Anzahl von Bahnen stattfindet, wird man es in der Dichteverteilung als Annäherung zu eine runderen Konfiguration wahrnehmen können. Als Folge sinkt der Einfluss der zentralen Masse auf die Form des Phasenraums mit zunehmenden Abstand vom Zentrum. Wir besprechen die Bedeutung von zukünftigen Analysen für kontrollierte Experimente (z. B. das Benutzen von analytischen Potenzialen anstelle von simulierte DM-Halos), um die Dynamik dieses Phänomens besser verstehen zu können.

Preface

The Hot Big Bang Model assumes that the universe was born from a very dense and hot state. Shortly afterwards it consisted of a mixture of many interacting elementary particles. Under these conditions electromagnetic radiation was scattered very efficiently by matter and this kept the universe in thermal equilibrium. After 380,000 years the Universe had cooled enough (to 3000 K) for the electrons and nuclei to combine into atoms. When this process, called recombination, completed the mean-free-path of the photons became large and they began to propagate (nearly) freely through the Universe. Before recombination the photons were in thermal equilibrium, thus having a black-body spectral distribution corresponding to a temperature of 3000 K. Since the universe expands the temperature of the radiation changes and so we see today (13.6 Gyrs after the Big Bang) the photons having a black-body spectrum corresponding to a temperature of 2.728 K. These photons in fact give a snapshot of the universe in its infancy and are seen today in the form of radiation in the microwave regime, called Cosmic Microwave Background radiation (CMB). Therefore the CMB has provided us with an excellent diagnostic to study the history of the universe. While the existence of the background radiation itself was originally discovered by Penzias & Wilson in 1965, the first instrument to measure the CMB temperature on the whole sky was the COBE satellite. It confirmed the result of other CMB probes, that we observe a black body spectrum with a temperature of 2.728 K on the whole sky.

In addition, however, each pointing COBE made showed slightly different temperature; these small fluctuations have been measured on the level of $\Delta T/T \approx 10^{-5}$. Such fluctuations in temperature across the sky are the precursors of structures we see today (galaxies, galaxy clusters, etc.); they have grown through gravitational instability from $\Delta\rho/\rho \approx 10^{-5}$ to the highly concentrated structures we observe around us. These results, however are in contradiction with the hypothesis that the universe consists only of the matter we see (i.e. luminous matter, also called baryonic). Namely we observe structures today with density contrast $\Delta\rho/\rho \gg 1$. For these structures the fluctuations should have been at least 10^{-3} at the time of recombination. This is, however, not what we observe. The solution to the problem is given by the presence of dark-matter which dominates the matter content in the universe and has $\Delta\rho/\rho \approx 10^{-3}$ at the epoch of recombination (i.e. they started to grow at earlier times). Baryons on the other hand were coupled to the photons up to that time, and the pressure kept the baryons from collapsing under their own gravity. The idea of the existence of dark matter has become increasingly accepted in cosmology, with CMB measurements giving strong evidence for the presence of dark matter at the largest scales. The first evidence for the existence of dark matter is however much older than CMB results, it came from dynamical studies of astronomical objects with Zwicky's estimation of the mass of Coma cluster in 1937. In addition the idea of the existence of dark matter is supported from other fields of research; X-ray studies and gravitational lensing among others. Unfortunately, we still do not know what the nature of dark matter is. Nowadays the most probable candidates are considered to be elementary particles that rarely interact with ordinary matter (e.g. weakly interacting massive particles or WIMPs); but such a particle has not been detected as of yet. The interface of particle physics and cosmology is therefore a fruitful field of research. Cosmologists need to study the properties of dark-matter on macroscopic scales, while a suitable candidate particle fitting these constraints needs to be detected in particle physics research. One of the most recent successes in measuring the temperature over the whole sky with an exquisite sensitivity and resolution was achieved by the WMAP and WMPA3 data. The results of WMAPs together with studies of large scale structure strengthened the idea that the sum of luminous and dark matter does not represent the total matter and energy content

in the universe. In addition to ordinary (luminous and dark) matter, there exist an additional form of matter or energy. In particular, the measurement that the universe is accelerating has come as a great surprise, since gravitational pull exerted by the matter in the universe slows down the expansion. The amazing conclusion was that the universe contains a combination of dark matter and dark energy, the latter being gravitationally repulsive, and the nature of both we do not understand. Cosmologists gave it the name dark energy (or also the cosmological constant). We argue that one of the best tools to study the dark matter distribution from the scales corresponding to stars to the large-scale-structure is gravitational lensing. In addition lensing can also be used to investigate the nature of dark energy, by studying the evolutionary effects of dark matter. We will focus on dark matter only, in particular we will study the mass and the mass distribution in galaxies and galaxy clusters. In this chapter we will give a very short introduction to both in the context of structure formation, mostly illuminating the problems of determining the mass distributions of galaxies and galaxy clusters and highlighting the questions we want to address in this thesis.

Growth and formation of structures in the universe

We have briefly mentioned before that the structures in the universe we see today grew from the primordial density fluctuations. However we did not explain their origin. The most probable (but not necessary correct) explanation we have to date is that they result from quantum vacuum fluctuations which were amplified by a rapid accelerated expansion (called inflation) in the very early universe ($\approx 10^{-35}s$ after the big bang). The model of structure formation, which describes how these fluctuations grew to the present state has three key ingredients. One needs to specify the cosmological model (the expansion rate, which follows from the cosmological density parameters) to define the background geometry of the universe. Further, a model for fluctuation generation and the amount and type of dark matter needs to be known. For example light neutrinos might be considered as dark matter particles, however since they were relativistic when their thermal equilibrium was frozen as well as at the time the structures started to form, they can easier escape the gravitational potential than non-relativistic particles. This influences the growth of structures and the results show that neutrinos are not a suitable candidates for a dark matter particle. Having specified these ingredients one is able to predict the evolution of dark matter. If the underlying assumptions are correct, the predicted structure formation scenario matches the observations, i.e. the CMB fluctuations and the matter structure we see in the universe today. The most successful model nowadays is the cold dark matter theory including dark energy (ΛCDM), with initial conditions from inflation. Although it might still be proven incorrect in detail, it is at present the model that most comprehensively explains the observations. It assumes nearly scale-invariant initial fluctuations resulting from inflation and a type of dark matter that is cold, meaning that particles are non-relativistic at the time the structures started to form and can not free-stream out of the potential wells at the scales of cosmological interest. Since the density fluctuations can only start growing when the universe is matter dominated, the growth process depends upon the cosmological parameters. In the framework of this model we can now investigate how the structures evolve to the present state (galaxies, clusters, large-scale-structure). In the CDM model the numerical simulations predict that we have a so-called bottom-up or hierarchical scenario of structure formation. This means that the small-scale structures formed first and the more massive clumps were assembled in the process of merging. By comparing the predictions from N-body simulations to observed systems we can test the hypotheses of the structure formation model and make a further step in understanding the cosmological history and future of the universe.

Why gravitational lensing

Light bundles travelling through an inhomogeneous universe will be deflected and therefore focused (or defocused). The inhomogeneities in fact act as a gravitational telescope (thus the term lensing). The gravitational lensing effects offer an excellent tool to study the matter in the universe, since it is independent of whether the matter is luminous or dark. Since other methods to determine the mass

distribution depend on the information we get from objects through their luminous parts, it is usually difficult to convert this information to reveal the total matter distribution. Gravitational lensing, on the other hand, probes the distribution directly and therefore it has become one of the major tools in cosmology. In this thesis I mostly concentrate on two applications of lensing: measuring the mass distribution of individual galaxies and galaxy clusters. In the case where source, observer and the lens are almost aligned, and the lens is strong enough, the light bundles can travel on different paths to the observer, and multiple images of the same source can be seen. Such systems are of particular interest in gravitational lensing. To date about 100 such systems with galaxies acting as lenses have been discovered. The properties of these multiple images (their positions w.r.t. the lens galaxy centre and fluxes) can be used to draw conclusions about the mass distribution of the lens galaxy. In particular, it turns out, that the flux ratios of the images are sensitive not only to the main lens potential but also to its small-scale structure (i.e. dwarf galaxies orbiting the main galaxy).

Their properties can thus be investigated. An example of such a lens system is presented in Fig. P-1 Four quasar images belong to the same source. The lens galaxy is in the center. Chapter 2 will briefly describes the status of the observed multiple galaxy lens systems and explores the image configurations of a recent descovered new lens spiral candidate.

In clusters of galaxies the same effect can be observed as well. In addition to these strong distortions (also called strong lensing effect), many background sources are weakly distorted (weak lensing effect). The statistical analysis of such distortion can give us further information (up to larger radii than strong lensing) about the mass and mass distribution of clusters. The latter can not be used to detect galaxies as lenses individually, since only the cluster potential is strong enough for this effect to be observed in practice.

An excellent example is given in Fig. P-2. The latest camera, ACS, on board the Hubble Space Telescope offers an exquisite resolution and many strongly distorted multiply imaged sources can be seen. The weakly distorted sources can not be readily recognised by eye, only when their statistical properties are studied do they reveal information about the mass-distribution of the cluster.

Gravitational lensing by galaxies

The main evidence in the past that large amounts of dark matter exist in galaxies is their flat rotation curves. The constant rotation velocities in the outer parts of the galaxy, instead of a Keplerian decline (typical if only visible matter is taken into account), indicate that each galaxy is surrounded by significant amounts of dark matter. This has made galaxies particularly interesting in terms of cosmological research.

It has been argued that the standard CDM paradigm is very successful in predicting the observed properties of dark matter on different mass scales. Therefore results that are in apparent contradiction with this theory are of extreme interest. In galaxies we seem to be facing two problems of this kind. From the numerical simulations one can identify collapsed structures (also called halos) and study their properties. It turns out that the density profile of halos has a universal form, almost independent of the mass of the halo. This result was first found by Julio Navarro, Carlos Frenk & Simon White in the nineties, and the functional form of the profile is simply referred to as the NFW profile (Navarro, Frenk and White 1997 [195]). It is a very remarkable result, since if the simulations are correct, galaxies and clusters of galaxies should have the same universal form (NFW) of the dark matter density distribution. In the very centre of the halos the density distribution is especially sensitive to the assumed nature of the dark matter. The CDM paradigm predicts a very steep dark matter profile in the centres of halos. This seems to be at odds with what we observe. However, on galaxy scales it is difficult to test this prediction accurately both from observations and simulations. Namely, these simulations were done with dark matter only and, especially on galaxy scales, the baryons are believed to play a very important role. Not only would they modify the density profile we measure (with gravitational lensing we measure together dark and luminous matter), they also influence the density profile of dark matter itself throughout the process of halo formation. The sec-

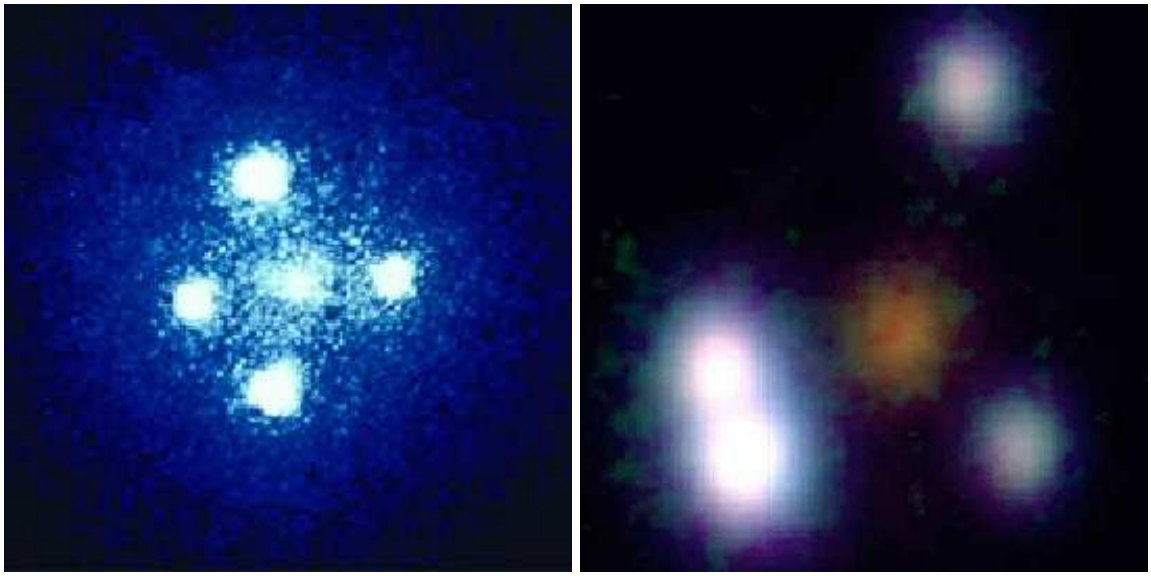

Figure P-1. Two lens configurations. On the left, the Einstein cross: a galaxy (in the center) acting as a lens. The gravitationally lensed system G2237-0305, as seen by the HST with a quasar being lensed to four images (from the web). On the right, another similar example, the system PG1115+080 (from the web)

ond problem is the substructure problem. In simulations representing halos similar to our Galaxy, the number of substructures (halos with mass smaller than the main galaxy) does not match to what we observe in the Milky Way. The problem is especially striking for low mass halos (10^6 times less massive than the main galaxy). This problem was independently discovered by Ben Moore and Anatoly Klypin and colleagues in 1998 and has ever since posed a serious challenge to the CDM paradigm. The solution to this problem is that either the simulations and/or assumptions entering the structure formation model are wrong on these scales, or the sub-halos are indeed present in the Milky Way, however they have lost baryons in the past and are too dark to be observed. In next Chapters we will investigate this discrepancy for galaxies other than the Milky Way using the gravitational lensing techniques.

Gravitational lensing by clusters of galaxies

Galaxy clusters have been the focus of a very intense ongoing research in the past decades. They are the most massive bound structures in the Universe; moreover, their large dynamical time scale allows them to retain the information about their formation history. A cluster contains hundreds or even thousands of galaxies, which however do not contain a large fraction of cluster mass. The galaxy clusters are believed to be a 'fair sample' of the matter content of the universe, therefore the ratio of their baryonic (i.e. luminous) mass to their total mass resembles the overall baryonic fraction in the universe. In addition the evolution in their number density as a function of mass and the time of their formation is a very important probe which can help us determine the matter content as well as the dark energy content in the universe.

It is therefore crucial to be able to make reliable estimates of cluster masses. This can be achieved by e.g. measuring the velocities of individual galaxies or from the properties of the X-ray emission of the intra-cluster gas. The latter technique has been successfully applied to many clusters. Unfortunately assumptions about hydrostatic equilibrium and spherical symmetry need to be made for to convert the luminosity of the X-ray emitting gas to the cluster mass. Gravitational lensing can also measure cluster mass to high accuracy and is free of the assumptions of baryonic physics. The problems of using gravitational lensing to determine the cluster mass are not in the underlying physics, which is well understood, but rather in the technical implementation. However, such problems are being resolved with advancing observational techniques and new instrumental

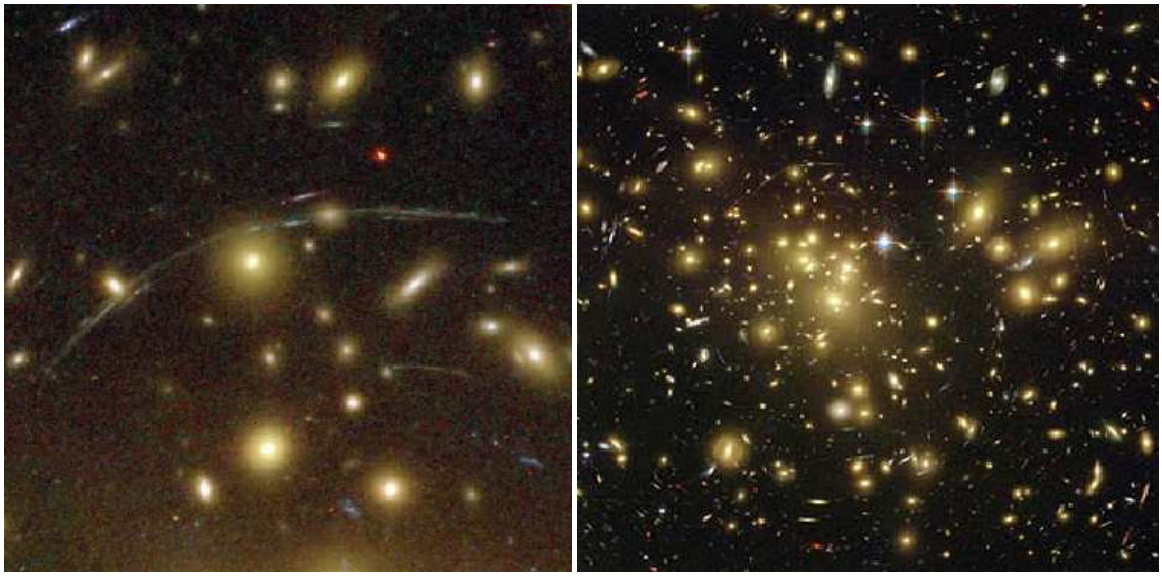

Figure P-2. Galaxy clusters acting as a lens. Many strongly distorted multiply imaged sources (arcs) can be seen (from HST press release).

tools (e.g. NGST will succeed HST telescope) and at present the measurements of cluster masses with gravitational lensing are a great success. In Chapter 7 we describe an application of the strong lensing joint to X-ray analysis to study the most X-ray luminous cluster at present and successfully measure its mass and mass distribution.

Chapter 1

Introduction to Gravitational Lensing

Gravitational lensing has developed into a versatile tool for observational cosmology. The deflection angle of a light ray is determined by the gravitational field of the matter distribution along its path. The gravitational field, and thus the deflection angle, depend neither on the nature of the matter nor on its physical state. Light deflection probes the total matter density, without distinguishing between ordinary (baryonic) matter or dark matter. In contrast to other dynamical methods for probing gravitational fields, no assumption needs to be made on the dynamical state of the matter. For example, the interpretation of radial velocity measurements in terms of the gravitating mass requires the applicability of the virial theorem (i.e., the physical system is assumed to be in virial equilibrium), or knowledge of the orbits (such as the circular orbits in disk galaxies) (Schneider, Ehlers, Falco 1992 [145]). In this way it is possible to directly investigate the dark-matter distribution led to substantial results over recent years. Constraints on the size of the dark-matter haloes of spiral galaxies were derived, the presence of dark-matter haloes in elliptical galaxies was demonstrated, and the projected total mass distribution in many cluster of galaxies was mapped. These results have a direct impact on our understanding of structure formation, providing essential informations on the cosmological parameters, supporting hierarchical structure formation in cold dark matter (CDM) models.

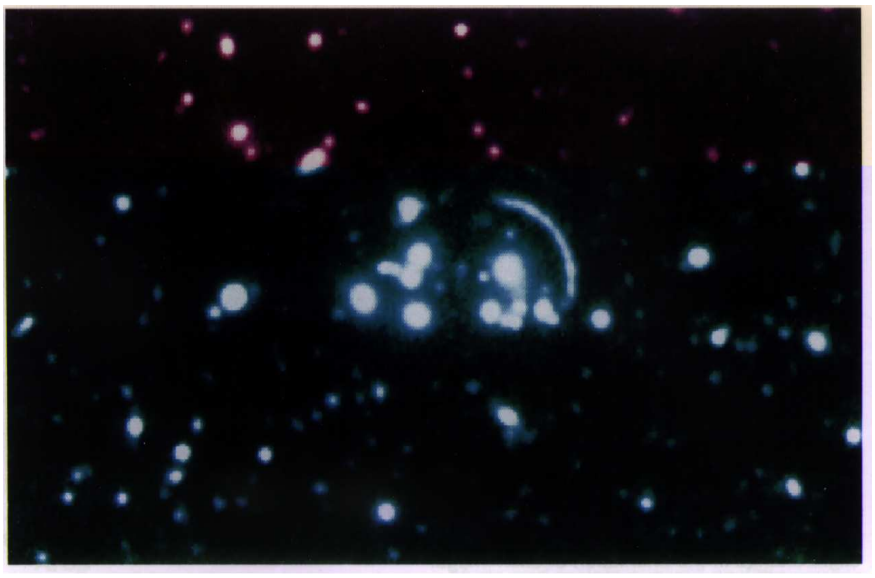

Figure 1.1. Giant arc in Cl2244-02 (image from CFHT). The lensing cluster is at $z = 0.329$ and the source of the arc is a very distant field galaxy at $z = 2.238$. (Courtesy of G. Soucail, Obs. Midi–Pyrénées, ESO Messenger 69, September 1992.)

1.1 Historical remarks

Nowadays we know that the light propagation in a gravitational field has to be described using the theory of general relativity by Einstein formulated in 1915. However, long before it was argued that gravity might influence the behaviour of light (for a historical account, see for instance the book by Schneider et al. [4]). Indeed, already Newton in the first edition of his book on optics appeared in 1704 discussed the possibility that celestial bodies could deflect the light trajectory. In 1804 the astronomer Soldner published a paper in which he computed the error induced by the light deflection on the determination of the position of stars. To that purpose he used the Newtonian theory of gravity assuming that the light is made of particles. He also estimated that a light ray which just grazes the surface of the sun would be deflected by a value of only 0.85 arc seconds. Within general relativity this value is about twice as much, more precisely 1.75 arc seconds. The first measurement of this effect has been made during the solar eclipse of 29 mai 1919 and confirmed the value predicted by general relativity [8].

In 1936 Einstein published a short paper in Science in which he computed the light deflection of light coming from a distant star by the gravitational field of another star [9]. He mentioned that if the source and the lens are perfectly aligned the image would be a ring. If instead the alignment is not perfect one would see two images with, however, a very small separation angle. Einstein also wrote: "Of course, there is no hope of observing this phenomenon". Actually, it has been found recently that Einstein made most of the calculations presented in that paper already in 1912 as can be seen on some pages of his notebook [10]. The recent developments of microlensing show that Einstein's conclusion, although understandable at that time, was too pessimistic. Indeed, the formulae developed by Einstein in his 1936 paper are still the basis for the description of gravitational lensing.

In the following year 1937 the swiss astronomer Zwicky wrote two short articles in Physical Review suggesting to consider galaxies as sources and lenses rather than stars as mentioned by Einstein [11]. He came to the conclusion that such a configuration would have much higher chances to be seen, since the typical mass of a galaxy is several billion times higher than the mass of as single star. He argued that such configurations must almost certainly be seen. Moreover, he gave also a list of possible applications among which the possibility to better determine the total mass of galaxies, including their dark matter content.

The first gravitational lens has been discovered in 1979, when spectra were obtained of two point-like quasars which lie only about 6 arc seconds away. The spectra showed that both objects have the same redshift and are thus at the same distance. Later on also the galaxy acting as lens has been found, making it clear that the two objects are the images of the same quasar, which is lensed. Since then many other examples have been found, and in 1986 the first lensing case with a galaxy acting as source was discovered. The galaxy appears then distorted as one or more arcs. Many such systems have since then be discovered, some thanks to the Hubble space telescope. The year 1988 saw the discovery of the extended radio source with the astronomical designation MG1131+0456, which turned out to be the first example of an "Einstein ring", with a diameter of 1.75 seconds of arc.

In 1979, Chang and Refsdal [12], and in 1981, Gott [13] noted that even though a point mass in a halo of a distant galaxy would create an unresolvable double image of a background quasar, the time variation of the combined brightness of the two images could be observed. In this way, the effect of non-luminous matter in the form of compact objects could be observed. The term *microlensing* was proposed by Paczyński [14] to describe gravitational lensing which can be detected by measuring the intensity variation of a macro-image made up of any number of unresolved micro-images.

In 1993 the first galactic microlensing events were observed, in which the source is a star in the Large Magellanic Cloud and the galactic bulge. In the former case the lens is a compact object probably located in the galactic halo, whereas in the later case the lens is a low mass star in the galactic disk or in the bulge itself.

Nowadays, astronomers know of many dozens of systems with multiple images, as well as of a few Einstein rings. In late 2006, the CfA-Arizona Space Telescope Lens Survey (CASTLeS) counted ≈ 90 clearly identified lens systems with multiple images, as well as 18 unconfirmed candidate systems.

In the twenty-first century, gravitational lensing is a highly active field of astrophysical research. Since the first conference exclusively devoted to gravitational lensing was held in Liege, France, in 1983, there have been similar international conferences every year.

The reason for the field's growth is that, today, gravitational lenses are much more than just an interesting general relativistic phenomenon. Now that a significant number of lens systems has been identified (see chapter 2), lensing is used more and more as an observation tool, allowing astronomers to answer astrophysical as well as cosmological questions, from estimates of the amount of dark matter contained in the lens mass to the determination of fundamental parameters of the big bang models.

1.2 Lens equation

1.2.1 Point-like lenses

The propagation of light in a curved space-time is in general a complicated problem, however, for almost all relevant applications of gravitational lensing one can assume that the geometry of the universe is described in good approximation by the Friedmann-Lemaître-Robertson-Walker metric. The inhomogeneities in the metric can be considered as local perturbations. Thus the trajectory of the light coming from a distant source can be divided into three distinct pieces. In the first one the light coming from a distant source propagates in a flat unperturbed space-time, nearby the lens the trajectory gets modified due to the gravitational potential of the lens and afterwards in the third piece the light travels again in an unperturbed space-time till it gets to the observer. The region around the lens can be described by a flat Minkowskian space-time with small perturbations induced by the gravitational potential of the lens. This approximation is valid as long as the Newtonian potential Φ is small, which means $\mid \Phi \mid \ll c^2$ (c being the velocity of light), and if the peculiar velocity v of the lens is negligible as compared to c. These conditions are almost always fulfilled in all cases of interests for the astrophysical applications. An exception, for instance, is when the light rays get close to a black hole. We will not discuss such cases in the following.

With the above simplifying assumptions we can describe the light propagation nearby the lens in a flat space-time with a perturbation due to the gravitational potential of the lens described in first order post-Newtonian approximation. The effect of the space-time curvature on the light trajectory can be described as an effective refraction index, given by

$$n = 1 - \frac{2}{c^2}\Phi = 1 + \frac{2}{c^2} \mid \Phi \mid \ . \tag{1.1}$$

The Newtonian potential is negative and vanishes asymptotically. As in geometrical optics a refraction index $n > 1$ means that the light travels with a speed which is less as compared with its speed in the vacuum. Thus the effective speed of light in a gravitational field is given by

$$v = \frac{c}{n} \simeq c - \frac{2}{c} \mid \Phi \mid \ . \tag{1.2}$$

Since the effective speed of light is less in a gravitational field, the travel time gets longer as compared to the propagation in the empty space. The total time delay Δt is obtained by integrating along the light trajectory from the source till the observer, as follows

$$\Delta t = \int_{source}^{observer} \frac{2}{c^3} \mid \Phi \mid dl \ . \tag{1.3}$$

This is also called the Shapiro delay.

The deflection angle for the light rays which go through a gravitational field is given by the integration of the gradient component of n perpendicular to the trajectory itself

$$\vec{\alpha} = -\int \vec{\nabla}_\perp n \; dl = \frac{2}{c^2} \int \vec{\nabla}_\perp \Phi \; dl \; . \tag{1.4}$$

For all astrophysical applications of interest the deflection angle is always extremely small, so that the computation can be substantially simplified by integrating $\vec{\nabla}_\perp n$ along an unperturbed path, rather than the effective perturbed path. The so induced error is of higher order and thus negligible.

As an example lets consider the deflection angle of a point-like lens of mass M. Its Newtonian potential is given by

$$\Phi(b,z) = -\frac{GM}{(b^2+z^2)^{1/2}} \; , \tag{1.5}$$

where b is the impact parameter of the unperturbed light ray and z denotes the position along the unperturbed path as measured from the point of minimal distance from the lens. This way we get

$$\vec{\nabla}_\perp \Phi(b,z) = \frac{GM \; \vec{b}}{(b^2+z^2)^{3/2}} \; , \tag{1.6}$$

where $\vec{b}$ is orthogonal to the unperturbed light trajectory and is directed towards the point-like lens. Inserting eq.(1.6) in eq.(1.4) we find for the the deflection angle

$$\vec{\alpha} = \frac{2}{c^2} \int \vec{\nabla}_\perp \Phi \; dz = \frac{4GM}{c^2 b} \; \frac{\vec{b}}{b} \; . \tag{1.7}$$

The Schwarzschild radius for a body of mass M is given by

$$R_S = \frac{2GM}{c^2} \; , \tag{1.8}$$

thus the absolute value of the deflection angle can also be written as $\alpha = 2R_S/b$. For the Sun the Schwarzschild radius is 2.95 km, whereas its physical radius is 6.96×10^5 km. Therefore, a light ray which just grazes the solar surface is deflected by an angle corresponding to $1.7''$.

1.2.2 Thin lens approximation

From the above considerations one sees that the main contribution to the light deflection comes from the region $\Delta z \sim \pm b$ around the lens. Typically, Δz is much smaller than the distance between the observer and the lens and the lens and the source, respectively. The lens can thus be assumed to be thin as compared to the full length of the light trajectory. Thus one considers the mass of the lens, for instance a galaxy cluster, projected on a plane perpendicular to the line of sight (between the observer and the lens) and going through the center of the lens. This plane is usually referred to as the lens plane, and similarly one can define the source plane. The projection of the lens mass on the lens plane is obtained by integrating the mass density ρ along the direction perpendicular to the lens plane

$$\Sigma(\vec{\xi}\,) = \int \rho(\vec{\xi}, z) \; dz \; , \tag{1.9}$$

where $\vec{\xi}$ is a two dimensional vector in the lens plane and z is the distance from the plane. The deflection angle at the point $\vec{\xi}$ is then given by summing over the deflection due to all mass elements in the plane as follows

$$\vec{\alpha} = \frac{4G}{c^2} \int \frac{(\vec{\xi} - \vec{\xi}')\Sigma(\vec{\xi}')}{|\,\vec{\xi} - \vec{\xi}'\,|^2} \; d^2\xi' \; . \tag{1.10}$$

In the general case the deflection angle is described by a two dimensional vector, however in the special case that the lens has circular symmetry one can reduce the problem to a one-dimensional

situation. Then the deflection angle is a vector directed towards the center of the symmetry with absolute value given by

$$\alpha = \frac{4GM(\xi)}{c^2 \xi} \ , \tag{1.11}$$

where ξ is the distance from the center of the lens and $M(\xi)$ is the total mass inside a radius ξ from the center, defined as

$$M(\xi) = 2\pi \int_0^{\xi} \Sigma(\xi') \ \xi' \ d\xi' \ . \tag{1.12}$$

1.2.3 Lens equation

The geometry for a typical gravitational lens is given in Figure 1.2 A light ray from a source S (in $\vec{\eta}$) is deflected by the lens by an angle $\vec{\alpha}$ (with impact parameter $\mid \vec{\xi} \mid$) and reaches the observer located in O.

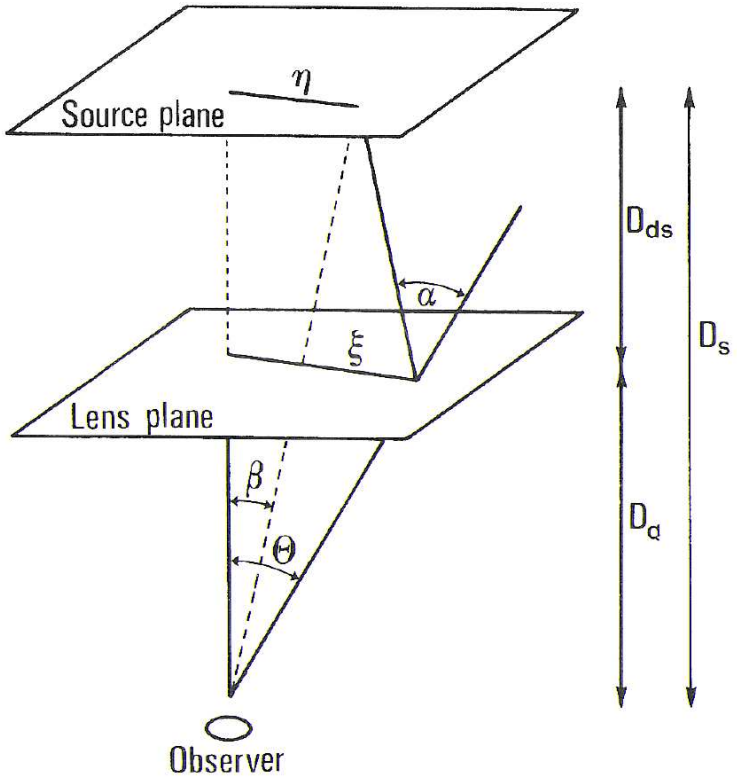

Figure 1.2. Notation for the lens geometry.

The angle between the optical axis (arbitrarily defined) and the true source position is given by $\vec{\beta}$, whereas the angle between the optical axis and the image position is $\vec{\theta}$. The distances between the obser and the lens, the lens and the source, and the observer and the source are, respectively, D_d, D_{ds} and D_s. From Figure 1.2 one can easily derive (assuming small angles) that $\theta D_s = \beta D_s + \alpha D_{ds}$.

Thus the positions of the source and the image are related by the following equation

$$\vec{\beta} = \vec{\theta} - \vec{\alpha}(\vec{\theta}\,)\frac{D_{ds}}{D_s}\ , \tag{1.13}$$

which is called the *lens equation*. It is a non-linear equation so that it is possible to have several images $\vec{\theta}$ corresponding to a single source position $\vec{\beta}$.

The lens equation (1.13) can also be derived using the Fermat principle, which is identical to the classical one in geometrical optics but with the refraction index as defined in eq.(4.1). The light trajectory is then given by the variational principle

$$\delta \int n\ dl = 0\ . \tag{1.14}$$

It express the fact that the light trajectory will be such that the traveling time will be extremal. Lets consider a light ray emitted from the source S at time $t = 0$. It will then proceed straight till it reaches the lens, located at the point I, and where it will be deflected and then proceed again straight to the observer in O. We thus have

$$t = \frac{1}{c}\int \left(1 - \frac{2\phi}{c^2}\right) dl = \frac{l}{c} - \frac{2}{c^3}\int \phi\ dl \tag{1.15}$$

where l is the distance SIO (Euclidean distance). The term containing ϕ has to be integrated along the light trajectory. From Fig. 1.2 we see that

$$\begin{aligned} l &= \sqrt{(\vec{\xi} - \vec{\eta})^2 + D_{ds}^2} + \sqrt{\vec{\xi}^2 + D_d^2} \\ &\simeq D_{ds} + D_d + \frac{1}{2D_{ds}}(\vec{\xi} - \vec{\eta})^2 + \frac{1}{2D_d}\vec{\xi}^2\ , \end{aligned} \tag{1.16}$$

where $\vec{\eta}$ is a two dimensional vector in the source plane If we take $\phi = -GM/\mid \vec{x}\mid$ (corresponding to a point-like lens of mass M) we get

$$\int_S^I \frac{2\phi}{c^3}\ dl = \frac{2GM}{c^3}\left[ln\frac{\mid \vec{\xi}\mid}{2D_{ds}} + \frac{\vec{\xi}\cdot(\vec{\eta} - \vec{\xi}\,)}{\mid \vec{\xi}\mid D_{ds}} + \mathcal{O}\left(\frac{(\vec{\eta} - \vec{\xi}\,)^2}{D_{ds}}\right)\right] \tag{1.17}$$

and similarly for $\int_I^O 2\phi/c^3\ dl$.

Only the logarithmic term is relevant for lensing, since the other ones are of higher order. Moreover, instead of a point-like lens we consider a surface mass density $\Sigma(\vec{\xi}\,)$ (as defined in eq.(1.9)) and so we get for the integral containing the potential term (neglecting higher order contributions)

$$\frac{2}{c^3}\int \phi\ dl = \frac{4G}{c^3}\int d^2\xi'\ \Sigma(\vec{\xi'})\ ln\frac{\mid \vec{\xi} - \vec{\xi'}\mid}{\xi_0}\ , \tag{1.18}$$

where ξ_0 is a characteristic length in the lens plane and the right hand side term is defined up to a constant.

The difference in the arrival time , between the situation which takes into account the light deflection due to the lens and without the lens, is obtained by summing eq.(1.16) to eq.(1.18) and by subtracting the travel time without deflection from S to O. This way one gets

$$c\Delta t = \hat{\phi}(\vec{\xi}, \vec{\eta}) + const.\ , \tag{1.19}$$

where $\hat{\phi}$ is the *Fermat potential* defined as

$$\hat{\phi}(\vec{\xi}, \vec{\eta}) = \frac{D_d D_s}{2D_{ds}}\left(\frac{\vec{\xi}}{D_d} - \frac{\vec{\eta}}{D_s}\right)^2 - \hat{\psi}(\vec{\xi}\,) \tag{1.20}$$

and

$$\hat{\psi}(\vec{\xi}) = \frac{4G}{c^2} \int d^2\xi' \; \Sigma(\vec{\xi}') \; ln \left(\frac{\mid \vec{\xi} - \vec{\xi}' \mid}{\xi_0} \right) \tag{1.21}$$

is the *deflection potential*, which does not depend on $\vec{\eta}$. The Fermat principle can thus be written as $\frac{d\Delta t}{d\vec{\xi}} = 0$, and inserting eq.(1.19) one gets again the lens equation

$$\vec{\eta} = \frac{D_s}{D_d}\vec{\xi} - D_{ds} \; \vec{\alpha}(\vec{\xi}\,) \; , \tag{1.22}$$

where $\vec{\alpha}$ is defined in eq.(1.10). (If we define $\vec{\beta} = \vec{\eta}/D_s$ and $\vec{\theta} = \vec{\xi}/D_d$ we get eq.(1.13)). One can also write eq.(1.22) as follows

$$\nabla_{\vec{\xi}} \; \hat{\Phi}(\vec{\xi}, \vec{\eta}) = 0 \; , \tag{1.23}$$

which is an equivalent formulation of the Fermat principle.

The arrival time delay of light rays coming from two different images (due to the same source in $\vec{\eta}$) located in $\vec{\xi}^{\,(1)}$ and $\vec{\xi}^{\,(2)}$ is given by

$$c(t_1 - t_2) = \hat{\Phi}(\vec{\xi}^{\,(1)}, \vec{\eta}) - \hat{\Phi}(\vec{\xi}^{\,(2)}, \vec{\eta}) \; . \tag{1.24}$$

1.2.4 Remarks on the lens equation

It is often convenient to write (1.22) in a dimensionless form. Let ξ_0 be a length parameter in the lens plane (whose choice will depend on the specific problem) and let $\eta_0 = (D_s/D_d)\xi_0$ be the corresponding length in the source plane. We set $\vec{x} = \vec{\xi}/\xi_0, \quad \vec{y} = \vec{\eta}/\eta_0$ and

$$\kappa(\vec{x}) = \frac{\Sigma(\xi_0\vec{x})}{\Sigma_{crit}} \; , \qquad \vec{\alpha}(\vec{x}) = \frac{D_d D_{ds}}{\xi_0 D_s}\hat{\vec{\alpha}}(\xi_0\vec{x}) \; , \tag{1.25}$$

where we have defined a critical surface mass density

$$\Sigma_{crit} = \frac{c^2}{4\pi G}\frac{D_s}{D_d D_{ds}} = 0.35 \; g \; cm^{-2} \left(\frac{1 \; Gpc}{D} \right) \tag{1.26}$$

with $D \equiv \frac{D_d D_{ds}}{D_s}$ ($1 \; Gpc = 10^9 \; pc$). Then eq. (1.22) reads as follows

$$\vec{y} = \vec{x} - \vec{\alpha}(\vec{x}) \; , \tag{1.27}$$

with

$$\vec{\alpha}(\vec{x}) = \frac{1}{\pi} \int_{R^2} \frac{\vec{x} - \vec{x}'}{\mid \vec{x} - \vec{x}' \mid^2} \kappa(\vec{x}') d^2x' \; . \tag{1.28}$$

In the following we will mainly use the previous notation rather than the above one.

An interesting case is a lens with a constant surface mass density Σ. With eq.(1.11) one finds then for the deflection angle

$$\alpha(\theta) = \frac{4G}{c^2\xi} \; \Sigma\pi\xi^2 = \frac{4\pi G\Sigma}{c^2} \; D_d\theta \; , \tag{1.29}$$

using $\xi = D_d\theta$. In this case the lens equation (1.13) is linear, which means that β is proportional to θ

$$\beta = \theta - \beta = \theta - \frac{4\pi G}{c^2}\frac{D_{ds}D_d}{D_s} \; \Sigma \; \theta = \theta - \frac{\Sigma}{\Sigma_{crit}}\theta \; . \tag{1.30}$$

From eq.(1.30) we immediately sy see that for a lens with a critical surface mass density we get for all values of θ: $\beta = 0$. Such a lens would perfectly focus, with a well defined focal length. Typical gravitational lenses behave, however, quite differently. A lens which has $\Sigma > \Sigma_{crit}$ somewhere in it

is defined as *supercritical*, and has in general multiple images.

Defining $k(\vec{\theta}\,) := \Sigma(\vec{\theta}D_d)/\Sigma_{crit}$ we can write the lens equation as follows

$$\vec{\beta} = \vec{\theta} - \vec{\tilde{\alpha}}(\vec{\theta}\,)\ , \tag{1.31}$$

with

$$\vec{\tilde{\alpha}}(\vec{\theta}\,) = \frac{1}{\pi}\int_{R^2} d^2\theta'\ k(\vec{\theta'})\ \frac{\vec{\theta}-\vec{\theta'}}{\mid \vec{\theta}-\vec{\theta'}\mid^2}\ . \tag{1.32}$$

Moreover

$$\vec{\tilde{\alpha}}(\vec{\theta}\,) = \nabla_{\vec{\theta}}\ \Psi(\vec{\theta}\,) \tag{1.33}$$

where

$$\Psi(\vec{\theta}\,) = \frac{1}{\pi}\int_{R^2} d^2\theta' k(\vec{\theta'})\ ln\mid \vec{\theta}-\vec{\theta'}\mid\ . \tag{1.34}$$

The Fermat potential is given by

$$\Phi(\vec{\theta},\vec{\beta}\,) = \frac{1}{2}(\vec{\theta}-\vec{\beta}\,)^2 - \Psi(\vec{\theta}\,) \tag{1.35}$$

and we get then the lens equation from

$$\nabla_{\vec{\theta}}\ \Phi(\vec{\theta},\vec{\beta}) = 0\ . \tag{1.36}$$

Notice that

$$\Delta\Psi = 2k \geq 0 \tag{1.37}$$

(using $\Delta\ ln\mid\vec{\theta}\mid = 2\pi\delta^2(\vec{\theta}\,)$), since k as a surface mass density is always positive (or vanishes).

The flux of a source, located in $\vec{\beta}$, in the solid angle $d\Omega(\vec{\beta}\,)$ is given by

$$S(\vec{\beta}\,) = I_\nu\ d\Omega(\vec{\beta}\,)\ . \tag{1.38}$$

I_ν is the intensity of the source in the frequency ν. $S(\vec{\beta}\,)$ is the flux one would see if there were no lensing. On the other hand the observed flux from the image located in $\vec{\theta}$ is

$$S(\vec{\theta}\,) = I_\nu\ d\Omega(\vec{\theta}\,)\ . \tag{1.39}$$

I_ν does not change, since the total number of photons stays constant as well as their frequency. The amplification factor μ is thus given by the ratio

$$\mu = \frac{d\Omega(\vec{\theta}\,)}{d\Omega(\vec{\beta}\,)} = \frac{1}{detA(\vec{\theta}\,)}\ , \tag{1.40}$$

with

$$A(\vec{\theta}\,) = \frac{d\vec{\beta}}{d\vec{\theta}}\ \ (A_{ij} = \frac{d\beta_i}{d\theta_j} = \delta_{ij} - \Psi_{,ij})\ , \tag{1.41}$$

(where $\Psi_{,ij} = \partial_i\partial_j\Psi$) which is the Jacobi matrix of the corresponding lens mapping given by eq.(1.31). Notice that the amplification factor μ can be positive or negative. The corresponding image will then have *positive or negative parity*, respectively.

For some values of $\vec{\theta}$, $detA(\vec{\theta}\,) = 0$ and thus $\mu \to \infty$. The points (or the curve) $\vec{\theta}$ in the lens plane for which $detA(\vec{\theta}\,) = 0$ are defined as *critical points (or critical curve)* . At these points the geometrical optics approximation used so far breaks down.

The corresponding points (or curve) of the critical points in the source plane are the so called *caustics* . Fig. 1.3 shows critical and caustic lines, and also the regions with different multiplicity (see sec 1.2.5), for an elliptical lens. The matrix A_{ij} is often parametrized as follows

$$A_{ij} = \begin{pmatrix} 1-k-\gamma_1 & -\gamma_2 \\ -\gamma_2 & 1-k+\gamma_1 \end{pmatrix} \tag{1.42}$$

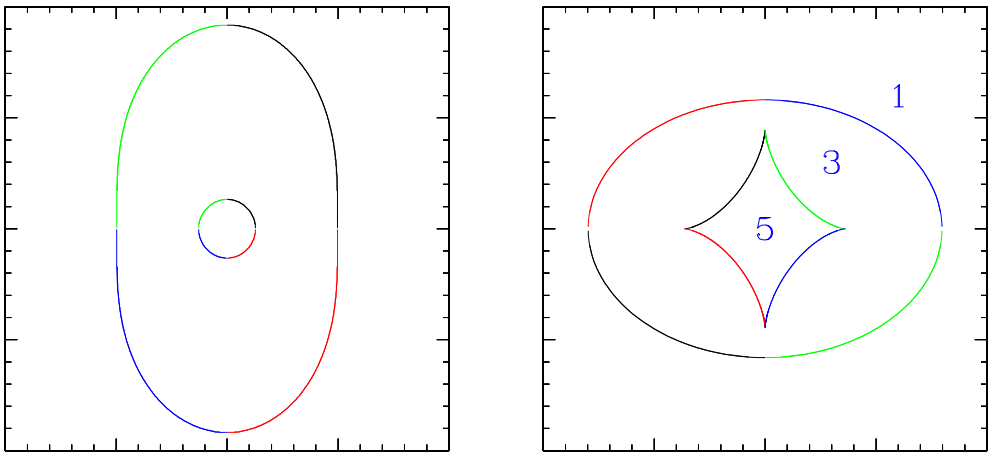

Figure 1.3. The critical curves (left panel) and caustics (right panel) for an elliptical lens. The numbers in the right panels identify regions in the source plane that correspond to 1, 3 or 5 images, respectively. The smooth lines in the right hand panel are called fold caustics; the tips at which in the inner curve two fold caustics connect are called cusp caustics.

with $\gamma_1 = \frac{1}{2}(\Psi_{,11} - \Psi_{,22})$, $\gamma_2 = \Psi_{,12} = \Psi_{,21}$ and $\vec{\gamma} = (\gamma_1, \gamma_2)$. We have therefore

$$detA_{ij} = (1-k)^2 - \gamma^2 \tag{1.43}$$

and $\gamma = \sqrt{\gamma_1^2 + \gamma_2^2}$,

$$trA_{ij} = 2(1-k) \ . \tag{1.44}$$

The eigenvalues of A_{ij} are $a_{1,2} = 1 - k \pm \gamma$.

As next, we study how small circles in the source plane are deformed. Consider a small circular source with radius R at $\vec{y}$, bounded by a curve described by

$$\vec{c}(t) = \vec{y} + \begin{pmatrix} R\ \cos t \\ R\ \sin t \end{pmatrix} \qquad (0 \le t \le 2\pi) \ . \tag{1.45}$$

The corresponding boundary curve of the image is

$$\vec{d}(t) = \vec{x} + A^{-1} \begin{pmatrix} R\ \cos t \\ R\ \sin t \end{pmatrix} . \tag{1.46}$$

Inserting the parametrization (1.42) one finds that the image is an ellipse centered on $\vec{x}$ with semi–axes parallel to the main axes of A, with magnitudes

$$\frac{R}{\mid 1 - \kappa \pm \gamma \mid} \ , \tag{1.47}$$

and the position angles $\varphi_\pm$ for the axes are

$$\tan\varphi_\pm = \frac{\gamma_1}{\gamma_2} \mp \sqrt{\left(\frac{\gamma_1}{\gamma_2}\right)^2 + 1} \ or \qquad \tan 2\varphi_\pm = -\frac{\gamma_2}{\gamma_1} \ . \tag{1.48}$$

The ellipticity of the image is defined as follows

$$\epsilon = \epsilon_1 + i\epsilon_2 = \frac{1-r}{1+r} e^{2i\varphi} \ , \quad r \equiv \frac{b}{a} \ , \tag{1.49}$$

where φ is the position angle of the ellipse and a and b are the major and minor semiaxes, respectively. a and b are proportional to the inverse of the eigenvalues of the matrix A_{ij} defined in eq. (1.42), thus: $a = R(1-k-\gamma)^{-1}$ and $b = R(1-k+\gamma)^{-1}$. ϵ describes the orientation and the shape of the ellipse and is thus observable. Lets denote $g = \mid \epsilon \mid$ with

$$g = \frac{\gamma}{1-\kappa} \qquad \left(\vec{g} = \frac{\vec{\gamma}}{1-\kappa}\right) \ , \tag{1.50}$$

which is called the *reduced shear*. Often one uses a complex notation with $\gamma = \gamma_1 + i\gamma_2$ and accordingly one defines then a complex reduced shear.

1.2.5 Lens mapping close to the critical curves

In general, the Jacobian matrix $\mathrm{A}(\theta)$ is not necessary invertible, i.e. there may exist points in the lens plane where the determinant of the matrix vanishes. We have seen that they form closed curves, called *critical curves*. Mapping them back to the source plane gives the *caustic curves*. The image of a point source that lies on the caustic curve is formally infinitely magnified. In practice, any deviation from a source being point like causes a finite (still very high) magnification. Physically, however, even point sources would have finite magnification, since in all derivations we use a description of lensing based on geometrical optics, which fails very close to critical curves. Namely two images located close to the critical curve have a very small differential time delay and one expects interferences to occur if this time delay is smaller than the coherence time of the light (Schneider et al., 1992). Nevertheless, the corrections in the framework of wave optics are very small and the geometric description is more than adequate for the purposes we are dealing with here.

We illustrate the image formation for a source crossing the caustic curve in Fig. 1.4 through an example of a typical singular isothermal elliptical (SIE) lens (see sec. 1.6). A SIE model is an approximate description for the projected mass density of a typical elliptical galaxy. In the left panel the lens plane is plotted and the critical curves are presented as solid lines. Through the lens mapping, the inner critical curve (i.e. inner ellipse) transforms onto the outer caustic curve (see right panel of the same figure, presenting the source plane) and the outer critical curve transforms into the inner, asteroid caustic. The asteroid caustic has four fold caustics (curved lines) and where two fold caustics join we get a so-called cusp.

Since images forming close to the inner critical curve are distorted preferentially in the radial and those forming close to the outer critical curve preferentially in the tangential direction, the inner critical curve is called "radial" and the outer one "tangential".

A source located in the centre of the asteroid caustic (c.f. green or dark blue image in Fig. 1.4) lies inside the inner as well as the outer caustic and therefore we observe 2 times 2 extra images, in total thus five. They are presented in the left panel and the fifth image (close to the centre) is highly demagnified. For the source close to a cusp (dark blue image, top panel) three of the images get highly magnified (which will eventually merge into a single remaining image when the source crosses the cusp). In the case of the source moving close to the fold (dark-blue image, bottom panel) two of the images are highly magnified and will eventually merge and dissappear on the fold caustic crossing. Finally we concentrate on sources located close to and inside a fold (dark blue source in the lower panel of Fig. 1.4) or a cusp (dark blue source in the upper panel of Fig. 1.4). For the singular elliptical lens both source positions will have five solutions of the lens equation (i.e. five images) correspond to two minima, two saddle points and a maximum of the Fermat potential.

In summary:

Saddle point images are images corresponding to the saddle points of the Fermat potential and have negative parity, i.e. $detA < 0$. As a consequence their magnification factor is negative (which can sometimes be a source of confusion, as we will speak then of images with negative magnifications - though their flux is proportional to the absolute value of magnification). They are also sometimes referred to as Type II images.

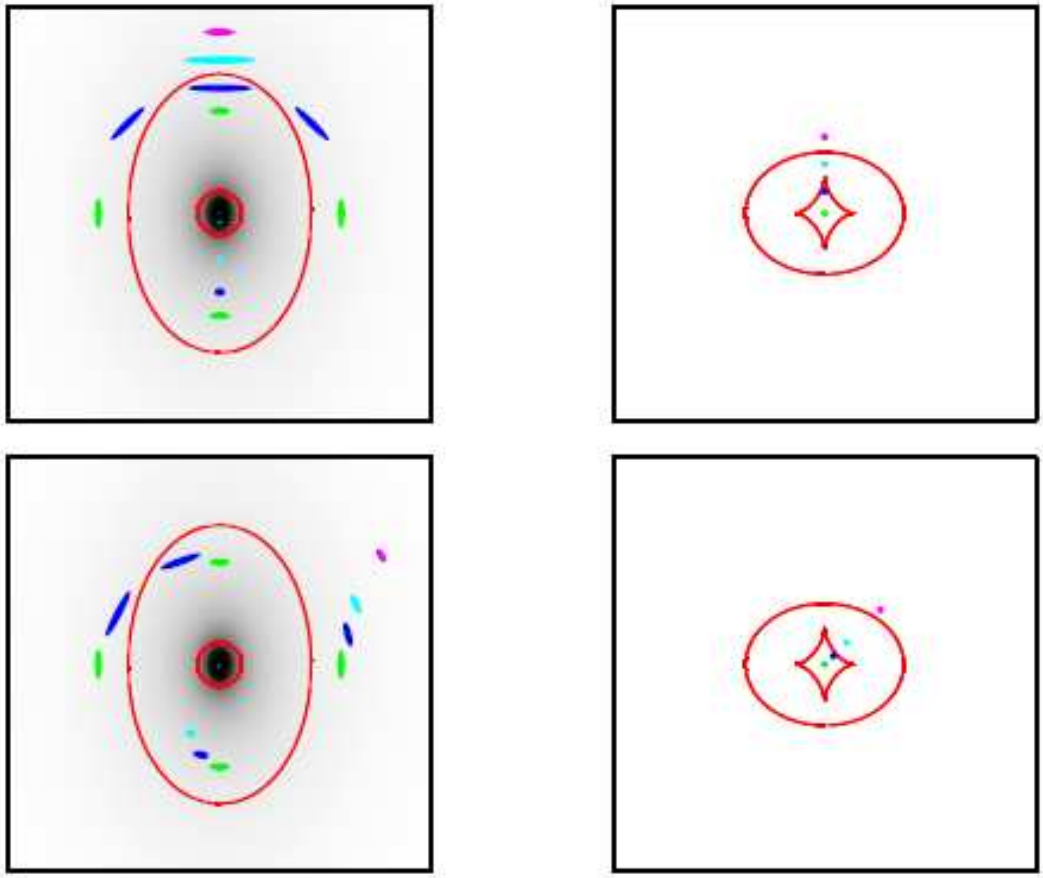

Figure 1.4. Compact source crossing a cusp caustic (top) and a fold caustic (bottom) of a singular elliptical lens. The diagram on the left shows critical curves and image positions and the diagram on the right shows caustics and source positions (courtesy by Bradac 2005, PhD thesis).

Minima or Type I images have a positive parity and trace, i.e. $detA > 0$ and $trA > 0$. They are never demagnified; i.e. $\mid \mu \mid = \mu \geq 1$ (for an infinitesimal source).

Maxima are Type III images and also have a positive parity, i.e. $detA > 0$, however $trA < 0$. For example, in the case of a non-singular isothermal lens the central image, corresponding to a maxima, will be highly demagnified and will in general escape observations.

These two specific configurations are interesting, since the images form in a configuration satisfying model-independent predictions for the magnifications of highly magnified images (Blandford & Narayan, 1986 [179]; Schneider & Weiss, 1992 [200]; Mao, 1992 [156]). These types of images form at positions x satisfying $detA(x) \simeq 0$. For such images the general mapping can be approximated by Taylor expanding the Fermat potential $\phi(x)$ around $x_i^{(0)}$ (exactly on the critical curve) including the third order in x (for details on the rules for this truncation and for full derivation of what follows see Chapter 6 in Schneider et al., 1992 [145]) .

Fold case. The approximation of the general mapping around the fold is thus given by a second order polynomial mapping. By studying the inversion of this transformation the properties of the two images that form close to the fold can then be studied. If the source approaches the fold from the "inner" side, two of the lensed images get closer and closer together and finally merge and disappear when the source crosses the caustic. In the limit of the source approaching the fold, the magnifications of the two merging images (denoted by A and B) have opposite parity, however the

same absolute value. Therefore asymptotically the following relation holds,

$$R_{fold} = \frac{\mu_A + \mu_B}{\mid \mu_A \mid + \mid \mu_B} \rightarrow 0 \tag{1.51}$$

We scaled the relation for convenience, since we only observe fluxes and not magnifications. The absolute value of magnification close to the fold varies inversely as the square root of the distance between the source and the (closest) point on the caustic.

Cusp case. Similarly the properties of the mapping near a cusp can be considered. The resulting correspondence is a third order polynomial mapping. For a given source position (close to the cusp) three solutions represent the three merging images. Two of them will have the same parity (we denote these two by A and C), and the third one (B) the opposite parity. If the source approaches the cusp from inside, image B will move on a line perpendicular to the critical curve, and A and C approach the critical curve tangentially. The sum of magnifications of all three images vanish when the source approaches the cusp,

$$R_{cusp} = \frac{\mu_A + \mu_B + \mu_C}{\mid \mu_A \mid + \mid \mu_B \mid + \mid \mu_C \mid} \rightarrow 0 \tag{1.52}$$

Both, the fold and cusp relations are very powerful, model independent predictions. In the next chapters I will study the behaviour of these equations by considering how the substructures influence the potential of smooth lens models and how they affect these relations.

1.3 Simple lens models

1.3.1 Axially symmetric lenses

Lets consider a lens with an axially symmetric surface mass density, that is $\Sigma(\vec{\xi}) = \Sigma(\mid \vec{\xi} \mid)$, in which case the lens equation reduces to a one-dimensional equation. By symmetry we can restrict the impact vector $\vec{\theta}$ to be on the positive θ_1-axis, thus we have $\vec{\theta} = (\theta, 0)$ with $\theta > 0$. We can then use polar coordinates: $\vec{\theta'} = \theta'(cos\phi, sin\phi)$ (thus $d^2\theta' = \theta' d\theta' d\phi$). With $k(\vec{\theta}) = k(\theta)$ we get for eq.(1.32)

$$\alpha_1(\theta) = \frac{1}{\pi} \int_0^\infty \theta' \; d\theta' k(\theta') \; \int_0^{2\pi} d\phi \; \frac{\theta - \theta' cos\phi}{\theta^2 + \theta'^2 - 2\theta\theta' cos\phi} \; , \tag{1.53}$$

$$\alpha_2(\theta) = \frac{1}{\pi} \int_0^\infty \theta' \; d\theta' k(\theta') \; \int_0^{2\pi} d\phi \; \frac{-\theta' sin\phi}{\theta^2 + \theta'^2 - 2\theta\theta' cos\phi} \; . \tag{1.54}$$

Due to the symmetry $\vec{\alpha}$ is parallel to $\vec{\theta}$ and with eq. (1.54) we get $\alpha_2(\theta) = 0$. Only the mass inside the disc of radius θ around the center of the lens contributes to the light deflection, therefore from eq. (1.53) one finds

$$\alpha(\theta) \equiv \alpha_1(\theta) = \frac{2}{\theta} \int_0^\theta \theta' \; d\theta' k(\theta') \equiv \frac{m(\theta)}{\theta} \; . \tag{1.55}$$

This way we can write the lens equation as

$$\beta = \theta - \alpha(\theta) = \theta - \frac{m(\theta)}{\theta} \tag{1.56}$$

for $\theta \geq 0$. Due to the axial symmetry it is enough to consider $\beta \geq 0$. Since $m(\theta) \geq 0$ it follows that $\theta \geq \beta$ (for $\theta \geq 0$). Instead of eq. (1.34) we get

$$\Psi(\theta) = 2 \int_0^\theta \theta' \; d\theta' \; k(\theta') \; ln \left(\frac{\theta}{\theta'} \right) \; , \tag{1.57}$$

whereas the Fermat potential can be written as

$$\Phi(\theta,\beta)=\frac{1}{2}(\theta-\beta)^2-\Psi(\theta)\ . \tag{1.58}$$

This way we get the lens equation (1.56) from

$$\frac{\partial\Phi(\theta,\beta)}{\partial\theta}=0\ . \tag{1.59}$$

To get the Jacobi matrix we write: $\vec{\alpha}(\vec{\theta})=\frac{m(\theta)}{\theta^2}\vec{\theta}$ (with $\vec{\theta}=(\theta_1,\theta_2)$ and $\theta=\mid\vec{\theta}\mid$) and thus

$$A=\begin{pmatrix}1&0\\0&1\end{pmatrix}-\frac{m(\theta)}{\theta^4}\begin{pmatrix}\theta_2^2-\theta_1^2&-2\theta_1\theta_2\\-2\theta_1\theta_2&\theta_1^2-\theta_2^2\end{pmatrix}-\frac{2k(\theta)}{\theta^2}\begin{pmatrix}\theta_1^2&\theta_1\theta_2\\\theta_1\theta_2&\theta_2^2\end{pmatrix}\ , \tag{1.60}$$

where we made use of $m'(\theta)=2\theta k(\theta)$. The determinant of the Jacobi matrix is given by

$$detA=\left(1-\frac{m}{\theta^2}\right)\left(1-\frac{d}{d\theta}\left(\frac{m}{\theta}\right)\right)=\left(1-\frac{m}{\theta^2}\right)\left(1+\frac{m}{\theta^2}-2k\right)\ . \tag{1.61}$$

1.3.2 Einstein radius

For a lens with axial symmetry we get, with (1.11), the following equation

$$\beta(\theta)=\theta-\frac{D_{ds}}{D_sD_d}\frac{4GM(\theta)}{c^2\theta}\ , \tag{1.62}$$

from which we see that the image of a source, which is perfectly aligned (that means $\beta=0$), is a ring if the lens is supercritical. By setting $\beta=0$ in eq.(1.62) we get the radius of the ring

$$\theta_E=\left(\frac{4GM(\theta_E)}{c^2}\frac{D_{ds}}{D_dD_s}\right)^{1/2}\ , \tag{1.63}$$

which is called *Einstein radius*. The Einstein radius depends not only on the characteristics of the lens but also on the various distances.

The Einstein radius sets a natural scale for the angles entering the description of the lens. Indeed, for multiple images the typical angular separation between the different images turns out to be of order $2\theta_E$. Moreover, sources with angular distance smaller than θ_E from the optical axis of the system get magnified quite substantially whereas sources which are at a distance much greater than θ_E are only weakly magnified.

In several lens model the Einstein radius delimits the region within which multiple images occur, whereas outside there is a single image. By comparing eq.(1.26) with eq.(1.63) we see that the surface mass density inside the Einstein radius precisely corresponds to the critical density. For a point-like lens with mass M the Einstein radius is given by

$$\theta_E=\left(\frac{4GM}{c^2}\frac{D_{ds}}{D_dD_s}\right)^{1/2}\ , \tag{1.64}$$

or instead of an angle one often uses also

$$R_E=\theta_ED_d=\left(\frac{4GM}{c^2}\frac{D_{ds}D_d}{D_s}\right)^{1/2}\ . \tag{1.65}$$

To get some typical values we can consider the following two cases: a lens of mass M located in the galactic halo at a distance of $D_d\sim 10$ kpc and a source in the Magellanic Cloud, in which case

$$\theta_E=(0.9''\times10^{-3})\left(\frac{M}{M_\odot}\right)^{1/2}\left(\frac{D}{10\ kpc}\right)^{-1/2} \tag{1.66}$$

and a lens with the mass of galaxy (including its halo) $M \sim 10^{12} M_\odot$ located at a distance of $D_d \sim$ 1 Gpc

$$\theta_E = 0.9'' \left(\frac{M}{10^{12} M_\odot}\right)^{1/2} \left(\frac{D}{Gpc}\right)^{-1/2} , \tag{1.67}$$

where $D = D_d D_s / D_{ds}$.

1.4 Schwarzschild lens

A particular case of a lens with axial symmetry is the Schwarzschild lens, for which $\Sigma(\vec{\xi}) = M\delta^2(\vec{\xi})$ and thus $m(\theta) = \theta_E^2$. The source is also considered as point-like, this way we get for the lens equation (1.13) the following expression

$$\beta = \theta - \frac{\theta_E^2}{\theta} , \tag{1.68}$$

where θ_E is given by eq. (1.64). This equation has two solutions

$$\theta_\pm = \frac{1}{2}(\beta \pm \sqrt{\beta^2 + 4\theta_E^2}) . \tag{1.69}$$

Therefore, there will be two images of the source located one inside the Einstein radius and the other outside. For a lens with axial symmetry the amplification is given by

$$\mu = \frac{\theta}{\beta} \frac{d\theta}{d\beta} . \tag{1.70}$$

For the Schwarzschild lens, which is a limiting case of an axial symmetric one, we can substitute β using eq.(1.69) and obtain this way the amplification for the two images

$$\mu_\pm = \left[1 - \left(\frac{\theta_E}{\theta_\pm}\right)^4\right]^{-1} = \frac{u^2+2}{2u\sqrt{u^2+4}} \pm \frac{1}{2} . \tag{1.71}$$

$u = r/R_E$ is the ratio between the impact parameter r, that is the distance between the lens and the line of sight connecting the observer and the source and the Einstein radius R_E defined in eq.(1.65). u can also be expressed as β/θ_E. Since $\theta_- < \theta_E$ we have that $\mu_- < 0$. The negative sign for the amplification indicates that the parity of the image is inverted with respect to the source. The total amplification is given by the sum of the absolute values of the amplifications for each image

$$\mu = \mid \mu_+ \mid + \mid \mu_- \mid = \frac{u^2+2}{u\sqrt{u^2+4}} . \tag{1.72}$$

If $r = R_E$ then we get $u = 1$ and $\mu = 1.34$, which corresponds to an increase of the apparent magnitude of the source of $\Delta m = -2.5\ log\mu = -0.32$. For lenses with a mass of the order of a solar mass and which are located in the halo of our galaxy the angular separation between the two images is far too small to be observable. Instead, one observes a time dependent change in the brightness of the the source star. This situation is also referred to as *microlensing*.

Much research activity is devoted to study microlensing in the context of quasar lensing. Today, several cases of quasars are known which are lensed by foreground galaxies, producing multiple observable images. The stars contained in the lensing galaxy can act as microlenses on the quasar and as a result induce time-dependent changes in the quasar brightness, but in a rather complicated way, since here the magnification is a coherent effect of many stars at the same time. This is an interesting field of research, which led to important results on the problem of the dark matter in galaxies [15].

The time delay between the two images of a Schwarzschild lens is given by

$$c\Delta t = \frac{4GM}{c^2} \left(\frac{1}{2} u\sqrt{u^2+4} + ln\frac{\sqrt{u^2+4}+u}{\sqrt{u^2+4}-u}\right) . \tag{1.73}$$

The two images have a comparable luminosity only if $u \leq 1$ (otherwise the difference is such that one image is no longer observable since it gets too faint). For $u = 1$ one gets $\Delta t \sim \frac{4R_S}{c}$ (typically for a galaxy with mass $M = 10^{12}\ M_\odot$ one finds $\Delta t \sim 1.3$ years). Such measurements are important since they allow to determine the value H_0 of the Hubble constant ([127] and references therein).

1.5 Singular isothermal sphere (SIS)

A simple model for describing the matter distribution in a galaxy is to assume that the stars forming the galaxy behave like the particles in an ideal gas, confined by the total gravitational potential, which we assume to have spherical shape. The equation of state of the "particles" (stars) has the form

$$p = \frac{\rho k_B T}{m} \ , \tag{1.74}$$

where ρ and m are the matter density and the mass of a star, respectively. In the equilibrium case the temperature T is defined via the one-dimensional dispersion velocity σ_v of the stars as obtained from

$$m\sigma_v^2 = k_B T \ . \tag{1.75}$$

In principle the temperature could depend on the radius, however in the simplest model, of the isothermal spherical model, one assumes that the temperature is constant and so also σ_v. The equation for hydrostatic equilibrium is given by

$$\frac{p'}{\rho} = -\frac{GM(r)}{r^2} \ , \tag{1.76}$$

with

$$M'(r) = 4\pi r^2 \rho \ , \tag{1.77}$$

where $M(r)$ is the mass inside the sphere of radius r. A solution of the previous equations is

$$\rho(r) = \frac{\sigma_v^2}{2\pi G}\frac{1}{r^2} \ . \tag{1.78}$$

This mass distribution is called *singular isothermal sphere* (it is indeed singular for $r \to 0$). Since $\rho(r) \sim r^2$, $M(r) \sim r$, the velocity of the stars in the gravitational field of an isothermal sphere is given by

$$v_{rot}^2(r) = \frac{GM(r)}{r} = 2\sigma_v^2 \ , \tag{1.79}$$

which is constant. Such a mass distribution can (at least in a qualitative way) describe the flat rotation curves of the galaxies, as measured beyond a certain galactic radius. Thus the dark matter in the halo can in a first approximation be described by a singular isothermal sphere model.

The projected mass density on the lens plane perpendicular to the line of sight is as follows

$$\Sigma(\xi) = \frac{\sigma_v^2}{2G}\frac{1}{\xi} \ , \tag{1.80}$$

where ξ is the distance (in the lens plane) from the the center of mass. For the light deflection angle we get

$$\hat{\alpha} = 4\pi\frac{\sigma_v^2}{c^2} = 1.4'' \left(\frac{\sigma_v}{220\ km\ s^{-1}}\right)^2 \tag{1.81}$$

independent of the position ξ ($220\ km\ s^{-1}$ is a typical value for the rotation velocity in spiral galaxies).

The Einstein radius R_E is given by

$$R_E = 4\pi\frac{\sigma_v^2}{c^2}\frac{D_{ds}D_d}{D_s} = \hat{\alpha}\frac{D_{ds}D_d}{D_s} = \alpha D_d \ . \tag{1.82}$$

Multiple images occur only if the source is located within the Einstein radius. Let be $\xi_0 = R_E$, then $\Sigma(\xi) = \Sigma(x\xi_0)$ where $x = \xi/\xi_0$. This way the lens equation becomes

$$y = x - \frac{x}{\mid x \mid} \ . \tag{1.83}$$

For $0 < y < 1$ we have two solutions: $x = y + 1$ and $x = y - 1$. For $y > 1$ (the source is located outside the Einstein radius) there is only one image: $x = y + 1$. The images with $x > 0$ are of type I, whereas the ones with $x < 0$ are of type II. If the singularity in $\xi = 0$ is removed then there will be a third image in the center.

The amplification of an image in x is given by

$$\mu = \frac{\mid x \mid}{\mid x \mid -1} \tag{1.84}$$

(the circle $\mid x \mid = 1$ corresponds to a tangential critical curve). For $y \rightarrow 1$ the second image (corresponding to the solution $x = y - 1$) gets very faint.

The potential is given by $\psi(x) = \mid x \mid$ and the time delay between the images is

$$c\Delta t = \left(4\pi \left(\frac{\sigma_v}{c}\right)^2\right)^2 \frac{D_d D_{ds}}{D_s} 2y \ . \tag{1.85}$$

1.6 Singular isothermal ellipsoid (SIE)

A singular isothermal ellipsoid (SIE) (Kormann, Schneider, & Bartelmann 1994, [85]) shows several advantages for its simplicity: this model has been widely used in lens modeling and successfully reproduces many lens systems (e.g. Keeton et al. 1998 [189], Chiba 2002 [109], Treu & Koopmans 2004 [162]). An isothermal profile for the total mass distribution of elliptical galaxies is well supported by the detailed dynamical studies of local ellipticals (Gerhard et al. 2001 [163]), individual lens modeling, and statistics (e.g. Maoz & Rix 1993 [165]; Kochanek 1995 [164]; Grogin & Narayan 1996 [168]). The generalizations of the isothermal sphere lens model to more realistic, elliptical lens is straightforward: let's replace in Eq. (1.80) the radial coordinate $\xi =: (\xi\cos\phi, \xi\sin\phi)$ by

$$\zeta = \sqrt{\xi_1^2 + f^2\xi_2^2}, \tag{1.86}$$

which is constant on ellipses with minor axis ζ and major axis ζ/f, and thus the axis ratio f. Hence, we define the surface mass density of the *singular isothermal ellipsoid* (SIE) to be

$$\Sigma(\zeta) = \frac{\sqrt{f}\sigma_v^2}{2G} \frac{1}{\sqrt{\xi_1^2 + f^2\xi_2^2}}, \tag{1.87}$$

where the normalization is chosen such that the mass inside an elliptical isodensity contour for fixed Σ is independent of f. The value of axis ratio is taken in the interval $0 < f \leq 1$; the symmetric model is obtained in the limiting case $f \rightarrow 1$. Using the length scale

$$\xi_0 = 4\pi \frac{\sigma^2}{c^2} \frac{D_d D_{ds}}{D_s}, \tag{1.88}$$

we have for the dimensionless surface mass density

$$\kappa(x, \phi) = \frac{\sqrt{f}}{2x\Delta(\phi)} = \frac{\sqrt{f}}{2b}, \tag{1.89}$$

where I have used the definitions

$$x = \xi/\xi_0 \tag{1.90}$$

$$\Delta(\phi) = \sqrt{\cos^2\phi + f^2 \sin^2\phi}, \tag{1.91}$$

and

$$b = \frac{\zeta}{\xi_0} = x\Delta = \sqrt{x_1^2 + x_2^2}. \tag{1.92}$$

An interesting property of the elliptical model is that the expression for the magnification is formally identical to the corresponding equation for the SIS. So the components for the shear are

$$\gamma_1 = -\kappa\cos(2\phi), \quad \gamma_2 = -\kappa\sin(2\phi) \tag{1.93}$$

and for the magnification we have

$$\mu = 1/detA = \frac{1}{1-2\kappa}. \tag{1.94}$$

In this thesis I will use this model which is largely used to reproduce the main galaxy lens properties, while the SIS profile has been considered for the subhaloes along the line of sight. Generalizations to these models (such as truncated models) and other useful ones will be introduced in the next chapters, when needed.

1.7 Galaxy clusters as lenses

Galaxy clusters similarly to galaxies can act as gravitational lenses for more distant galaxies. One classifies the observed lensing effects due to clusters into two types.

1) Rich centrally condensed clusters produce sometimes giant arc when a background galaxy turns out to be almost aligned with one of the cluster caustics (*strong lensing*). (See, for instance, Fig. 1.1.)

2) Every cluster produces weakly distorted images of a large number of background galaxies (*weak lensing*). A nice example is in Fig. 1.6.

Both these cases have been observed and allow to get important information on the distribution of the matter in galaxy clusters. For the analysis of giant arcs, we have to use parametrized lens models which are fitted to the observational data. The situation is much better for weak lensing, because there now exist several parameter–free reconstruction methods of projected mass distributions from weak lensing data.

Strong lensing requires that the mass density per surface Σ has to be in some parts of the lens bigger than the critical mass density given by

$$\Sigma \geq \Sigma_{crit} = \frac{c^2 D_s}{4\pi G D_d D_{ds}} \ . \tag{1.95}$$

Indeed, if this condition is satisfied there will be one or more caustics. The observation of an arc in a cluster of galaxies allows to easily estimate the projected cluster mass which lies inside a circle traced by the arc, even if no ring-shaped image is produced. For an axisymmetric lens, the average surface mass density within the tangential critical curve is given by Σ_{crit}. Tangentially oriented large arcs occur nearby the tangential critical curves, and thus the radius θ_{arc} of the circle traced by the arc gives an estimate of the Einstein radius θ_E. Inside the so defined circle the surface mass is Σ_{crit}, and this way, knowing the redshifts of the lens and the source, one finds the total mass enclosed by $\theta = \theta_{arc}$

$$M(<\theta) = \Sigma_{crit}\ \pi\ (D_d\ \theta)^2 \simeq 1.1 \times 10^{14} M_\odot \left(\frac{\theta}{30''}\right)^2 \left(\frac{D_d}{1Gpc}\right) \ , \tag{1.96}$$

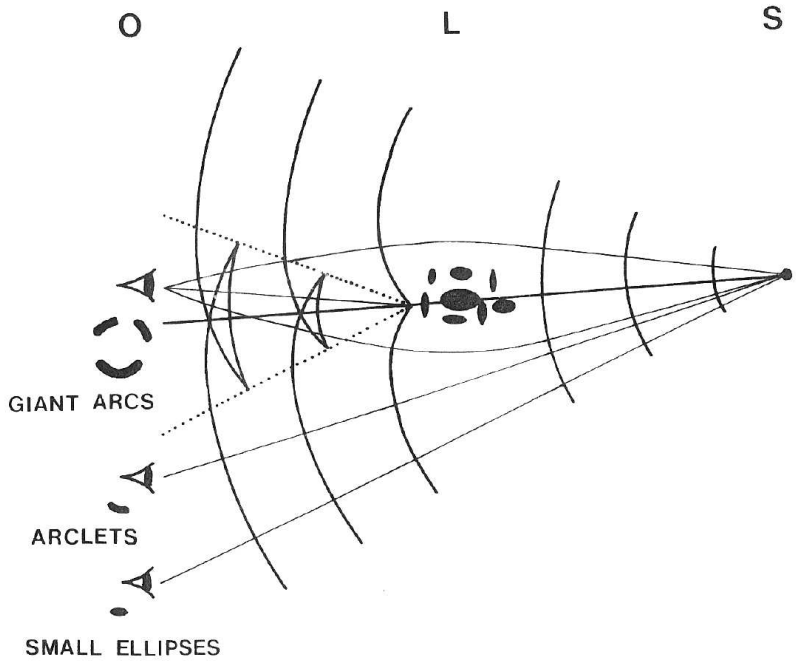

Figure 1.5. Wave fronts in the presence of a cluster perturbation.

A mass estimate with this procedure is useful and often quite accurate.

If we assume that the cluster can be at least as a first approximation be described as a singular isothermal sphere, then using eq. (1.82) we obtain for the dispersion velocity in the cluster

$$\sigma_v \simeq 10^3 \text{ km/s} \left(\frac{\theta}{28''}\right)^{1/2} \left(\frac{D_s}{D_{ds}}\right)^{1/2} . \tag{1.97}$$

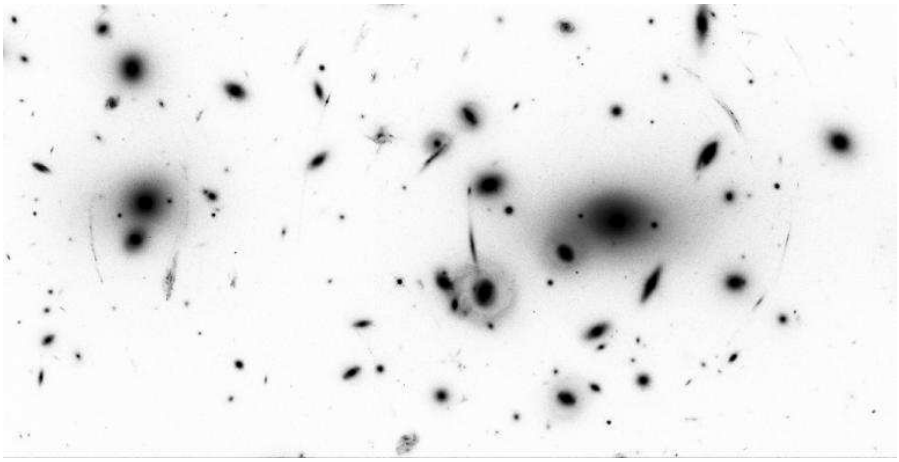

Figure 1.6. Hubble Space Telescope image of the cluster Abell 2218. Beside arcs around the two centers of the cluster, many arclets can be seen (NASA HST Archive).

A limitation of strong lensing is that it is model dependent and moreover one can determine only the mass inside a cylinder of the inner part of a lensing cluster. The fact that the observed giant

arcs never have counter-arc of comparable brightness, and rarely even small counter-arcs, implies that the lensing geometry has to be non-spherical.

A remarkable phenomenon is the occurrence of so–called *radial arcs* in galaxy clusters. These are *radially* rather than tangentially elongated, as most luminous arcs are. They are much less numerous (examples: MS 2137, Abell 370). Their position has been interpreted in terms of the turnover of the mass profile and a core radius $\sim 20\ h^{-1}$ kpc has been deduced, quite independent of any details of the lens model. There are, however, other mass profiles which can produce radial arcs, and have no flat core; even singular density profiles can explain radial arcs [61]. Such singular profiles of the dark matter are consistent with the large core radii inferred from X–ray emission.

1.7.1 Weak lensing

There is a population of distant blue galaxies in the universe whose spatial density reaches 50–100 galaxies per square arc minute at faint magnitudes. The images of these distant galaxies are coherently distorted by any foreground cluster of galaxies. Since they cover the sky so densely, the distortions can be determined statistically (individual weak distortions cannot be determined, since galaxies are not intrinsically round). Typical separations between arclets are $\sim (5-10)''$ and this is much smaller than the scale over which the gravitational cluster potential changes appreciably.

Starting with a paper by Kaiser and Squires [62], a considerable amount of theoretical work on various parameter-free reconstruction methods has recently been carried out. The main problem consists in making an optimal use of limited noisy data, without modeling the lens. For reviews see [63, 64]. The derivation of most of the relevant equations gets much easier when using a complex formulation of lensing theory (see for instance [65]). In the following we will, however, not use it.

The reduced shear $\vec{g}$, introduced in Section 1.2.4, is in principle observable over a large region. What we are really interested in, however, is the mean curvature κ, which is related to the surface mass density. Since

$$\vec{g} = \frac{\vec{\gamma}}{1-\kappa} \tag{1.98}$$

we first look for relations between the shear $\vec{\gamma} = (\gamma_1, \gamma_2)$ and κ.

From equation (1.37) we get that

$$\Delta\Psi = 2k \tag{1.99}$$

or if instead we use the notation $\vec{\theta} = (\theta_1, \theta_2)$ for the image position eq.(1.99) can explicitely be written as

$$k(\vec{\theta}) = \frac{1}{2}\left(\frac{\partial^2\Psi(\vec{\theta})}{\partial\theta_1^2} + \frac{\partial^2\Psi(\vec{\theta})}{\partial\theta_2^2}\right) \ . \tag{1.100}$$

Using the definition for γ_i as given in eq.(1.42) we find

$$\gamma_1(\vec{\theta}) = \frac{1}{2}\left(\frac{\partial^2\Psi(\vec{\theta})}{\partial\theta_1^2} - \frac{\partial^2\Psi(\vec{\theta})}{\partial\theta_2^2}\right) \equiv D_1\Psi \tag{1.101}$$

and

$$\gamma_2(\vec{\theta}) = \frac{\partial^2\Psi(\vec{\theta})}{\partial\theta_1\partial\theta_2} \equiv D_2\Psi \ . \tag{1.102}$$

where

$$D_1 := \frac{1}{2}\left(\partial_1^2 - \partial_2^2\right) \ , \qquad D_2 := \partial_1\partial_2 \ . \tag{1.103}$$

Note the identity

$$D_1^2 + D_2^2 = \frac{1}{4}\Delta^2 \ . \tag{1.104}$$

Hence

$$\Delta\kappa = 2\sum_{i=1,2} D_i\gamma_i \ . \tag{1.105}$$

Here, we can substitute the reduced shear, given by eq.(1.98), on the right for γ_i. This gives the important equation

$$\Delta\kappa = 2\sum_{i} D_i[g_i\,(1-\kappa)] \ . \tag{1.106}$$

For a given (measured) $\vec{g}$ this equation does not determine uniquely κ, indeed eq. (1.106) remains invariant under the substitution

$$\kappa \to \lambda\kappa + (1-\lambda) \ , \tag{1.107}$$

where λ is a real constant. This is the so-called *mass–sheet degeneracy* (a homogeneous mass sheet does not produce any shear).

Eq. (1.106) can be turned into an integral equation, by making use of the fundamental solution

$$\mathcal{G} = \frac{1}{2\pi}\ln \mid \vec{\theta} \mid \ , \tag{1.108}$$

(see Section 2.4) for which $\Delta\mathcal{G} = \delta^2$ (δ^2 is the two-dimensional delta function). Then we get

$$k(\vec{\theta}) = 2\int_{R^2} d^2\theta'\ \mathcal{G}(\vec{\theta}-\vec{\theta}')\sum_{i=1,2}(D_i\gamma_i)(\vec{\theta}') + k_0 \ . \tag{1.109}$$

After some manipulations we can bring eq.(1.109) into the following form

$$k(\vec{\theta}) = \frac{1}{\pi}\sum_{i=1,2}\int_{R^2} d^2\theta'\ \left[\tilde{\mathcal{D}}_i(\vec{\theta}-\vec{\theta}')\gamma_i(\vec{\theta}')\right] + k_0 \ , \tag{1.110}$$

or in terms of the reduced shear

$$k(\vec{\theta}) = k_0 + \frac{1}{\pi}\sum_{i=1,2}\int_{R^2} d^2\theta'\ \left[\tilde{\mathcal{D}}_i(\vec{\theta}-\vec{\theta}')(g_i(1-k))(\vec{\theta}')\right] \ , \tag{1.111}$$

where

$$D_1\ln \mid \vec{\theta} \mid = \frac{\theta_2^2-\theta_1^2}{\mid \vec{\theta} \mid^4} \equiv \tilde{\mathcal{D}}_1 \ , \qquad D_2\ln \mid \vec{\theta} \mid = -\frac{2\theta_1\theta_2}{\mid \vec{\theta} \mid^4} \equiv \tilde{\mathcal{D}}_2 \ . \tag{1.112}$$

The crucial fact is that $\gamma(\vec{\theta})$ is an observable quantity and thus using eq.(1.110) one can infer the matter distribution of the considered galaxy cluster. This result is, however, fixed up to an overall constant k_0 (problem of the mass-sheet degeneracy).

As discussed in Section 1.2.4 we can define the ellipticity ϵ of an image of a galaxy as

$$\epsilon = \epsilon_1 + i\epsilon_2 = \frac{1-r}{1+r}e^{2i\varphi} \ , \quad r \equiv \frac{b}{a} \ , \tag{1.113}$$

where φ is the position angle of the ellipse and a and b are the major and minor semiaxis, respectively. a and b are given by the inverse of the eigenvalues of the matrix defined in eq. (1.42). If we take the average on the ellipticity due to lensing and make use of eq.(1.113) as well as of the expressions for a and b we find the relation

$$< \epsilon > \ = \ \left\langle \frac{\gamma}{1-k} \right\rangle \ . \tag{1.114}$$

The angle bracket means average over a finite sky area. In the weak lensing limit $k \ll 1$ and $\mid \gamma \mid \ll 1$ the mean ellipticity directly relates to the shear: $< \gamma_1(\vec{\theta}) > \simeq < \epsilon_1(\vec{\theta}) >$ and $< \gamma_2(\vec{\theta}) > \simeq < \epsilon_2(\vec{\theta}) >$. Thus a measurement of the average ellipticity allows to determine γ, and making use of eq.(1.110) one can get the surface mass density k of the lens. Recently, several groups reported the detection of cosmic shear, which clearly demonstrates the technical feasibility of using weak lensing surveys to measure dark matter clustering and the potential for cosmological measurements, in particular with the upcoming wide field CCD cameras [67, 68].

1.7.2 Comparison with results from X–ray observations

Beside the lensing technique, there are two other methods for determining mass distributions of clusters:
1) The observed velocity dispersion, combined with the Jeans–equation from stellar dynamics gives the total mass distribution, if it is assumed that light traces mass.
2) X–ray observations of the intracluster gas, combined with the condition of hydrostatic equilibrium and spherical symmetry lead also to the total mass distribution as well as to the baryonic distribution.

If the hydrostatic equilibrium equation for the hot gas

$$\frac{dP_g}{dr} = -\rho_g \frac{GM_t\,(r)}{r^2} \tag{1.115}$$

is combined with the ideal equation of state $P_g = (k_B T_g/\mu m_H)\,\rho_g$ and assuming spherical symmetry, one easily finds for the total mass profile

$$M_t\,(r) = -\frac{k_B T_g}{G\mu m_H}\left(\frac{d\ln\rho_g}{d\ln r} + \frac{d\ln T_g}{d\ln r}\right) r. \tag{1.116}$$

The right hand side can be determined from the intensity distribution and some spectral information. (At present, the latter is not yet good enough, because of relatively poor resolution, which, however, will change with the XMM survey.)

Weak lensing together with an analysis of X–ray observations offers a unique possibility to probe the relative distributions of the gas and the dark matter, and to study the dynamical relationship between the two. As an example consider the cluster of galaxies A2163 (z=0.201) which is one of the two most massive clusters known so far.

ROSAT measurements reach out to 2.3 h^{-1} Mpc ($\sim$ 15 core radii)(h being the Hubble constant in units of 100). The total mass is 2.6 times greater than that of COMA, but the gas mass fraction, $\sim 0.1\ h^{-3/2}$ is typical for rich clusters. The data together suggest that there was a recent merger of two large clusters. The optical observations of the distorted images of background galaxies were made with the CFHT telescope. The resulting lensing and X–ray mass profiles are compared in Fig. 1.7. The data sets only overlap out to a radius of $200'' \simeq 500\ h^{-1}$ kpc to which the lensing studies were limited. It is evident that the lensing mass estimates are systematically lower by a factor of $\simeq 2$ than the X–ray results, but generally the results are consistent with each other, given the substantial uncertainties. There are reasons that the lensing estimate may be biased downward. Correcting for this gives the results displayed by open squares. The agreement between the lensing and X–ray results becomes then quite impressive. The rate and quality of such data will increase dramatically during the coming years. With weak lensing one can also test the dynamical state of clusters. By selecting the relaxed ones one can then determine with some confidence the relative distributions of gas and dark matter.

In addition, it is possible to extend the investigations to super clusters scales, with the aim to determine dark energy properties, the power spectrum and get information on the cosmological parameters [63, 64, 70, 71, 72].

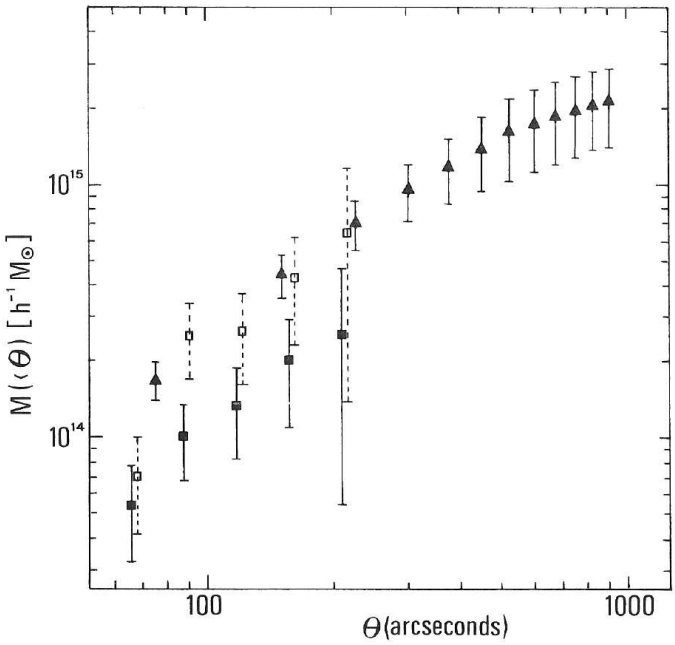

Figure 1.7. The radial mass profiles determined from the X–ray and lensing analysis for Abell 2163. The triangles display the total mass profile determined from the X–ray data. The solid squares are the weak lensing estimates "corrected" for the mean surface density in the control annulus determined from the X–ray data. The conversion from angular to physical units is $60'' = 0.127\ h^{-1}$ Mpc (taken from G. Squires et al., 1997 [66]).

Chapter 2

Q0045-3337: models including strong lensing by a spiral galaxy

2.1 Introduction

[1]The number of known strong lensed quasars boosted in the last years up to the current value of ~ 90 (Kochanek, Schneider & Wambsganss [84]; CASTLES web site, http://cfa-www.harvard.edu/castles/). The reason for this increase is mainly the availability of new observational facilities, in particular the Hubble Space Telescope, of dedicated surveys (CLASS, Myers et al. [87], Browne et al. [75]) and of large public observational databases, like the FIRST (White et al. [99]) and in particular the Sloan Digital Sky Survey (York et al. [100], Adelman-McCarthy et al. [73]).

The lion's share of the lens population is made by early-type galaxies. In fact, up to now, only 5 systems are confidently identified with spiral galaxies: first of all, the Einstein cross, Q2237+0305 (Huchra et al. [78]), then B1600+434 (Jackson et al. [80]), PMNJ2004-1349 (Winn, Hall, & Schechter [98]), B0218+357 (Patnaik et al. [89]) and PKS 1830-211 (Pramesh Rao & Subrahmanyan [93]). Each of these systems has its own peculiarities (inclination of the lens galaxy, richness of the lens environment, etc.), up to the point of making it unique, and can therefore bring its own precious contribution to the knowledge of spiral galaxies mass distribution.

The discovery of a late-type galaxy at $\sim 1.2''$ from Q0045-3337 (Falomo et al. [77]) suggested the existence of another candidate.

In fact, while there is no evident image splitting, Falomo et al. inferred a galaxy Einstein radius of size comparable to the distance between the galaxy and the QSO, under reasonable hypotheses on galaxy redshift and mass-to-light ratio, and considering the galaxy as a point mass.

Existing, limited data hamper detailed modeling of Q0045-3337. We investigated some simple configurations compatible with the known properties of the system, in the hope of restricting the range of possibilities and to focus future observations.

2.2 Observational parameters

Q0045-3337 (R.A. = 00 47 41.85, DEC = -33 20 55.1) is a radio quiet quasar with a reported redshift of z=2.14 (Iovino, Clowes & Shaver [79]) and a V magnitude of 18.75 (Véron-Cetty & Véron [97]). The NAOS-CONICA VLT K band image of Q0045-3337 (Falomo et al. [77]) revealed a galaxy at $1.14''$ SE from the quasar (respectively A and B in Figure 2.1). The K magnitude of the QSO is 17.80, while the one of the galaxy is 16.97 (see the following paragraph for a discussion of the galaxy

[1] accepted for publication in A&A, astro-ph arXiv:0707.2675 [101]

surface photometry). The only other object seen in the field, apart from the guide star, is source C, with a K magnitude of 20.90, 3.5″ N of A.

The quasar itself appears noticeably elliptical (see Section 2.5.2 for a discussion on the ellipticity). There is no redshift measurement for the galaxy. Falomo et al. ([77]) estimated a redshift range of 0.4-1 from an educated guess on the galaxy absolute K magnitude (-24 to -26) and effective radius (2 to 3 kpc).

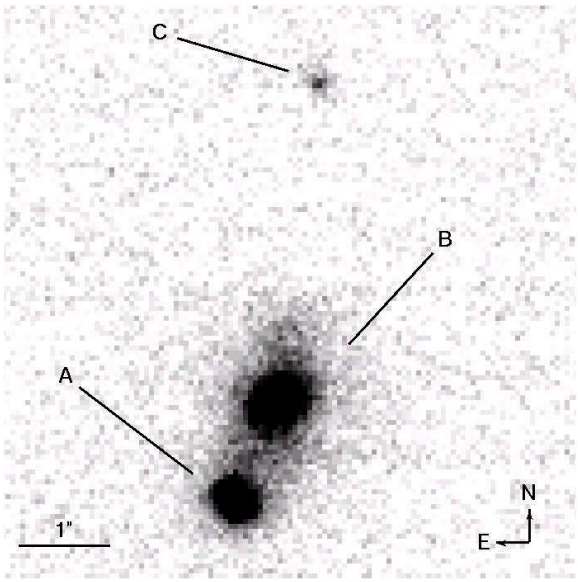

Figure 2.1. Q0045-3337 and its foreground galaxy. A close-up of the NAOS-CONICA image of Q0045-3337 and its foreground galaxy.

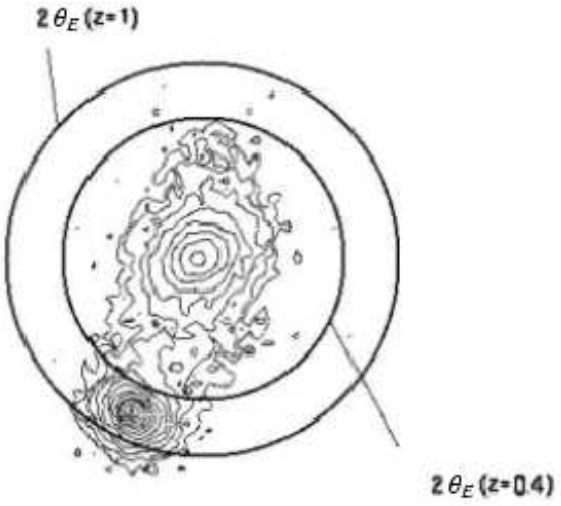

Figure 2.2. Contour map and Einstein radii. Contour map from the NAOS-CONICA image, with superimposed circles of twice the Einstein radius for SIS with dispersion velocities calibrated with the Tully-Fisher law (see text for details).

2.3 Surface photometry and galaxy image subtraction

We performed two-dimensional surface photometry on the NAOS CONICA image of the galaxy with the aid of the software GALFIT (version 2.0.3c; Peng et al. [90]). Two dimensional photometry for adaptive optics is complicated by the peculiarities of the Point Spread Function (PSF). In fact, each extended component of the GALFIT models is usually convolved with the PSF of the image; moreover, the PSF is used to fit point-like sources. It is a well known feature of adaptive optics that the PSF can assume complex shapes, in particular it usually varies with angular distance from the guide star, and it can be elongated in direction of the guide star. Usually, analytical modelling of the PSF from ancillary data is not possible, though the situation is likely to change in the future (see Clénet et al. [76] for the NaCo case). What should be done is therefore to infer a PSF template from observations of bright stars at similar angular distance from the guide star, observations performed just before and after the one to be analyzed. Unfortunately, this part of the program was not executed for the NaCo observation of Q0045-3337 (see Falomo et al. [77]).

The QSO itself, besides being "contaminated" from light from the galaxy, appears visibly elliptical, and it is not clear if its ellipticity is an effect of PSF elongation or it is due to a different cause (Figure 2.2; Section 2.5.2). The only other source, object C, is very faint and irregular, and its point-like or extended nature is not well determined.

We therefore performed a simultaneous fit of the galaxy and the QSO without convolving a PSF, using GALFIT models also for the QSO light distribution.

A two component model is required to account for the galaxy light distribution (plus two other components to fit the QSO); in particular, we obtained the best results with two Sérsic models of integrated magnitude 17.19 and 18.80, both with Sérsic index 0.63 (1 is the exponential disk, 0.5 the gaussian) and R_e respectively $13.5''$ and $3.4''$. The inner model is tilted of 50 degrees with respect to the outer.

After galaxy model subtraction, the main residual feature is an irregularly shaped object at $0.85''$ N of the galaxy centroid ($\sim 2''$ from the QSO; see Figure 2.3). The residual is very elongated, but due to its faintness (K $\sim$ 22.6, poorly constrained) it is not possible to firmly establish its point-like or extended nature.

We checked the robustness of our results using PSF templates obtained from the QSO, keeping in mind the already mentioned caveat. In particular, we used both the background subtracted QSO cropped image and the best fit QSO analytical profile (this last case should be less contaminated from galaxy light; however, it has the additional difficulty that the QSO fit is not perfect, with a noticeable residual left).

Even using these PSF templates, the need for two components to account for the galaxy light distribution still stands. In particular, the large difference in orientation between the outer and inner ellipsoids is unchanged.

The residual component is also unchanged. The only appreciable difference is a slight change in the two Sérsic indexes; the inner one becomes steeper (0.71), the outer one shallower (0.57). In order to verify if the residual image could have an explanation in terms of inefficient removal of bad pixels or cosmic rays, we carefully examined each of the frames that compose the summed NACO image. We did not find anything suspicious in none of the frames, and therefore we conclude that such interpretations of the residual image are unlikely.

2.4 Single image or multiple images

The zero-th order question that Q0045-3337 and its foreground galaxy pose to us is whether the lensing effect is strong, i.e. whether there are other, still unseen, QSO images, and eventually where

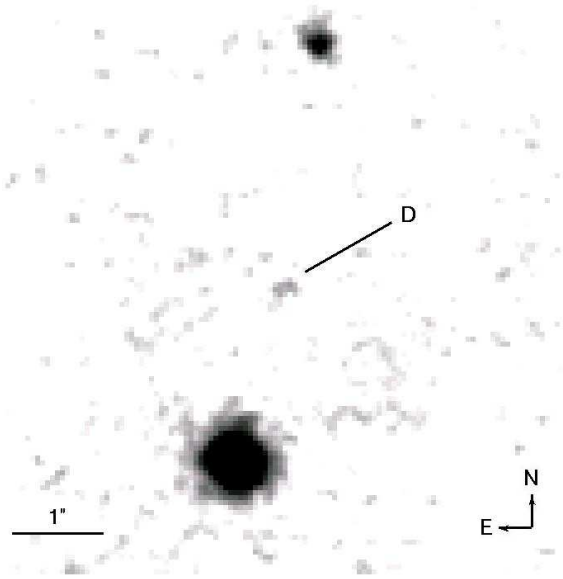

Figure 2.3. Q0045-3337 galaxy subtracted. The NAOS-CONICA image of Q0045-3337 after galaxy model subtraction, top-hat smoothing and contrast enhancing, in logarithmic scale. The residual feature (D) is well visible midway between object C and QSO.

they should be looked for.

In fact, if truly there is no image splitting, only a reduced amount of information can be extracted on the galaxy (e.g. Narayan & Schneider [88], Le Brun et al. [86]), though it can be still useful, in our case, to probe the behaviour of the strong lensing cross section for a spiral galaxy.

The simplest galaxy lens model with some physical meaning is the singular isothermal sphere (SIS). Within the SIS framework, all lens and source quantities are tied by simple analytical relations. In particular, necessary and sufficient condition for multiple images formation is that the Einstein radius θ_E has to be greater than half of θ_I, the distance of the brightest image from the lens ($\theta_E \geq 1/2\theta_I$; Narayan & Schneider [88]). The Einstein radius is defined as $\theta_E = 4\pi \times (\sigma_\mathrm{v}/c)^2 \times D_\mathrm{ds}/D_\mathrm{s}$, where σ_v is the velocity dispersion of the SIS, D_ds is the angular diameter distances between the source and the lens and D_s is the angular diameter distance between the source and the observer. The $0.57''$ discriminating threshold corresponds to a SIS velocity dispersion of 167 km s $^{-1}$ for a lens galaxy redshift of 0.4, and of 228 km s $^{-1}$ for a redshift of 1. The mass enclosed in θ_I is respectively 7.8×10^{10} $\mathrm{M}_\odot$ inside 6.1 kpc and 2.2×10^{11} $\mathrm{M}_\odot$ inside 9.1 kpc. Since the companion galaxy of Q0045-3337 is a spiral, the Tully-Fisher relationship (Pierini & Tuffs [92]) can be used to infer a circular velocity range of 218-351 km s $^{-1}$ from the (guessed) absolute magnitude. Under the assumption that the σ_v parameter of the SIS mass distribution is $1/\sqrt{2}$ of the maximum circular velocity, the obtained σ_v are 154 km s $^{-1}$ and 248 km s $^{-1}$, and the inferred Einstein radius ranges from $0.49''$ to $0.68''$ (Figure 2.2). Such values do not allow us to confirm or reject image splitting, keeping in mind the intrinsic dispersion in the Tully-Fisher relationship, the possibility of evolutionary effects and in particular the extreme simplification used in assuming a SIS model.

If the lensing is weak, its effects are magnification of point sources and tangential stretching of extended sources. We will discuss the stretching effect later. In the SIS framework the maximum magnification without image splitting is 2. Much higher values can be reached, at least in principle, with different mass models (Keeton, Kuhlen & Haiman [83]).

2.5 Multiple images

In this section we investigate the hypothesis that additional, yet unseen (or not recognized) images are produced. We slightly complicate the galaxy model abandoning the spherical symmetry. Singular and non-singular Isothermal Ellipsoidal Mass Distribution (SIEMD, PIEMD) and ellipsoidal potential have been studied in some details in the last $\sim$ 15 years (e.g. Kassiola & Kovner [81], Schramm [96], Kormann, Schneider & Bartelmann [85]). The structure of the caustic curves of non-spherical models is changed qualitatively, with the appearance of the astroid-shaped tangential caustic. The odd image theorem needs no more infinite demagnification of the central maximum image, and the presence of two caustics allows the production of up to five images. These models should be more realistic than the SIS oversimplification; however, they still lack "on the field" tests for spiral lenses, due to the already mentioned paucity of known cases.

Our goal in this section is not to make a detailed model of the galaxy mass distribution, but only to check if strong, image splitting, lensing configurations can be compatible with the constraint that no other image is seen in the NAOS-Conica data, and if that is the case to lead the way for future observations. To reproduce the qualitative behaviour of different cases, we extensively used the Java applet SimpLens (Saha & Williams [95]). Subsequently, we ran some simple simulations with the Gravlens software (Keeton [122]) to verify if the proposed configurations require a non-realistic choice of parameters. Table 2.1 shows the models used later in the text.

Table 2.1. GravLens models. Parameters are, from top to bottom, SIEMD Einstein radius parameter, exponential disk central surface density (in units of critical density), ellipticity (defined as (1-q)/q, with q axis ratio), position angle (North over East), shear strength, shear angle and exponential disk elliptical scale radius.

Parameter	Model I	Model II	Model III	Model IV
Type	SIEMD	SIEMD	SIEMD$_\gamma$	ExpDisk
$R_{E,gal}$ ($''$)	0.86	0.49	0.86	–
κ_0	–	–	–	2.45
e	0.34	0.34	0.30	0.67
PA(deg)	-13	0	-5	-5
γ	–	–	0.06	–
${\phi_\gamma}^d$ (deg)	–	–	-20	–
$R_{\rm d}(''$)	–	–	–	0.5

2.5.1 Three images

The easiest, and therefore favoured by the Ockham's razor, image splitting configuration is a three image configuration (like the one shown in Figure 2.4, top panels). In this case, the source has to be positioned between the external, radial, caustic and the internal astroid. The maximum, demagnified image is hidden by the lens galaxy bulge. Let us suppose that the residual image found in Section 2.3 is unrelated. If this is the case, the absence of other point sources requires a large magnification ratio between the minimum and the saddle point images. As a working hypothesis we chose a magnification ratio value of 20 as threshold of validity for the models. Even if this threshold would be too low to be compatible with the absence of any visible trace of the saddle point image, there are other ways to boost the magnification ratio. In particular, the saddle point image could be hidden by a strong obscuration if there is enough dust in the galaxy (even if no evidence of a dust lane is found from the surface photometry), or the minimum image flux could be enhanced by substructure lensing, microlensing and by the QSO variability itself.

A large magnification ratio can be obtained with a SIEMD in two ways (see Keeton, Kuhlen & Haiman [83] for an extensive discussion). First, you can put the source in one of four drop shaped

areas just outside the astroid cusps (see Figure 2.5; Keeton, Kuhlen & Haiman [83], Figure 1). We will refer to this case as to the drops configuration. If the source is in one of the two, very small, drops along the minor axis, the saddle point is the brightest image. This do not correspond to our case, and would require an unphysical mass distribution orthogonal to the light distribution.

If instead the source is in one of the two larger drops along the major axis, the minimum image is greatly magnified, and it forms very close to the tangential critical curve; thus the mass scale of the system is roughly fixed by the distance between the minimum image and the galaxy center. Model I of Table 2.1 is an example of a situation of this kind. The ellipticity is chosen to not differ too much from the light distribution; then the Einstein radius parameter (minor semiaxis of the tangential critical curve) is settled by the distance between the QSO and the galaxy center, and the position angle by the need to stay in the drop area.

The other way to obtain a large magnification ratio is to put the source close to the radial caustic, in the external grey area of Figure 2.5. We refer to this case as to the mouth configuration. In this case, the saddle point image is strongly demagnified. The minimum image forms further away from the tangential critical curve. Therefore, for a fixed distance between the minimum image and the lens center, the mass scale of the system is reduced. The constrain on the position angle is relaxed too. Model II of Table 2.1 is an example of this scenario. Note that in this case the Einstein radius parameter is at the lower end of the SIS range of Section 2.4, and the mass distribution is not aligned with neither of the light distribution components.

A misalignment between mass and light can be mimicked by the presence of shear, or be due to the aftermath of a major merger; this last hypothesis could be supported by the isophotal twisting and core-disk misalignment of the galaxy. In model III of Table 2.1 we added a shear component, that can be either due to real shear or just a way to simulate an intrinsic complex angular structure of the galaxy mass distribution. With this model the production of large magnification ratios is easier, so at our 20 threshold the two areas of Figure 2.5 are actually merged (e.g. Keeton, Kuhlen & Haiman [83], Figure 1).

Let us consider instead the hypothesis that the residual image is the saddle point image.

The elongated shape of the residual seems to contradict this speculation; however, since we are dealing with an object near to the plate limit, obtained after subtraction of an extended component and possibly absorbed, and after all we have no firmly established PSF shape, the morphological evidence can not be decisive. In the same way the position and the faintness of the residual are less than conclusive clues against the saddle point image interpretation. The face value magnification ratio between the QSO and the residual is ~ 80; allowing an underestimate of the residual luminosity of ~ 0.5 magnitudes, as common for faint sources, and another ~ 0.5 magnitudes of absorption, we obtain ~ 40. If indeed the residual feature marks the saddle point image, it is not possible to reproduce the positions of images and the required magnification ratio with a SIEMD (though this is not necessarily true for more complex models). Note that in this case absorption is probably less effective in boosting the magnification ratio, since the saddle point image is not so close to the galaxy core.

We envisaged also the possibility that the object C is an additional image of the quasar. It seems that somehow this interpretation creates more problems than it solves. In fact the system size of $\sim 4.7''$ is excessive for a single galaxy lens. Furthermore, fitting object C in a configuration like that of Figure 2.4, top panels, would require a reversed magnification ratio (A would be the most luminous image), very difficult to produce unless the mass is orthogonal to light. Finally, it is not clear if object C is truly point-like, since it seems to have a slightly smeared light profile, and the uncertainty on the PSF prevents us from a definite conclusion in this sense.

In the three image configuration, the elongation of the quasar has to be of instrumental origin, as is explained in the following subsection.

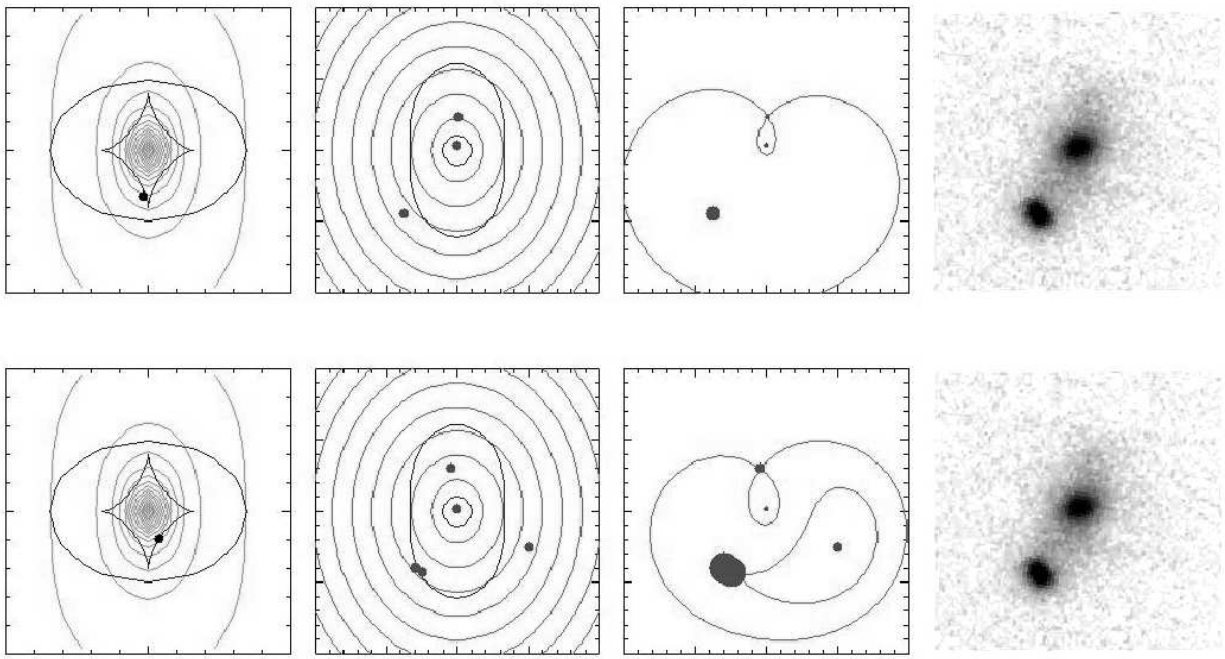

Figure 2.4. Lensing scenarios for Q0045-3337. A qualitative representation of lensing scenarios for Q0045-3337. From up to down: three images case with the saddle point image hidden; five images case with a saddle point image merged with a minimum image, the other saddle point and the other minimum images hidden. From left to right: SimpLens source position (point), isodensity contours (light curves) and caustics (grey curves); SimpLens images positions (points) and critical curves (grey curves); SimpLens image positions (points) with area proportional to the magnification and virtual light-travel time contours (grey curves); Q0045-337 and foreground galaxy, properly rotated and scaled to be directly comparable with the SimpLens images. The SimpLens model used is a non-singular isothermal ellipsoidal potential, with a core radius of 0.01 and an ellipticity of 0.37.

2.5.2 Quasar ellipticity

The first, most obvious, explanation for the ellipticity of Q0045-3337 in the NACO image is instrumental, i.e. due to adaptive optics PSF deformation (see section 2.3). As noted by Falomo et al. ([77]), Q0045-3337 is elongated in a direction almost aligned to the vector radius of the guide star, but not equal (with a difference of $\sim$ 10-15 degrees). The galaxy itself, and its brightest core in particular, do not appear to suffer similar deformation, but since their intrinsic brightness distribution is not radially symmetric, no definite conclusion can be drawn. If the ellipticity is real and not an instrumental artifact, a gravitational lensing effect can be invoked. In principle, image deformation can be produced by lensing of resolved sources, since in that case lensing conserves surface brightness, stretching the sources in the tangential directions and originating the well known arclets. However, it seems unlikely that this can be the case for Q0045-3337. In fact, while we stress one last time that the PSF in an adaptive optical image can be intrinsically complex, a magnified point source superimposed to a tangentially stretched extended source (like a QSO with its host galaxy) should result in a sharp bright core with a faint extended wing, i.e. the image should appear more elliptical at low brightness, and less at the brightness peak, where it should be dominated by the point source. This is exactly the opposite of what we see for Q0045-3337 (see the contour map of Figure 2.2). The only way in which gravitational lensing can produce such a behaviour is by means of merging two or more images, unresolved by the NACO observation (note that the merging of two equal circular PSFs can produce an elliptical PSF with stronger ellipticity at the peak and weaker at the periphery). In the following subsection we will explore in some more detail this possibility.

2.5.3 Five images

If we require a lensing explanation to the quasar ellipticity, we need to produce five images. This can be obtained in any model with two at least partially nested caustic curves. For our purpose, we want the merging of two (or even three) images near to the tangential critical curve, in such a way that the NACO observation is not sufficient to resolve the contribution of the different images (as in Figure 2.4, bottom panels). Images so close to a critical curve are strongly magnified. This can provide a explanation to the absence of the other images in the NACO observation based solely on strong lensing.

In particular, it is crucial to explain the non detection of a minimum image, that is foreseen quite far away from the galaxy and therefore can not be obscured. A conservative view assumes that the missing minimum image is fully undisturbed and therefore the full limit of the plate can be reached. We estimated a plate limit of 22.8 using the barely visible 22.6 residual object. In that case the obtained magnification ratio between the merged images and the missing minimum image is ~ 100. A less dramatic magnification ratio is allowed taking into account absorption and the effect of residual galaxy luminosity, and again an underestimate of object D magnitude. In particular we educatedly guessed a ~ 40 value. Note that the centroids of the merged images have to be very close each other; to give an order of magnitude example, the plate scale of the NACO image is only $0.054''$, and the distance between the two components used to fit the QSO with GALFIT in Section 2.3 is $0.052''$.

We verified the viability of the five images scenario numerically with Gravlens simulations.

It is possible to obtain such a configuration with a SIEMD at two conditions: first, the tangential critical line must cross the position of the merged images (thus setting the galaxy mass scale), second, the source needs to be very close to the astroid caustic fold (see Figure 2.5). Assuming fulfilled the first condition, like in Model I, the source plane area allowed by the second condition is very small. This result can be improved using different models of mass distribution. In particular, we employed an highly flattened distribution (so to obtain a naked cusp geometry), like the exponential disk mass distribution of Model IV.

Although such a strong flattening can barely represent the observational parameters that we have, the simulation proves that in principle this model can produce more easily five images with the required magnification ratio.

2.5.4 Five images versus three images

We evaluated the relative probability of the five images scenario in respect to the three images scenario in a statistical way. We chose a galaxy mass model able to reproduce either the three or the five images changing the source position. Therefore, the relative probability of the two scenarios can be evaluated as a ratio of weighted cross-sections, where the weight is needed to keep into account properly the magnification bias. We simulated one million source positions for model I with the mock1 GravLens command (see Figure 2.5). We then picked up only the realizations able to exceed a fixed magnification ratio threshold, and we integrated the area spanned, weighting each source realization with its own magnification bias (e.g. in the integrand). For the three images scenario we used a 20 threshold of magnification ratio, defined as ratio between the fluxes of the two brightest images. For the five images scenario, we defined the magnification ratio as the sum of the fluxes of the two brightest images over the flux of the third brightest image, and we chose the (optimistic) value of 40 for the threshold. As quasar number counts function we used a power law with two different values of the index, 1.85 and 2.23 (taken from the literature, e.g. Richards et al. [94]). The obtained relative probability is respectively 2.44% and 13.2%. As expected (it appears as an exponent) the impact of the index of the quasar number counts function is very strong. Such probability values are not sufficiently low to firmly exclude the five images scenario on the basis of this calculation alone. In fact while sources producing the five images configuration are rare (look

again at Figure 2.5), their overall magnification is large, so the inclusion of the magnification bias strongly enhances their weight.

The relative probability of the three and five image cases does not keep into account the distinction between drops and mouth configurations; in fact to evaluate such a probability as a ratio between weighted cross-sections, we must make the hypothesis that the galaxy models is fixed; otherwise, we should evaluate the relative probability of the different galaxy models, something that goes beyond the scope of this analysis. However, it is important to make clear that while the five images case requires strictly such a (rather large) value of the Einstein radius parameter, since the merged images are on the two sides of the tangential critical curve, with the three images it is allowed a wider range of values. In particular, in the mouth configuration, it is possible to reproduce the observational constraints with a much lower value of the Einstein radius parameter. Such a smaller Einstein radius would be favoured both by the SIS/Tully-Fisher evaluation of Section 2.4, and by the different normalizations proposed for application of the SIEMD to disk galaxies (e.g. Keeton & Kochanek [82]). Furthermore, the mouth configuration leaves much more room for explaining the absence of the saddle point image, since it puts it much closer to the galaxy core.

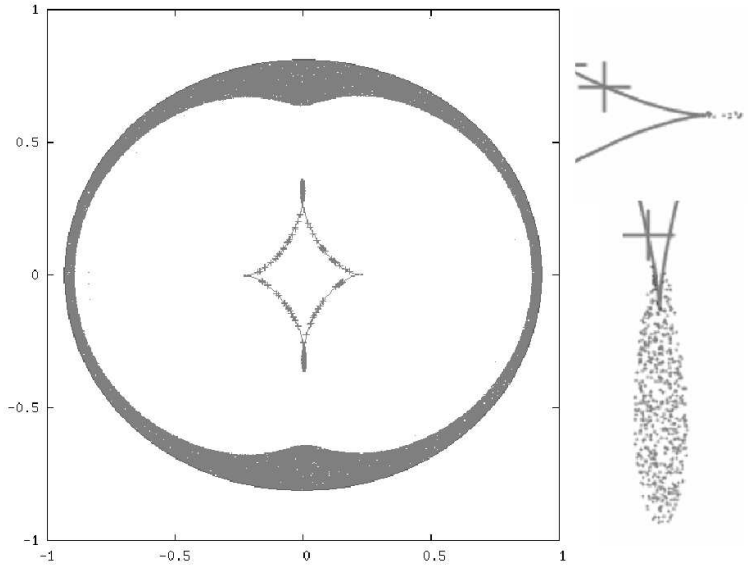

Figure 2.5. Simulated sources. Source plane of a SIEMD model (see Table 2.1 for parameters) with simulated sources. The grey area is the locus of sources producing three images with a magnification ratio >20, crosses are sources producing five images with a magnification >40. On the right, close-ups of two drop areas. More details are reported in the text.

2.6 Discussion

We performed two dimensional photometry on the galaxy near to Q0045-3337. We confirmed its spiral nature and found evidence for two components with different orientations. We found a residual image after model subtraction, that is most likely due to a spiral arm, even if more interesting possibilities can not be excluded. We then verified that no unusual parameters for the galaxy are required to produce, or not produce, image splitting. We also found some very simple strong lensing configuration capable of not contradicting existing data, either assuming a) that no other image is seen and Q0045-3337 observed elongation is instrumental, b) that the residual image is truly another lensed image of Q0045-3337, and still the elongation is instrumental, c) that Q0045-3337 elongation is due to the merging of two or more images, and no other image is seen. We evaluated the likelihood of the different cases, finding that case a) is the most probable, even if cases b) and c) can not be rejected.

All these speculations can be easily verified observationally. In particular, another optically adaptive image with more information on the PSF behaviour would confirm or rule out the ellipticity of Q0045-3337 and en passant it would also verify if object C is point-like. A measurement of the galaxy redshift, while probably not conclusive, would help to constrain how likely is the production of multiple images. Deeper pointings could reveal additional images or put tighter constraints on required magnification ratios. If case c) turns out to be the most probable, an HST image could resolve the merged images. At present, strong lensing effects on Q0045-3337 can only be labelled as possible. Spiral strong lenses are rare objects. The current view assumes that the cross-section for image splitting is not generally increased by the presence of a thin massive disk, at least once corrected for the inclination and once properly taken in account the current observational capabilities; furthermore, absorption biases strongly against the detection (Bartelmann & Loeb [74]; Keeton & Kochanek [82]; Perna, Loeb & Bartelmann [91]). In such a context, the galaxy close to Q0045-3337 can offer valuable help to our knowledge of spiral galaxy mass distributions, and to lensing statistics too. Even in the case without image splitting, as it is likely both for the sample of Narayan & Schneider ([88]) and for the Lyman absorbers of Le Brun et al. ([86]), interesting upper limits can be placed on the galaxy mass inside the Einstein radius (once the redshift is known). Furthermore, the lensing effect of stretching of resolved sources could make Q0045-337 again a valuable target for deeper host galaxy studies (as it was originally selected by Falomo et al.([77]). As a final comment, it is interesting to note that this case can be a perfect example of advantages and drawbacks of adaptive optics applied to strong lensing.

In the last years, HST has been the principal instrument in strong lensing studies, and it is interesting to evaluate if it can be -at least partially- surrogated by adaptive optics earth telescopes, especially in the case of a gap between the end of HST operations and the start of the James Webb Space Telescope operations. As Q0045-3337 and its neighbour galaxy tell us, a necessary condition to be fulfilled in this case is a correct PSF evaluation observational procedure (as was at first proposed for Q0045-3337); otherwise, the unresolved uncertainty between real and instrumental deformations hampers the exploitation of the optimal resolution for the purpose of lens studies.

Chapter 3

Cold Dark Matter models and strong lensing

3.1 Success and crisis of CDM

Whereas the current Cold Dark Matter (CDM) paradigm for structure formation is widely accepted, two major problems for CDM still remain. While simulations predict cuspy dark matter halos (Moore, 1994 [193]), observed rotation curves of low surface brightness galaxies indicate that their dark matter halos have cores (Kravtsov et al., 1998 [208]; Swaters et al., 2000 [209]; van den Bosch & Swaters 2001 [210]; de Blok & Bosma, 2002 [207]). The other is the apparent over-prediction of the small-scale power in CDM simulations. As was shown by Moore et al. (1999) [137] and Klypin et al. (1999) [126], the number of satellite halos seen in N-body simulations appears to far exceed the number of dwarf galaxies observed around the Milky Way. Particular discrepancies have been found for satellite masses . If one takes the observed satellites of the Milky Way as the total amount of substructure present, one needs to modify the CDM paradigm and include e.g. selfinteracting dark matter (Spergel & Steinhardt, 2000 [159]) or a cut-off in the power spectrum (which might occur in a warm dark matter-dominated universe, Bode et al. 2001 [180]; Coln et al. 2000 [184]). Another possibility pointed out by Stoehr et al. (2002) [185] and Hayashi et al. (2003) [186] is that the problem might be the misidentification of the observed satellites with the substructure seen in N-body simulations. Many mechanisms have been proposed which might prevent star formation in halos of mass, making them too dim for observations (Bullock et al., 2000 [107]; Benson et al., 2002 [277]; Somerville, 2002 [278]; Springel & Hernquist, 2003 [279]). Zentner & Bullock (2003) [158] investigate a semi-analytic model that describes the properties of galaxy-sized halo substructure. The effects of the "tilt" and overall normalisation of the primordial power spectrum are discussed. All these predictions need to be tested within our own Galaxy as well as at cosmological distances.

3.2 Strong Lensing to probe structures at all scales

Gravitational lensing is at present the only tool for investigating CDM substructure in galaxies outside the local group. As first noted by Mao & Schneider (1998) [130], mass-substructure other than stars on scales less than the image separation can substantially affect the observed flux ratios in strong gravitational lens systems. Chiba (2002) [109], Dalal & Kochanek (2002) [114], Metcalf & Madau (2001) [132], Metcalf & Zhao (2002) [133], Keeton (2001) [122], Mao & Schneider (1998) [130] Bradac et al. (2002) [106], Chiba et al. 2005 [110], Pooley et al. 2006 [142] Miranda & Jetzer 2007 [172] have argued that substructure can provide the explanation for the flux anomalies in various systems. Dalal & Kochanek (2002) [114] further conclude that the amount of substructure needed to explain the flux ratios of quadruply-imaged systems broadly agrees with the CDM predictions. At least for some systems the flux mismatches are probably not just an artifact of oversimplified macromodels of the main lens galaxy (see e.g. Evans & Witt 2003 [117]; Metcalf & Zhao 2002 [133]). As discussed by Keeton (2003) [124] and Chen et al. (2003) [111], fluxes can be further affected by clumps of matter at a redshift different from that of the lens, lying along the line of sight between the

observer and the source; however, this effect is not dominant. It is also possible that the small scale structure does not consist of compact CDM clumps, also tidal streams or offset disc components can affect the flux ratios (see Moller et al. 2003; Quadri et al. 2003). Keeton (2001) [122] and Gaudi & Petters (2002) [280] recently focused on the magnification relations that should be satisfied by particular four-image geometries (so called *fold* and *cusp* configurations). Cusp and fold relations are model-independent predictions for the magnifications of highly magnified images (Blandford & Narayan, 1986 [179]; Blandford 1990 [281]; Schneider & Weiss, 1992 [201]; Mao, 1992 [156]). Strictly speaking, however, they hold only for ideal fold or cusp configurations and it is therefore difficult in some cases to disentangle the effects of the source being further away from the cusp from that of substructure, purely by employing these relations. The influence of substructure can not only be seen on image flux ratios, but also in the structure of multiple-imaged jets. The lens system B1152+199 is a case of doubly-imaged jets, one of which appears bent, whereas the other is not (Metcalf, 2002 [282]). Another explanation is that an intrinsic bend in the jet is simply magnified in one image, and produces only a small effect in the other. Flux ratio anomalies can also be introduced by propagation effects in the interstellar medium (ISM) in the lens galaxy. Microlensing can change the flux ratios not only in the optical (e.g. Wozniak et al. 2000 [283]), but also at radio wavelengths (Koopmans & de Bruyn, 2000 [284]). Flux ratios can further be affected by galactic scintillation and scatter broadening (Koopmans et al. 2003 [191]). Fortunately, these effects are frequency dependent and one can recognise them using multi-frequency observations. These electromagnetic phenomena are similar for images of different parities. For substructure, however, Schechter & Wambsganss (2002) [285] found that magnification perturbations should show a dependence on image parity. Microlensing simulations showed that the probability distributions for magnifications of individual images are no longer symmetric around the unperturbed magnification. The distribution can, depending on image parity, become highly skewed in the direction of demagnification. This skewness causes a substantial probability for the brightest saddle point image to be demagnified. The two saddle point images in the quadruply-imaged system are the ones with negative parity, the other two have positive parities and are called minima (they correspond to the local minima and saddle points in the arrival time surface - see Sect. 1.2.5 for details). Observed lens systems seem to show this image parity dependence (Kochanek & Dalal, 2004 [160]), and this indicates that the flux ratio anomalies arise from gravitational lensing, rather than propagation effects.

These perturbers can be roughly divided in two categories: haloes that are inside the primary lens, usually referred as sub-haloes, and haloes that are along the line of sight, in between the source and the observer. This first category of haloes has been extensively studied in the past years both trough analytic calculation (Metcalf & Madau 2001 [132], Dalal & Kochanek 2002 [114], Metcalf and Zhao 2002 [133], Keeton 2003 [124]) and both using numerical simulations (Bradač et al 2002 [106], Amara et al 2006 [102], Macciò et al 2006 [128]). The latter two studies have came to the conclusion that the impact on lensing of sub-haloes in the mass range $10^7 - 10^{10}\mathrm{M}_\odot$ is very small. Even considering the impact of less massive subhaloes, usually not resolved in Nbody/hydro simulations, does not help in reproducing the observed number of anomalous flux ratio (Macciò & Miranda 2006 [129]).

The effect of the second category of haloes, the ones along the line of sight, is still somehow controversial (Chen et al. 2003 [111], Metcalf 2005a,b [135], [194]). In particular Metcalf (2005a,b) found that dark matter haloes with masses around $10^6 - 10^8\mathrm{M}_\odot$ can produce anomalies in the flux ratios at a level similar to those that are observed. The presence of a WDM particle even with a mass around 10 keV will strongly reduce the number density of such small mass haloes giving a different signature on the images fluxes. As a consequence the observed anomalous flux ratio can be used to constrain the abundance of small haloes along the line of sight and therefore to put an independent constrain on the mass of the sterile neutrino as a possible WDM candidate.

In this thesis I investigate the effects induced by both these substructure categories The chapters 4,5 analyse the subhaloes signature inside a primary lens galaxy, by considering both a semianalytical approach and a numerical one. The chapter 6 describes the effects of substructures along the line of sight by considering both a ΛCDM model and a ΛWDM model in order to give an independent estimate on the warm dark matter mass particle candidate: the sterile neutrino.

Chapter 4

Substructures towards PG1115+080 and B1555+373

4.1 Introduction

The standard lens models, although reproduce in general the relative positions of the images quite accurately, often have difficulties explaining the relative fluxes of multiply-imaged sources. Several possible explanations have been considered in the literature, the most plausible being that the lensing potential of real galaxies are not fully described by the simple lens models used to compute the lens characteristics. The most often invoked solution is to consider additional small-scale structures, which if located nearby the images can modify significantly the observed flux ratio between different images, in particular the so-called cusp or fold relations.

The presence of substructures is naturally expected within the Cold Dark Matter (CDM) model, which has been successful in explaining a large variety of observational results like the large scale structure of galaxies on scales larger than 1 Mpc or the fluctuations of the CMB (Spergel et al 2003 [146]). However, one of the predictions of this scenario is a distribution of matter, with a large number of small-mass compact dark matter (DM subhalos) halos, both within virialized regions of larger halos (Moore et al. 1999, Klypin et al. 1999 [126]) and in the field (DM extragalactic halos, Metcalf 2005). At the same time, the observed number of dwarf galaxy satellites in the Local Group is more than an order of magnitude smaller than expected. Many theoretical studies suggest models to reduce the abundance of substructure or to suppress star formation in small clumps via astrophysical mechanisms (as feedback), making them dark (Bullock, Kravtosov & Weinberg 2000 [107], Bekki & Chiba 2005 [104]). Anyway, if the CDM paradigm is correct, we expect $\sim 10 - 15\%$ of the mass of a present-day galactic halo ($\sim 10^{12} M_{\odot}$) within the virial radius to be in substructures with mass $\geq 10^{7} M_{\odot}$. Thus in the CDM model anomalous flux ratios should be common.

At present, the only way to detect these subclumps is through gravitational lensing, which is directly sensitive to the mass. This is because substructures (like globular clusters, gas clouds or satellite galaxies) can strongly modify the fluxes of lensed images relative to those predicted by smooth lens models. Even a clump as small as a star can perturb the image of small sources (~ 100 AU), but in this case we would see a microlensing effect such as variability in the image brightness with a time scale of order months. Some authors tried to fit systems (for example the radio system B1422+231) with anomalous flux ratios using smooth lens and multipole models: although it seems necessary to investigate further whether the multipoles can fit the lens configurations, these methods are not exhaustive (Evans & Witt 2003, [117] Congdon & Keeton 2005 [112]) and it is not yet possible to conclude that the multipole approach can explain the anomalous flux ratios. Mao & Schneider (1998) [130], Keeton (2001) [122], Metcalf & Madau (2001) [132], Bradač et al. (2002) [106], Dobler & Keeton (2006) [116] noted that a simple way of solving the puzzle was to put a satellite near the images, and they found that this could explain the anomaly in B1422+231.

Generally the flux ratios between the images do not depend on wavelength since they are independent of the intrinsic flux and variability of the source (Keeton et al. 1997, Mao & Schneider 1998 [130], Keeton 2001 [122], Metcalf & Zhao 2002 [133]). Such discrepancies would probably be due to sub-lensing or microlensing effects. On the other hand when modeling a multiple QSO lens system, one can either include or disregard the flux ratios of the images. As pointed out by Chang & Refsdal (1979) [108] (and in the following by several authors, as for instance Metcalf 2005, Keeton, gaudi & Petters 2005 [125], Mortonson et al. 2005 [138]) we have to pay attention to the fact that the projected (on the lens plane) sizes of the optical continuum emitting regions of QSOs are expected to be of the same order as the Einstein radius of a star in the lens galaxy ($\sim$ 100AU), so that the optical magnitudes may well be affected by gravitational microlensing (see Metcalf et al. 2004 [134], Mortonson et al. 2005 [138], and references therein), even if averaged over long periods of time. The radio and mid-IR regions, when projected on the lens plane, are typically of the order of 10 pc and change in their magnification should be dominated by larger scales than stars (Metcalf 2005 [135], Chiba et al. 2005[110]). If the lens galaxies contain substructures with an Einstein radius comparable or greater than the projected size of the radio component (corresponding for the substructure to masses $\geq 10^8 M_\odot$) we should see image splitting and distortions if they lie close enough to the images (see section 3.2, Wambsganss & Paczyński 1994 [149], Mao & Schneider 1998 [130]), which have not yet been detected (this might be the case for B0128+437, Biggs et al. 2004 [105]).

The existence of anomalous fluxes in many lens systems has been known since some time. The substructure lensing effects have been studied by considering single substructures (Mao & Schneider 1998 [130], Metcalf & Madau 2001 [132]), by assuming a statistically distributed sample of substructures (Chiba 2002 [109], Chen et al. 2003, Keeton et al. 2005) or by simulations (Amara et al. 2006 [102], Macciò et al. 2005 [128]).[1] An explanation by lensing of substructures for the anomalous flux ratio for the PG1115+080 system has already been considered (Chiba 2002 [109], Dalal & Kochanek 2002 [114], Chen et al. 2003[111], Keeton, Gaudi, Petters 2005 [125]), however, mainly within a statistical treatment to determine whether a plausible collection of mass clumps could explain the strange flux ratio. As pointed out by Chiba (2002) [109], even if it seems difficult to reproduce anomalous flux ratios with CDM subhalos, he concluded that the main role in reproducing the observed flux ratio is played by the one satellite which is located in the vicinity of an image (either A1 or A2 in PG1115+80).

In this chapter we analyze in detail the lens system by adding one or two subclumps nearby one of the images and by solving the lens equation. In section 4.2 we review the main observation and analysis done so far on the two lens systems PG1115+080 and B1555+375. In section 4.3 we briefly recall the relevant formalism for gravitational lensing and how we proceed when we consider a lens model with a perturbation induced by one or more substructures. Assuming a SIS model for the substructures we can then get an estimate on their position and Einstein radius (or mass) such as to modify the flux of the image pair nearby the critical curve due to a source located close to a fold. In section 4.4 we present the numerical simulations and fits to the two considered lens systems. We conclude with a short summary and discussion of our results in section 4.5.

4.2 About PG1115+080 and B1555+375

PG1115+080 is the second gravitationally lensed quasar which was discovered (Weymann et al. 1980 [150], Impey et al. 1998 [119] and references therein). The source is at redshift $z_s = 1.722$ and the lens galaxy at $z_l = 0.310$. It is an optically selected, radio-quiet quasar. Hege et al. (1981) [118]first resolved the four quasar images (a close pair A2/A1, B and C), confirming the early model of Young et al. (1981) [154]that the lens is a five-images system, one image being hidden by the core of the lens galaxy.

Young et al. (1981) [154] noted that the lens galaxy seems to be part of a small group centered to the southwest of the lens, with a velocity dispersion of approximately 270 ± 70 km s^{-1} based only

[1] These works deal with violations of the cusp relation.

on four galaxy redshifts. The group is an essential component of any model to successfully fit the lens constraints (Keeton et al. 1997; Schechter et al. 1997 [144]). Also two time delays between the images were successfully determined by Schechter et al. (1997)[144] and confirmed by Barkana (1997) [103]. Their results were analyzed by Keeton & Kochanek (1997) [123]and Courbin et al. (1997) [113]leading to a value of $H_0 = 53^{+15}_{-7}$ km s^{-1} Mpc^{-1}, with comparable contributions to the uncertainties both from the time delay measurements and the models.

We take the data for the PG1115+080 system from Impey et al. (1998) [119] (their Fig.1 and Tables 1 and 2) who presented a near-infrared observation of the PG1115+080 system obtained with the Hubble Space Telescope (HST) NICMOS camera. The flux ratio of the close pair of images (A1 and A2, see Fig.4.1) is approximately 0.67 and showed little variation with wavelength from the multiple wavelength observations by Impey et al. (1998) [119] [2]. Simple lens models require instead an A2/A1 flux ratio close to 1, because the images are symmetrically arranged near a fold caustic. There is no smooth lens model that can explain this anomalous flux: while each of such models can differ in complexity or in parameterization, the observed discrepancy in the flux ratio, compared with the expected universal relations for a cusp or fold singularity, suggests that it is an intrinsic difficulty for smooth lens models, not associated with a particular choice of the parameters (Yoo et al. 2005 [155]).

Recently, Chiba et al. (2005) [110] analyzed observations of the PG1115+080 system done in the mid-infrared band and found a flux ratio A2/A1 of 0.93 for the close pair, which is virtually consistent with smooth lens models but clearly inconsistent with the optical fluxes. The observations indicated that the measured mid-infrared flux originate from a hot dust torus around a QSO nucleus. Based on the size estimate of the dust torus, they placed limits on the mass of the substructure causing the optical flux anomaly[3]. For a substructure modeled as a SIS the subclumps should have a mass of at most $2.2 \times 10^4 M_\odot$ inside a radius of 100pc to prevent anomalies in the mid-infrared band. However, it has to be pointed out that this latter result is based on several assumptions and few observations (Minezaki et al. 2004 [136]), so that the given value may be subject to substantial modifications. Indeed, if the size of the cooler dust torus causing the mid-infrared flux is underestimated then the above limit gets increased. Furthermore, Pooley et al. 2006 [142] analyzed the system using recent X-ray observations, which show also a strong anomalous flux ratio. They do not exclude the microlensing hypothesis in order to explain the anomaly in the X-ray band, nonetheless they conclude that the optical emission region should be much larger (by a factor $\approx 10 - 100$) than predicted by a simple thin accretion disk model. Within this model the source size should be $R_s \approx 10^{15} cm$ (e.g. Wambsganss, Schneider, & Paczyński 1990 [148]; Rauch & Blandford 1991 [143]; Wyithe et al. 2000 [153]). Therefore, if it is 10-100 bigger, $R_s \approx 0.01 - 0.1$ pc, the effect of stellar microlensing could be ruled out (Metcalf 2005).

An interesting quadruply imaged lens system is B1555+375 with a maximum separation of only 0.42 arcsec, which was discovered some years ago (Marlow et al. 1999 [131]). It has an anomalous flux ratio in the radio: the system was observed at 8,4 GHz at VLA and with MERLIN 5 GHz snapshot observations. There are only few observations in the optical and near-infrared band. Marlow et al. (1999) [131] considered a model for B1555+375, which describes well the positions of the images but fails to reproduce accurately the flux ratio between the two images near the fold critical point (labeled by A and B, see Fig.4.3). The observed ratio is about B/A ~ 0.57. This anomaly has also been discussed by Keeton Gaudi and Petters [125]and Dobler & Keeton (2006) [116]. As the redshifts of lens and source have not yet been measured we will adopt the same values as used by Marlow et al. (1999) [131]: $z_l = 0.5$ and $z_s = 1.5$.

[2] Pooley et al. (2006) [142], however, report that there has been some variation also in the optical.
[3] They also considered for this system the microlensing hypothesis and estimated the time variability of the images flux in the mid-infrared band, which turned out to be rather long (more than a decade). This estimate is consistent with the fact that the optical flux ratio has remained unchanged over the past decade. It is thus clearly not yet possible to assess the microlensing hypothesis.

Image	H mag	I mag	V mag
A1	15.75±0.02	16.12	16.90
A2	16.23±0.03	16.51	17.35
B	17.68±0.04	18.08	18.87
C	17.23±0.03	17.58	18.37
Lens	16.57±0.10	18.40	-

Table 4.1. Photometric data in 3 bands for the four images of PG1115+080, from Impey et al. (1998) [119].

4.3 Analytical treatment

We briefly recall the general expressions for the gravitational lensing and refer, e.g., to the book by Schneider et al. (1992) [145] (which we will denote afterwards with SEF [145]) and the review by Kochanek (2006) [127]. The lens equation is

$$\vec{\beta} = \vec{\theta} - \vec{\alpha}(\vec{\theta}) \ , \tag{4.1}$$

where $\vec{\beta}(\vec{\theta})$ is the source position and $\vec{\theta}$ the image position. $\vec{\alpha}(\vec{\theta})$ is the deflection angle, which depends on $\kappa(\vec{\theta})$ the dimensionless surface mass density or convergence in units of the critical surface mass density $\Sigma_{\rm crit}$, defined as

$$\Sigma_{\rm crit} = \frac{c^2}{4\pi G}\frac{D_S}{D_L D_{LS}}, \tag{4.2}$$

where D_S, D_L, D_{LS} are the angular diameter distances between observer and source, observer and lens, source and lens, respectively.

4.3.1 Lens Mapping

In the vicinity of an arbitrary point, the lens mapping can be described by its Jacobian matrix $\mathcal{A}$:

$$\mathcal{A} = \frac{\partial\vec{\beta}}{\partial\vec{\theta}} = \left(\delta_{ij} - \frac{\partial\alpha_i(\vec{\theta})}{\partial\theta_j}\right) = \left(\delta_{ij} - \frac{\partial^2\psi(\vec{\theta})}{\partial\theta_i\partial\theta_j}\right). \tag{4.3}$$

Here we made use of the fact (see SEF [145]), that the deflection angle can be expressed as the gradient of an effective two-dimensional scalar potential ψ: $\vec{\alpha} = \vec{\nabla}_\theta\psi$, which carries information on the Newtonian potential of the lens. The magnification is defined as the ratio between the solid angles of the image and the source (since the surface brightness is conserved) and is given by the inverse of the determinant of the Jacobian $\mathcal{A}$

$$\mu = \frac{1}{\det\mathcal{A}}. \tag{4.4}$$

The Laplacian of the effective potential ψ is twice the convergence:

$$\psi_{11} + \psi_{22} = 2\kappa = \text{tr } \psi_{ij}. \tag{4.5}$$

With the definitions for the components of the external shear γ:

$$\gamma_1(\vec{\theta}) = \frac{1}{2}(\psi_{11} - \psi_{22}) = \gamma(\vec{\theta})\cos[2\varphi(\vec{\theta})] \tag{4.6}$$

and

$$\gamma_2(\vec{\theta}) = \psi_{12} = \psi_{21} = \gamma(\vec{\theta})\sin[2\varphi(\vec{\theta})] \tag{4.7}$$

(where the angle φ gives the direction of the shear) the Jacobian matrix can be written as

$$\mathcal{A} = \begin{pmatrix} 1-\kappa-\gamma_1 & -\gamma_2 \\ -\gamma_2 & 1-\kappa+\gamma_1 \end{pmatrix} \tag{4.8}$$

$$= (1-\kappa)\begin{pmatrix} 1 & 0 \\ 0 & 1 \end{pmatrix} - \gamma \begin{pmatrix} \cos 2\varphi & \sin 2\varphi \\ \sin 2\varphi & -\cos 2\varphi \end{pmatrix}, \tag{4.9}$$

where $\gamma = \sqrt{\gamma_1^2 + \gamma_2^2}$. With eq.(8) the magnification can be expressed as a function of the convergence κ and the shear γ at the image point:

$$\mu = (\det \mathcal{A})^{-1} = \frac{1}{(1-\kappa)^2 - \gamma^2}. \tag{4.10}$$

Locations at which $\det A = 0$ have formally infinite magnification are the critical curves in the lens plane. The corresponding locations in the source plane are the caustics. For spherically symmetric mass distributions the critical curves are circles, whereas for elliptical lenses or spherically symmetric lenses with external shear, the caustics can have cusps and folds.

Near a fold the lens equation can be reduced to a one-dimensional model and a Taylor expansion can be performed (see SEF [145], Kochanek 2006 [127]), for which we get

$$\beta - \beta_0 = \frac{\partial \beta}{\partial \theta}(\theta - \theta_0) + \frac{1}{2}\frac{\partial^2 \beta}{\partial \theta^2}(\theta - \theta_0)^2, \tag{4.11}$$

i.e.

$$\beta = \theta\,(1 - \psi'') - \frac{1}{2}\psi'''\theta^2 \rightarrow -\frac{1}{2}\psi'''\theta^2 \tag{4.12}$$

and inverse magnification

$$\mu^{-1} = (1 - \psi'') - \psi'''\theta \rightarrow -\psi'''\theta. \tag{4.13}$$

We choose the coordinate system such that there is a critical line at $\theta = 0$ (i.e. $1 - \psi'' = 0$) and the primes denote derivatives with respect to θ. These equations are easily solved and one finds that the two images are at $\theta_\pm = \pm(-2\beta/\psi''')^{1/2}$ with inverse magnifications $\mu_\pm^{-1} = \mp(-2\beta\psi''')^{1/2}$ that are equal in magnitude but with opposite sign. Hence, if the assumptions for the Taylor expansion hold, the images merging at a fold should have identical fluxes. Using gravity to produce anomalous flux ratios requires terms in the potential with a length scale comparable to the separation of the images to significantly violate the rule that they should have similar fluxes.

4.3.2 Perturbing the system

Let's consider a general lens system configuration for which we know flux ratios and image positions and we assume to be able to reproduce with a smooth lens model, such as a singular isothermal ellipsoid (SIE), the main features of the lens, besides the anomalous flux ratio. Adding an external potential term in the lens equation and correspondingly in the Jacobian matrix such as induced by singular isothermal sphere (SIS) substructures perturb the system. Keeton (2001) [122]analyzing the system B1422+231 (cusp case), could put limits on the subclump mass range by considering the different effects they would induce on optical and radio bands. For the same system Bradač (2002) [106] suggests a way to estimate the minimum value for the convergence k in order to get agreement with the observed flux ratios.

Here we constrain the mass and the position of a substructure by considering its effects on the flux of the images. At each image position the perturbed Jacobian matrix can be written as

$$\mathcal{A} = \begin{pmatrix} 1-\kappa_1-\tilde{\gamma}_1 & -\tilde{\gamma}_2 \\ -\tilde{\gamma}_2 & 1-\kappa_1-\tilde{\gamma}_1 \end{pmatrix}, \tag{4.14}$$

where $\kappa_1 = (\kappa + \Delta\kappa), \tilde{\gamma}_1 = (\gamma_1 + \Delta\gamma_1), \tilde{\gamma}_2 = (\gamma_2 + \Delta\gamma_2)$ and $\Delta\kappa, \Delta\gamma_1$ and $\Delta\gamma_2$ are the perturbations induced by a substructure.

If the substructure is modeled by a SIS, it is possible to express the shear components as a function of $\Delta\kappa$ (this is true for models that have radial symmetry, Kormann et al. (1994) [192]): $\Delta\gamma_1 = \Delta\kappa cos\theta_{sis}$ and $\Delta\gamma_2 = \Delta\kappa sin\theta_{sis}$, where

$$\Delta\kappa = \frac{R_{sis}}{2\sqrt{(x_{sis} - x_P)^2 + (y_{sis} - y_P)^2}}. \tag{4.15}$$

(x_{sis}, y_{sis}) is the position of the substructure and (x_P, y_P) is the considered image position. R_{sis} is the Einstein radius of the substructure, which depends on its mass and the distances (or redshifts) to the lens and the source, the latter ones being known quantities. The θ_{sis} is given through the relation $tg\theta_{sis} = (x_{sis} - x_P)/(y_{sis} - y_P)$ and it is the angle between the SIS and the considered image position (x_P, y_P). We first consider a model with one additional substructure located at the same distance as the lens. Its mass and position have to be determined such that the substructure does not significantly (within the observational errors) modify the positions of all the images as well as the fluxes of the images which lie far from the two ones nearby the fold critical point. These requirements clearly put constraints on the mass and position of the substructure.

For the determination of the magnification of an image the additional terms due to the substructure depend only on the position (x_{sis}, y_{sis}) and the mass (Einstein radius R_{sis}) of the subclump, thus we have 3 unknown quantities (see Appendix). We consider only three images, thus getting a system with three equations for three unknown quantities, and assume that the 4th image is far enough such as not to be perturbed by the substructure. We then verify a posteriori that the found solution satisfies this latter assumption within the measurement errors. It turns out indeed to be the case, as the subclump is located far from the 4th image, which is chosen as being the most distant one from the two nearby the fold. The system of equations is non-linear, so that the solution is not unique (see Appendix A). However, some solutions have to be discarded as being not physical (imaginary values or a negative Einstein radius). All acceptable solutions are taken as input parameters for the simulations, as will be discussed in the next Section (see also Fig 4.1).

Note that the substructure could produce further multiple images of the original one. In our case, where we model the substructures as SIS, necessary and sufficient condition for multiple images formation is that the Einstein radius (of the subclump) θ_{Esub} has to be greater than half of θ_I, the distance of the image from the subclump ($\theta_{Esub} \geq (1/2)\theta_I$) (Narayan & Schneider 1990 [139]). In Tables 4.4 and 4.7 we give the positions of the substructures and of the images for the two considered lens systems as obtained from the simulations as discussed in the next section. From these data one easily verifies that the Einstein radius of the substructures, as given in Tables 4.2 and 4.6, do not satisfy the above condition, thus ruling out the formation of further images. As noticed by Keeton (2003) [124], for SIS subclumps positive-parity images get always brighter, whereas negative-parity images get fainter. In our case for PG1115+080 (B1555+375) A1 (A) is the positive-parity image and A2 (B) the negative-parity one.

4.4 Numerical simulations

In this section we present our simulations and results. We use the gravlens code developed by Keeton (2001) [122][4], modeling the main galaxy acting as lens (in both cases) by a SIE and then by adding an external shear term (which we will in the following denote by SIE_γ) and/or a SIS term to take into account the influence of the group in which the galaxy is embedded. Moreover, we add one or two substructures to take into account the effects on small scales. For PG1115+080 we use data in H band (see Table 4.1) taken from Impey et al. (1998) [119], and for B1555+375 the data in the 5 GHz radio band (see Table 4.6) from Marlow et al. (1999) [131]. We allowed a conservative 1 σ error in the relative x- and y- positions of the image components (corresponding to an error of at most 5 mas), and 1 σ error on the values of the fluxes (corresponding to a variation by 20%). In each model we have different parameters and constraints, and the goodness of the fit is given by the χ^2 value, evaluated on the image plane (χ^2_{img}), and is a sum of different contributions: image

[4] The software is available via the web site: http://cfa-www.harvard.edu/castles

positions and fluxes, and main galaxy position[5].

4.4.1 PG1115+080

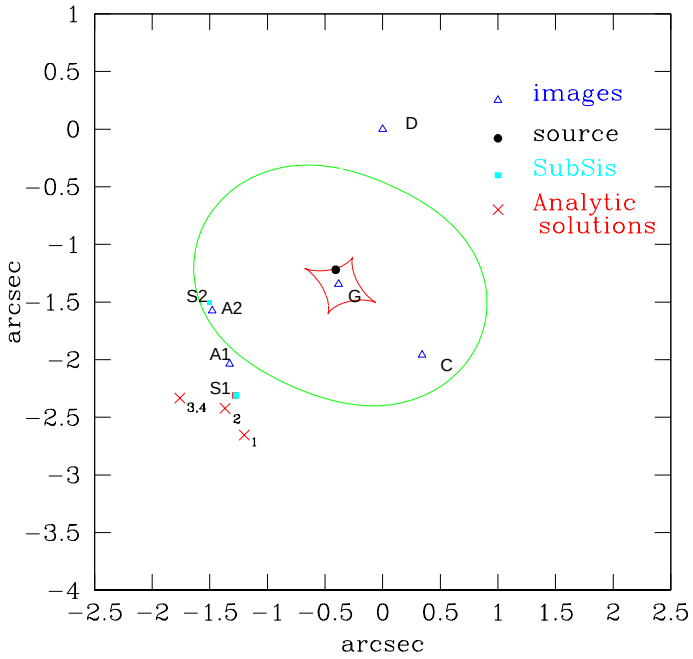

Figure 4.1. PG1115+080: images, source and galaxy (G) positions are shown assuming a SIE$_\gamma$+SIS model. The position of the substructure for both models is also given: note that S1 is closer to the A1 image, while S2 to A2. The critical curve and the caustic are for the SIE$_\gamma$ model without the modifications induced by the substructure. The analytic solutions as discussed in the Appendix are also shown. The solutions labeled as 3 and 4 are so close that on the figure they coincide.

We model the main lens galaxy as a SIE and take into account the contribution due to the group of which the galaxy is part of either by adding a SIS_{group} component (Keeton 2003 [124], Chen et al. 2003) or an external shear term. We consider both models to which we add one substructure described as a small SIS.

The results for PG1115+080, modeled as a SIE and an external shear or a SIS, are given in Tables 4.2, 4.3 and 4.4 (in the following we indicate with M the mass inside the Einstein radius) and in Fig4.1. In both cases we find good agreement with previous results (Impey et al. 1998 [119], Chiba 2002 [109]). In the case SIE_γ we find for the external shear γ=0.11 and for its direction an angle of $\phi = 56^0$, which agree well with the results of Chiba (2002) [109].

In a further step we add one substructure, using as starting parameters for its position and mass the analytic results as determined following the method outlined in the previous section [6].

[5] There is an alternate way to define the χ^2 that is evaluated in the *source plane* (χ^2_{src}) (e.g., Kayser et al. 1990 [121]), which is an approximate version of χ^2_{img}: when using the minimization within this approximation the formation of additional images is not excluded, maybe yielding to a not realistic model. However, the approximation inherent χ^2_{src}, should properly be used only if a good model is already known, not in an initial search for a good model (Keeton 2001 [122]).

[6] Moreover, since we don't know a priori the source flux, we take the value we get from the SIE_γ model and, considering the observational fluxes with respect to the A1 image, we use them as starting values in the analytical system.

In the model $SIE_\gamma + SIS$ we have 11 parameters, i.e. for the main galaxy : Einstein radius (i.e. mass), ellipticity e and orientation PA, shear γ and its direction ϕ; for the substructure: the Einstein radius, position (corresponding to 2 parameters) and, moreover, the source position (2 parameters) and its flux. The observational constraints are 12, namely the 4 x 2 image positions and 4 fluxes.

In the model SIE+SIS$_{group}$+SIS, in which the group is modeled by a SIS, the substructure (denoted in Fig.4.1 by S2) is close to A2, whereas for the previous model it is close to A1 (denoted as S1 in Fig 4.1). By adding one substructure the value of the anomalous flux ratio improves substantially for both models: getting lowered from 0.91 to 0.69 for the first model and to 0.66 for the second model, with χ^2_{tot}=1.3 and ≈ 0.4, respectively, which is quite good. [7]

Parameter	SIE$_\gamma$	SIE+SIS$_{group}$	SIE$_\gamma$+SIS	SIE+SIS$_{group}$+SIS
$R_{E,gal}$	1.03	1.14	1.12	1.03
$M_{gal}(M_\odot)$	1.23×10^{11}	1.05×10^{11}	1.24×10^{11}	1.05×10^{11}
$R_{E,group}$	–	2.30	–	2.11
M_{group} $(M_\odot)$ –		4.10×10^{11}	–	4.0×10^{11}
$R_{E,sub1}$ –		–	0.033	0.001
$M_{sub1}(M_\odot)$	–	–	1.00×10^{8}	1.00×10^{5}
A2/A1	0.91	0.95	0.69	0.66
γ	0.11	–	0.11	–
ϕ	56^0	–	56^0	–
χ^2	77	3.9	1.30	0.08

Table 4.2. PG1115+080: Parameters for different models, with and without substructure. γ and ϕ are the values of the external shear and its direction. By adding a substructure the agreement between predicted and observed fluxes increases substantially.

Model	Image	κ	γ	μ	A2/A1
SIE$_\gamma$	A1	0.498	0.421	13.35	0.91
	A2	0.535	0.545	-12.17	–
SIE+SIS$_{group}$	A1	0.534	0.411	20.21	0.95
	A2	0.551	0.504	-19.31	–
SIE$_\gamma$+SIS	A1	0.554	0.372	16.54	0.69
	A2	0.561	0.531	-11.54	–
SIE+SIS$_{group}$+SIS	A1	0.531	0.410	19.46	0.66
	A2	0.565	0.517	-12.83	–

Table 4.3. PG1115+080: Values of shear, convergence and amplification for A1 and A2 images from simulations for the considered models.

The results from the simulations agree, as expected, quite well with the analytical ones. Since the mass of the substructures is very small as compared to the mass of the lens galaxy, the approximation used in the analytical approach to neglect the influence induced on the positions of the images by the substructures is quite well fulfilled. We checked this, indeed, on the results obtained from the numerical simulations.

Since the positions and magnifications of the images are only known within a certain accuracy, we computed the corresponding 1σ and 2σ ranges for the value of the mass of the substructure. Starting from our best model we consider two approaches. In the first we let all parameters (i.e. the main galaxy ones and the position of the substructure) vary, whereas in the second one we keep the main galaxy parameters fixed at the values given by the best fit model and let the remaining parameters vary. The high values for the total χ^2 are due to the bad galaxy position fit (in the first

[7] By further adding a second substructure to the first model, we find even a lower value for the flux ratio, however, χ^2_{tot} and χ^2_{flux} increase, which indicates that this model does not correspond to a global minimum, but rather to a local minimum of the χ^2_{tot} surface.

Object	x (arcsec)	y (arcsec)	e	PA
Galaxy	-0.381	-1.345	0.14	-84^0
A1	-1.328	-2.037	–	–
A2	-1.478	-1.576	–	–
Sub1	-1.33	-2.20	–	–
Sub2	-1.52	-1.57	–	–

Table 4.4. PG1115+080: positions of the lens galaxy center, the close pair A1 and A2, as well as the substructure with respect to the C image (see Fig.4.1). Also ellipticity e and orientation PA of the semi major axis with respect to x-axis (as measured from East to North and centered in the C image) are given. The distances between the substructure and the images A1 and A2 are bigger than twice their corresponding Einstein radius. Thus no further images will be formed.

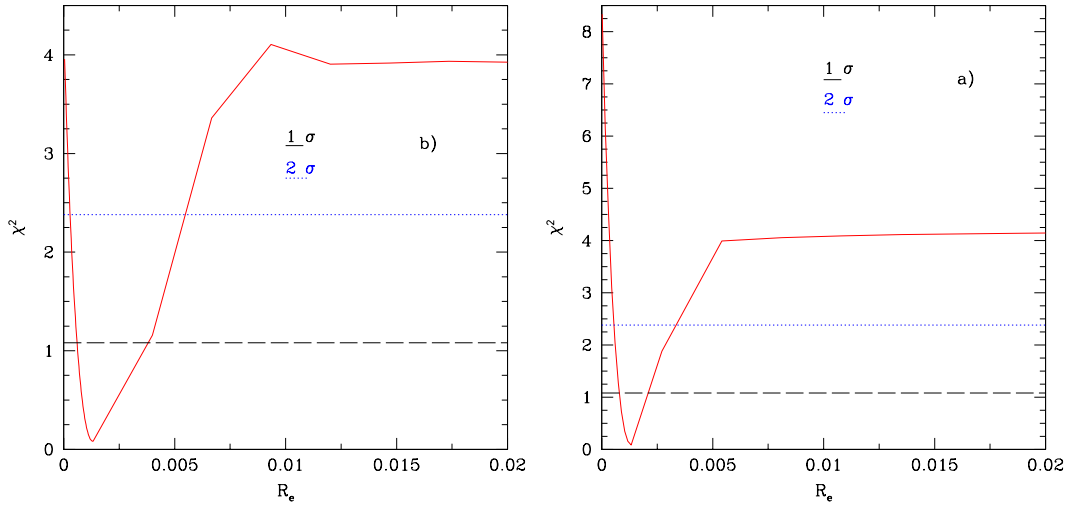

Figure 4.2. 1σ and 2σ limits for the Einstein radius for the model SIE+SIS$_{group}$+SIS: a): letting all parameters fixed but the position of the subclump; b): letting all parameters vary.

case) and to the bad image position fit (in the second case). In Fig.4.2 we report χ^2 as a function of the substructure Einstein radius for the SIE+SIS$_{group}$+SIS model for both cases mentioned above. We do not consider larger values for the Einstein radius as this would correspond to masses for the substructure of order $M(< R_e) \approx 10^9 - 10^{10} M_\odot$, too big to be realistic and for which one would see effects on the image position or even image splitting. On the other hand we can also exclude Einstein radius that are too small. In fact, if it is true that with a standard accretion disk model we get a source size radius $R_s \approx 10^{15} cm$ (Chiba et al 2005) [110]and that for the PG1115+080 system the real source size should be about 10-100 times bigger (Pooley et al 2006 [142]), we can estimate roughly the limit of the Einstein radius for which the effects on the images become negligible. For a stellar $R_E \approx 10^{-5}$ arcsecs, that corresponds to 0.03 pc (on the lens plane), there would be no (or little) effect on an image of a source with $R_S \approx 0.1$ pc. The minimum value of the curve corresponds to an Einstein radius ≈ 0.001 arcsec. Anyway, the curve within the 2σ range is rather constrained (in both cases), leading thus in practice to a small degeneracy, with a rather narrow range for acceptable values of the substructure mass. The 2σ range is within an Einstein radius of 0.0005 and ≈ 0.005 arcsec corresponding to $\sim 2.5 \times 10^4\ M_\odot$ and $\sim 2.5 \times 10^6\ M_\odot$.

The 2σ range for the $SIE_\gamma + SIS$ model is somewhat larger. Considering for example the first case, the Einstein radius for the substructure could be as high as 0.1 arcsecs, leading to quite a big mass ($\approx 10^9 M_\odot$).

4.4.2 B1555+375

B1555+375 is another lens system for which the agreement between observations and model can be improved. Already by adding an external shear one can quite substantially improve the flux fitting, assuming for the lens galaxy a SIE model. Anyway, Dobler & Keeton (2005) consider this model unphysical (since ellipticity and shear turn out to be almost perpendicular) and discuss other models, adding substructures and giving lower limits on their masses. They find an acceptable model using two substructures in front of B and C images, respectively. Adding one substructure to the model SIE_γ does not improve the fit further[8]. On the other hand, adding two substructures (modeled as SIS with comparable masses and located nearby the pair of images due to the fold) to the simple SIE model, we get a value for the flux ratio B/A of 0.59, which is only slightly higher then the observed one of 0.57

The results are reported in Tables 4.6, 4.7 and 4.8 and in Fig.4.3. For the model of a SIE_γ we get $\chi^2 = 1.29$ and $\chi^2_{flux} = 0.35$. For the solution with two substructures we find a $\chi^2 \approx 5$, with $N_{dof} = 5$.

As we pointed out above, in the radio band up to now the only successful explanation for the flux anomalies is to consider substructures. Moreover, we notice that the SIE model does neither fit very well the fluxes of the other images besides the close pair ones.

As mentioned in the SIE_γ model we get a rather high value for the ellipticity (0.85) and for the external shear (0.23): such a strong shear can be induced by a group of galaxies located around the main lens. One has also to consider possible effects due to groups of galaxies which lie on the line-of-sight, both in the foreground and in the background (Williams et al. 2005 [151]). Other systems (like B1608+656 or HST 12531-2914) show such a high value for the external shear (see Witt & Mao 1997 [152]). In particular, B0128+437 seems to be quite similar to B1555+375 (see Phillipps et al. 2000 [141]). Anyway, there are still not enough observations neither about the main galaxy nor about its environment, so that it is not possible to choose among the different solutions. However, our solution with two substructures involves a SIE lens model with an angular structure which is in agreement with previous works (Marlow et al. 1999 [131] and Keeton, Gaudi & Petters 2005). Also for this model we computed the confidence intervals for the various parameters. As an example in Fig.4.4 we show the contour ellipses for the confidence intervals of the Einstein radii of the substructures as obtained fixing the main galaxy parameters.

Image	x (arcsec)	y (arcsec)	S_5 (mJy)
A	0.0±0.005	0.0±0.005	17.0
B	-0.073±0.005	0.048±0.005	9.7
C	-0.411±0.005	-0.028±0.005	8.3
D	-0.162±0.005	-0.368±0.005	1.3

Table 4.5. B1555+375: Positions and photometric data of the 4 images as given by CLASS (from Marlow et al. 1999 [131]).

4.5 Discussion

We have analyzed two lens systems, PG1115+080 and B1555+375, which show an anomalous flux ratio for the two images near the critical curve, due to a fold configuration. These systems cannot be modeled using only smooth lens models like SIE, although they fit well all the positions of the images. We added one or two substructures, taking as starting parameters for our numerical simulations the ones obtained by an approximated analytical treatment. This way we reproduce

[8] We tried, as in the previous case, also analytically to estimate mass and position for a single SIS added to a SIE model, but the system of equations does not have in this case real solutions.

Parameter	SIE	SIE$_\gamma$	SIE+2SIS
$R_{E,gal}$	0.22	0.165	0.21
M_{gal} $(M_\odot)$	0.50	0.45	0.50×10^{10}
$R_{E,sub1}$	–	–	0.009
$R_{E,sub2}$	–	–	0.012
$M_{sub1}(M_\odot)$	–	–	8.1×10^6
$M_{sub2}(M_\odot)$	–	–	1.4×10^7
B/A	0.93	0.61	0.59
e	0.53	0.85	0.53
PA	-2.42^0	-6.39^0	0.41^0
γ	–	0.23	–
ϕ	–	-78^0	–
χ^2	13.9	1.9	5.2

Table 4.6. B1555+375: Results from the simulations for two models without substructures and one model with two substructures. (Notice that for the latter model the χ^2 is higher, see text). The Einstein radii are expressed in arcsec. The system is well fitted already by adding external shear.

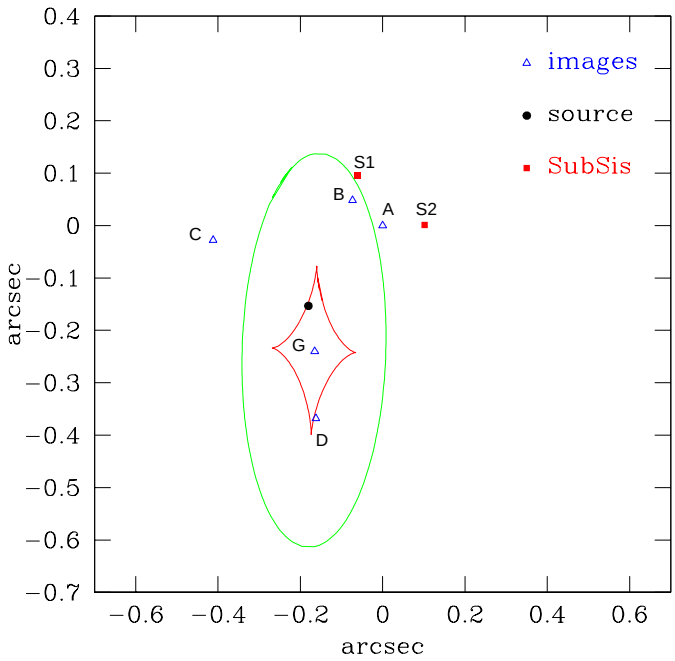

Figure 4.3. B1555+375: images, source and galaxy (G) positions are shown assuming a SIE+2SIS model. The positions of the two substructures are also given. The critical curve and the caustic are for the SIE model alone without the modifications induced by the two substructures.

Object	x (arcsec)	y (arcsec)	e	PA
Lens	-0.162	-0.246	0.53	0.75^0
A	0.0	0.0	–	–
B	-0.075	0.043	–	–
Sub1	-0.060	0.094	–	
Sub2	0.101	0.001	–	

Table 4.7. B1555+375: Parameters of the lens model and of the added substructures. e and PA are ellipticity and orientation of the semi major axis with respect to x-axis (as measured from East to North and centered in the A image).

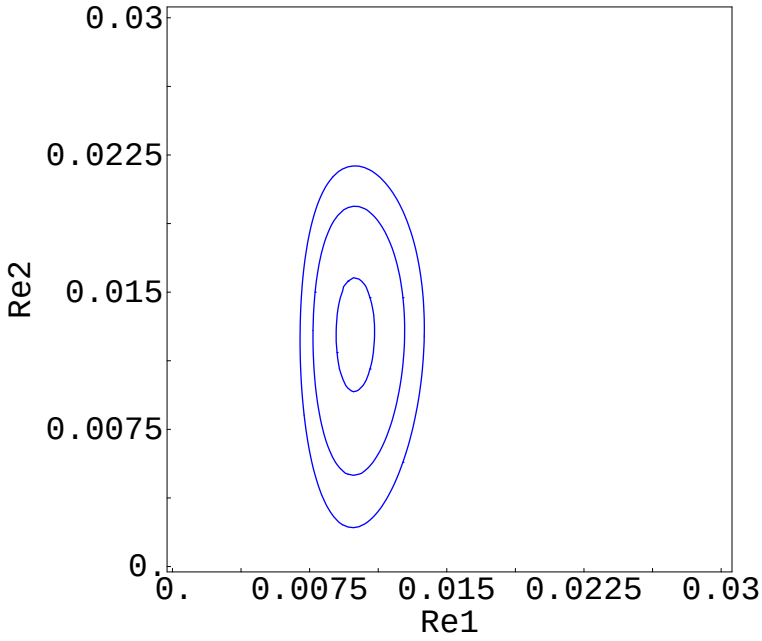

Figure 4.4. B1555+375: Contour plot for the $1, 2$ and 3σ confidence intervals for the Einstein radii of the substructures.

well, in addition to the positions, also the fluxes of the pair of images near the critical curve. In the PG1115+080 case we get a ratio of 0.69 as compared to the observed one of 0.65 if we consider a model SIE_γ + SIS or 0.66 for a model SIE+SIS_{group}+SIS and for B1555+375 a ratio of 0.59 instead of 0.57 with a SIS+2SIS model. In both cases the best models are the ones with additional substructures. Previously, the best models gave values for the anomalous flux ratio of 0.91 for PG1115+080 and 0.93 for B1555+375, respectively. The improvement achieved by just adding substructures is remarkable. For PG1115+080 when we consider the model SIE+SIS_{group}+ SIS we find that the substructure needed to explain the anomaly in the optical band lies close to the A2 image and has a mass $\approx 10^5 M_{odot}$. On the other hand, the model SIE_γ requires a mass $\approx 10^8 M_\odot$ close to the A1 image that could in principle affect also larger λ bands, for which no anomaly has been reported yet (Chiba et al 2005 [110]). Therefore this latter model is certainly less plausible if not already excluded. Clearly, new observations are still needed to better constrain the models.

The masses of the substructures are in the range $\approx 10^5 - 10^8\ M_\odot$, and distant enough from the images not to induce the formation of additional ones. Given the mass range it may well be that the perturbers are globular clusters (in particular for the lower one) or small satellite galaxies for the

larger ones. The mass range is, however, also compatible with dark substructures as predicted by CDM. To get a rough estimate of the number of substructures expected to lie close to the images we follow the work of Diemand et al. (2004) [115]. They compute the two dimensional radial number density of subhalos inside a galaxy virial radius, from which it is then possible to get an estimate of the number of substructures inside a small area surrounding an image in a lens system. The number of subhalos with a mass greater than m inside an area A at a distance r from the center of the galaxy is given by (Macciò & Miranda 2006 [129])

$$N_A(>m,r) = \frac{\langle N_{r_v}(>m_0)\rangle \frac{m_0}{m} N(r) A}{\pi r_v^2} \ , \tag{4.16}$$

where $\langle N_{r_v}(>m_0)\rangle$ is the average number of subhalos with $m > m_0$ inside the virial radius r_v of the galaxy and $N(r)$ describes the radial dependence of the number of substructures. The cumulative mass function of subhalos within the virial radius of an halo scales as $\propto m^{-1}$.

As an example for PG1115+080, we consider $m \geq 10^5 M_\odot$, ($m_0 \approx 10^7$) and a distance of the images from the center $r \approx 1.5$ arcsec ($N(r) \approx 2-6$, $\langle N_{r_v}(>m_0)\rangle \approx 166, r_{vir} = 268\ kpc$, see Macciò & Miranda 2006). Typically, a substructure is expected to lie at a distance from an image comparable to the separation between the close pair, which is about ≈ 0.5 arcsec. We, therefore, consider an area corresponding to a small disc with a radius about twice the separation distance, thus ≈ 1.0 arcsec (corresponding at $z_d = 0.31$ to A$\approx \pi(4.5)^2 kpc^2$). With these assumptions we expect 10 to 30 substructures in the considered area. If instead we require $m \geq 10^6 M_\odot$ then we find about 1 to 3 substructures, and 0.1 to 0.3 for $m \geq 10^7 M_\odot$. From these considerations we see that the expected number of substructures within the CDM model seems, in particular, to be lower than required when considering the model with a $10^8 M_\odot$ mass subclump, whereas for the model with $10^5 M_\odot$ mass subclump it might be in better agreement.

Anyway, with the information at disposal it is obviously not possible to distinguish between different possibilities, moreover it could also be that some of the substructures are actually located along the line of sight rather than being in the surroundings of the lens galaxy.

To this respect it is interesting to notice that with future ALMA observations one could solve this latter problem as pointed out by Inoue & Chiba (2005) [120]. They proposed a method to realize a 3D mapping of CDM substructures in extragalactic halos, based on astrometric shift measurements (at submillimeter wavelengths) of perturbed multiple images with respect to unperturbed images, with which it should be possible to break the degeneracy between the subhalo mass and a position along the line of sight to the image.

Also other explanations of the flux anomaly in multiple QSOlens systems have been considered in the literature, however the best solution, seems to be the presence of substructures in the halo of the lens galaxy.

For the second case there are two acceptable solutions: with and without any substructure. Even if a high shear value seems unplausible, we cannot yet rule out this possibility. A recent work (Williams et al. 2005 [151]) shows the importance of galaxy groups along the line of sight that can significantly impact the lens model. High-resolution VLA radio observations could help to constrain the lens model further. On the other hand, starting from the simple SIE model, we find a real good fit for the image positions and fluxes, if we add two substructures, still keeping acceptable values for the main lens parameters (in agreement with Marlow et al. 1999 [131]).

Finally, we observe that the PG1115+080 system is radio-quiet, so that the microlensing hypothesis can not be ruled out (Pooley et al. 2006 [142]). However, given the different observations at the various wavelengths it might also be possible that both microlensing and millilensing are at work. A more accurate analysis about the source size could cast some light in constraining the substructure size. Since there are discussions about it, more high resolution observations are needed to definitely rule out the millilensing or microlensing hypothesis. On the other hand, for the B1555+375 system there are radio anomalies data, for which the most plausible explanation are CDM substructures in galactic halos.

4.6 Analytic estimates for convergence and shear due to a substructure

We briefly present here the formalism used for the analytical approximation of the total convergence κ_{tot} and the total shear γ_{tot} in the presence of one perturber, located in the main lens plane. At each point of the lens plane we can evaluate the total amplification using the quantities:

$$\kappa_{tot} = \kappa_{sie} + \Delta\kappa, \tag{4.17}$$

$$\gamma_{1tot} = \gamma_{1sie} + \Delta\gamma_1, \tag{4.18}$$

$$\gamma_{2tot} = \gamma_{2sie} + \Delta\gamma_2, \tag{4.19}$$

$$\mu^{-1} = (1-\kappa_{tot})^2 - \left[(\gamma_{1tot})^2 + (\gamma_{2tot})^2\right]. \tag{4.20}$$

κ_{sie} is the convergence due to the main lens and $\Delta\kappa$ is due to the perturber and similarly for the shear γ_{sie} and $\Delta\gamma$ (see Sec. 3.2). Dealing with a SIE model allows us to write (see Kormann et al. 1994 [192]):

$$\kappa_{sie} = \frac{R_{sie}}{2\sqrt{(\frac{2q^2}{1+q^2})(x_{sie}-x_P)^2 + (y_{sie}-y_P)^2}}, \tag{4.21}$$

Where q is the axis ratio of the elliptical model used for the galaxy acting as lens. The values for κ_{sie}, γ_{1sie} and γ_{2sie} are taken, for instance in the PG1115+080 case, from the SIE_γ model (which corresponds to the zero order approximation), computed in A1 and A2 (see Table 3) as well as the magnification factors with respect to the image A1 (and keeping the source flux as obtained from SIE_γ model). In this way the system

$$\begin{cases} \mu_{A1}^{-1} &= (1-\kappa_{totA1})^2 - \left[(\gamma_{1totA1})^2 + (\gamma_{2totA1})^2\right] \\ \mu_{A2}^{-1} &= (1-\kappa_{totA2})^2 - \left[(\gamma_{1totA2})^2 + (\gamma_{2totA2})^2\right] \\ \mu_{B}^{-1} &= (1-\kappa_{totB})^2 - \left[(\gamma_{1totB})^2 + (\gamma_{2totB})^2\right] \end{cases} \tag{4.22}$$

has only three unknown quantities, namely R_{sis} and the perturber position given by (x_{sis}, y_{sis}). Since the system is non-linear, we get different sets of solutions, some of which turn out to be unphysical. The allowed solutions are near the close pair (see Table A1). We marked their positions on Fig 4.1. We used then these solutions as input parameters for the numerical simulation. It turns out that all converge to the same model $SIE_\gamma + SIS$ discussed in Sect. 4.1.

	R_E	x	y
	arcsec	arcsec	arcsec
1	0.030	-1.199	-2.65
2	0.035	-1.825	-2.352
3	0.049	-1.363	-2.421
4	0.050	-1.76	-2.332

Table 4.8. Analytic solutions for PG1115+080 as discussed in the text.

Chapter 5

The effect of low mass substructures on the Cusp lensing relation

5.1 Introduction

[1]Cold Dark Matter (CDM) simulations predict many more low mass satellite haloes than are actually observed in the Milky Way (Klypin et al. 1999 [126], Moore et al. 1999 [137]). It seems that 10-15% of the mass was left in satellites with perhaps 1-2% at the projected separations of 1–2 Einstein radii (R_e) where we see most lensed images (e.g. Zentner & Bullock 2003 [158], Mao et al. 2004 [157]); this is far larger than the observed fraction of 0.01–0.1% in observed satellites (e.g. Chiba 2002 [109]). Solutions to this mismatch were proposed in three broad classes: satellites are present but dark if star formation is prevented (Bullock, Weinberg & Kravtsov 2000) [107], satellites are destroyed due to self-interacting dark matter (Spergel & Steinhardt 2000 [159]), or their formation is prevented by changing the power spectrum to something similar to warm dark matter with significantly less power on the relevant mass scales (e.g. Bode et al. 2001 [180]). These hypotheses left the major observational challenge of distinguishing dark satellites from non-existent ones. This became known as the CDM substructure problem.

It has been argued that a possible signature of the presence of dark matter substructures can be found in strong gravitational lensing of QSOs (Mao & Schneider 1998 [130]; Metcalf & Madau 2001 [132]; Chiba 2002 [109]; Metcalf & Zhao 2002 [133]; Dalal & Kochanek 2002 [114], Kochanek & Dalal 2004 [160]). If a distant image source is close to a cusp (from inside) in a caustic curve, three of the images will be clustered together and the sum of their magnifications will be zero (Zakharov 1995 [214], taking the negative parity image to have negative magnification). This relation holds for a wide class of smooth analytic lens models (Keeton et al. 2003 [124]); on the other hand all known observed lensed QSOs violate this relation. This has been explained with the presence of cold dark matter substructures within the lensing galaxy's halo.

However, the discrepancy found in some systems may be due to microlensed stars rather than to cold dark matter substructures (Keeton et al. 2003 [124]), even if the most peculiar problem is the anomalous flux ratios in radio lenses. Radio sources are essentially unaffected by the ISM of the lens galaxy (see however Koopmans et al. 2003 [191]), true absorption appears to be rare, radio sources generally show little variability and most of the flux should come from regions too large to be affected by microlensing. Therefore dark matter subhaloes appear to be the most likely explanation.

By using low resolution simulation of galaxy formation Bradac et al. (2004) [161] claimed that the level of substructures present in simulation produces violations of the cusp relation comparable to those observed. Amara et al. (2006) [102] implanted an idealized model of a galaxy into the center of a high resolution galactic halo extracted from dissipationless N-Body simulations to test the effects of substructures on lensed images. Their findings contrast those of Bradac et al. (2004)[161] , since

[1] Published, 2006 Monthly Notices of the Royal Astronomical Society 368, 599, [129]

they found that the substructures produced in a ΛCDM halo are not abundant enough to account for the observed cusp caustic violation. The results of Amara et al. (2006) [102] were also confirmed in a recent work by Macciò et al. (2006) [128]. In the later work, in which a fully hydrodynamical simulation of galaxy formation is used, it is shown that the presence of a dissipative component greatly enhances the surviving probability of satellites, expecially close to the center of the galaxy. Nevertheless Macciò et al. (2006) [128] also demonstrated that the impact on lensing of subhaloes in the mass range $10^7 - 10^{10}$ $M_\odot$ is very small. Even with a number of subhaloes about 8 higher of the observed one in this mass range, the number of multiple lensed QSOs that show a violation of the cups relation is less than 24%, in contrast with an observed one of about 60%. This means that if the violation of the cusp relation is due to substructures inside the primary lens, these must have a mass smaller than 10^7 $M_\odot$.

The aim of this work is to study the influence of subhaloes with mass $10^5 - 10^7 M_\odot$ on the cusp relation violation.

The outline of the chapter is the following: first we briefly summarize the cusp relation, then in section 5.3 we present the lensing numerical simulations and our modeling for the primary lens, subhaloes and extra-haloes. Tests for our models and results for three different cusp configurations are presented in section 5.4. Section 5.5 is devoted to a short discussion on the fold relation. A discussion of the results and our conclusions are presented in section 5.6. Throughout this chapter the single large halo that is causing the QSO multiple images is referred to as the primary lens. The additional small scale haloes (inside the host halo) are referred to as subhaloes or substructures. Haloes beyond the virial radius of the primary lens are referred to as extragalactic haloes. We adopt the standard ΛCDM cosmological model with the following parameters $\Omega_m = 0.3$, $\Omega_\Lambda = 0.7$, $\sigma_8 = 0.9$ and $H_o = 70$ km s^{-1} Mpc^{-1}.

5.2 The cusp relation

There are basically three configurations of four-image systems: fold, cusp, and cross (Schneider & Weiss 1992 [200]). In this chapter we will mainly concentrate on the *cusp* configuration, that corresponds to a source located close to the cusp of the inner caustic curve. The behavior of gravitational lens mapping near a cusp was first studied by Blandford & Narayan (1986) [179], Schneider & Weiss (1992) [200], Mao (1992) [156]and Zakharov (1995) [214], who investigated the magnification properties of the cusp images and concluded that the sum of the signed magnification factors of the three merging images approaches zero as the source moves towards the cusp. In other words:

$$R_{cusp} = \frac{\mu_A + \mu_B + \mu_C}{|\mu_A| + |\mu_B| + |\mu_C|} \rightarrow 0, \quad for \quad \mu_{tot} \rightarrow \infty \tag{5.1}$$

where μ_{tot} is the unsigned sum of magnifications of all four images, and A,B & C are the triplet of images forming the smallest opening angle (see figure 6.3). By opening angle, we mean the angle measured from the galaxy center and being spanned by two images of equal parity. The third image lies inside such an angle. This relation is an asymptotic relation and holds when the source approaches the cusp from inside the inner caustic "astroid". This can be shown by expanding the lensing map to third order in the angular separation from a cusp (Schneider & Weiss 1992 [200]). Small scale structure on scales smaller than the image separation will cause $R_{\rm cusp}$ to differ from zero fairly independently of the form of the rest of the lens. Indeed, a substructure is more likely to reduce the absolute magnification for negative magnification images (Metcalf & Madau 2001 [132], Schechter & Wambsganss 2002 [201], Keeton et al. 2003 [124]) and to increase it for positive parity images.

5.3 Lensing Simulations

We use the *lensmodel* package (Keeton 2001 [122])[2] modeling the main lens galaxy as a singular isothermal ellipsoid (SIE) and the substructures as NFW (Navarro, Frenk & White 1997 [195]) haloes. First, using the *gravlens* task, we find three lens configurations for which the cusp relation is roughly satisfied (figures 6.3, 5.10 and 5.16).

As second step a variable number of substructures is added to the main lens (see section 5.3.2 for details on their number density and physical properties). For this new lensing system (main lens plus subhaloes) we compute again positions and fluxes of the images (subhaloes mainly tend to modify fluxes more than positions, see Kochanek (2006) [127] and section 5.4.1), obtaining a new value for the cusp relation $R_{\rm cusp}$. This procedure is repeated more than 20.000 times for each of three studied positions of the source (figures 6.3, 5.10 and 5.16): this allows us to compute the probability distribution of the $R_{\rm cusp}$ value in presence of subhaloes (i.e. figure 5.8).

5.3.1 Primary Lens

The observed discrepancy in the flux ratios, compared with the expected universal relation from a cusp or fold singularity, suggests that it is an intrinsic difficulty for smooth lens models, not associated with a particular parameterization. For the scope of this analysis it is sufficient to choose just a single smooth lens model for the primary lens. Therefore, we select, as a smooth lens model, a singular isothermal ellipsoid (SIE) (Kormann, Schneider, & Bartelmann 1994 [192]) to take advantage of its simplicity. This model has been widely used in lens modeling and successfully reproduces many lens systems (e.g. Keeton & Kochanek 1998 [82], Chiba 2002 [109], Treu & Koopmans 2004 [162]). An isothermal profile for the total mass distribution of elliptical galaxies is well supported by the detailed dynamical studies of local ellipticals (Gerhard et al. 2001 [163]), individual lens modeling, and statistics (e.g. Maoz & Rix 1993 [165]; Kochanek 1995 [164]; Grogin & Narayan 1996 [168]).

The ellipsoidal primary lens has a mass equal to $5 \times 10^{11} {\rm M}_{\odot}$, it is oriented with the major axis along the y axis in the lens plane and has an ellipticity of 0.33. The redshifts of the lens and he source are fixed to $z_l = 0.3$ and $z_s = 1.71$ respectively, agreement with the typical observed ones (in this case we use PG1115+080 data, see Tonry 1998 [206])

5.3.2 Subhaloes

Since it has been shown that the number density of subhaloes with mass $M > 10^7 {\rm M}_{\odot}$ is not sufficient to explain the observed number of violation in the cusp relation (Amara et al. 2006 [102], Macciò et al. 2006 [128]), the aim of this work is to investigate the impact of substructures below this mass threshold that is fixed by the current resolution limits of numerical simulations.

We would like to emphasize that we are using only one lensing plane, this means that we will consider only effects due to substructures being at the same redshift of the main lens (see Chen, Kravtsov & Keeton 2003 [111], Metcalf 2005a [135]for an estimation of the effects of haloes along the line of sight). In order to evaluate the number density substructures in the mass range $10^5 - 10^7 {\rm M}_{\odot}$ we have made some extrapolations based on results from high resolution N-body simulations. The mass function of subhaloes inside the virial radius of an halo is close to a power law (Diemand et al. 2004 [115], DMS04 hereafter, Gao et al. 2004 [166], Reed et al. 2005 [167]):

$$N(> m) \propto m^{-\beta}, \tag{5.2}$$

with a slope $\beta \approx 1$, so that we expect to have a factor ≈ 100 more subhaloes inside the viral radius if we move our mass threshold from $10^7 {\rm M}_{\odot}$ to $10^5 {\rm M}_{\odot}$.

[2] The software is public available via web site: http://cfa-www.harvard.edu/castles

As said in the previous section such small haloes will affect the $R_{\rm cusp}$ relation only if their distance from the images is of the same order or smaller than the distance between the images themselves. Therefore we need an estimation of the number of haloes inside a small area surrounding the images. This number will also depend on the distance of our area from the center, due to the fact that the number density of haloes increases approaching the center of the main halo (primary lens) as clearly shown in fig 5.1, which is based on numerical simulations of 4 galaxy size haloes (DMS04).

Consequently the number of subhaloes with a mass greater than m inside an area A at a distance R from the center of the galaxy is:

$$N_A(>m,R) = \frac{\langle N_{r_v}(>m_0)\rangle \frac{m_0}{m} N(R) A}{\pi r_v^2}, \tag{5.3}$$

where $\langle N_{r_v}(>m_0)\rangle$ is the average number density of subhaloes with $m > m_0$ (being m_0 an arbitrary mass value) inside the virial radius r_v and $N(R)$ is the radial 2D number density of satellites at a projected distance R from the center in units of $\langle N_{r_v}(>m_0)\rangle$ (see figure 5.1). These last two quantities can be obtained directly from N-body simulations. In the following we will use results from DMS04 (table 1 of their paper, simulations G0-G3). Macciò et al. (2006) [128] have shown that the presence of baryons inside subhaloes enhance the probability to find haloes close to the center of the galaxy with respect to results from dissipationless simulations. This is true for satellites with $m > 5\times10^7 \mathrm{M}_\odot$, which are massive enough to retain baryons inside their potential well and then form stars. Since we do not expect such effect for the mass scales involved in this work ($\approx 10^5 - 10^6 \mathrm{M}_\odot$) we can use pure N-body simulation as starting point for our analysis.

Since the typical separation between images in lensed QSOs is roughly a few arcsec, we fix $R \approx 1$ arcsec and $A = 6$ arcsec^2 (A_6 hereafter). We remind that at a redshift of $z_l = 0.3$ one arcsec corresponds to 4.55 kpc for the cosmological model adopted in this chapter. Using eq. 5.3 and adopting a mass threshold for substructures of $m = 5\times10^5 \mathrm{M}_\odot$ the number of subhaloes inside A ranges from 4 to 12 (depending on the uncertainties on $N(R)$, see figure 5.1). For two $10^7 \mathrm{M}_\odot$ haloes the surface mass density within the selected area A is $0.69h^{-2}\mathrm{M}_\odot$ pc^{-2}, this means a fraction $\approx 10^{-3}$ of the total dark matter surface density in substructures, in good agreement with the results of Mao et al 2004.

For each lensing configuration analyzed in this work we added a random number of substructures between $4-12$ to the primary lens with a random mass generated according to eq. 5.2 in the range $5\times10^5 - 10^7 \mathrm{M}_\odot$. These subhaloes are then placed following the 2D density profile inside the area A_6 that encloses the three images (cfr the (blue) square in figure 6.3). We have modeled our subhaloes with an NFW density profile; for the $\approx 10^6 \mathrm{M}_\odot$ subhaloes relevant for lensing substructure studied in this work, the NFW profile inferred from N-body simulation is the most natural choice, because on these mass scales the effect of baryons (that are able to modify the slope of the density profile for greater masses (Macciò et al. 2006 [128]) is very tiny because the potential well of these haloes is not deep enough to retain them expecially in presence of a ionizing background. We have adopted different concentration parameters (see sec. 5.4.1) to mimic the scatter present in the mass-concentration relation (Bullock et al. 2000 [107]).

5.3.3 Extrahaloes

Lensing galaxies are not isolated object, since they usually belong to group of galaxies (Keeton et al. 2000 [169]). Moreover each galaxy has its own satellites galaxies with masses in the range $10^9 - 10^{11}\mathrm{M}_\odot$. Consequently we have modeled the presence of these *extrahaloes* in the same way of the *innerhaloes*. In this work we call substructures or innerhaloes, haloes with mass $< 10^7\mathrm{M}_\odot$ that are close to the image position; we reserve the term extrahaloes for haloes with $M > 10^9\mathrm{M}_\odot$. We do not consider extrahaloes that for projection effects can lie inside the primary lens close to the images positions (i.e. Oguri 2005 [170]).

We considered three different categories of extrahaloes: i) haloes with mass $10^9 < M < 10^{10}\mathrm{M}_\odot$

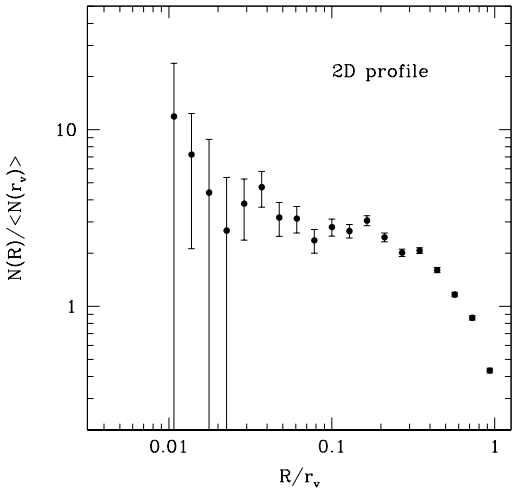

Figure 5.1. Two dimensional radial number density of subhaloes in units of the average number density inside the virial radius. Result obtained averaging the 4 high resolution galaxies presented in DMS04, using three different projections for each galaxy.

and with a projected distance r between 60 and 200 kpc, these represent the satellites galaxy of the primary lens (the expected number for these haloes can be estimated again form N-body simulation and it is roughly 6-8); ii) haloes with mass $10^{11} < M < 10^{12}\mathrm{M}_{\odot}$ and distance $300 < r < 700$ kpc in order to mimic the presence of companion galaxies; iii) haloes with $10^{12} < M < 5 \times 10^{13}\mathrm{M}_{\odot}$ and $700 < r < 1200$ kpc to take into account the possible presence of a nearby cluster of galaxies.

The number of extrahaloes has been fixed between 2-8 and 2-4 for the ii) and iii) case respectively, as suggested by observations/simulations (Metcalf 2005 [194], Amara 2006 [102]). While the extrahaloes in case i) are placed in a circularly symmetric way around the center of the galaxy, the position of groups and clusters of galaxies must be modeled in an asymmetric way. Therefore we placed them only in the quadrant with positive coordinates in the lens plane (being the lens in $[0, 0]$, center of the coordinate system we chose). We used SIE as lens model for extrahaloes to take into account the presence of baryons their-inside and we have generated 20.000 different configurations.

5.4 Results

In this section we present results of our Monte Carlo simulations. We have analyzed 3 cusp configurations: Config1 (figure 6.3), Config2 (figure 5.10) and Config3 (figure5.16). They mainly differ for the value of R_{cusp} in the unperturbed case that grows from 0.01 for Config1 to 0.243 for Config3, due to a different position of the source inside the inner caustic curve.

5.4.1 Testing our model

Before proceeding further in our analysis we present some tests on the parameter adopted in our lensing simulation. The presence of substructures acts both on positions and fluxes of the images. When a substructure is added the *gravlens* code adjusts the positions and fluxes of the images by minimizing the χ^2 between the old (unperturbed) and new (perturbed) positions/fluxes. The value of χ^2 depends on the error that we assign to the unperturbed positions and fluxes (usually these are the observational errors); this means that if the error on positions is smaller than the error on fluxes the code will change the latter ones more than moving the images to obtain a lower value for χ^2.

Therefore in principle the value of the perturbed $R_{\rm cusp}$ is influenced by the error assigned to the position of the images. In figure 5.2 we clearly show that this effect is very small even for a big variation of the image position errors. This plot illustrates the probability distribution for $R_{\rm cusp}$ (obtained using 20.000 realizations) when 4 substructures are added to the primary lens : the solid line is for an error on positions of $\epsilon_1 = 10^{-2}$ arcsec ($\approx 5\%$) the dashed one for $\epsilon_2 = 10^3$ arcsec (i.e. the code has complete freedom in moving the images). The two distributions of the $R_{\rm cusp}$ values are very similar, and this also confirms findings of other authors: the influence of substructures on the image positions is less strong than the one on fluxes (Kochanek 2006 [127]). We will adopt 10^{-2} arcsec for the error on positions for all our simulations.

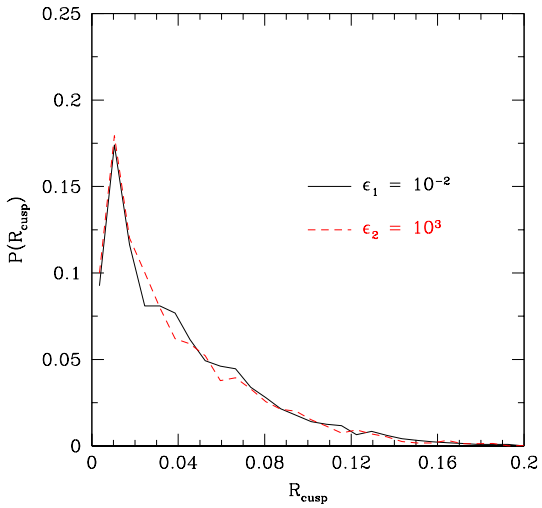

Figure 5.2. Probability distribution of $R_{\rm cusp}$ values for 2 substructures inside A_3 for different position errors.

A correct determination of the subhaloes properties (see section 5.3.2) is a key ingredient in computing the $R_{\rm cusp}$ value: figure 5.3 shows the influence of the number density and mass range of substructures on the $R_{\rm cusp}$ relation. Both changing the area in which subhaloes are distributed (keeping fixed their number: left panel) or their mass range (right panel) leads to complete different results.

As second step we have tested if the subhaloes that live outside the small area (A) surrounding the images can substantially modify the $R_{\rm cusp}$ relation. For this purpose we have defined three different areas for substructures for Config2: $A_3 = [-1.5 : 1.5] \times [1 : 2]$, $A_6 = [-1.5 : 1.5] \times [0 : 2]$ and $A_{12} = [-1.75 : 1.75] \times [-1.25 : 2.25]$. The last one ($A_{12}$) is big enough to cover all the image positions. Changing the size of the area and his position in respect to the center of the lens, the number of substructures changes according to eq: 5.3. The number of subhaloes inside the three areas is 4, 9 and 19 respectively. Figure 5.4 shows our results. The $R_{\rm cusp}$ probability distribution is weakly affected by the size of the area. This indicates that are the subhaloes close to the image positions the ones responsible for the $R_{\rm cusp}$ relation modification.

Figure 5.5 shows results for Config2 (figure 5.10) of the $R_{\rm cusp}$ probability distribution for 3 subhaloes with mass $5 \times 10^5 < m < 10^7 {\rm M}_\odot$ inside A_3 (solid line) and for 8 subhaloes with $10^7 < m < 10^9 {\rm M}_\odot$ inside an area of 57 arcsec^2 ($[-5 : 5] \times [0 : 6]$ with the exclusion of A_3). For this second population of substructures both the number density and the masses are over estimated by a large fraction. Nevertheless its effect on the cusp relation is very small and the $R_{\rm cusp}$ probability distribution is close to a delta function centered on the unperturbed value.

Modeling our subhaloes as NFW structures we have one more free parameter: the concentration. It is well know that the concentration correlates with the mass of the halo, even if a consistent scatter is present in this relation. Extrapolating results from Bullock et al 2000 [107], the mean concentration

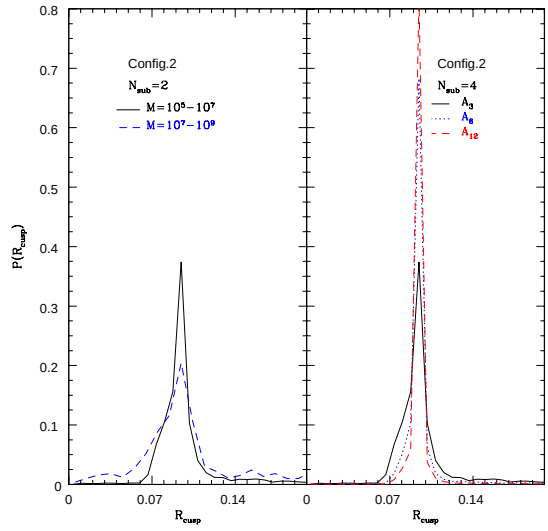

Figure 5.3. Probability distribution of $R_{\rm cusp}$ with 4 substructures: left panel influence of the substructure mass. Right panel effects of the projected number density.

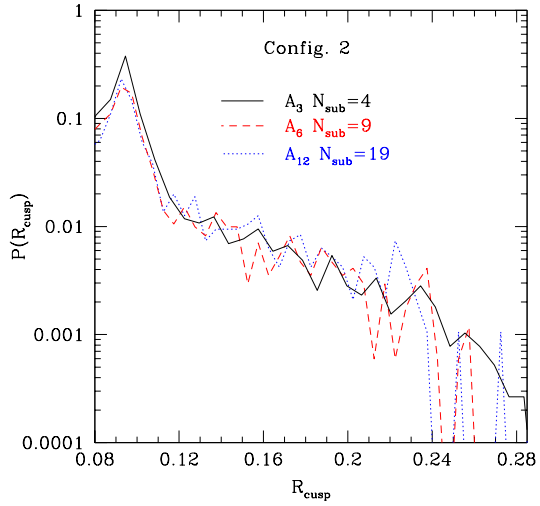

Figure 5.4. Probability distribution of $R_{\rm cusp}$ for substructures distributed on different areas.

in our mass range is around 33. In order to test the influence of the concentration of our subhaloes in modifying the $R_{\rm cusp}$ relation we repeated our analysis keeping fix mass and position of the subhaloes and varying their concentrations. Results are shown in figure 5.6. As expected denser haloes have a stronger impact on the $R_{\rm cusp}$ relation. We have also considered two other mass profiles for the subhaloes: SIS (singular isothermal sphere) and point like approximation. The first one, less favored by simulations, can be seen as an upper limit for the NFW profile, due to the fact that its inner slope for the density profile is proportional to r^{-2}. For this kind of subhalo model the $R_{\rm cusp}$ probability is just slightly above the ones for NFW haloes with c=35, so we do not expect a big change in our results using SIS instead of NFW subhaloes. On the other hand the point mass approximation leads to an underestimate of the effect of subhaloes on $R_{\rm cusp}$ since for a fixed mass a point-like object has a smaller Einstein radius than an NFW halo (Keeton 2003 [124]). In the following we have adopted a concentration parameter of 35 for our subhaloes in order to try to maximize their effect on the $R_{\rm cusp}$ relation.

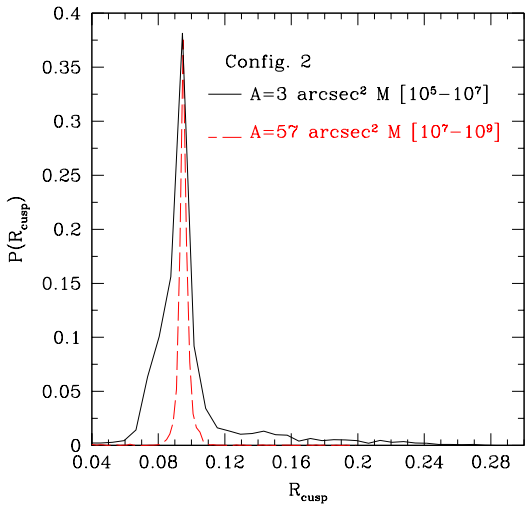

Figure 5.5. Effects on the $R_{\rm cusp}$ relation of substructures inside a small area (A_3) surrounding the images (solid line) and in a larger area $[-5:5]\times[0:6]$ (57 arcsec) outside A_3 (dashed line). In the first case the subs are in the mass range $[5\times10^5:10^7{\rm M}_\odot]$ in the second one $[10^7:10^9{\rm M}_\odot]$.

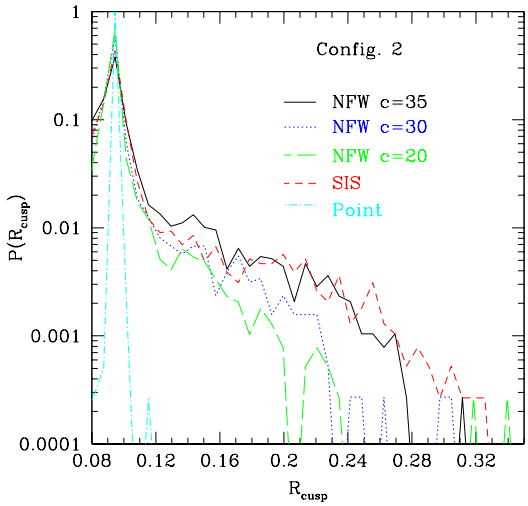

Figure 5.6. $R_{\rm cusp}$ distribution probability for different subhaloes mass profiles: NFW profile with different concentration values, SIS profile and point-like approximation.

5.4.2 Configuration 1

In the first configuration analyzed (Config1 hereafter) the source is close to the right cusp of the inner caustic curve (see fig 6.3) and the unperturbed $R_{\rm cusp}$ value is 0.01. The critical and caustic curves refer to the unperturbed case but they are not different from perturbed ones at the level of resolution.

For this configuration we have generated 20.000 different lensing systems that include substructures according to eq: 5.3. In figure 5.8 is shown the probability distribution for $R_{\rm cusp}$ for different numbers of substructures. The maximum of the probability is obtained for the unperturbed value (0.01) and the tail of the distribution extends to $R_{\rm cusp}=0.12$ but for a very low number of configu-

rations (less than 1.0%). Figure 5.9 shows in a logarithmic plot the tail of the distribution presented in figure 5.8: it is possible to note that an increase of the total number of substructures (from 4 to 6) does not substantially change the value of $R_{\rm cusp}$.

From figure 5.8 one see that in the 10% of the configurations the final value of $R_{\rm cusp}$ is even less than the unperturbed value and it is closer to the theoretical expectation of $R_{\rm cusp} = 0$ (see next section on the second configuration for more details).

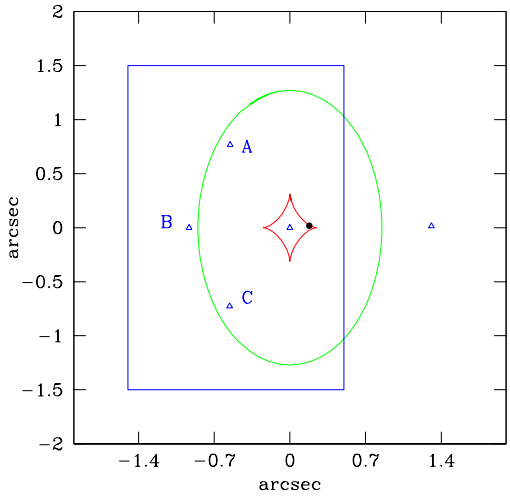

Figure 5.7. Unperturbed lens configuration: Config1 (R=0.01)

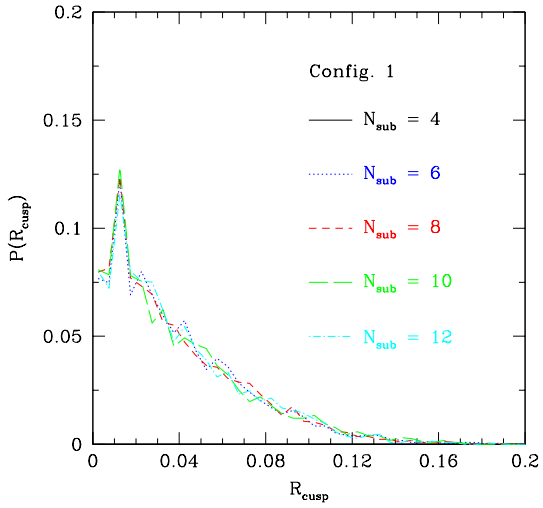

Figure 5.8. Probability distribution of R-variation for a different number of substructures inside A_6.

5.4.3 Configuration 2

In this configuration (Config2 hereafter) the source is close to the upper cusp of the inner caustic curve (see fig 5.10) with an unperturbed value of $R_{\rm cusp} = 0.09$.

Figure 5.11 shows the analogous of figure 5.8 for Config2 and figure 5.12 shows the tail of the distribution for large values of $R_{\rm cusp}$. Even in this case the maximum of the probability distribution

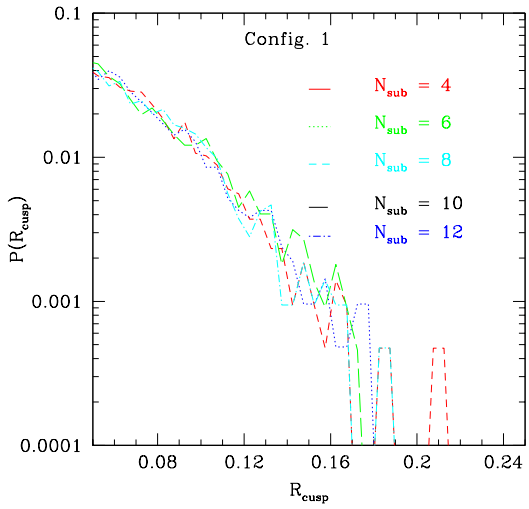

Figure 5.9. Same of figure 5.8 with logarithmic scale for the y axis.

is centered on the unperturbed value. Here the distribution of the values of $R_{\rm cusp}$ is more symmetric than for Config1 and it is more evident that the effect of substructures not only increase the value of the cusp ratio but can also reduce it.

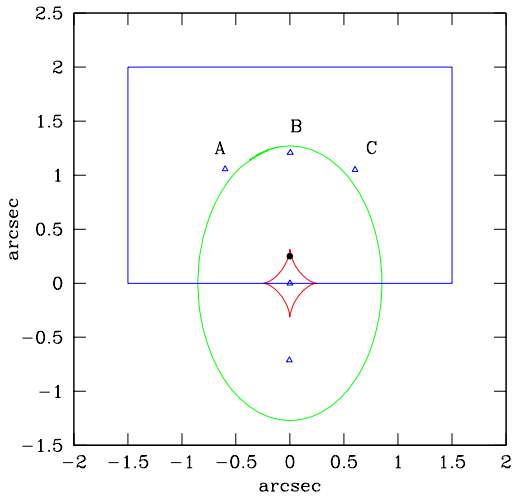

Figure 5.10. Second unperturbed lens configuration: Config2 (R=0.09)

To better illustrate this effect we have isolated one of the configurations in which we find a reduction of $R_{\rm cusp}$ (figure 5.13). When the distribution of subhaloes is non symmetric in respect to the triplets of images and one of the perturbers is close to one of the external images the latter image results to be more magnified than the others. In the unperturbed configuration $|\mu(B)| > \mu(A)+\mu(C)$ and this causes $R_{\rm cusp} \neq 0$. On the other hand if the perturbers increase $\mu(A)$ without changing considerably the magnification of the other images, this will enhance the sum $\mu(A)+\mu(C)$ pushing it closer to $\mu(B)$, giving a smaller $R_{\rm cusp}$ (0.07 in the case of figure 5.13).

Figure 5.14 shows the effects of extra haloes on the $R_{\rm cusp}$ value for Config2. For all the three extra-haloes mass ranges considered, the modifications in the cusp relation are very small and the value of $R_{\rm cusp}$ is not very sensitive to the total number of extra-haloes we generated (results for

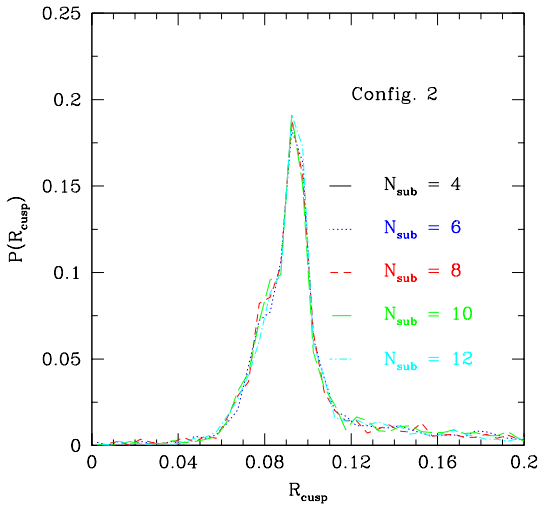

Figure 5.11. Probability distribution of R-variation for config 2, for a different number of substructures inside A_6.

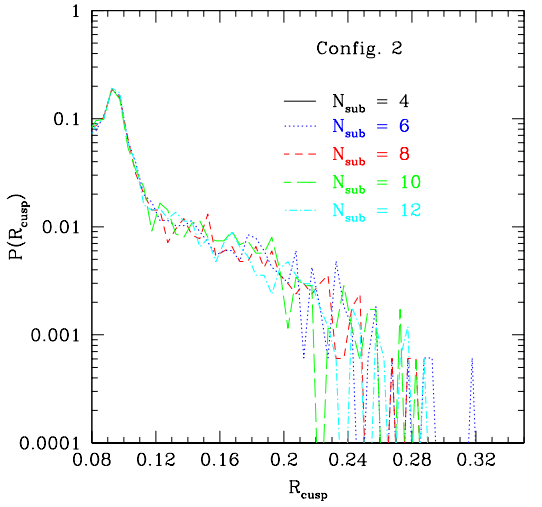

Figure 5.12. Same of figure 5.11 with logarithmic scale for the y axis.

different number of subhaloes are shown by different curves, which are almost overlapping in the various panels).

For this configuration we have performed one more test: we have modified by hand the fluxes of the three images in order to obtain an high value of $R_{\rm cusp}$ (> 0.37). Then we used the *gravlens* software to find positions and masses of two subhaloes (with masses $5\times10^5 < M < 5\times10^6 {\rm M}_\odot$) with the constrain of simultaneously reproducing positions and fluxes of our modified images. We have found two configurations for subhaloes that are shown in figure 5.15. In the first case (solid squares) the mass of the substructures is roughly the same ($\approx 2.0\times10^6$), they are close to the external images with a distance of 0.08 arcsec and the perturbed value of $R_{\rm cusp}$ is 0.387. In the second case (open circles) the mass of the subhalo close to the central image is $1.6 \times 10^5 {\rm M}_\odot$ with a distance of 0.06 arcsec, while $7.8\times10^5 {\rm M}_\odot$ is the mass of the second one that is far away from the central image, for a perturbed value of $R_{\rm cusp}$ equal to 0.372.

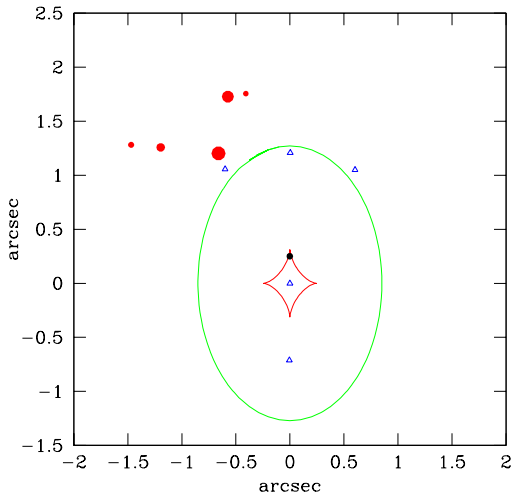

Figure 5.13. One perturbed configuration where $R_{\rm cusp}$ is less than the unperturbed value (0.091 *vs* 0.07). The solid circles show the position of the subhaloes, the point size is proportional to their mass.

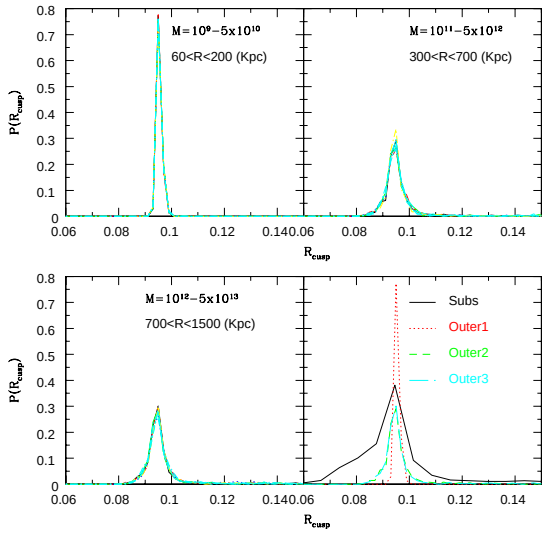

Figure 5.14. Probability distribution of R-variation considering Extra Haloes with different masses and distances from the primary lens (Config2). Bottom right panel: comparison between the effects of extra haloes and subhaloes.

The aim of this test is to show that there is nearly always the possibility to explain an anomalous flux ratio using subhaloes, but that their positions and masses must be tuned in a very precise way (i.e distances between images and subhaloes must be less than 0.08 arcsec). Most important, our Monte Carlo simulations show that the probability of obtaining such a fine tuning is very low. As a consequence we conclude that an explanation for the high number of observed anomalous flux ratios in lensed QSOs based on the presence of subhaloes in the mass range we have tested is very unlikely.

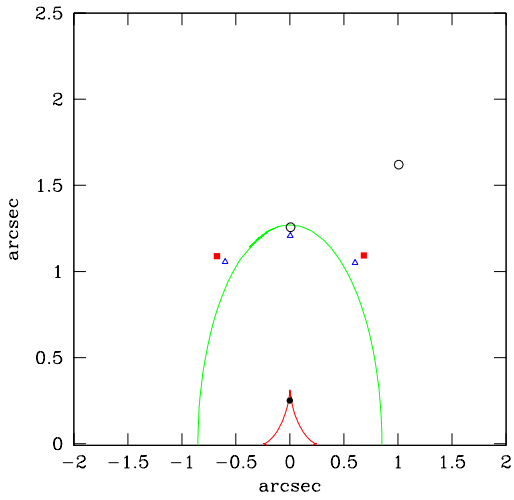

Figure 5.15. Two subhaloes configurations with high $R_{\rm cusp}$ value. The first one is indicated by solid squares and gives $R_{\rm cusp} = 0.387$. The second (one indicated by open circles) gives $R_{\rm cusp} = 0.274$. In both cases $M_{sub} \approx 10^6$.

5.4.4 Configuration 3

In the last cusp configuration analyzed (Config3) the R-cusp relation is not completely satisfied even in the unperturbed case ($R_{\rm cusp} = 0.243$, fig 5.16). Figure 5.17 shows the R-cusp probability distribution for Config2 and Config3 normalized to the unperturbed value. There are no appreciable differences between the two configurations. The probability distributions have almost the same width and the same maximum value (≈ 0.35) and both are centered on the respective unperturbed value. This means that the ability of substructures to modify the $R_{\rm cusp}$ relation is nearly independent on the original value of the cusp ratio.

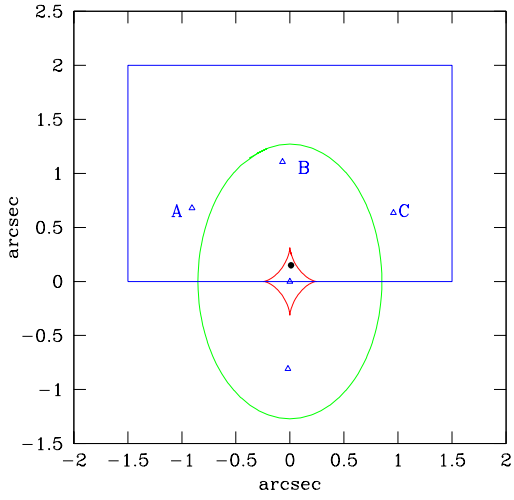

Figure 5.16. Third unperturbed lens configuration: Config3 (R=0.243)

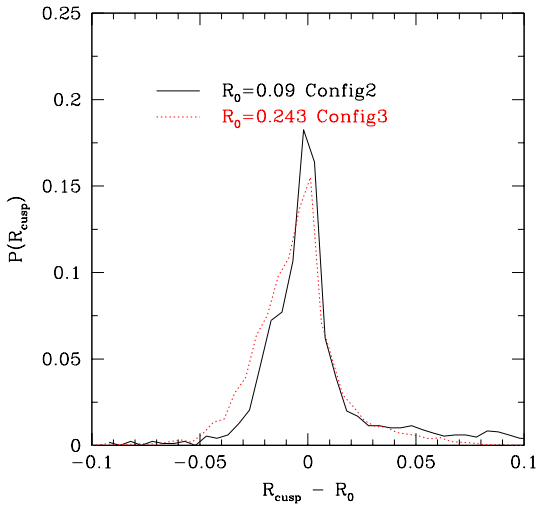

Figure 5.17. Probability distribution for 4 subhaloes within A_6 for Config2 and Config3

5.5 Fold Relation

For sake of completeness we have also considered a fold case similar to the configuration of the well known system PG1115 (Impey et al. 1998 [119]). In this case we define the fold relation as the ratio between the magnification of the closest pair on opposite sides of the critical curve (cfr fig 5.18):

$$R_{fold} = \frac{\mu(A_1)}{\mu(A_2)} = 1. \tag{5.4}$$

By applying our procedure to this test fold case we found that it is easier to modify the value of the unperturbed R_{fold} with respect to the one of $R_{\rm cusp}$, as clearly shown in fig 5.19. In our computational procedure the position of the source can be changed by the *gravlens* code, in order to minimize the χ^2 of the lens configuration. While this does not affect the $R_{\rm cusp}$ relation it can be important in the fold case: as pointed out by Keeton, Gaudi and Petters (2005) [125] the degree to which R_{fold} can differ from one for realistic smooth lenses depends, in addition to the angular structure of the lens potential, not only on the distance of the source from the caustic but also on its location along the caustic itself. So the the values we got for R_{fold} are due both to the effects of subhaloes and both to the shift along the caustics of the source.

Thus, it is not possible to conclude from $R_{\rm fold}$ alone whether observed flux ratios are anomalous or not.

5.6 Discussion

Quasars that are being gravitationally lensed into multiple images have recently been used to place limits on the surface density of cold dark matter subhaloes (Mao & Schneider 1998 [130], Metcalf & Madau 2001 [132], Chiba 2002 [109], Metcalf & Zhao 2002 [133], Dalal & Kochanek 2002 [114], Chen Kravtsov & Keeton 2003 [111], Bradac et al. 2004 [161], Mao et al. 2004 [157]). Small mass clumps that happen to lie near the images affect the observed magnification ratios. The question arises as to whether these observations are compatible with distortions expected to occur from dark matter substructures and satellite galaxies within the ΛCDM model. Recent results based on numerical N-body (Amara et al. 2006 [102], Rozo et al. 2006 [171]) and hydro simulations (Macciò et al. 2006 [128]) have shown that it is hard to reconcile the observed high number of cups relation violation with the total amount of substructures predicted by the ΛCDMmodel. These studies were limited

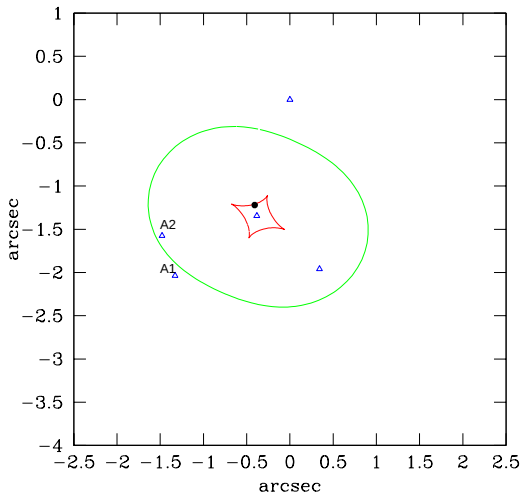

Figure 5.18. Unperturbed fold lens configuration (similar to PG1115, $R_{fold} = 0.92$)

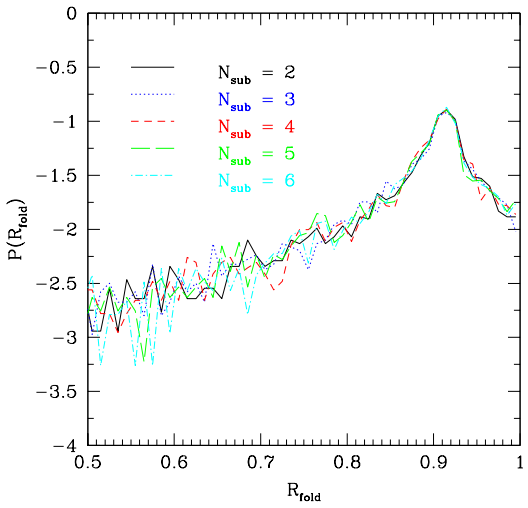

Figure 5.19. Probability distribution of R_{fold} for a different number of substructures within an area of 3 arcsec^2 ($5 \times 10^5 < M_{sub} < 10^7 \mathrm{M}_\odot$).

by the present achievable numerical resolution that permits to resolve DM haloes down to masses $\approx 10^7 \mathrm{M}_\odot$.

In this work we have quantified the effects of smaller mass clumps ($10^5 - 10^7 \mathrm{M}_\odot$) on the observed violation of the R cusp relation. We employed results from N-body simulations to estimate the expected number of subhaloes in this low mass range. Due to the small mass of the perturbers we have restricted our analysis only to those close (in 2D) to the images positions. For the mass range inspected in this work and for the typical distance between images (few arcsecs) this leads to a number of perturbers ≈ 6. All the subhaloes are modeled as NFW spheres and we have generated more than 10^5 different lensing configurations, varying masses, positions and number of subhaloes.

The main finding of our work is that on a statistical basis this class of perturbers is not able to modify consistently the unperturbed R-cusp relation. Values of R_{cusp} in the observed range (≈ 0.25) are obtained in only less than 1% of the analyzed systems. The ability of subhaloes in modifying

the unperturbed value of $R_{\rm cusp}$ is found to be independent from the value of $R_{\rm cusp}$ itself.

These results are not in contradiction with the ones in the literature (Keeton et al. 2003 [124], and more recently Miranda & Jetzer 2007 [172]and references therein). As shown in figure 5.15 it is possible to use subhaloes in the mass range $10^5 - 10^7 {\rm M}_\odot$ to obtain high values of $R_{\rm cusp}$ case by case, but a tight *fine tuning* between the location of the images and masses/positions of the perturbers is needed .

In addition, we have also considered the impact of massive haloes placed outside the primary lens (from groups of galaxies to a close cluster) by modeling them in the same way of the subhaloes. Our simulations show, as expected, that their contribution in modifying the R cusp relation is tiny and almost negligible with respect to the effect of subhaloes.

Results from this work together with results from numerical simulations seem to be in disagreement with the standard picture which explains the anomalous flux ratio by means of dark matter satellites. Interestingly, while on dwarf galaxy scale there is an excess of dark matter subhaloes with respect to visible satellites, we have shown that the predicted level of substructures on smaller scales is not sufficient to explain the observed level of violation in the cusp relation.

Possible solutions to this problem can reside in microlensing for some of the lensing systems observed in the optical band (Metcalf 2005 [135], Keeton et al 2005 [125]), or in the presence of haloes lying along the line of sight between the lens and the observer (Chen et al. 2003 [111], Metcalf 2005b [194], Miranda & Macció 2007 [173]), although total effect of this kind of perturbers is not yet clear.

Chapter 6

Constraining Warm Dark Matter using QSO gravitational lensing

6.1 Introduction

The Cold Dark Matter (CDM) model has been successful in explaining a large variety of observational results like the large scale structure of the universe or the fluctuations of the Cosmic Microwave Background (CMB, Spergel et al. 2003, 2006 [146], [147]). However, the CDM model faces some apparent problems on small scales: namely the overprediction of galactic satellites, the cuspy and high density of galactic cores and the large number of galaxies filling voids (Klypin et al. 1999 [126], Moore et al. 1999 [137], Bode, Ostriker & Turok 2001 [180], Avila-Reese et al. 2001 [177], Peebles 2001 [197]and references therein). These problems may well have complex astrophysical solutions. For instance feedback process such as heating and supernovae winds can inhibit the star formation in low-mass haloes (Bullock, Kravtsov & Weinberg 2000 [107]) alleviating the problem of the excess of galactic satellites.

Another natural cosmological solution to these problems is to replace cold dark matter with a warm species (ΛWDM, see Bode, Ostriker & Turok 2001 [180] and references therein). The warm component acts to reduce the small-scale power, resulting in fewer galactic subhaloes and lower halo central densities.

One of the most promising WDM candidate is a sterile (right-handed) neutrino with a mass in the keV range, such a particle may occur naturally within extensions to the standard model of particle physics (Dodelson & Widrow 1994 [181], Dolgov & Hansen 2002 [182], Asaka et al. 2005 [175], Viel et al. 2005 [212]). A sterile neutrino is non-thermal in the extensions of the minimal standard model with a life-time larger than the age of the universe.

A strong constrain on the mass of WDM candidates comes from Lyman-α forest observations (neutral hydrogen absorption in the spectra of distant quasars), since they are a powerful tool for constraining the matter power spectrum over a large range of redshifts down to small scales. Recent analysis of SDSS quasars spectra combined with CMB data and galaxy clustering have set a lower limit for the mass of the sterile neutrino around $m_\nu \approx 10 - 13$ keV (Seljak et al. 2006 [204], Viel et al. 2006 [213]). In this chapter we use a completely different approach to put independent constrains on m_ν using QSO gravitational lensing and the so-called anomalous flux ratio.

The standard lens models, although reproduce in general the relative positions of the images quite accurately, often have difficulties explaining the relative fluxes of multiply-imaged sources (Mao & Schneider 1998 [130], Metcalf & Madau 2001 [132], Dalal & Kochanek 2002 [114], Metcalf and Zhao 2002 [133]), giving rise to the so-called problem of anomalous flux ratio.

Several possible explanations have been considered in the literature, the most plausible being that the lensing potential of real galaxies are not fully described by the simple lens models used to

compute the lens characteristics. The most often invoked solution is to consider additional small-scale perturbation (i.e. dark matter haloes), which if located nearby the photons light path can modify the overall lens potential (e.g. Raychaudhury at al 2000 [198], Saha et al. 2007 [199]) and alter significantly the observed flux ratio between different images, in particular in the cusp or fold configuration (Metcalf & Madau 2001 [132], Chiba 2002 [109], Chen et al. 2003 [111], Metcalf 2005a,b [135], [194], Dobler & Keeton 2006 [116]). Those perturbers can be roughly divided in two categories: haloes that are inside the primary lens, usually referred as sub-haloes, and haloes that are along the line of sight, in between the source and the observer. This first category of haloes has been extensively studied in the past years both trough analytic calculation (Metcalf & Madau 2001 [132], Dalal & Kochanek 2002 [114], Metcalf and Zhao 2002 [133], Keeton 2003 [124]) and both using numerical simulations (Bradač et al. 2002 [106], Amara et al. 2006 [102], Macciò et al. 2006). The latter two studies have came to the conclusion that the impact on lensing of sub-haloes in the mass range $10^7 - 10^{10} M_{\odot} h^{-1}$ is very small. Even considering the impact of less massive subhaloes, usually not resolved in Nbody/hydro simulations, does not help in reproducing the observed number of anomalous flux ratio (Macciò & Miranda 2006 [129]).

The effect of the second category of haloes, the ones along the line of sight, is still somehow controversial (Chen et al. 2003 [111], Metcalf 2005a,b [135], [194]). In particular Metcalf (2005a,b) [135], [194] found that dark matter haloes with masses around $10^6 - 10^8 \mathrm{M}_{\odot}$ can produce anomalies in the flux ratios at a level similar to those that are observed. The presence of a WDM particle even with a mass around 10 keV will strongly reduce the number density of such small mass haloes giving a different signature on the images fluxes. As a consequence the observed anomalous flux ratio can be used to constrain the abundance of small haloes along the line of sight and therefore to put an independent constrain on the mass of the sterile neutrino as a possible WDM candidate.

In this chapter we analyze in detail the effect of the subhaloes along the line of sight on an unperturbed cusp configuration in a ΛCDM model and in ΛWDM models with different values for m_ν. We found that WDM models with $m_\nu < 10$ keV fail in reproducing the observed anomalies in the flux ratio of lensed QSO. Our results provide a new and independent constrain on the mass of sterile neutrino, and they are in good agreement with previous constrains coming from Lyman-α forest and CMB analysis.

The format of the chapter is as follows: in section 6.2 we compute the expected halo abundance in different models; in section 6.3 we review briefly the lensing formalism we adopt. Section 6.4 is devoted to the description of our lensing simulations. In section 6.5 we present the numerical results, matching them with observations. We conclude with a short summary and discussion of our results in section 6.6.

6.2 Intergalactic haloes mass function

The main goal of this work is to study the effect of dark matter haloes along the line of sight on fluxes of QSO multiple images. In order to achieve it we first computed the number density of those haloes in the light cone between the source plane and the observer.

For this purpose we used the Sheth and Tormen mass function (ST: Sheth & Tormen 2002 [202]), taking into account its evolution with redshift. We adopted a WMAP1-like cosmology (Spergel et al 2003 [146]) with the following values for dark energy and dark matter density, normalization and slope of the matter power spectrum: $\Omega_\Lambda = 0.74$, $\Omega_m = 0.26$, $\sigma_8 = 0.9$ and $n = 1$.

The transfer function for the CDM model has been generated using the public code CMBFAST (Seljak & Zaldarriaga 1996 [203]). For computing the transfer function for WDM models we used the fitting formula suggested by Bode, Turok and Ostriker (2001) [180]:

$$T^2(k) = \frac{P^{WDM}}{P^{CDM}} = [1 + (\alpha k)^{2\nu}]^{-10/\nu} \tag{6.1}$$

where α, the scale of the break, is a function of the WDM parameters, while the index ν is fixed. Viel et al (2005 [212], see also Hansen et al 2002 [183]), using a Boltzmann code simulation, found that $\nu = 1.12$ is the best fit for $k < 5\ h\ \mathrm{Mpc}^{-1}$, and they obtained the following expression for α:

$$\alpha = 0.049 \cdot \left(\frac{m_x}{1keV}\right)^{-1.11} \cdot \left(\frac{\Omega_\nu}{0.25}\right)^{0.11} \cdot \left(\frac{h}{0.7}\right)^{1.22} h^{-1}\{Mpc. \tag{6.2}$$

This expression applies only to the case of thermal relics. In order to apply it to a sterile neutrino we take advantage of the one-to-one correspondence between the masses of thermal WDM particles (m_x) and sterile neutrinos (m_ν) for which the effect on the matter distribution and thus the transfer function for both models are identical (Colombi *et al* 1996). We used the $m_x - m_\nu$ relation given by Viel *et al* (2005), that reads:

$$m_{\nu,\mathrm{sterile}} = 4.43 \left(\frac{m_{x,\mathrm{thermal}}}{1\,\mathrm{keV}}\right)^{4/3} \left(\frac{0.25}{\Omega_\nu}\right)^{1/3} \left(\frac{0.7}{h}\right)^{2/3} \mathrm{keV}. \tag{6.3}$$

We used the expression given in eq:6.2for the damping of the power-spectrum for simplicity and generality. More accurate expressions for the damping for concrete models of sterile neutrinos exist (Abazajian 2006 [174], Asaka et al. 2007 [176]) and show that the damping depend on the detailed physics of the early universe in a rather non-trivial way. Naturally the results of this chapter can be repeated using other expressions for the damping.

The main effect of WDM is to dampen the power spectrum of fluctuation on small scales, reducing the number of haloes at low masses (Bode, Turok & Ostriker 2001 [180], Barkana et al. 2001 [178], Padoroiu et al. 2007 in prep.). Figure 6.1 shows the ration between halo number density in WDM and CDM models as a function of the WDM mass m_ν.

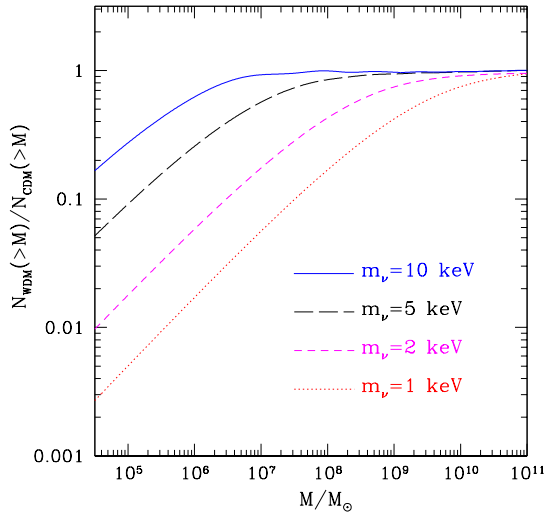

Figure 6.1. Effects of WDM particles on the dark matter halo mass function at redshift zero.

Typically lensed QSO are located at a redshift around 3. This implies that we need to take into account also the redshift evolution of the mass function in different models. Figure 6.2 shows the number of haloes more massive than $10^6 M_\odot h^{-1}$ (upper solid curve) and $10^7 M_\odot h^{-1}$ (lower solid curve) per Mpc cube at different redshifts. It is interesting to note that on such a small mass scales the halo number density tends to increase moving towards high redshift. We found that the evolution of the mass function,both in CDM and WDM models, can be well represented by the following fitting formula:

$$\log N(>M, z) = 0.11 + N_0 \cdot z^{0.7} \tag{6.4}$$

where N_0 is the logarithm of the halo number density at redshift zero ($N_0 = \log N(> M, z = 0)$). The use of this fitting formula has the advantage to speed up the calculation of the number of haloes in each lensing plane (see section 6.4).

To conclude this section we want to emphasize that our particular choice of cosmological parameters does not influence the results we will present in the next section. For instance on the mass scales we are interested in ($M < 10^{10} M_\odot h^{-1}$) changing σ_8 from 0.9 to 0.7 will increase the number of haloes only by a few percent.

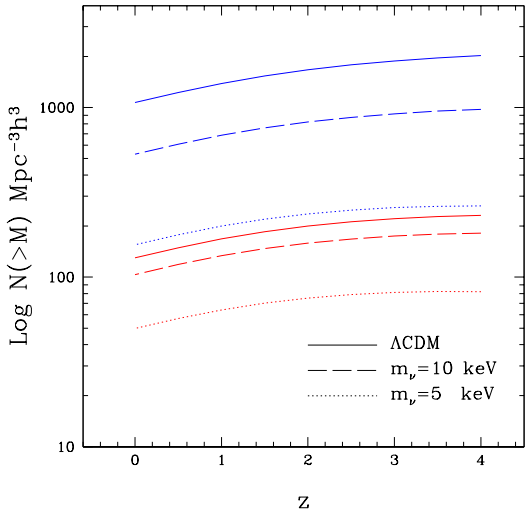

Figure 6.2. Evolution with redshift of the number of haloes above a fix mass threshold in different models. The upper most solid (blue) line is for $M > 10^6 M_\odot h^{-1}$ in the ΛCDM model; the dashed and the dotted lines are for the same mass threshold but for a WDM mass of $m_\nu = 10, 5$keV respectively. The second set of (red) lines refers to a mass threshold of $M > 10^7 M_\odot h^{-1}$.

6.3 Lensing Formalism

We briefly recall the general expressions for gravitational lensing and refer, e.g., to the book by Schneider et al. (1992) [145]for more details. The lens equation is defined as:

$$\vec{\beta} = \vec{\theta} - \vec{\alpha}(\vec{\theta}) \ , \tag{6.5}$$

where $\vec{\beta}(\vec{\theta})$ is the source position and $\vec{\theta}$ the image position. $\vec{\alpha}(\vec{\theta})$ is the deflection angle, which depends on $\kappa(\vec{\theta})$ the dimensionless surface mass density (or convergence) in units of the critical surface mass density $\Sigma_{\rm crit}$, defined as:

$$\Sigma_{\rm crit} = \frac{c^2}{4\pi G} \frac{D_S}{D_L D_{LS}}, \tag{6.6}$$

where D_S, D_L, D_{LS} are the angular diameter distances between observer and source, observer and lens, source and lens, respectively.

6.3.1 The cusp relation

There are basically three configurations of four-image systems: fold, cusp, and cross (Schneider & Weiss 1992 [200]). In this chapter we will mainly concentrate on the *cusp* configuration, that

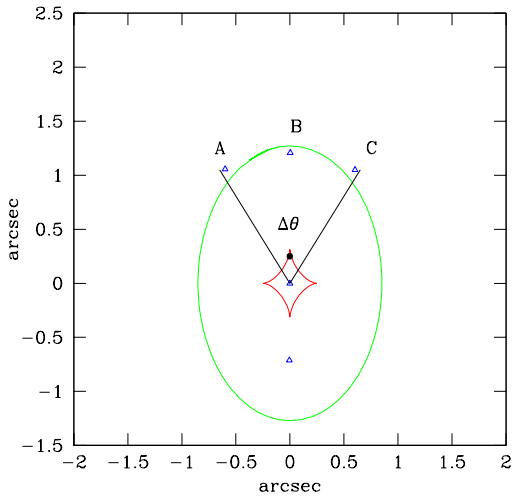

Figure 6.3. Unperturbed cusp configuration: $R_{cusp} = 0.09$. The source and image positions are marked by a solid circle and open triangles respectively. The opening angle is also shown.

corresponds to a source located close to the cusp of the inner caustic curve (see figure 6.3). The behavior of gravitational lens mapping near a cusp was first studied by Blandford & Narayan (1986) [179], Schneider & Weiss (1992) [200], Zakharov (1995) [214], who investigated the magnification properties of the cusp images and concluded that the sum of the signed magnification factors of the three merging images approaches zero as the source moves towards the cusp. In other words:

$$R_{cusp} = \frac{\mu_A + \mu_B + \mu_C}{|\mu_A| + |\mu_B| + |\mu_C|} \rightarrow 0, \quad for \quad \mu_{tot} \rightarrow \infty \tag{6.7}$$

where μ_{tot} is the unsigned sum of magnifications of all four images, and A,B & C are the triplet of images forming the smallest opening angle (see figure 6.3). By opening angle, we mean the angle measured from the galaxy center and being spanned by two images of equal parity. The third image lies inside such an angle. This relation is an asymptotic relation and holds when the source approaches the cusp from inside the inner caustic " astroid". This can be shown by expanding the lensing map to third order in the angular separation from a cusp (Schneider & Weiss 1992 [200]). Small scale structure on scales smaller than the image separation will cause R_{cusp} to differ from zero fairly independently of the form of the rest of the lens. Indeed, a perturbers is more likely to reduce the absolute magnification for negative magnification images (Metcalf & Madau 2001 [132], Schechter & Wambsganss 2002 [200], Keeton et al. 2003 [124]) and to increase it for positive parity images.

6.3.2 The unperturbed lens

We used the GRAVLENS code (Keeton 2001 [122])[1] to create a lens configuration for which the cusp relation is roughly satisfied (see figure 6.3). The main, smooth, lens has been modeled as singular isothermal ellipsoid (SIE) (Kormann, Schneider, & Bartelmann 1994 [192]) to take advantage of its simplicity. This model has been widely used in lens modeling and successfully reproduces many lens systems (e.g. Keeton et al. 1998 [189], Chiba 2002 [109], Treu & Koopmans 2002 [211]). The ellipsoidal primary lens has a mass equal to $5 \times 10^{11} M_{\odot}$, it is oriented with the major axis along the y axis in the lens plane and has an ellipticity of 0.33. The redshifts of the lens and has been fixed to $z_l = 0.3$ in agreement with the typical observed ones (i.e. Tonry 1998 [206]). The cusp relation, defined according equation 6.7, for this smooth lens reads $R_{cusp} = 0.09$, and this is one of the configurations previously studied in Macciò and Miranda (2006 [129], namely Config2).

[1] The software is available via the web site:http://cfa-www.harvard.edu/castles

6.4 Subhaloes along the line of sight: Idea and Procedure

The purpose of this work is to compute the effects of intergalactic haloes, along the line of sight, on an unperturbed cusp lensing configuration to extract information on the matter power spectrum on small scales. In this approach, we model our haloes as singular isothermal spheres (SIS). A SIS, with density profile $\rho \propto r^{-2}$, is a simple model that is often used in lensing because its simplicity permits detailed analytic treatment (e.g., Finch et al. 2002). The model has been used to represent mass clumps for studies of substructure lensing, after taking into account tidal stripping by the parent halo (Metcalf & Madau 2001 [132]; Dalal & Kochanek 2002 [114]). Again, the simplicity of the SIS makes it attractive for theoretical studies: a tool that not only reveals, but also elucidates, some interesting general principles. For the $10^6 M_\odot$ haloes relevant for this work, the SIS profile does not differ dramatically from the NFW (Navarro, Frenk, & White 1996 [195]) profile inferred from cosmological N-body simulations (Keeton 2003 [124]). Besides, the SIS model yields *conservative* results. Since an NFW halo is centrally less centrally concentrated than a SIS halo, it is less efficient as a lens and therefore would have to be more massive in order to produce a given magnification perturbation. Macciò & Miranda (2006) [129]have shown that a SIS model will induces lensing effects slightly stronger then those caused by an NFW profile with concentration parameter $c \sim 55$, corresponding to a mass around $10^6 \mathrm{M}_\odot$.

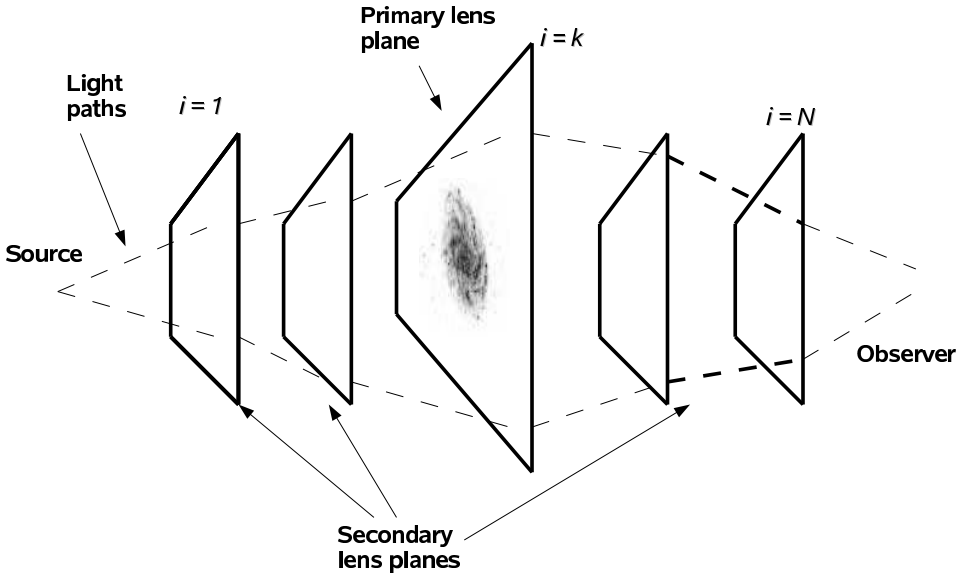

Figure 6.4. A schematic diagram of the type of lensing system being considered. There is one primary lens that is responsible for the multiple images of the source. In addition, there are many secondary lenses (most not shown). The unperturbed light paths are deflected only by the primary lens and with an appropriate model for the primary lens will meet on the source plane. If the deflections from secondary lens planes are taken into count without changing the primary lens model the light will follow the perturbed light paths (dashed curves). This diagram is not to scale in any respect.

A SIS halo model is completely characterized by its Einstein radius:

$$\theta_E = \frac{4\pi\sigma^2}{c^2}\frac{D_{LS}}{D_S}, \tag{6.8}$$

where σ is the halo velocity dispersion, and D_S, D_{LS} are the angular diameter distances introduced in sec. 6.3. We adopt a source redshift $z_s = 2$ and a main typical lens redshift $z_l = 0.3$.

We filled the portion of Universe along the line of sight with cubes, then the subhaloes inside each cube are projected onto the middle plane (see figure 6.4). We used a total of 100 different lens planes roughly equally distribute in space between the source and the observer. This results in $N_1 = 85$ planes behind the main lens and $N_2 = 15$ planes in front of it.

Two close planes are separated by $\Delta z_1 = (z_{max} - z_l)/N_1$, if situated behind the main lensing galaxy and by $\Delta z_2 = (z_l - z_{min})/N_2$, for planes in front if it, where $z_{min} = 0.01$ and $z_{max} = z_s - 0.1$,

The size of a comoving volume inside a solid angle $d\Omega$ and a redshift interval dz is given by (Hogg 1999 [187]):

$$dV_{\rm C} = D_{\rm H} \frac{(1+z)^2 D_{\rm A}^2}{E(z)} d\Omega\, dz \tag{6.9}$$

where $D_{\rm A}$ is the angular diameter distance at redshift z and $E(z)$ is defined as:

$$E(z) \equiv \sqrt{\Omega_{\rm M}(1+z)^3 + \Omega_k (1+z)^2 + \Omega_\Lambda} \tag{6.10}$$

with $\Omega_{\rm M}$, Ω_k and Ω_Λ the density parameters of matter (cold and warm), curvature and cosmological constant, respectively. Then we populated each cube with dark matter haloes, their total number and their mass distribution has been chosen accordingly to the ST mass function at the appropriate redshift (see section 6.2). Haloes positions and redshifts (within $\Delta z_{1,2}$) have been randomly assigned. Within a solid angle $d\Omega$ of 3"×3" squared arcsec, the total number of haloes with mass larger than $10^6 {\rm M}_\odot$ results to be 512 for the ΛCDM model adopted in this chapter. This number drops in a consistent way in a warm dark matter scenario, depending on m_ν. For a WDM particles mass of 10 keV we obtain 238 haloes along the line of sight within the same $d\Omega$, and even less (156, 135 for a less massive choice for m_ν (7.5, 5 keV, see fig 6.1).

Since we are interested in the flux anomalies, we consider only cases in which we do not have image splitting due to the extra haloes along the line of sight. So we do not allow any of those haloes to be closer than twice its Einstein radius (θ_E) from any images, in order to prevent image splitting (see Schneider, Ehlers & Falco 1992 [145]and references therein). On average only few haloes (3, for LCDM) fail in satisfying this criterium and we tested their removal/inclusion do not affect the final R distribution in any way.

Let η denote the two-dimensional position of the unperturbed image with respect to the perturber on the I plane , measured with respect to the intersection point of the optical axis with the I plane and ξ the light ray impact parameter on the I' plane. In the absence of image splitting a SIS perturber will affect the position of each image according the following:

$$\eta = \xi \frac{D_I}{D'_I} - \alpha(\xi) D_{I'I}. \tag{6.11}$$

Introducing the angular coordinates $\eta = D_I \theta_I$ and $\xi = D'_I \theta'_I$, and given that $\alpha(\xi) = \theta_E$ for a SIS, the equation for the flux becomes

$$\mu = \frac{\theta'_I}{\theta'_I - \theta_E}, \tag{6.12}$$

where the quantities with subindex I refer to the (unperturbed) image position with respect to the perturber and so $D_I, D_{I'}, D_{I'I}$ are the distances between observer and the I plane, observer and I' plane, I plane and I' plane, respectively. On each single lens plane the total effect on the image magnification factor μ is obtained by summing up contributions by each perturber. In principle one should sum the magnification tensors first and then take the determinant. The two methods (scalar or matrix sum) do not lead to the same result because $\det({\rm A}+{\rm B}) \neq \det({\rm A}) + \det({\rm B})$. In the case of scalar sum and two SIS perturbers with Einstein radii $\theta_{E,1}$ and $\theta_{E,2}$, the total magnification depends on the order in which the two lenses act on the source: $\mu_{1,2}$ is different from $\mu_{2,1}$. The error introduced by a direct sum is of the order of the ratio between the $\mu_{1,2}$ and $\mu_{2,1}$. This quantity can be directly computed from eqs: 6.11 and 6.12 and it is always $< \max(\theta_{{\rm E},1}, \theta_{{\rm E},2})/\beta$. In our case, due to the low mass of our perturbers, the ratio $\theta_I/\theta_{E,i}$ is of the order of 200-800, which gives an error less than 1% for the total μ.

Generally a matter clump will change the positions of the images slightly so if a lens model is chosen to fit the observed image positions perfectly it will not do it anymore after the perturber is added. To produce a perfectly consistent lens model one would have to adjust the main lens model for each realization of the intergalactic haloes. This is very computationally expensive and not necessary in practice. The shifts in positions are generally small when the masses of the secondary

lenses are small (≈ 0.1" for M $\approx 10^8 M_\odot$ Metcalf 2005a [135]) and, in addition, since the host lens model is degenerate it is ambiguous how it should be adjusted to correct for the shift. The goal here is to reproduce all the significant characteristics of the effects induced by the observed lens (image configuration, fluxes) so that one can determine whether lenses, that look like the observed ones and have the observed ratio anomalies, are common in CDM/WDM models. For the source, we adopt the point-like approximation. The importance of considering the source size resides mainly in the capability to disentangle different subhaloes mass limits (Chiba et al. 2005 [110], Dobler & Keeton 2006 [116]). As remarked by Chang & Refsdal (1979) [108] and many authors afterwards (see Metcalf 2005a [135]and references therein) the projected (on the lens plane) size of the emitting regions of QSOs are expected to be different and this can be used to remove, eventually, lens model degeneracy and improve the sensitivity to substructure properties. In our cases, the size of radio emitting region, when projected on the lens plane, are expected to be affected by structures with mass larger then $10^5 M_\odot$ (Metcalf 2005a,b [135], [194]).

In a single realization of our perturbed lens configuration the light coming from the source is deflected by ≈ 500 haloes (plus the main lens) before reaching the observer. Each one of the three images forming the cusp configuration is shifted and amplified, giving as a result a modified R_{cusp}value, different from the original (unperturbed) one of $R_{cusp} = 0.09$. Sometimes, when a massive halo ($M > 10^8 M_\odot$) happens to be close to one of the images, this image can be strongly deflected, having as a result a breaking of the cusp configuration. In the statistical studies presented here these cases are simply excluded from the final sample. In total we performed 2,000 realizations (with different random seeds for generating masses and positions of perturbers) of each model (CDM/WDM), obtaining 2,000 final different lensing configurations. For some of such final configurations (with high R_{cusp}values), we try to fit images positions and magnification factors with the Gravlens code, using a smooth lens model. While is relatively simple to reproduce the image geometrical properties, it is always not possible to get the right flux ratios, with such a simple model.

6.5 Results

The first part of this section is devoted to present the effects of haloes along the line of sight, on the cusp relation, in a standard (Λ)CDM scenario. The plots show the probability distribution for the cusp relation value, considering 2,000 different realizations of same model. Those realizations share the same total number of perturbers, but differ for their masses (randomly drawn from a PS distribution), positions (randomly assigned within the lens plane) and redshift (randomly chosen within $\Delta z_{1,2}$).

The cusp relation defined by equation 6.7 holds when the source is close to the cusp. As soon as the source moves away from the cusp, deviations from $R_{cusp} = 0$ are observed, even for the smooth lens model. On the other hand the closer the source is to the cusp, the smaller is the angle spanned from the three images. Therefore in order to take into account the position of the source in evaluating the cusp relation it is better to define the anomalous flux ratio as:

$$R = \frac{2\pi}{\Delta\theta} R_{cusp}. \tag{6.13}$$

where $\Delta\theta$ is the opening angle spanned by the two images with positive parity defined from the center of the galaxy. With this new definition of the cusp relation a set of three images is said to violate the cusp relation if $R > 1$. This makes the comparison between simulations and observations much more straightforward. For this comparison we used the same data presented in Macciò et al (2006) [128]. There are 5 observed cusp caustic lenses systems: B0712+472 (Jackson et al 1998 [188]), B2045+265 (Koopmans et al 2003 [191]), B1422+231 (Patnaik & Narasimha 2001 [196]), RXJ1131-1231 (Sluse et al. 2003 [205]) and RXJ0911+0551 (Keeton et al 2003 [190]); the first three are observed in the radio band, the last two in optical and IR. Three of them violate the reduced cusp relation (i.e. $R > 2\pi/\Delta\theta$). Properties of the observed cusp caustic lenses are summarized in table 6.1.

Figure 6.5 shows the R probability distribution for the three possible categories of perturbers.

lens	$\Delta\theta$	$R_{\rm cusp}$	observed band
B0712+472	79.8°	0.26 ± 0.02	radio
B2045+265	35.3°	0.501 ± 0.035	radio
B1422+231	74.9°	0.187 ± 0.006	radio
RXJ1131-1231	69.0°	0.355 ± 0.015	optical/IR
RXJ0911+0551	69.6°	0.192 ± 0.011	optical/IR

Table 6.1. The image opening angles and cusp caustic parameters for the observed cusp caustic lenses.

The dotted (red) line shows the effect of subhaloes inside the primary lens that can be directly tested by current numerical simulations (i.e with masses $> 10^7 M_\odot$, Macciò et al 2006 [128]). The short-dashed (cyan) line shows the effect of lower mass subclumps (still inside the primary lens) as measured by Macciò and Miranda (2006). The solid (blue) line shows the effect of the haloes along the line of sight considered in this work, here we considered only haloes with $M > 5 \times 10^6 M_\odot$. As already noticed the first two categories of perturbers fail in reproducing the high value tail that arises in the observational data around $R = 2$. On the contrary, the signal coming from haloes along the l.o.s. has a probability distribution which remains almost flat in R range 1-2, where 2 (over 5) of the observed systems lay.

Thanks to this pronounced tail at high R value, haloes filling the light cone between the source and the observer can easily account for all the observed cusp systems, providing a solution to the anomalous flux ration issue. Our results are in fairly agreement with those previously obtained by Metcalf (2005b) [194]. In above mentioned work the author used an approach similar to ours making a direct lensing simulation in order to compute the effects of haloes along the l.o.s., modeling them using an NFW density profile. Although in those works the author analyzed each observed configuration separately, finding slightly different individual R probabilities for different systems, the similarity of the results is a good proof *a posteriori* that our assumptions of SIS parameterization for perturbers and point-source approximation did not introduce a strong bias in the results.

In the previous analysis we restricted the mass range to haloes more massive than $M = 5 \times 10^6 M_\odot$. In figure 6.6 the probability distribution for R is shown for two different choice of the minimum halo mass: $M > 5 \times 10^6 M_\odot$ (solid, blue line) and $M > 10^5 M_\odot$. In the latter case the total number of structures is around 5,500 and the lensing simulation code slows down considerably. A close comparison of the two histograms clearly shows that considering less massive haloes does not not improve the results substantially; so in the following we will only consider haloes with $M > 5 \times 10^6 M_\odot$.

In some cases, when the averaging process is restricted to a lower number of realizations (~ 200) we found that the observational data are reproduced with a high confidence level as shown in figure 6.7. These results are probably due to effects induced by single massive perturbers close to a particular image: in this case or a positive image is highly magnified or a negative one is demagnified (note that in equation 6.7 we consider the absolute values for μ_i), providing an anomalous R. While with a low number of realizations (~ 200) these single events contribute significantly to the global R, an higher number of realizations ($> 10,000$) permits all the images to be affected by massive clumps, smoothing the final probability distribution.

The introduction of a WDM particle dumps the matter power spectrum on small scales, reducing the number of haloes along the l.o.s. In figure 6.8 we show the probability distribution of R as a function of the mass of the WDM candidate. Changing the WDM particle mass from $m_\nu = 12.5$ to $m_\nu = 7.5$ keV, the tail at $R = 2$ drops from a 10% probability to a 1.5% one. For $m_\nu = 5$ keV we have a $P(R)$ higher than 5% only for $R < 1.3$. In the latter case only 20 haloes are inside the volume sampled by the three images. and this model tends to leave the value of R close to the unperturbed one. A model with a 10 keV sterile neutrino, if compared to a model with $m_\nu = 12.5$ keV, gives a slightly lower probability (8% *vs* 10%) to have a configuration with $R = 2$. Due to limited amount of observed cusp systems it is hard to disentangle between those two models, and we think that it is fair to say that $m_\nu = 10$ keV is still in agreement with the data.

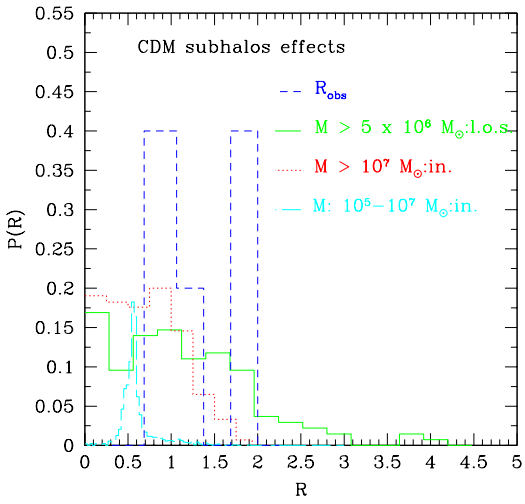

Figure 6.5. R probability distribution for different categories of (sub)haloes within the CDM scenario. The dotted line shows the effect of substructures (with $M > 10^7 \mathrm{M}_\odot$) inside the lens galaxy (Macciò et al. 2006); the long-dashed line is for less massive subhaloes ($M = 10^5 - 10^7 \mathrm{M}_\odot$) still inside the primary lens (Macciò & Miranda 2006). The solid line is for the haloes along the line of sight with mass $> 5 \times 10^6 \mathrm{M}_\odot$ studied in this work. Observational results are also shown (long dash histogram).

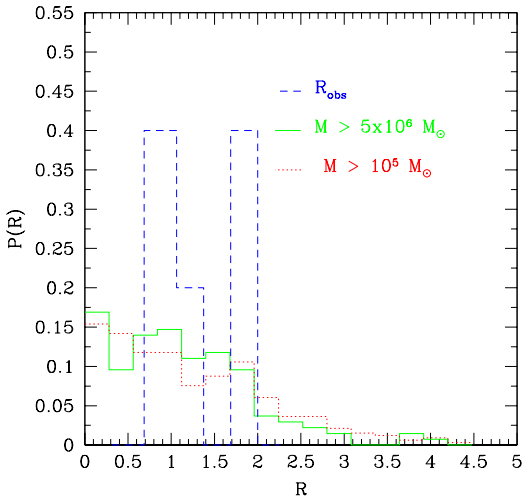

Figure 6.6. R distribution for haloes along the line of sight for two choice of their minimum mass: $M > 10^5$ (dot line) and $M > 5 \times 10^6 M_\odot$ (solid line). The dashed histogram shows the observational data.

Figure 6.9 shows the comparison between the observational data, the standard (Λ)CDM model and a WDM model with a sterile neutrino mass of 12.5 keV, which is close to the current limit provided by Lyman-α + CMB analysis (Seljak et al 2006 [204]). In this case in both the warm and cold dark matter scenario, haloes along the line of sight can easily account for the two observed cusp systems with $R \approx 2$, offering a viable solution to the anomalous flux ration issue. On the contrary a warm dark matter model with less massive particle (i.e. with a higher free streaming scale length) fails in reproducing the observational data due to the reduce number density of haloes along the line of sight.

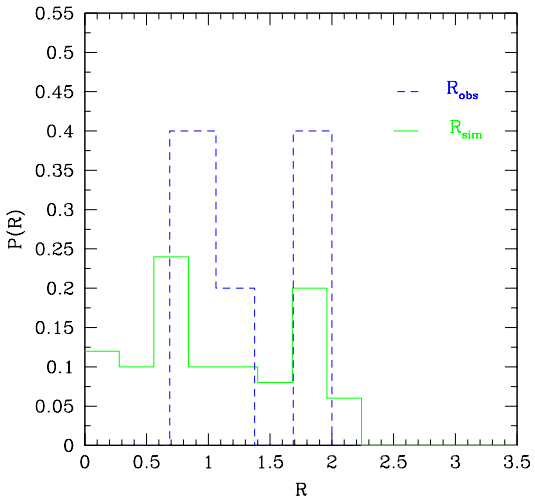

Figure 6.7. R probability distribution for CDM considering a lower number of realization (≈ 200) in the averaging process (see text). The dashed histogram shows the observational data.

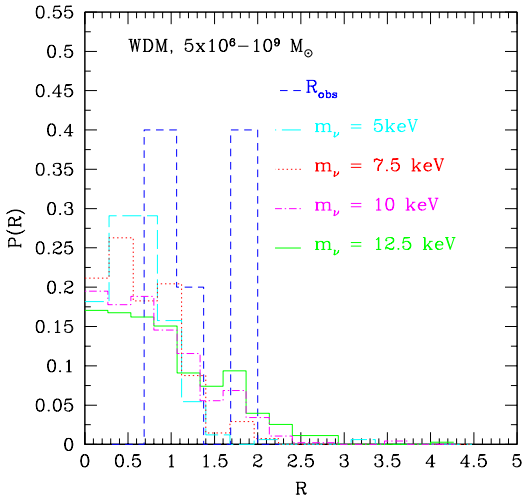

Figure 6.8. Probability distributions for different warm particle masses: $m_\nu = 5keV$ (long-dashed line), $m_\nu = 7.5$ keV (dot line), $m_\nu = 10$ keV (dashed-dot line), $m_\nu = 12.5$ keV (solid line). Dashed line shows the probability distribution of observational data.

6.6 Discussion

Interest in warm dark matter models has been sporadic over the years, however this class of models could help alleviate several problems on small scales that occur with cold dark matter. In order to constrain the WDM scenario precise measurements of the matter power spectrum on small scales are needed; for this purpose Lyman-α forest and CMB data have been extensively used (Seljak et al. 2006 [204], Viel et al. 2006 [213]).

In this chapter we show that images flux ratios in multiple gravitational lensed QSO can be modified by haloes along the line of sight in the mass range $10^6 - 10^7 M_\odot$; this effect opens a new window to study the matter power spectrum on small scales and provides a new and independent

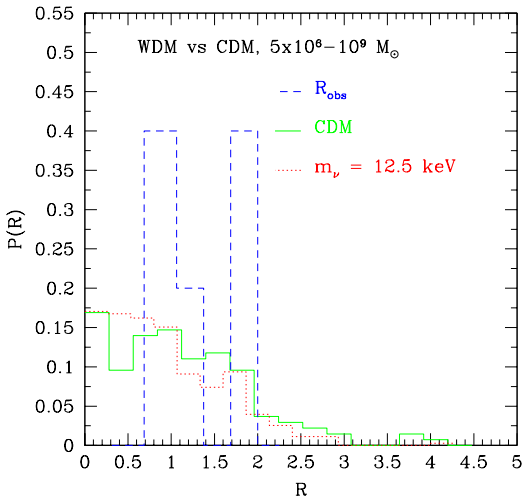

Figure 6.9. R distribution probability for: observed values (dashed line), CDM haloes more massive than $5 \times 10^6 M_\odot$ (solid line) and WDM subhaloes with m_ν =10keV (dotted line).

method to constrain the mass of WDM candidates m_ν.

The observed anomalous flux ratio in lensed QSO can be explained by adding small perturbations to the smooth model use to parameterize the main lens. Those perturbers can be identified with dark matter haloes that happen to be close to the images light path. Recent results based on numerical N-Body (Amara et al. 2006 [102], Rozo et al. 2006 [171]) and hydrodynamical simulations (Macciò et al. 2006 [128]) have shown that it is hard to reconcile the observed high number of cusps relation violations with the total amount of substructures inside the primary lens predicted by the ΛCDM model. This is true even when the limited mass resolution of numerical simulations is taken into account (Macciò and Miranda 2006 [129]).

The hierarchical formation scenario predicts that the universe should be filled by a large number (more then 10^3 per $h^{-1}\{Mpc^3\}$) of dark matter haloes with masses $M \approx 10^6 \mathrm{M}_\odot$. We employed the Sheth & Tormen mass function to estimate the expected number of haloes in this mass range along the line of sight of lensed QSO. We found that on average there more than 500 haloes in between the source and the observer, within a light cone with an aperture of 3 arcsec. Using direct lensing simulations and singular isothermal sphere approximation we computed the effects of those haloes on an unperturbed cusp configuration. We generated more than 10^4 different realizations of our global (lens + perturbers) lensing system, varying masses, positions and number of haloes.

We found that on a statistical basis (averaging on different realizations) this class of perturbers can modify consistently the fluxes of QSO multiple images at a level comparable to the observed one, in good agreement with previous studies on this subject (see mainly Metcalf 2005a,b [135, 194]). In some cases when the averaging process is restricted to a lower number of realizations ($\approx$ 200, see figure 6.7) we found that the observational data are reproduced with a high confidence level.

An important result of our study is that the bulk of the signal on QSO fluxes is due to haloes in the mass range $10^6 - 10^7 \mathrm{M}_\odot$. Since the number density of such haloes, and therefore their effect on the cusp relation, can be strongly dampen by the presence of a WDM candidate, the observed number of anomalous flux ratio can be used to constrain the mass of WDM particles.

Adding an exponential cut-off in the transfer function of WDM models we computed the number density of small haloes as a function of the mass of the warm particles. We show that if WDM is due to a sterile neutrino, then, in models with $m_\nu < 10$ keV, the number of dark haloes along the line of sight is too low to affect in a consistent way the fluxes of lensed QSO, failing in reproducing

the observed abundance of systems with high R values. This lower limit for the mass of the sterile neutrino is in good agreement with results obtained using different methods.

The main limitation of this study is represented by the few observational data that are available in the literature. However, future experiments such as Dune, are likely to observe more then 1000 lensed quasars, of which several hundreds should be quadruples due to the magnification bias. It will provide new lensing systems to be analyzed and thus more tightly constrain the WDM scenario.

Chapter 7

The dynamical state of RX J1347.5-1145 from strong lensing and X-ray analysis

7.1 Introduction

An accurate determination of the total mass of galaxy clusters is important to understand the properties and the evolution of these systems, as well as for many cosmological applications. Gravitational lensing, through multiple image systems (strong lensing) as well as from distortions of background sources (weak lensing), provides a reliable method to determine the cluster mass, which is independent of the equilibrium properties of the cluster ([69]). The lensing mass determination can be compared to estimates based on measured X-ray surface brightness and temperature, which is instead based on the assumption of hydrostatic equilibrium ([240]) or to dynamical estimates, which rely on the assumption of virialized systems. Combining optical, X-ray and radio observations of galaxy clusters is a major tool to investigate their intrinsic properties. In particular, the comparison of lensing and X-ray studies can give fundamental insights on the dynamical state of the galaxy clusters (see for example [216, 224]), on the validity of the equilibrium hypothesis and on their 3D structure ([225, 243]).

RXJ1347.5-1145 ($z = 0.451$) is one of the most X-ray luminous and massive galaxy cluster known. This cluster has been the subject of numerous X-ray ([241, 242, 216, 227]), optical (Sahu et al.1998 [238]) and Sunyaev-Zeldovich (SZE) effect studies ([233, 229]).

Formerly believed to be a well relaxed cluster, with a good agreement between the weak-lensing ([226, 230]), strong lensing ([238]) and X-ray mass estimates ([242]), more recent investigations revealed a more complex dynamical structure. In particular a region of enhanced emission in the South-Eastern quadrant was first detected by SZE effect observations ([233]) and later confirmed by X-ray observations that also measured an hotter temperature for the excess component ([216]).

This feature has often been interpreted as an indication of a recent merger event ([216, 229]). Furthermore, a spectroscopic survey on the cluster members found a velocity dispersion of 910 ± 130 km s^{-1}, which is significantly smaller than that derived from weak lensing (1500 ± 160 km s^{-1}, Fisher & Tyson 1997), strong lensing (roughly 1300 km s^{-1}, [219]) and X-ray analyses (1320 ± 100 km s^{-1}, [219], especially their Tab. 4). A major merger in the plane of the sky was proposed as a likely scenario to reconcile all measurements ([219]).

In this chapter, we further investigate the merger hypothesis by performing a combined strong lensing and X-ray analysis of RX J1347.5-1145, exploiting archive optical and X-ray data. We perform a strong lensing investigation based on a family of multiple arc candidates first proposed in Bradac et al. (2005) [217] using deep VLT observations. Differently from previous studies, we take care of performing the statistical analysis in the lens plane, which is a more reliable approach than the source-plane investigation when working with only one multiple image system. We further refine our analysis by taking into account not only the image positions, but also the shape and

orientation of the arcs. In addition, we exploit *Chandra* observations to gain additonal insights into the dynamical status of the cluster, through spectral and morphological analysis of the X-ray halo, and to discriminate between different evolutionary scenarios.

The chapter is organized as follows. Sect. 7.2 discusses the strong lensing image candidates selection from archive VLT data. Sect. 7.3 describes the statistical method used. The fitting procedure and models are presented in Sect. 7.4. Sect. 7.5 is devoted to X-ray data and analysis. Sect. 7.6 discusses a merger hypothesis. Summary and conclusion are presented in Sect. 7.7.

Throughout this chapter we use, unless otherwise stated, a flat model of Universe with a cosmological constant ($\Omega_m = 0.3$, $\Omega_\Lambda = 0.7$) and $H_0 = 70$ km s^{-1}Mpc^{-1}. This implies a linear scale of 5.77 kpc$''$ at the cluster redshift $z = 0.451$.

7.2 Optical data: cluster members and arc candidates

The lensing data analysis was performed using the same dataset of Bradač et al. (2005). The data were obtained with VLT-FORS1 in high resolution mode (pixel scale 0.09“, total field of view $\sim 3.2' \times 3.2'$), using UBVRI Bessel filters. The final images in each band were produced stacking 20 single exposures, obtained with a dither pattern of 30.0“. The seeing in the I-filter is of 0.57“. Further details on the data reduction can be found in [217]). We generated object catalogs for each band, using SExtractor v2.4.4 to measure photometric and geometrical parameters.

So far, more than five arc candidates for this cluster have been reported in the literature (see Fig.7.1). The first two (A1 and A4) were discovered by Schindler et al. (1995) [241]; later, HST STIS images revealed three additional ones (A2, A3, A5, [238]). Recently, Bradac et al. (2005) [217]reported the discover of several new arc candidates (AC, B1 B2, C, D1, D2, D3, D4, E) using VLT data. Arc A1 ($z = 0.806$) is the only one with measured spectroscopic redshift (Allen et al. 2002 [216]). Despite A3 could appear as a likely counter arc, this identification is still pretty uncertain. For the rest of the arcs only photometric redshift estimates are available so far ([217]). Thus, based on the existing literature we decided to start to use the most likely multiple-image system, e.g. the A4-A5 arcs, to model the cluster mass distribution. We then searched for additional images.

Following Bradac et al. (2005), we compared photometric properties and used flux measurements in UBVRI to distinguish different arc families. We inspected the galaxies having I-band magnitude up to three magnitudes fainter than the BCG and with a distance to the BCG smaller than $1'$. We confirm that the most plausible counter arc candidate is AC, giving a system of three images A4, A5 and AC (see Fig. 7.1) which have consistent multi-band colors (using 5” aperture magnitudes) and surface brightness within the errors. Such a system is likely due to a source redshift at $z_s \simeq 1.76$ ([217]). It is important to stress that, while we can not exclude that there are additional multiple-image systems, our analysis indicates that there are no additional lensed images belonging to the A4-A5 system within the inspected region and above our detection limit.

7.3 Statistical analysis

In this section we describe the mass profiles used to model the mass component and the statistical method employed to fit the observational data.

Let us describe the density profiles for the mass components. We consider two profiles: the first one for the cluster-sized halos and the second one for the galaxy-sized objects. Generally, an elliptical mass distribution model is described by a minimum number of 5 free parameters: the total mass, the centroid 2-D position, the ellipticity and the orientation. Two further parameters, the scale radius and the slope of the mass profile, are usually added.

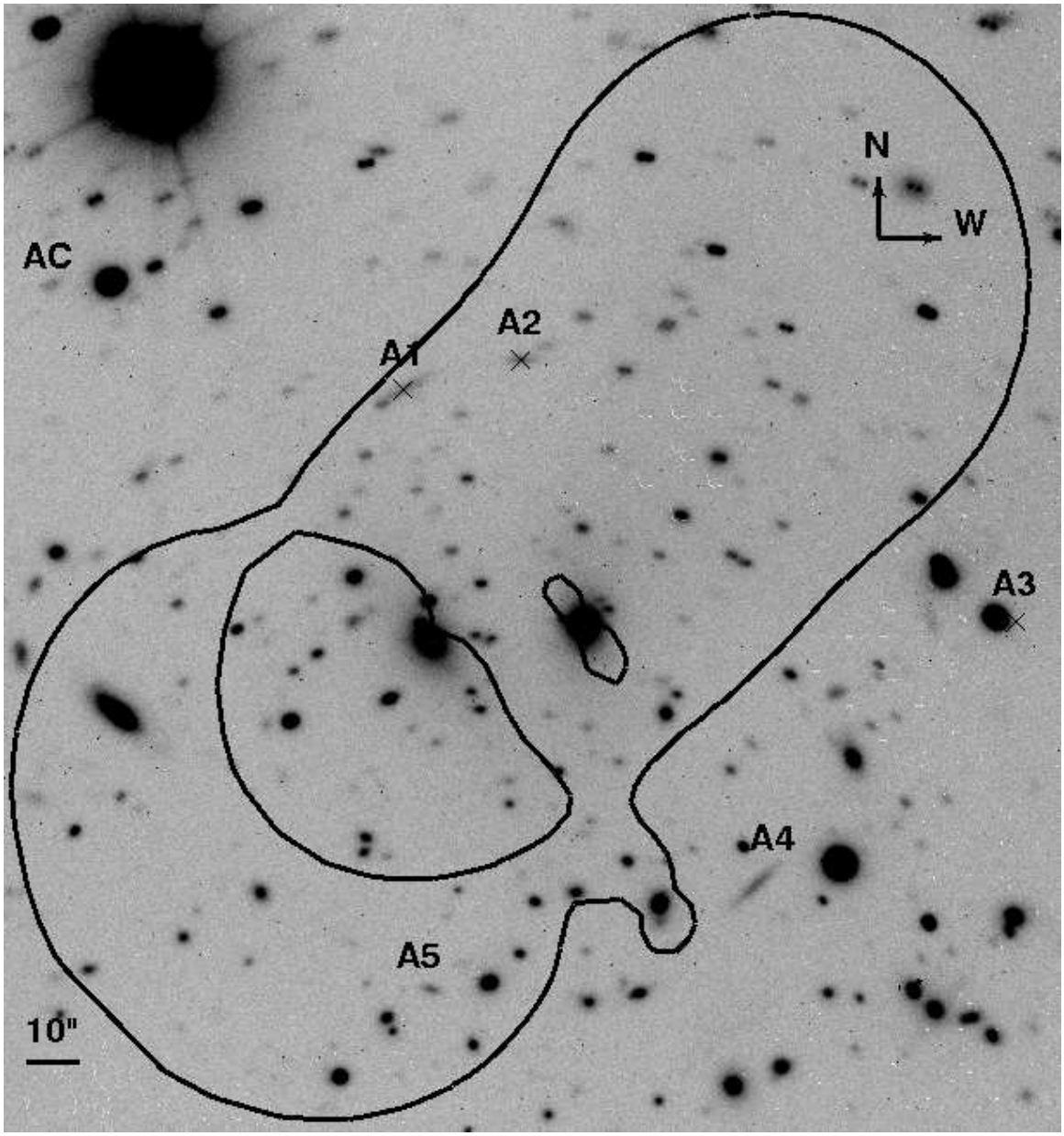

Figure 7.1. VLT-FORS1 Image of the cluster RXJ1347-1145. The full lines are the critical lines for the bimodal model (see Sect. 4).

For our purpose, we model the main mass (dark matter plus baryonic intracluster medium) components as softened power law ellipsoids ([122]). The projected surface mass density at the projected position $\mathbf{x}$ in the plane of the sky is as usual expressed in terms of the convergence κ, i.e the ratio of the local surface mass density of the lens $\Sigma(\mathbf{x})$ to the critical surface mass density $\Sigma_{\rm cr} = c^2 D_s/(4\pi G D_d D_{ds})$, being D_s, D_d and D_{ds} the source, lens and the lens-source angular diameter distances, respectively. For a general softened power law ellipsoidal model,

$$\kappa(\xi) \equiv \frac{\Sigma(\xi)}{\Sigma_{\rm cr}} = \frac{1}{2}\,\frac{b^{2-\alpha}}{(\theta_c^2+\xi^2)^{1-\alpha/2}} \quad \text{where} \quad \xi^2 = x_1^2 + x_2^2/q^2 \tag{7.1}$$

where b gives the mass normalization, q is the projected axis ratio, α is the slope index and θ_c is a core radius and ξ is an elliptical coordinate; Eq.(7.1) is the functional form in a coordinate system with the ellipse centered on the origin and aligned along the coordinate axes. We will adopt for the main dark components, the non singular isothermal ellipsoid (NSIE) which has α fixed to 1. For an isothermal model, the mass enclosed by a cylinder of radius ξ grows as $M_{\rm cyl}(\xi) \propto \xi$ asymptotically

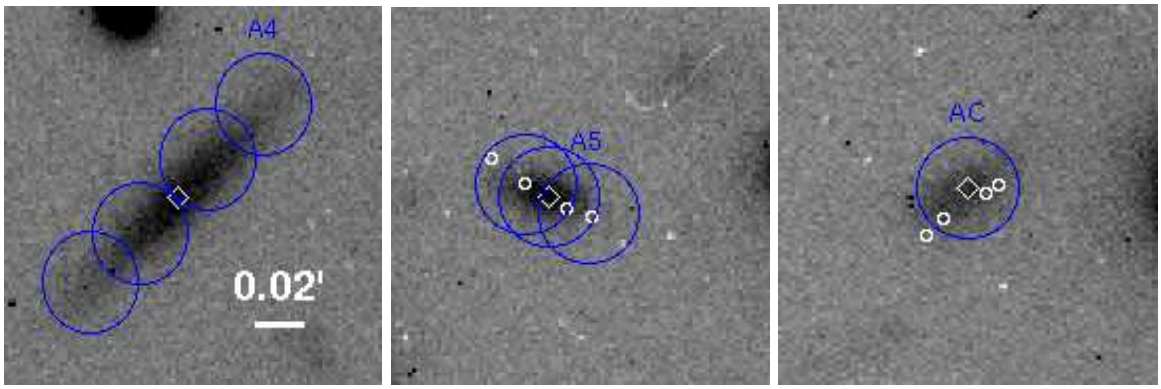

Figure 7.2. Arcs A4, A5, AC. On the left, we show the test curve A4; in the middle (right) panel, we show the reference curve A5 (AC). Each observed arc is sampled in a number of points, represented by the centers of the (blue) circles. The circle radius is 0.02': it corresponds to the error-bar used in our fitting analysis. Diamonds correspond to the observed arc centroids. The small white circles represent the counter-images of the four points sampling the test curve A4 used for the calculation of the χ^2_{arcs}.

and b scales as the square velocity dispersion, $b = 4\pi\sigma^2 D_d D_{ds}/c^2 D_s$. Note that when the core radius is zero, the model reduces to the singular isothermal model (SIE) (Kormann et al. 1994).

We model the galaxy-sized (dark matter plus stellar content) haloes as pseudo-Jaffe model ([122]). The pseudo-Jaffe model is equivalent to a combination of two softened isothermal ellipsoids.

The projected surface density of the elliptical model has the form

$$\kappa(\xi) = \frac{b}{2}\left[\frac{1}{\sqrt{\theta_c^2+\xi^2}} - \frac{1}{\sqrt{\theta_{cut}^2+\xi^2}}\right], \tag{7.2}$$

where $\theta_{cut}(>\theta_c)$ is the cut-off radius. The projected density is nearly constant inside θ_c, falls as ξ^{-1} between θ_c and θ_{cut}, and as ξ^{-3} outside θ_{cut}. The total mass is given by: $M = \pi\Sigma_{\rm cr} q b(\theta_{cut}-\theta_c)(D_d)^2$.

7.3.1 χ^2 statistic

We performed a χ^2 fit taking care of both the contribution from the image positions, χ^2_{img}, and the arc shapes and orientations, χ^2_{arcs}, so that $\chi^2 = \chi^2_{img} + \chi^2_{arcs}$. The χ^2_{img} accounts for the agreement between the observed positions of the arc centroids and their predicted values. When evaluated in the *image plane*, it can be expressed as ([122])

$$\chi^2_{img} = \sum_i \delta\mathbf{x}_i^T \cdot S_i^{-1} \cdot \delta\mathbf{x}_i\,, \tag{7.3}$$

$$\delta\mathbf{x}_i = \mathbf{x}_{obs,i} - \mathbf{x}_{mod,i}\,, \tag{7.4}$$

where the sum extends over all images i, and $\mathbf{x}_{obs,i}$ and $\mathbf{x}_{mod,i}$ are the observed and modeled positions of each image, respectively. The astrometric uncertainties for image i are described by the covariance matrix

$$S_i = R_i^T \begin{bmatrix} \sigma_{1,i}^2 & 0 \\ 0 & \sigma_{2,i}^2 \end{bmatrix} R_i\,, \tag{7.5}$$

$$R_i = \begin{bmatrix} -\sin\theta_{\sigma,i} & \cos\theta_{\sigma,i} \\ -\cos\theta_{\sigma,i} & -\sin\theta_{\sigma,i} \end{bmatrix}, \tag{7.6}$$

where the error ellipse has semi-major axis $\sigma_{1,i}$, semi-minor axis $\sigma_{2,i}$, and position angle $\theta_{\sigma,i}$ (measured North over East). In our analysis, we will assume isotropic errors for the images with $\sigma_{1,i} = \sigma_{2,i}$=0.02'

Computing the $\chi^2_{\rm img}$ in the image plane is the more reliable technique when dealing with just one multiple image system.

In fact, the alternative procedure of estimating χ^2 in the *source plane*, χ^2_{src}, (e.g., [121]; Kochanek 1991 [232]), despite of being computationally faster, does not take into account how many images make up the observed system, and might prefer in a flawed way mass models that yield a good fit adding fictious images. The approximation inherent χ^2_{src} should then be properly used only if an approximate good fit is already known, not in an initial search for a good model([122]).

In order to get a better estimate of the model parameters, the shape and orientation of the observed arcs must be taken into account as well ([122]). The basic idea of matching two curves C and D, each one sampled by a number of points, is as follows. Let's take the *test* curve C and let's map it to the source plane to find the intrinsic curve, then map that back to the image plane to find all the other images of the curves.

One of those curves (let's say C') should be near the *reference* curve D. A useful χ^2_{arcs} is based on the perpendicular distance between C' and D. For each independent j test point a $\chi^2_{test,j}$ contribution is calculated as

$$\chi^2_{test,j} = \min_i \left(\frac{|\mathbf{y}_j - \mathbf{x}_i|^2}{\sigma^2}, \frac{d_{i-1,i}(\mathbf{y_j})^2}{\sigma_{i-1}\sigma_i} \right) \tag{7.7}$$

where $d_{i-1,i}(\mathbf{y}_j)$ is the distance between the $\mathbf{y}_j$ test point (i.e. the image of the y_j test point mapped to image plane that should be close to one of the points making another arc) and its projection on the segment with extremes $\mathbf{x}_{i-1}$, and $\mathbf{x}_i$ of the reference curve; i runs over the reference points and the uncertainty σ are is estimated as the geometric mean of the errorbars at the endpoints. The total χ^2_{arcs} will be the sum over all the test points i: $\chi^2_{arcs} = \sum_i \chi^2_{test,i}$. Both χ^2_{img} and χ^2_{arcs} were implemented in the Gravlens code, used throughout the following section ([122])[1].

7.4 Fitting analysis

Our strong lensing statistical analysis was performed considering the system A4-A5-AC as a multiple image system. We considered both the centroid position and shape and orientation of the arcs as input data. Arcs are sampled by a finite number of points according to their total length and shape. Arc A4 is sampled in five points, arc A5 in three, and the rounder arc AC in only one point. We chose A4, the longest and better defined arc, as test curve, leaving the other one as reference curves. The positions of the sampling points are listed in Table 7.1) and showed in Fig. 7.2. The total number of constraints (N_{const}) is then $14 = 6 + 8$, being 3×2 the centroid positions and 4×2 the

[1] The software is available via the web site:http://cfa-www.harvard.edu/castles

Table 7.1. The position of the points sampling the arcs A4, A5 and AC used in the strong lensing analysis of the cluster. The error on each point is 0.″02. The coordinate origin is centered in the BCG

Arc	x [arcmin]	y [arcmin]
$A4_1$	0.370	-0.466
$A4_2$	0.346	-0.488
$A4_3$	0.333	-0.502
$A4_4$	0.317	-0.517
$A4_5$	0.294	-0.538
$A5_1$	-0.320	-0.698
$A5_2$	-0.302	-0.701
$A5_3$	-0.284	-0.706
AC_1	-1.038	0.651

additional sampled positions of the test arc. The image centroid of A4 is used only for χ^2_{img}, so that χ^2_{img} and χ^2_{arcs} are independent. We indicate with N_{par} the number of free parameters for each model. The distances between the sampled points in each arc are taken to be $\sim 0\farcs02$, nearly a factor two larger than the PSF and comparable to the arc width, so that the sampled points can be safely considered independent. Note that the $\chi^2_{\rm arc}$ approach, which requires multiple arc-like images of a single source to be present and identified, is best suited to exploit the A4-A5 system, where both arcs are elongated and well defined and are very likely to be images of the same lensed source.

We start our modeling procedure using a standard approach, i.e. fixing the main dark matter component(s) in the center of the brightest galaxie(s). In order to achieve a better fit, we will then relax these constraints. We will here describe our analysis step by step, going through models with either one or multiple main dark matter components. Finally, we will refine our model adding 10 galaxy-sized halos corresponding to the 10 brightest galaxies.

As a further indication of the goodness of the fit, we define the mean image shift, i.e. the distance between the observed image centroid and the corresponding predicted one, as:

$$\Delta_{pos} \equiv \frac{(\Delta_{A4} + \Delta_{A5} + \Delta_{AC})}{3}, \tag{7.8}$$

where $\Delta_{A*} = |\mathbf{x}_{\rm obs,*} - \mathbf{x}_{\rm mod,*}|$.

7.4.1 One component

As a first step, we consider the simplest tentative model, i.e a single main mass component centered in the neighborhood of the BCG. Although we performed the whole investigation in the image plane, we first considered also the χ^2 minimization in the source plane. This allows *i*) to further check if other additional images of the chosen lens system are formed and *ii*) to allow an easy comparison with previous works.

A model with a single dark matter component provides a good fit only if two further images are present in the A4-A5-AC system. They appear when we check the χ^2_{src} fitting result on the image plane. These two additional images should be lensed in the field of view of the VLT-FORS1 observation, $\sim 0\farcs2$ SW of the BCG, with amplification factors of the same order of the other three images and should then be easily detected, if present. As discussed in Sec. 7.2, no other image, with photometric properties consistent with A4-A5-AC, is observed; this model has hence been discarded. We note that in the χ^2_{src} approximation, this first model is essentially the same as the one used in Bradač et al. (2005). It provides, in fact, similar results. However, this point was not throughfully explored by these authors since they used it just as a first step in their fitting procedure, which accounts also for the weak lensing data.

We then performed the χ^2 minimization in the image plane by requiring the number of images to be fixed to three and let all the dark component parameters vary . A single mass component yields a very poor fit (Δ_{pos} =$0\farcs14$, $\chi^2_{img} = 61$), with the mass component located $0\farcs13$ East of the BCG. Furthermore, when adding the observed arcs configuration data, the same model shows a very high $\chi^2_{arcs} \approx 2800$

We also tried fixing two arcs (A4 and A5) and leaving AC free. In this case, by requiring the arc A4 to be tangential, the arc A5 appears to be radial. Furthermore, a wing of the arc A4 would cross a caustic so that part of it would be imaged in a tangential arc located near one of the additional images expected from the χ^2_{src} approximation.

A single dark matter component model is therefore not appropriate to describe the matter content in RX J1347.5-1145, hence revealing a possible more complex configuration. Even if the details of the results in the following subsections strongly relies on the position of the counter-arc AC, the information contained in the shapes and orientations of A4 and A5 alone indicates a somewhat irregular mass distribution.

7.4.2 Bimodal structure: two components

We then tried to improve the fit by adding a second main mass component. We first considered the model with the two main matter components being fixed at the positions of the two brightest galaxies. This model is similar to the one proposed by [216], where the mass components were constrained by requiring that the overall potential was able to produce the northern Arc 1. It is worth noticing that, as [216] themselves remarked, their best model could not explain A4 and A5 as images of the same source, as instead later photometric observations suggest.

When we consider the A4-A5-AC system as input data, the image positions are poorly reproduced ($\Delta_{pos} \simeq 0\farcs11$, $\chi^2_{img} = 57$) and we still get a radial A5 with an extremely high $\chi^2_{arcs} = 618$ for 10 free parameters. Even if we move the position of the second mass component from the second brightest cluster galaxy (SCG) towards the peak of the south-eastern X-ray substructure, the fit is still very poor.

We then made an additional step further, and let the position of the second dark matter halo free to vary, while leaving the main one fixed on the BCG. A first acceptable result is that a second component at $\sim 1\farcs2$ East of the BCG can improve the fit substantially, giving $\Delta_{pos} = 0\farcs03$, $\chi^2_{img} = 9.71$ and $\chi^2_{arcs} = 75.96$ (N_{par}=12). The main improvement obtained with this model is that the Arc 5 is now tangential, even if too much elongated and shifted towards North with respect to what observed. Adding a second component clearly improves our fit, strongly suggesting a bimodal structure for the cluster.

We further explored the bimodal structure of the cluster by relaxing also the position of the first main mass component. The fit obtained with two components, both free to vary, is pretty good ($\Delta^2_{pos} = 0\farcs002$, $\chi^2_{img} = 0.12$ and $\chi^2_{arcs} = 6.58$ for N_{par}=14). The two dark matter components have comparable masses and their centers do not coincide with either the BCG or SCG (see Fig. 7.3). The first component is located North-West of the BCG, the second one South-East (but far away from the secondary X-ray peak).

7.4.3 Adding complexity

For the models with two components discussed above, the number of observational constraints considered is either slightly less or equal to the number of free parameters, see Table 7.2. Given our conservative adopted sampling of the arcs, a bimodal structure is the only meaningful physical result we can get on the cluster. Nevertheless, we want to test the reliability of this scenario by exploring some alternatives. We then considered some unconstrained models which account for other physical effects and give an insight on some possible degeneracies of our lensing model.

7.4.3.1 Multiple components

We explored the effect of adding some further cluster-sized mass components, by considering a model with three main components, keeping the first two dark matter components fixed and adding a third free component (see Fig. 7.3). We fixed the first component in the BCG (coincident with the first X-ray peak) and the second one in the second X-ray peak leaving the third one free to vary. Even if the image positions are well reproduced ($\Delta_{pos} = 0\farcs03$, $\chi^2_{img} = 8.91$), this model does not improve substantially the fit to the observations with respect to the model with two components (one fixed plus one free), since $\chi^2_{arcs} = 62.8$ (for $N_{par} = 16$) and the predicted arc A5 is still shifted and too much elongated. Furthermore, while the second mass component is more or less as massive as a galaxy, the third component is much more massive and is located in the eastern part of the cluster, where no other observable (i.e. galaxies, X-rays) points to the possible presence of a large matter component. Fixing the second component to the SCG yields a similar result. We got the same values (within the errors) for the first component parameters (mass, ellipticity, orientation and core radius) as in the previous lensing scenario.

For all models, when leaving only one component free to vary, while fixing the other/s one/s, the free component is always located in the eastern part of the system, showing a mass of the same order of the other main component, while the second frozen component, located either in the SCG or in the second X-ray peak, tends to be much smaller .

7.4.3.2 Adding galaxies

Model	N_{par}	N_{const}	χ^2_{tot}	AIC	BIC
One Comp	8	14	2861.00	2877.00	2875.33
Two Comp:2 fixed	10	14	675.00	695	701.40
Two Comp:1 free 1 fixed	12	14	85.67	109.67	117.98
Three Comp:2 fixed 1 free	16	14	71.71	103.71	113.74
Two Comp:2 free	14	14	6.70	34.70	43.6
Two Comp:2 free +10 galaxies	16	14	6.00	38.00	48.2

Table 7.2. Summary of our models: N_{par} is the number of free parameters of the different models, N_{const} is the number of constraints. The total χ^2, the Akaike (AIC) and Bayesian (BIC) information criteria are also reported. Note that N_{par} counts 2 more free parameter to take into account the unknown source position during the fitting procedure.

Cluster-Size	b (arcmin)	x_1(arcmin)	x_2 (arcmin)	e	PA (deg)	θ_c(arcmin)	θ_{cut}
$1DM_{comp}$	0.872 ± 0.03	0.333 ± 0.04	0.522 ± 0.03	0.08 ± 0.04	-12.4 ± 0.2	0.520 ± 0.03	–
$2DM_{comp}$	0.748 ± 0.03	-0.494 ± 0.02	-0.278 ± 0.01	0.05 ± 0.03	27.34 ± 0.09	0.40 ± 0.03	–
Galaxy-Size	σ (km/s)					θ_c(kpc)	$\theta_{cut}(kpc)$
BCG	250 ± 100	[0.0]	[0.0]	[0.3]	[-0.10]	[0.5]	100 ± 20

Table 7.3. Parameters for the dark matter halos of our best fit model. Values in square brackets are fixed and not minimized.

We eventually considered the effect of galaxy-sized halos. Starting from our bimodal model with two free components, we added 10 galaxy-sized mass components centered at the location of the 10 brightest galaxies of the cluster (selected in the I-band). We expect that only those close to the images can affect the lens configuration. We scale the p-Jaffe parameters (mass normalization, core radius and cut-off radius) with the luminosity using the following relations ([231]):

$$\sigma_0 = \sigma^*(L/L^*)^{1/4}; \quad r_{cut} = r^*_{cut}(L/L^*)^{1/2}, \tag{7.9}$$

where the velocity dispersion σ is related to the parameter b through

$$b = 4\pi \frac{D_{ds}}{D_s} \frac{\sigma^2}{c^2} \frac{\theta_{cut}}{\theta_{cut} - \theta_c}. \tag{7.10}$$

We scale the core radius in the same way as r_{cut}. The total mass of a galaxy halo scales with the luminosity as:

$$M_{tot} = \frac{\pi}{G}(\sigma^*)^2 r_{cut}(L/L^*). \tag{7.11}$$

The proportionality constants σ^*, r^*_{cut} and r^*_0 are then fitted together with the parameters of the main mass components. For the BCG, as derived from the photometric analysis in Sec. 2, we took the ellipticity $e = 0.30$ (defined here as $1 - q$, where q is the axis ratio), $PA = -0.10\,\mathrm{deg}$

(North over East); for the SCG, $e = 0.23$ $PA = 33.0$ deg. The remaining galaxies are assumed to be circular. Our best fit gives a $\Delta^2_{pos} = 0\farcs001$ $\chi^2_{img} = 0.08$, $\chi^2_{arcs} = 5.92$ with N_{par}=16. The model is shown in Fig. 7.1 and the best fit values are listed in Table 7.3. Adding galaxy-sized halos causes a shift in the positions of the total mass distributions, towards the two main cluster galaxies.

We note that when we introduce a galaxy-halo located at the SCG, the peak of the second main component moves South-East. Fig. 7.2 reports three enlargements of the cluster image showing the data and fitted points for the system A4 (on the left), A5 (in the middle) and AC (on the right). Circles have a radius =0.02' and denote the data points we chose. Diamonds indicate the centroid of each arc we chose as point-image input data. White points show the best fit positions for the arc images. The test curve, A4, is on the left.

The errors on the parameters of this final model were estimated using Monte Carlo simulations. A Monte-Carlo run consists of reassigning a new set of image and arc data points, running a fit using the *lensmodel* code and finally finding the parameters that better match the new simulated data. Each data point (the multiple image positions and the arcs points) was drawn from a Gaussian distribution centered on the original one with a width corresponding to the estimated error ($0\farcs02$).

We collected 100 sets of new data and used them as input in the same way as the 'original' ones. This means that we find sets of optimal parameters for the smooth dark components and for the 10 brightest galaxies. The standard deviations of the parameter distributions provide us the uncertainty on our model.

7.4.4 Model degeneracies

Lensing information strongly supports a bimodal structure. The reliability of this result appeared by considering different alternative scenarios, which are summarized in Table 7.2. To further asses the goodness of our models, we exploited the Akaike (AIC) and the Bayesian information criteria (BIC) (see Liddle 2004 [245] and references therein). AIC is defined as $AIC = \chi^2 + 2N_{par}$, while $BIC = \chi^2 + N_{par} \log N_{const}$ where χ^2 is the total χ^2 for the model. The best model is the model which minimizes the AIC. Generally, models with too few parameters give a poor fit to the data and hence have a low log-likelihood (χ^2), while those with too many are penalized by the second term. The BIC comes from approximating the Bayes factor, which gives the posterior odds of one model against another presuming that the models are equally favoured prior to the data fitting.

By looking at Table 7.2, we can see that the one component model is highly disfavoured, while adding a second mass component improves the fit, since the BIC value drops down, from ≈ 2800 to ≈ 700 suggesting a bimodal structure for the cluster. When we let one component position vary, the BIC value becomes smaller (≈ 120) and a substantial melioration is obtained when you let both component positions be free: the BIC value is now ≈ 40. Adding the 10 galaxies does not improve considerably the fit, but it helps to better refine the features of the cluster model. In other words, a bimodal model is naturally favoured by our analysis, which definitely rules out the case with just one component.

The consideration of different configurations allowed also an insight into model degeneracies. As can be inferred by the previous analysis, the main degeneracy is connected to the positions of the two cluster-sized halos making up the binary lens. A comparison between the model with two free components and the alternative model with one component fixed and the other one free shows that the fit does not change in a dramatic way if the two centers are translated keeping the separation fixed at $\sim 1'$.

Our result on the model configuration does not depend on the estimated source redshift. In fact, a variation of z_s implies a rescaling of the critical density, but does not affect the positions and the relative mass ratios of the components of the cluster.

We also explored the effect of using a larger number of observational constraints by adopting a

more dense sampling for the test curve. We performed a test by sampling the arc A4 in eight points. Results did not change in a significant way. The total χ^2 for the models remain substantially the same. In particular for the model with two free components we got $\chi^2 = 6.90$ (instead of 6.58, see Table 7.2) with $N_{constr} = 22$. It is then clear that our conservative approach was enough to show the main feature of the cluster, i.e. its bimodality.

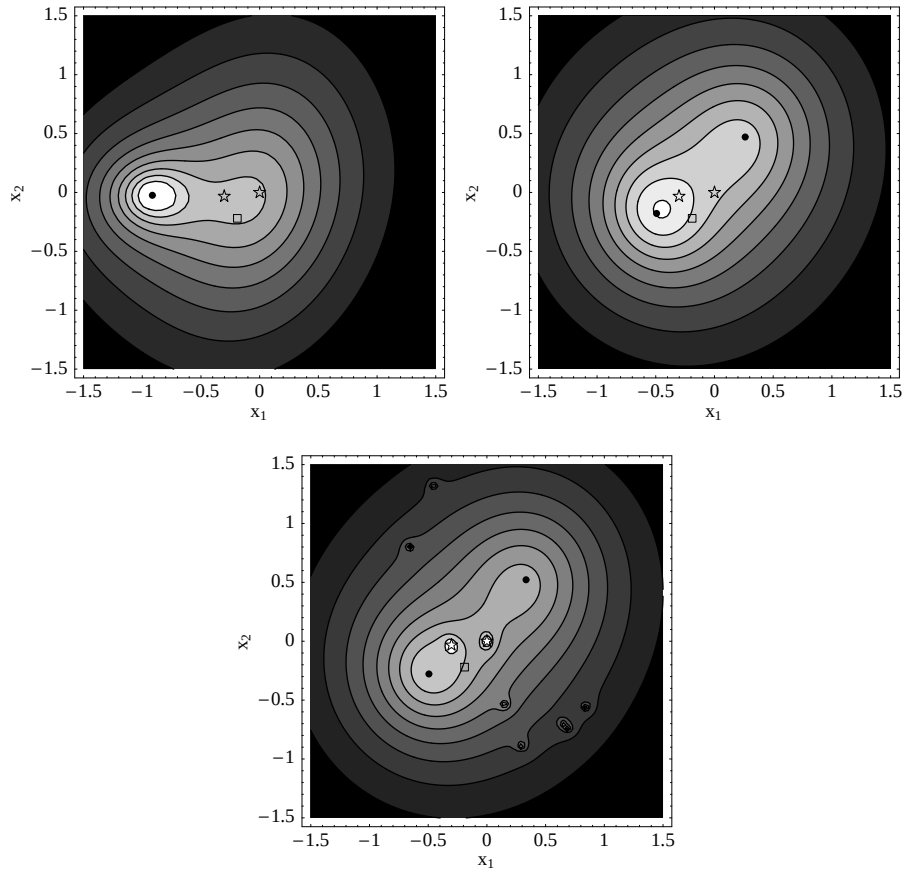

Figure 7.3. Projected mass distribution as inferred from the strong lensing analysis of the system A4-A5-AC for some of the models discussed in the text. Left panel : multiple smooth dark components, one component fixed in the BCG, the second one fixed in the second X-ray peak, and the third one being free to vary. Middle panel: two smooth and free dark matter components. Right panel: our best fit model, composed by two smooth dark matter components plus the 10 brightest galaxies. The coordinate system is centered at the BCG; units are in arcminutes. The surface mass density is in units of $\Sigma_{cr} = 3100\ hM_{\odot}\mathrm{pc}^{-2}$; contours represent linearly spaced values of the convergence k from 1.3 to 0.5 with a step $\Delta\kappa$ =0.1. The two star shaped symbols denote the positions of the BCG and the SBG; filled dots represent the centers of cluster-sized mass components; the position of the SE X-ray sub-clump is given by an empty box.

7.5 X-Ray analysis

We looked for further evidence of the complex structure of RX J1347.5-1145 by analyzing the intracluster gas at X-ray wavelengths. RX J1347.5-1145 was first detected in the X-rays by ROSAT in the All-Sky Survey, which showed and extremely X-ray bright extended source ([241]).

Subsequent ROSAT HRI and ASCA pointed observations revealed it as the most luminous X-ray cluster known at that time, with a bolometric luminosity $L_X \sim 2 \times 10^{46}$ ergs s^{-1} ([242]). These first pointings showed an extremely sharp surface brightness peak located close to the optical position of the dominant cluster galaxy, and a strong cool central region.

Based on subsequent $\sim$ 20 ksec *Chandra* observations, Allen et al. (2002) [216] reported the discovery of a region of relatively hot, enhanced X-ray emission, approximately 20" to the south-east of the main X-ray peak (which is located at , Dec= -11 45'09" (J2000)). This sub-clump, with a roughly circular morphology, appeared to be separated from the main cluster core by a region of reduced emission. The hotter temperature of this sub-clump, respect to the gas at the same radius in other directions from the X-ray peak suggested that it probably contained shocked gas resulting from a recent merging event. Later XMM-Newton observations confirmed these results ([227]).

In this work we analyzed an archival *Chandra* observation of RX J1347.5-1145, carried out on September, 2003, using ACIS-I. The net good exposure time, after removing all periods of high background, is of 56 ksec. This longer *Chandra* exposure roughly confirms previous findings detailed above. In the following we will hence exclusively point out some new results, compared to what already published in literature. For the extraction of the azimuthally averaged temperature profile (see §7.5.1), we have also used the two shorter Chandra ACIS-S exposures (obsID 506 and 507) already analyzed by [216], with net exposure times of 9 and 10 ksec, respectively.

In the innermost regions of the cluster the hot gas closely follows the BCG gravitational potential, with the X-ray emission approximately oriented in the NS direction (Fig. 7.4).

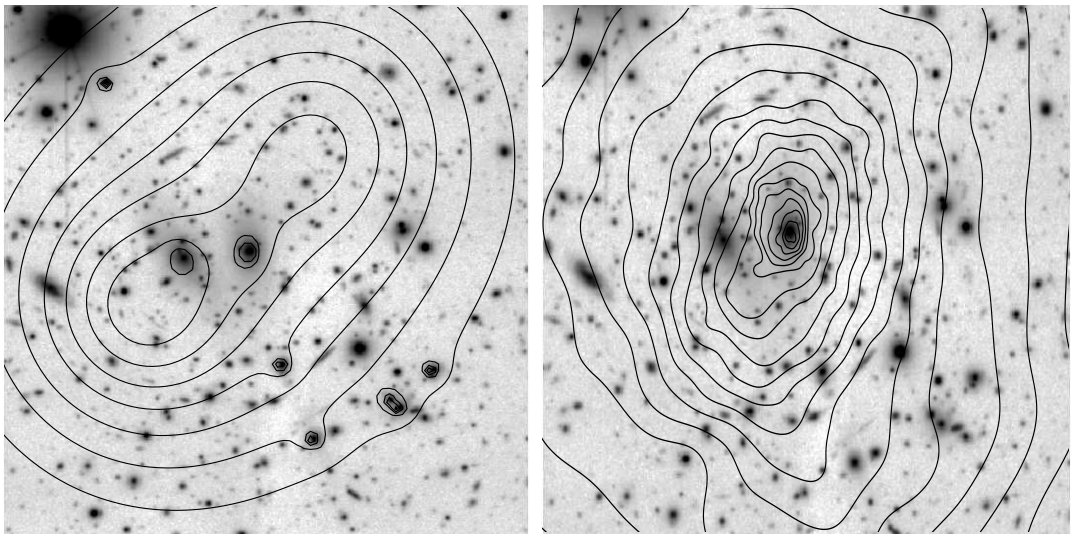

Figure 7.4. VLT-FORS1 image of RX J1347+1145. Superposed are the contours representing the lensing mass distribution (left panel) and the X-ray surface brightness (right panel). The units are the same as in Fig.1

The main X-ray peak is slightly shifted towards SW respect to the centroid of the overall cluster emission, hence producing a slight isophote compression with a sharper surface brightness decrease in this direction and a plume-like tail in the opposite one, respect to the cluster center. The effect is small and is probably due to the BCG proper motion (e.g. [235]).

Going to larger radii ($r0'.23$) the X-ray emission becomes more elliptical (with $e \sim 0.3$). The orientation also changes with the radius. The PA is in fact $\sim 0°$ in the inner 0.2', while it remains approximately constant at $\sim -16°$ N over E, for $0.2' < r < 1'$. We then isolated the SE sub-clump by subtracting the model that best approximates the surface brightness emission in the remaining quadrants. The substructure shows a moderate ellipticity with $e \sim 0.2$ and an orientation angle of $\sim 46.4°$ N over E.

7.5.1 X-ray Spectroscopy

Throughout this section, spectra have been modeled (in the $0.3 - 7.0$ keV band) to an absorbed XSPEC isothermal plasma emission code by Kaastra 1993 [228], including the FeL calculations of Liedahl et al 1995 [234] Mekal, folded through the appropriate response matrices and corrected for the ACIS time dependent absorption due to molecular contamination. The absorbing column density was fixed at the nominal Galactic value $n_H = 4.85 \times 10^{20}$ cm^{-2} ([221]). All errors, if not otherwise stated, are 90% ($\Delta\chi^2 = 2.71$) confidence limits.

Within 1.5‘ from the main X-ray peak (to the full 360°), we measure a mean emission-weighted temperature of $kT = 11.7 \pm 0.5$ keV and a metal abundance $Z = 0.30 \pm 0.06\ Z_{\odot}$ for the whole cluster, in agreement with previous Chandra ([216]) and ASCA ([242]) measurements.

The azimuthally averaged temperature behaviour was inspected by extracting spectra into elliptical annular bins centered at the cluster X-ray main peak, and excluding the south-eastern quadrant, from all three Chandra pointings (see §7.5). We observe a sharp temperature decrease within the central $\sim$ 200 kpc, consistent with the presence of a massive cool core, and a more gentle decline in the outer regions, in agreement with what observed by Allen et al. (2002) [216] and Gitti & Schindler (2004) [227]. The resulting temperature profile is shown in Fig.7.5.

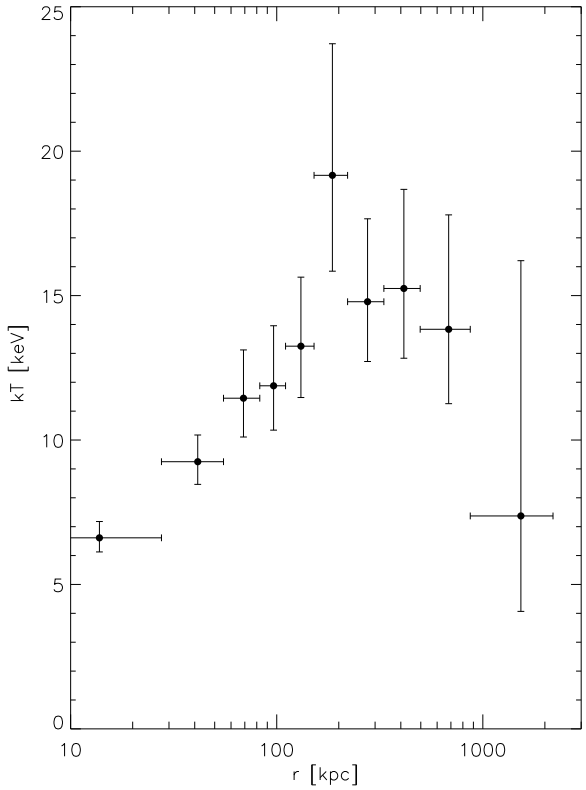

Figure 7.5. Projected X-ray gas temperature profile in the $0.3 - 7.0$ keV energy range.

Up to now, we have treated the cluster as a two-dimensional object in order to learn about the overall spectral properties. Since projection effects must be present due to the cluster irregular morphology, we attempt to get rid of part the projection effects that are present, providing a

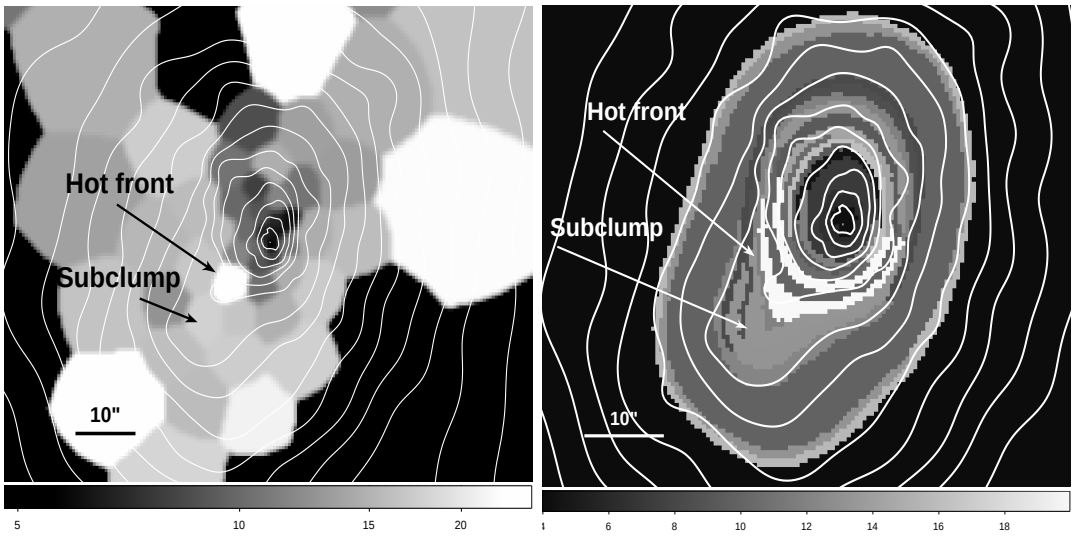

Figure 7.6. Adaptively binned temperature maps of the central (1.6‘ × 1.6‘) performed using a Voronoi binning algorithm (left panel) and a contour binning algorithm (right panel). The temperature scale on x-axis is expressed in keV. Superposed are the logarithmically spaced smoothed X-ray contours.

more accurate description of the gas temperature spatial distribution, obtained performing a two-dimensional spectral analysis of the central 1.6‘ × 1.6‘ of the cluster. This was done with the aid of the WVT binning algorithm by S. Diehl and T.S. Statler ([222]) , which is a generalization of Cappellari and Copin's Voronoi binning algorithm ([218]) , and then extracting spectra for each resulting Voronoi cell (each containing at least 900 photons in the $0.3-7.0$ keV energy range, after background subtraction). The resulting temperature map is shown in the left panel in Fig. 7.6 (where different shades of gray reflect the different temperatures of each region).

Since the detected temperature structure is partly due to the size and shape of the binning performed on the image, we produced an additional temperature map using a totally different binning technique: the *contour binning* algorithm by Sanders et al. 2006 [239]. This method chooses regions by following contours on a smoothed image of the cluster; the generated bins closely follow the surface brightness distribution.

As above, spectra were extracted from each resulting region, each containing at least 900 photons (S/N$\sim$ 30). The fit in each cell was performed with a fixed metallicity to the value obtained from a S/N$\sim$ 60 map, only allowing the temperature and normalization to vary. The resulting temperature map is shown in the right panel in Fig. 7.6. The relative errors of the temperatures in two resulting temperature maps are of the order of $10-20\%$, with a slight dependance on the temperature. Regions with larger errors were cut off from the final maps. Despite the relatively large uncertainties, the two temperature maps provide a reliable qualitative description of the spatial temperature distribution which is clearly not provided by means of radially averaged profiles. The two temperature maps reveal a cool core ($kT \sim 5.8$ keV) which appears slightly flattened, extending from North to South (see left panel in Fig. 7.6). Out to $r \leq 1'$ the temperature is approximately constant around $\sim 14.0-17.0$ keV. Several much hotter regions are observed, one of which lies surprisingly close to the cool cluster core (the "*hot front*" at 9“ south-east of the cluster center, left panel in Fig. 7.6); the gas temperature at that radius, in all other directions, is instead equal to the average value. This *hot front* is located in the region of reduced emission that separates the cluster core from the X-ray sub-clump, where neither optical nor X-ray point sources are observed. The same feature is observed in the temperature map produced with the *contour binning* technique (see right panel in Fig. 7.6), showing that this is not a results of the binning technique. Instead, contrary to what previously thought ([216]), the X-ray sub-clump is not significantly hotter than the gas in the other directions, at the same distance respect to the main X-ray peak.

A trail of cold gas ($\sim 8.0-10.0$ keV), approximately 130 kpc long and extending form the BCG

toward N, is also visible. More than half of the detected photons at that position will be projected from the surrounding gas; the intrinsic temperature of the cold trail is hence likely to be lower than the values quoted above. The cold filament is probably a cooling wake, caused by the motion of the cD galaxies inside the cool core region ([220, 223]), in agreement with our morphological analysis results (see §7.5.1).

The other observed hotter regions (see Fig. 7.6) are located further out in the cluster environment ($r \sim 0'.5 - 0'.6$, between ($\sim 150 - 300$ kpc), where the average cluster gas temperature reaches indeed its highest value (see Fig.7.5).

7.5.2 Mass Distribution

To obtain a quantitative estimate of the cluster morphology out to large radii, we modeled the emission of the cluster in the $0.3 - 7.0$ keV band, excluding the South-Eastern quadrant, using the longest *Chandra* available pointing (obsID 3592). Pixel values of all detected point sources were replaced with values interpolated from the surrounding background regions; the *CIAO* tools *wavdetect* and *dmfilth* were used for this purpose.

We then fitted the cluster surface brightness to elliptical 2D β-models (see Eq. (7) in De Filippis et al. (2005) [225]. The resulting model is centred in R.A.=13 47 30.7 and Dec.=−11 45 09.1 and has a projected axial ratio of $e_{proj} = 1.45 \pm 0.02$ and a position angle $\theta = 158.5 \pm 1.0$ (N over E).

We then extracted 1D surface brightness profiles within elliptical concentric annuli, with the projected axial ratio, position angle and center estimated above, and spaced by 8 arc-seconds. The distance r from the cluster center is measured along the major axis of the ellipses. The profiles were extracted in the 0.3-7.0 keV energy range. A background region was chosen, in a peripheral region of the field of view, at approximately 11 ‘ from the cluster centre. Corresponding profiles, extracted from the exposure map of the observation, provided the required average values of the effective exposure time within each annulus. The extracted surface brightness profiles were then background subtracted and exposure corrected.

The electron density and gas density distributions were consequently computed deprojecting radial surface brightness profile using an onion peel (model independent) method ([244, 215]). Given the gas density distribution, the total gravitating mass density was hence obtained under the hypothesis of hydrostatic equilibrium, using the radial temperature distribution estimated in § 7.5.1. The resulting total gravitating mass profiles is plotted as solid dots in Fig. 7.7. Due to the restricted field of view of ACIS-S, surface brightness profiles extracted from the two shorter *Chandra* pointings (obsID 506 and 507) extend to much smaller radii, and were hence not used in this analysis.

Furthermore, we fitted the extracted surface brightness profile with both a single and a double β-model. The best-fit single β-model, which fairly reproduces the observed profile, is described by: $S_0 = 12.2 \pm 0.7$ [cts s^{-1} arcmin^{-2}], $\beta = 0.588 \pm 0.003$, $r_c = 0.152 \pm 0.006$ arcmin, though leading to a high $\chi^2_{\rm red.} = 18$. A double β-model further increases the quality of the fit, providing a more accurate description of the cluster profile: $S_{01} = 14.8 \pm 1.1$ [cts s^{-1} arcmin^{-2}], $\beta_1 = 0.599 \pm 0.008$, $r_{c1} = 0.136 \pm 0.006$ arcmin, $S_{02} = 0.07 \pm 0.03$ [cts s^{-1} arcmin^{-2}], $\beta_2 = 1.9 \pm 1.7$, $r_{c2} = 2.5 \pm 2.0$ arcmin, $\chi^2_{\rm red.} = 2.5$.

The electron density $n_{\rm e}$ is then obtained by inverting the model which describes the surface brightness distribution. In the spherically symmetric case the inversion of the double β model has been resolved by [246]. Since we are dealing with elliptical distributions, we extended the formalism to a more general ellipsoidal symmetry as done in De Filippis et al. (2004) [224]. Once the gas distribution is known, the total mass density was obtained under the hypothesis of hydrostatic equilibrium. The resulting total mass profile, for the double-β model is shown as a solid gray line in Fig. 7.7. Results are consistent with what obtained using a model-independent method, confirming that a double β-model provides an adequate description of the cluster profile.

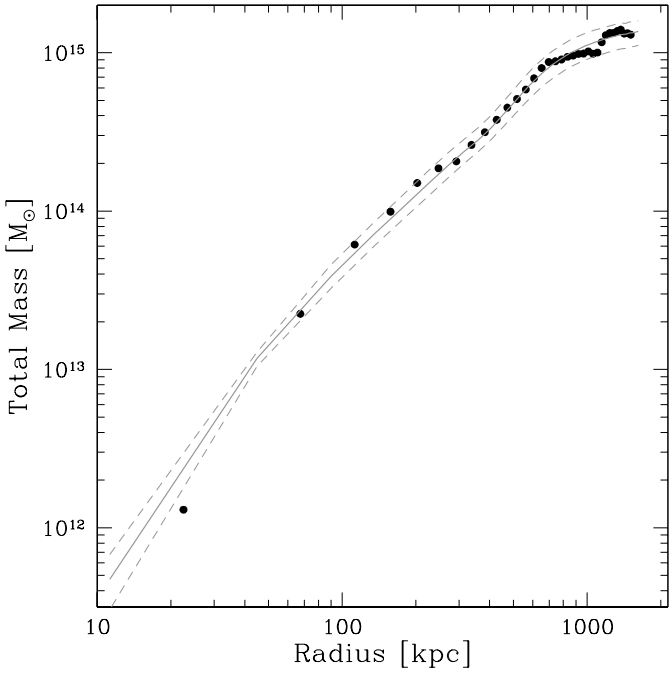

Figure 7.7. Filled dots: integrated total mass profile. Solid line: integrated total mass profile estimated using a double β-model; 90% error on the mass, coming from the temperature measurement, are plotted as dashed lines.

7.5.3 X-ray and SZE face to face

Our X-ray analysis has revealed hot gas ($kT \sim 20$ keV) in the SE quadrant, associated to a hot front located between the cool core and the SE sub-clump rather than to the sub-clump itself.

This front is most probably what remains of a shock front, a clear indication of a recent merger event.

SZE effect studies, despite their low spatial resolution, further strengthen the above conclusions. The SE sub-clump of enhanced emission was first detected through SZE measurements by Komatsu et al. (2001) [233] . Subsequent X-ray and SZE observations revealed a substantial agreement with previous SZE data ([229, and references therein]).

In order to characterize the high temperature substructure, Kitayama et al. (2004) [229] performed a combined X-ray-SZE analysis. They assumed that the hot substructure was embedded in an ambient gas identical to that in the other directions, deriving a temperature of $\sim 28 \pm 7$ keV for the hot component, in agreement with our X-ray measurement for the hot front.

7.6 A merger hypothesis

Our mass estimates for the inner regions in RX J1347+1145 are in substantial agreement with previous lensing analyses. Lensing mass determinations do not depend on the dynamical and hydrostatic status on the cluster matter but only on the total mass distribution. From our bootstrap error analysis, we estimated an integrated total projected mass of $(9.9 \pm 0.3) \times 10^{14} M_\odot$ inside a radius of 1.5 arcmin, consistent with the estimate of $(1.2 \pm 0.3) \times 10^{15} M_\odot$ from a combined weak and strong lensing analyses in Bradač et al. (2005) . We should point put that our results depend upon the correct redshift determination and identification of members of the multiple image system we use. An error of ± 0.5 on the source redshift implies an error of $\pm 1.0 \times 10^{14} M_\odot$ on the mass estimate.

A first weak lensing result by Fisher & Tyson (1997) gave a total integrated mass within $\sim 5'$ of $(1.5 \pm 0.3) \times 10^{15} M_{\odot}$ and a corresponding velocity dispersion of $\sigma_{\rm v} = 1500 \pm 160$ km s^{-1} assuming singular isothermal sphere model[2]. This result was later confirmed considering a larger field of view by Kling et al. (2005), which obtained $\sigma_{\rm v} = 1400^{+130}_{-140}$ km s^{-1} under the same assumptions, while our mass estimate translates into a velocity dispersion $\sigma_{\rm v} = 1620 \pm 30$ km s^{-1} . Results from both our lensing and X-ray analysis indicate that the cluster is not in virial equilibrium; the inferred estimate of $\sigma_{\rm v}$ has hence been derived only for comparison with weak lensing results.

Since our analysis showed indications of dynamical complexity, estimates of the cluster mass as inferred from X-ray data under the hypothesis of hydrostatic equilibrium should be treated with caution. Nevertheless, just for comparison with the lensing mass we performed an X-ray analysis excising from the X-ray data the perturbed South-East quadrant, see Sec. 7.5.2. We obtained a X-ray estimate of the projected mass within 1.5 arcmin of $(8 \pm 1 \pm 2) \times 10^{14} M_{\odot}$, where the first error is statistical and the second one accounts for the uncertainty on the intrinsic geometry of the cluster, which might be either oblate or prolate. The total 3-dimensional mass within a spherical region of radius 1 Mpc (2.9 arcmin) is $M_{\rm tot} = (1.1 \pm 1 \pm 2) \times 10^{15} M_{\odot}$. These estimates are consistent with previous *XMM-Newton* ([227]) and *Chandra* ([216]) X-ray analyses, and are consistent as well with our results from gravitational lensing. However, X-ray mass estimates of perturbed system may be strongly biased. On one hand, neglecting the X-ray South-East sub-clump implies that we are not considering an additional contribution to the total mass, which is consequently underestimated. On the other hand, the temperature in a merging system might be inflated with respect to the temperature of a relaxed cluster, which implies an over-estimate of the mass.

Whereas X-ray and lensing estimates are in good agreement, the dynamical mass estimate is considerably smaller ([219]). Cohen & Kneib (2002) suggested a merger scenario to solve this puzzle. Until the merger is complete and galaxy orbits have virialized to the new total mass, the dynamical mass estimate would be biased toward the mass of the larger clump. Then, a major merger between two clumps of comparable mass could reconcile the discrepant observations.

The bimodal mass distribution inferred in our analysis is in agreement with this merging scenario . Moreover the merger is possibly happening in the plane of the sky, since the redshift distribution of the cluster members does not show any feature along the line of sight.

The merger scenario is also supported by the X-ray and SZE observations of the intracluster medium. Both the gas sub-clump and the hot front in the SE quadrant are indications of a merger process. The overall agreement between the X-ray and lensing mass estimates might suggest that the emitting gas has had time to virialize. Hydrostatic equilibrium is also supported by the fact that the overall mass, temperature and luminosity of RX J1347+1145 relate as expected by a typical for massive cluster ([216]). A major merger scenario was also considered in Kitayama et al.(2004) [229], which discussed as an head-on collision of two $\sim 5 \times 10^{14} M_{\odot}$ clusters with relative velocity of ~ 4000 km s^{-1} would result in a bounce-shock with $kT \gtrsim 25$ keV, as detected in the SE quadrant.

7.7 Discussion

We have analyzed both the lensing and X-ray properties of RX J1347.5-11.45, one of the most luminous and massive X-ray cluster known. Based on the analysis of an arc family, photometrically selected, we have estimated the total cluster mass distribution, within a radius of ~ 450 kpc from the cluster center.

We performed a χ^2 analysis in the lens plane and scrupulously modeled the arc configuration. A model with two smooth dark matter components of similar mass accurately reproduces the observations and yields a mass estimate in agreement with previous strong and weak lensing and X-ray studies.

[2] The values for $\sigma_{\rm v}$ and M have been converted to our reference ΛCDM model.

The detailed features of our model are strictly related to the selection of the members of the multiple image system, in particular to the inclusion of the arc AC. Despite all candidates should be confirmed spectroscopically, a photometric analysis suggests that A4 and A5 almost undoubtedly belong to the same system. Based on the shapes and orientations of A4 and A5 alone, without any constraint on AC, we can exclude the presence of a single mass component, and require a more complex structure. Our strong lensing analysis suggests a major merger between two sub-clumps of similar mass located within the central 300 kpc. X-ray observations further strengthen our view of a complex structure of the inner regions of RX J1347.5-1145, revealing a hot front in the South-Eastern area, most probably a remnant of the occurred merger. This merging framework, which arises naturally from our strong lensing model, can also reconcile the observed discrepancy between dynamical mass estimates and X-ray, lensing and SZE ones, which instead give consistent results. Agreement between X-ray and lensing mass estimates further indicates that the gas might have had time to virialize. Spectroscopic measurements additionally suggest that the merger is taking place in the plane of the sky.

Whereas the presence of a merger is confirmed on several grounds, its properties are though still unclear. A spectroscopic confirmation of further arc candidates is the required step to confirm and accurately define the merging scenario and to provide a final, more accurate description of the dynamical state of RX J1347.5-1145.

APPENDIX A:

Influence of Orbital Behaviour and Chaos on the Shape of Dark Matter Halos

Currently, the favored cold dark matter (CDM) model of structure formation suggests that dark matter (DM) halos of galaxies and clusters should admit triaxial density profile (Barnes & Efstathiou 1987 [248], Dubinski & Carlberg 1991 [252], Warren et al. 1992 [276], Jing & Suto 2002 [256], Moore et al. 2004 [266]). This expectation is well-accepted, but (in principle) it could also be tested against observations. In this respect, triaxial dark halos surrounding both elliptical and disk galaxies could, not only provide clues about the underlying physics of galaxy formation, but also impose constraints on different formation scenarios (Dubinsky & Carlberg 1991 [252]). On the other hand, the recently observed coherence of the tidal stream of the Sagittarius dwarf spheroidal suggests a nearly spherical halo configuration for the Milky Way (Ibata et al. 2001 [261], Mayer et al. 2002 [264], Majewski et al. 2004 [263]), in contradiction with what has been obtained by cosmological simulations (i.e. Jing & Suto 2002 [256], Allgood et. al 2005 [247], Macciò et al 2007 [262]).

This inconsistency could possibly be resolved by carefully examining the effect gas cooling has on halo shapes. In 1994 Dubinsky [251] studied the effects of dissipative gas infall on the shape of DM halos by adiabatically growing central-mass concentrations inside initially triaxial DM halos. A more extensive study was made recently by Kazantzidis et al. (2004; K04 hereafter [259]), where a number of cosmological gas dynamics simulations were performed; the main result was that halos formed in simulations with gas cooling are significantly more spherical than corresponding halos formed in adiabatic simulations.

Aiming to extend the aforementioned investigations (Dubinsky 1994 [251] and K04), this part attempts to address the question of *why* and *how* the gas dissipation alters the halos shape. The main addition is that we approach the problem from a dynamical point of view.

The relation between particle orbital properties and the shape of bound structures has been already studied by several authors (i.e. Jesseit, Naab & Burkert 2005 [255], Naab, Jesseit & Burkert 2006 [268], Valluri et al 2007 [275]). In this appendix we present results of the first broad analysis of particle orbits in cosmological DM halos, and we investigate how these orbits modify their behaviours when a baryonic core is grown inside the original triaxial dark matter halo.

The analysis of the orbits is two-leveled. Firstly, we study them in a statistical fashion, investigating quantities like the evolution of axes ratios of the configuration. Secondly, we examine the behaviour of individual orbits; we ask how their shapes are affected when there is a dissipational component at the center of the configuration, but we also employ a frequency analysis scheme to quantify the chaoticities, and we attempt to investigate how chaos connects to the change of their shapes.

This appendix is organized as follows: in section A-1 we present our codes and modeling; results are presented in section A-2; section A-3 contains our conclusions and description of follow-up for this study.

A-1 Numerical Simulations

All simulations were performed using PKDGRAV, a tree-code for cosmological simulations of N bodies, written by J. Stadel and T. Quinn (Stadel 2001 [273]). This code uses spline kernel softening, for which the forces become completely newtonian at two softening lengths. Individual time-steps for each particle are chosen to be proportional to the square root of the softening length ϵ, over the acceleration, a: $\Delta t_i = \eta\sqrt{\epsilon/a_i}$. Forces are computed using terms up to hexadecapole order and a node-opening angle θ which we set to 0.6.

The original dark matter halo was extracted from an existing N-body simulation where we had followed the evolution of 250^3 particles in a volume of 20 Mpc with a softening $\epsilon = 0.6$kpc. We adopted a flat ΛCDM cosmology with parameters from the first year WMAP results (Spergel *et al* 2003): matter density $\Omega_M = 0.268$, baryon density $\Omega_b = 0.044$, Hubble constant $h \equiv H_0/(100\mathrm{km\,s^{-1}Mpc^{-1}}) = 0.71$, and a scale-invariant, Harrison-Zeldovich power-spectrum with normalization $\sigma_8 = 0.9$. A detailed analysis of this simulation has been already presented in Macciò et al. (2007).

At redshift zero we selected a galaxy-like halo having the following characteristics: $\mathrm{M}_{vir} = 1.7 \times 10^{12}\mathrm{M}_\odot$, $\mathrm{R}_{vir} = 248$ kpc and about 110000 particles within the virial radius. This halo is well-fitted by an NFW (Navarro, Frenk and White 1997 [195]) profile with a concentration parameter of 9.5. We also computed the shape of this halo with the same technique described in Macciò et al. (2007), getting for the axis ratio $b/a = 0.82$ and $c/a = 0.71$, where a, b, c are the long intermediate and short axis respectively. For our further studies we cut from the original simulation a cubic region of 1x1x1 Mpc h^{-1} centered around the selected halo. This region sets the new simulation volume for the baryonic mass growth experiment.

A-1.1 Baryonic core modeling

The investigation of galaxy formation inside dark matter halos is a challenging problem. In hierarchical models a collection of smaller scale fluctuations (protogalaxies) merge into forming a smooth, centrally concentrated galaxy. Both gravitational collapse and dissipation occur at the same time; if the cooling time of dissipation is shorter than the gravitational free-fall time, then gas will sink into the center of the system to form a luminous galaxy. Following Dubinski (1994) [251] we modeled the formation of the baryonic core of our galaxy-model by slowly growing a mass distribution at the center of a previously selected dark matter halo. The mass-growth follows a linear law, until it reaches a maximum mass comparable to the expected luminous mass of galaxies. We chose $M_b = 1.8 \times 10^{10}\mathrm{M}_\odot$ for the final baryonic mass and $T = 7$ Gyrs as growth time (this is the time elapsed from $z = 1$ to $z = 0$ in our ΛCDM universe). We also performed two more simulations with a smaller final mass for the baryonic core (keeping constant the growth time), namely we used a 1/4 and 1/16 of the previous value for M_b. For comparison purposes, we also performed a simulation with no growing mass at the center, where we simply allowed our halo to evolve in isolation (i.e. once extracted from the N-body simulation) for 7 Gyrs. After that time we stopped the mass growth on the baryonic core, and we let all the aforementioned simulations evolve for an additional 7 Gyrs, in order for our halos to reach a well-relaxed configuration.

In first approximation, we treated the luminous component of the galaxy as a single particle within the simulation. At time $T = 0$ we gave to this new particle the same coordinates and velocities components of the dark halo center of mass. This particle was then free to move in the usual self-consistent fashion of an N-body simulation, but, in practice, it quickly settled at the center of mass of the dark matter halo because of dynamical friction.

One may object that this zeroth-order approximation might generate unphysical effects; for example having only one particle at the center of the configuration may cause unphysical close encounters with the dark matter particles, with subsequent scattering of the last. To assure that this was not the case in our experiments, we quantified the importance of these effects in order

to separate physical phenomena from numerical artifacts generated by the approximations of our schemes.

To this end we performed two additional simulations. Keeping constant the growth-rate of the central mass we: i) increased the kernel softening for the growing particle to four times the one on the surrounding *dm* particles, from 0.6 kpc to 2.4 kpc, and ii) instead of using one particle we split its mass into 500 particles. The initial spacial size of this particle-cluster was 5 kpc and all the particles increased their masses following the same growth-rate. As is clearly stated in the discussion section our results suggest that there is no significant, quantitative or qualitative, variation between these two simulations and the original one (one particle and small softening). This encourages us to be confident about the physical (as opposed to the numerical) origin of our results.

A-2 Numerical Experiments

We performed a number of simulations of collapsing halos with and without a growing central baryonic mass. The density configuration of the initial conditions was triaxial with axes $a > b > c$. In these simulations we selected the same sample of 300 particles to analyze. For these particles we recorded their positions and velocities for more than 55.000 time-steps throughout the total evolution time (14 Gyrs). The recording time-step of the orbits was set equal to the smallest time-step achieved by each particle during the force integration. Those *tracked* particles uniformly cover the energy distribution of all the particles at $T = 0$ and their distance from the center ranges from 4 to 150 kpc. We also tracked the orbits of all the growing particles although we did not use them for the orbits modification analysis.

We investigated carefully both the behaviours of individual orbits, and the way these behaviours affect the morphological nature of the central regions of our systems. The evolutions of the axes ratios of both dissipational and dissipationless regimes were determined by employing an analysis of their inertial tensors.

The general phenomenology seen already in previous works (K04), emerged in our simulations too; in the absence of a central baryonic mass, the original triaxiality insists throughout the evolution of the system. On the other hand, when the central dissipational component is present, there is a rapid increase of the values of the axes ratios b/a and c/a which is more evident at the central parts of the system, and intensifies as time evolves (Fig. A-1). This increase is manifested as a visual "rounding" of the contours of the density configuration (Fig. A-2).

Several investigators (Norman et al., 1985 [270], Gerhard and Binney 1985 [253], Barnes and Hernquist 1996 [248],Merritt and Quinlan 1998 [265], Valluri, and Merrit 1998 [274]) have provided a dynamical explanation for a similar behaviour occurring in the context of galactic systems with central black holes. They have shown that black holes alter the potential at the center of the system to a rounder one, and they modify several of the box orbits and tube orbits with low angular momentum (these orbits naturally visit the center of the system and serve as important building blocks for the triaxial backbone of ellipticals.) Also, the phase space at the center should follow the potential and become rounder too. Since a significant number of orbits behave chaotically they will attempt to cover all the phase space energetically available to them. Therefore one expects the motion of orbits to build density configurations with rounder shapes.

A comment about timescales of chaotic diffusion may be useful here. In general, chaotic orbits attempt to access all the phase space energetically available to them. However, the timescale necessary to achieve that, relates closely to the dynamical structure of the phase space. When parts of the phase space are occupied by regular orbits, chaotic orbits located very close to them try to behave like regular too, and remain constrained in restricted regions of the phase space for a long time, often longer than the age of the system (Contopoulos 2002 [250], Efthymiopoulos et al. 1997 [254], Sideris 2006 [272]); these orbits are usually called "sticky" or "weakly chaotic". Sticky orbits may need a significantly long time to escape into a wider chaotic sea and thus become "wildly chaotic". Only

then they can occupy a much broader phase space area. On top of that, in a three-dimensional phase space although different chaotic areas are interconnected, it is the location and extent of the regular regions which determines how fast the diffusion of chaotic orbits occurs, and whether different parts of a chaotic sea can work as "bottlenecks" of the evolution.

Another issue is the influence of the time-dependence. In the experiments we performed there was the significant time-dependence associated with the growth of the central mass. In time-dependent regimes every energy at every time is associated with its own phase space structure. Orbits do not conserve energy, they move from energy level to energy level, thus they visit a plethora of different phase spaces; this means that their nature can actually alternate from regular to chaotic and viceversa (Kandrup et al. 2003 [258]).

We investigated the chaoticity of a sample of 300 orbits randomly chosen from the orbits located at the central part of our density configuration. The maximum initial radius of the sample was about 150 kpc. The first question we asked was: how does the chaoticity of the dissipational system compare to the chaoticity of the dissipationless one?

Regular orbits are associated with a limited number of frequencies of motion (these being the main frequency per degree of freedom and its harmonics). Theoretically these frequencies should be singular, e.g. delta-functions. On the other hand, chaotic orbits are associated with many frequencies; their spectra are broad and theoretically continuous (Lichtenberg & Lieberman 1992 [260]).

Numerically one does not have the luxury to integrate orbits for infinite or even sufficiently long time. This causes some unavoidable numerical artifacts; frequencies of regular orbits, although very localized, appear to have small but measurable tails in the power spectrum. Frequencies of chaotic orbits are numerous but discrete. Despite these difficulties, one can usually distinguish easily between regular and chaotic orbits, provided that the orbit has been integrated for an adequate number of orbital periods. As the number of available orbital periods decreases, our confidence regarding the characterization of the orbit decreases accordingly. A method of computing localized frequencies in localized time would be invaluable, especially for limited-time evolutions, but such method has not been clearly formulated yet.

In this spirit, we quantified chaos using a straightforward numerical technique associated with Fourier analysis (Press et al. 1993 [271]; Kandrup et al. 1997 [257]). For every orbit we computed its three Fourier spectra, one per degree of freedom. Then (after we sorted the frequencies in descending order of their power) we simply counted how many of the emerging frequencies consist the 90% of the power spectrum (starting with the strongest frequency and moving down to weaker ones). (Similar experiments with 80% and 95% gave similar results qualitatively). Finally we added the numbers of all three dimensions:

$$n_{0.90} = n_{x0.90} + n_{y0.90} + n_{z0.90} \tag{A-1}$$

The results of this analysis suggest that, when there is dissipation, chaos increases significantly at least close to the center of the system (Fig. A-3). The characterization results for orbits moving close to the center are reliable since the number of orbital periods is about 30-50. As one moves away from the center, the number of orbital periods decreases and the reliability of the characterization unavoidably deteriorates. Still the trend close to the center is obvious; the dissipational component makes the system more chaotic.

Naturally, one may ask; what does really cause this increase of orbital chaoticity? And is this increase associated closely to the rounding of the shape of the halo at the central parts of the configuration? To answer these questions a number of elements have to be examined. Firstly, one can look at the Poincaré section of the orbits. Such a section, recorded when the orbits cross the $v_x = 0$ plane, reveals that when the dissipational component is present, velocities increase close to the center (Fig. A-4). This is not a surprise and is clearly associated with close encounters of the

orbits with the central baryonic mass; the particles approach close to the baryonic mass and get deflected.

It is reasonable to assume that the close encounters with the central mass, and the time-dependence caused by the growth of the central mass can combine to cause a shift to the frequencies of motion of individual orbits with subsequent randomization of the direction of the orbital evolution. This way any regularity or sense of shape disappear, the orbit attempts to occupy phase space in many different directions, thus becoming highly chaotic. This process should be manifested as a broadening of the power spectra of orbits (since new frequencies appear fast). A look at the three frequency spectra of same orbit moving in the two different configurations (with or without a growing central baryonic element) makes obvious that the spectrum is much broader in the second case (Fig. A-5). The existence of the broader spectra obviously correlates to the increase of chaoticity observed in Fig A-3.

Although we have important hints about the dynamical process followed, one needs a careful quantification of if and how the direction of the emerging orbital components is really randomized. This effect can be visualized clearly for an orbit passing very close to the center. One may ask how the distribution of the angles $\theta = tan^{-1}(x/y)$ changes between the dissipational and dissipationless regime. In a triaxial dissipationless regime such a distribution should have some preferences, because there are no intense phenomena like strong deflections. On the other hand a randomization of the orbit should be associated or approach a distribution closer to normal, since all possible angles must have equal probability to be visited. Indeed by overplotting the θ distributions for the same orbit in both regimes it is obvious that what was expected actually happens Fig A-6.

This randomization will not happen for every orbit in the system, but a significant percent of orbits in our sample followed the aforementioned process. By visual inspection of a number of orbits one can easily identify a significant percentage which try to mimic and are restrained in the box-orbits fashion. The close encounters with the central dissipational components will make these orbits rounder. It has to be emphasized that although box-like orbits with bigger amplitudes can in principle experience similar dynamics, one has to remember that as the amplitude increases the randomization effect decreases simply because the number of orbital periods is smaller. This means that the opportunities for close encounters with the central gas are decreased. This seems to explain why the effect of rounding is limited only in the central parts. A second reason should be that the effect the central mass has on the rounding of the phase space weakens in bigger distances from the center. Box-like weakly chaotic orbits with big amplitude do not have enough time to "break" and explore many new directions during their evolution. In an imaginary system which evolves for far longer times we would probably observe a rounding of the density in bigger radii too. It is the evolution time of the system that puts a limit in the maximum radius it gets rounder because of deflections by a central growing baryonic mass.

Figure A-1 also shows that the shape modification is not constant with respect to time. It is faster in the first 5 Gyrs for both the axis ratios: b/a and c/a. This is related by the total fraction of box-like orbits within the central region of the halo. The 3-dimensional distribution of the mass is intimately connected to its orbital content. Jesseit et al. (2005) [255] showed correlations between orbital fractions and the shape parameters as determined by the axis ratios of the inertial tensor. To give a rough estimate on the box orbit fraction in our initial halo, we selected the merger remnant from the original sample of Naab & Burkert (2003) [267] which resembles the analysed DM halo the most. Hence we conclude that the DM Halo has a box orbit fraction of at least 0.67 for the inner 10% , 0.49 for the inner 20 %, 0.39 for the inner 30% , 0.33 for the inner 40% , 0.27 for the inner 50% and 0.23 at 60% of all particles. The fast change in the shape in the first Gyrs is related to the high number of box-like orbits (i.e. highly modificable orbits) within the central region of the halo.

Some additional experiments were necessary in order to corroborate the understanding of the physics. First we performed the same simulation using a much bigger softening parameter $\epsilon = 2.4$. This simulation was necessary in order to show that the effects we observed where not caused by the numerics of the experiment. Comparison of the evolution of the axes ratios show clearly that the larger epsilon does not alter the results (Fig. A-7). Moreover, the chaoticities of the orbits in this

regime do not differ significantly from the ones evolving in a central growing mass regime (Fig. A-9). This is a strong indication that the observed effects are not numerical artifacts.

The second experiment was a more realistic version of the first one. Specifically, we replaced the central baryonic mass with a set of 500 smaller baryonic masses. The total mass and the rate of mass growth were kept the same. The 500 baryonic masses were localized at the center. By comparing the effects of the two dissipational simulations one can establish that the crucial aspects of dynamics are similar in both cases. Indeed, the evolution of the axes ratios are similar although they start differing as we approach very close to the center (Fig A-8). This is reasonable since the deflections are not very strong anymore, therefore the effect needs more time to become evident. An analysis of the chaos of the system suggests that the chaoticity of the 300 orbits we analyzed are in relatively lower level than when we had one central mass but still higher than the dissipationless case (Fig A-9).

It is very instructive to see how the same orbit changes in the four different cases, (a) dissipationless system, (b) dissipational system, one central mass, (c) dissipational system one central mass $\epsilon = 2.4$, (d)dissipational system 500 central masses. Fig. A-10 provides the three projections $x-y$, $y-z$, and $x-z$, of the same orbit for all the above cases. We chose this specific orbit because the difference between the dissipationless and dissipational cases are dramatic and thus make the phenomenon clearer. The effect we described is particularly obvious in the $y-z$ projection. In the dissipationless case the orbit has a strong radial component and passes very close to the center. When there is dissipation the central mass makes the potential rounder in the central areas where its influence is strong and it also deflects the orbit to several different directions. When $\epsilon = 2.4$ the orbit also becomes thicker. For the case with 500 at the center the rounding effect is also present.

A-3 Discussion and Conclusions

This investigation suggests that the dissipational component is responsible for repeatedly deflecting orbits which visit often the center of the system. Also the time-dependence associated with the growth of the central mass, (probably in combination with general nonlinearities of the triaxial configuration evolution), seem to shift the frequencies of the orbits, making them extremely chaotic. These effects randomize the directions achieved during the evolution of the orbit. This randomization makes orbits explore many more angles, and therefore they occupy rounder shapes. When this effect takes place for a significant number of orbits it will be manifested in the density distribution as an approach to a rounder configuration.

This approach can easily serve as an explanation of why the rounding is limited only at the central parts of the configuration. Orbits with extensive amplitude cannot visit the center many times during the life-time of the system, thus they cannot be deflected repeatedly. This way their directions cannot be fully randomized in the sense this happens for orbits with smaller amplitude and they never get the opportunity to explore a much rounder space. Moreover, the influence of the central mass on the shape of the phase space decreases with increasing distance from the center. Since the shape of the orbits with bigger amplitude is not significantly altered by the existence of the central mass, there is no reason to expect any morphological alteration on the distribution in larger radii.

It has to be noticed that this interpretation does not disagree with previous ones. It simply incorporates into the picture the role of extra influences into the evolutionary history of orbits by repeated central deflections, as well as the time-dependence of the central baryonic mass. Two main questions are to be explained in future work in more controlled experiments: (a) What is the influence of each one of the two components? What is the exact role of the time-dependence of the central mass, and how does it combine with (or affected by) the nonlinearities of the self-consistent evolution in a triaxial regime? (b) Is there a general pattern in the way the frequencies of motion emerge for individual orbits? If yes how does this connect with the average location of the orbit as well as the rate of growth of the central mass? The answers to these questions can probably decipher

the fundamental dynamics of this phenomenon and provide important clues for the treatment of the problem using analytics.

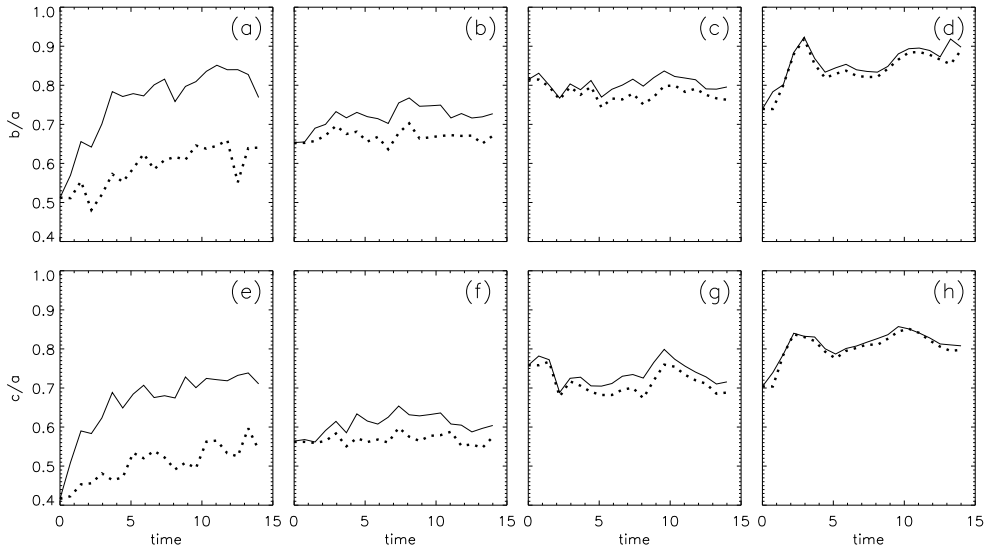

Figure A-1. Top row panels: evolution of the axes ratio b/a of two systems, one without central baryonic mass (dotted line) and one with central baryonic mass (solid line) for different distances r from the center. (a) $r = 14.9kpc$, (b) $r = 163.4kpc$, (c) $r = 311.9kpc$, (d) $r = 460.4kpc$. Bottom row panels: same as top row panels but for axes ratio c/a. (e) $r = 14.9kpc$, (f) $r = 163.4kpc$, (g) $r = 311.9kpc$, (h) $r = 460.4kpc$.

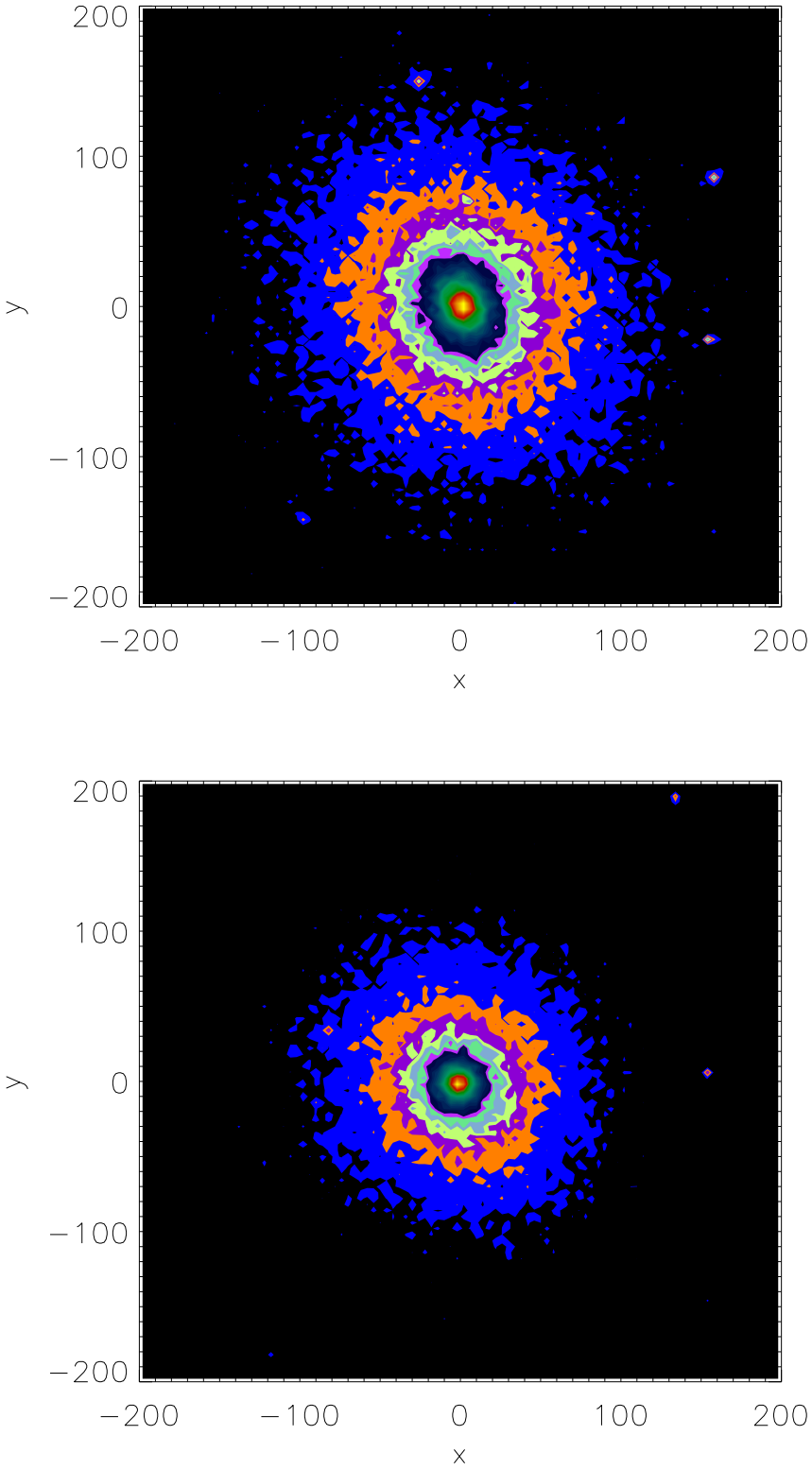

Figure A-2. Density contours for the central parts of a dissipationless (top) and dissipational (bottom) halo at the end of the evolution (14Gy). There is an obvious rounding of the bottom configuration.

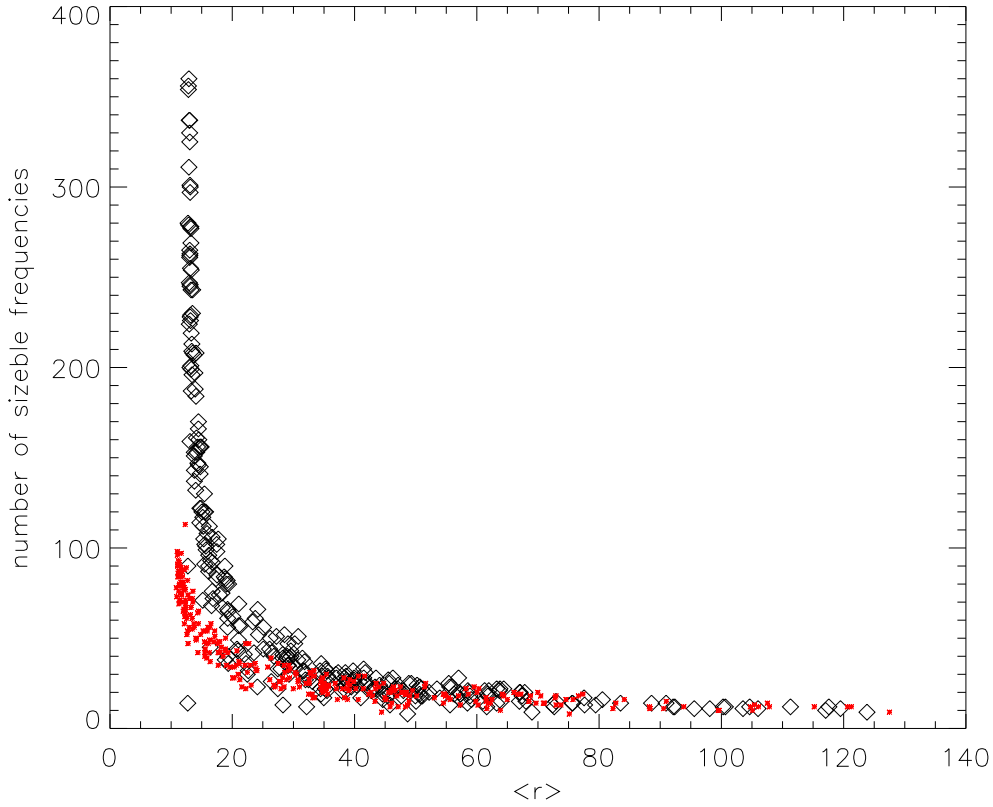

Figure A-3. Complexities (number of important frequencies of motion) for 300 orbits versus mean radial distance from the center. Red asterisks represent the dissipationless points while black diamonds the dissipational ones.

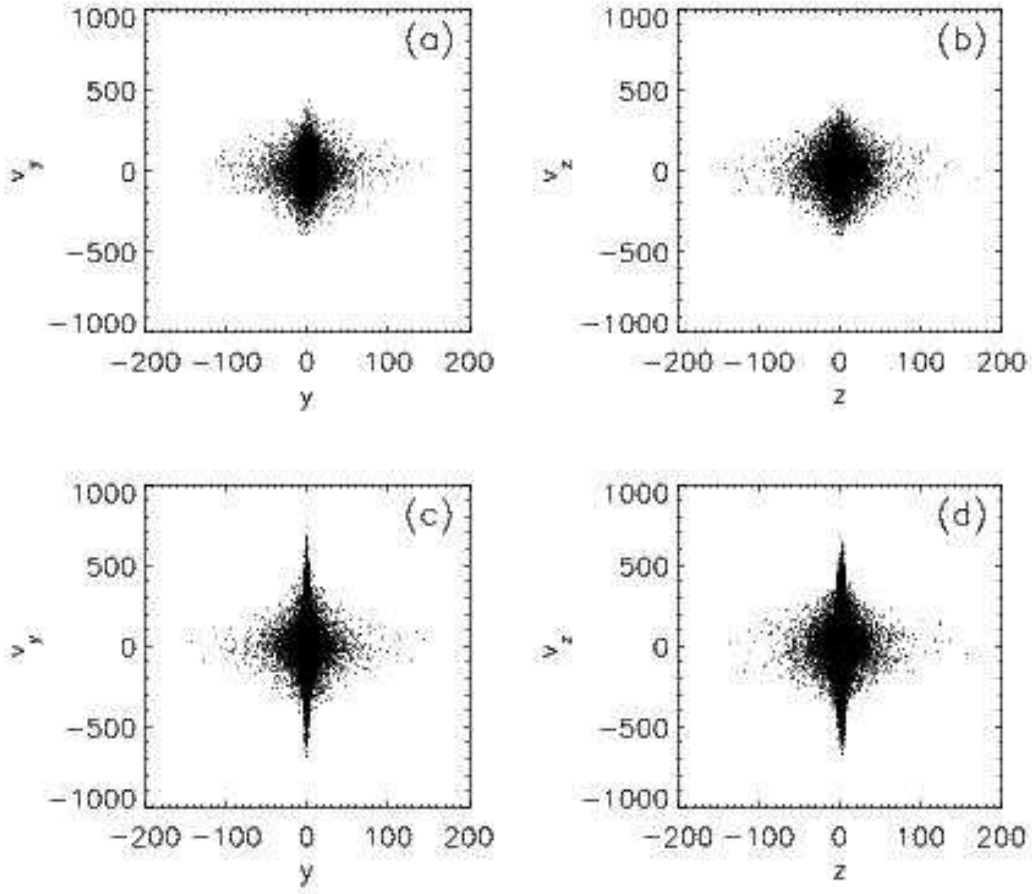

Figure A-4. (a) and (b) Poincaré sections of the dissipational points recorded at $v_x = 0$. (c) and (d) same for the simulation with a growing central baryonic mass.

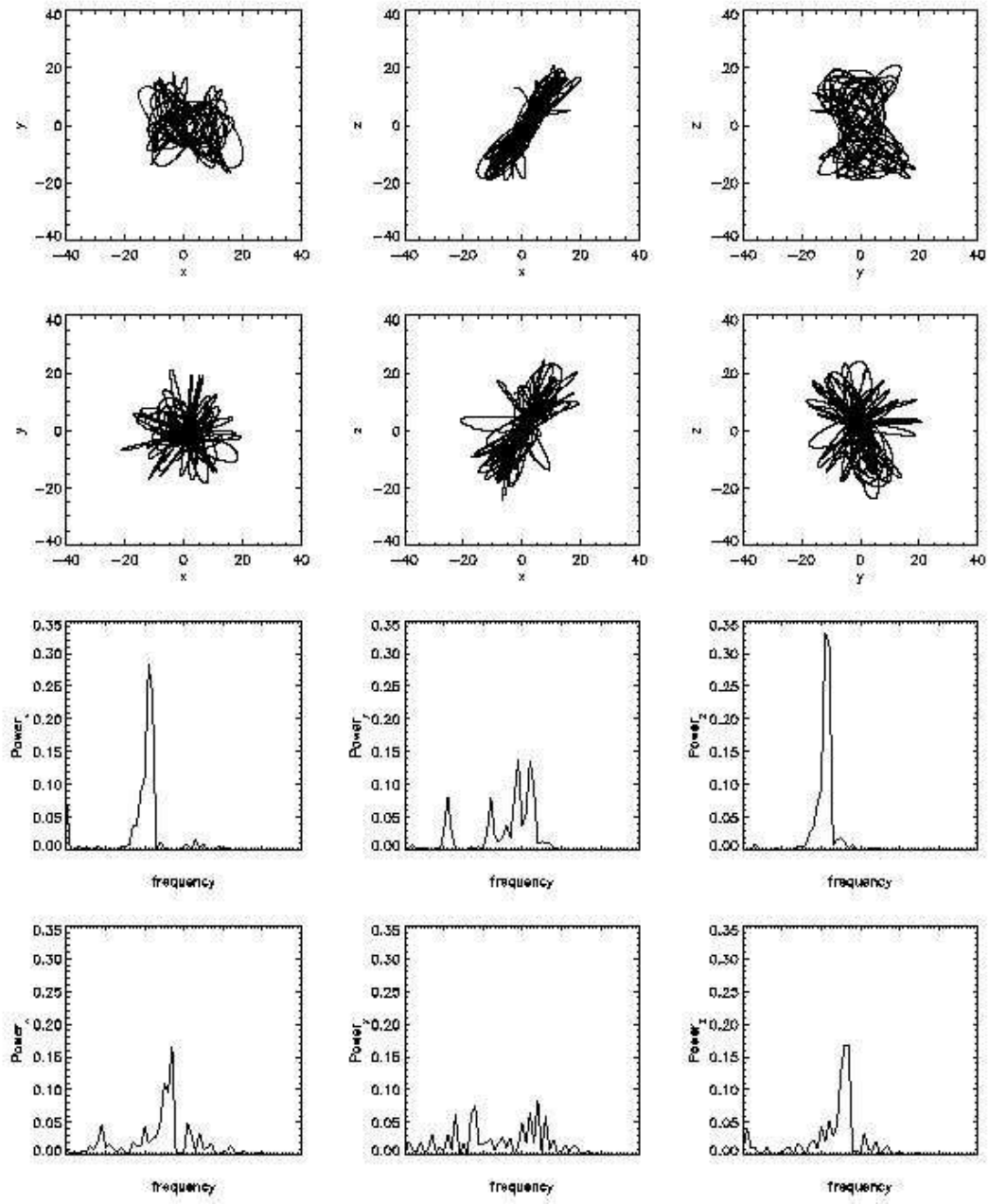

Figure A-5. First row panels: x-y, x-z, and y-z projections of an orbit evolving in a halo without a central baryonic mass. Second row panels: x-y, x-z, and y-z projections of the same orbit evolving in a halo with a central baryonic mass. Third row panels: Fourier spectra of the first (without central mass) orbit. Fourth row panels: Fourier spectra of the second (with central mass) orbit. The Fourier spectra in the three dimensions are broader in the second case.

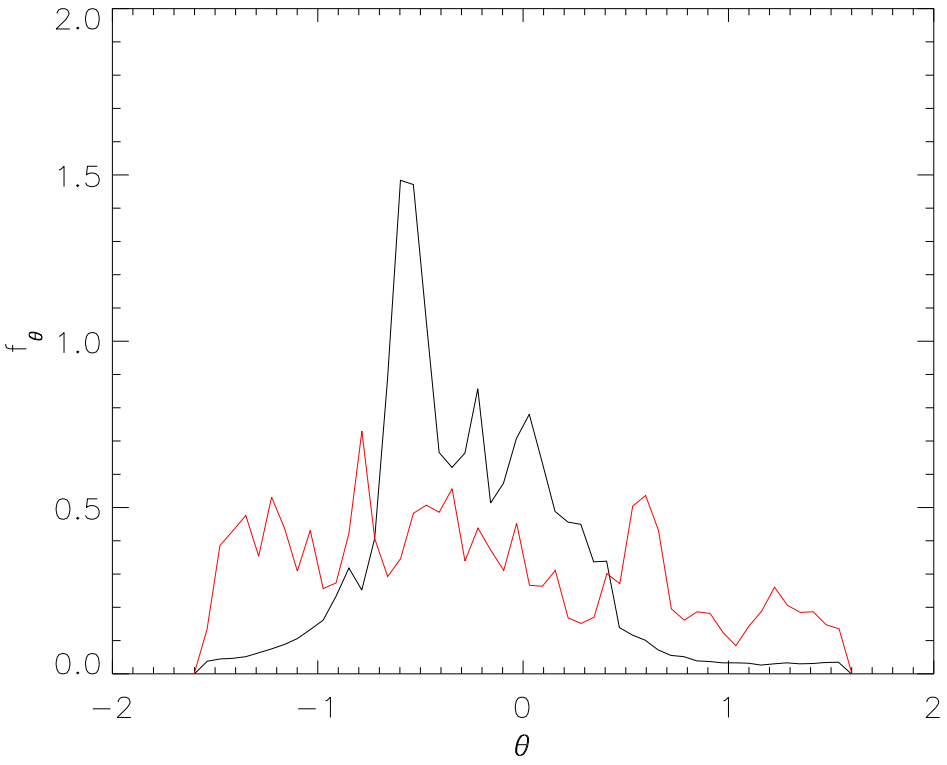

Figure A-6. Distribution of angles $\theta = tan^{-1}(x/y)$ explored for the dissipationless orbit (black) and the dissipational one (red).

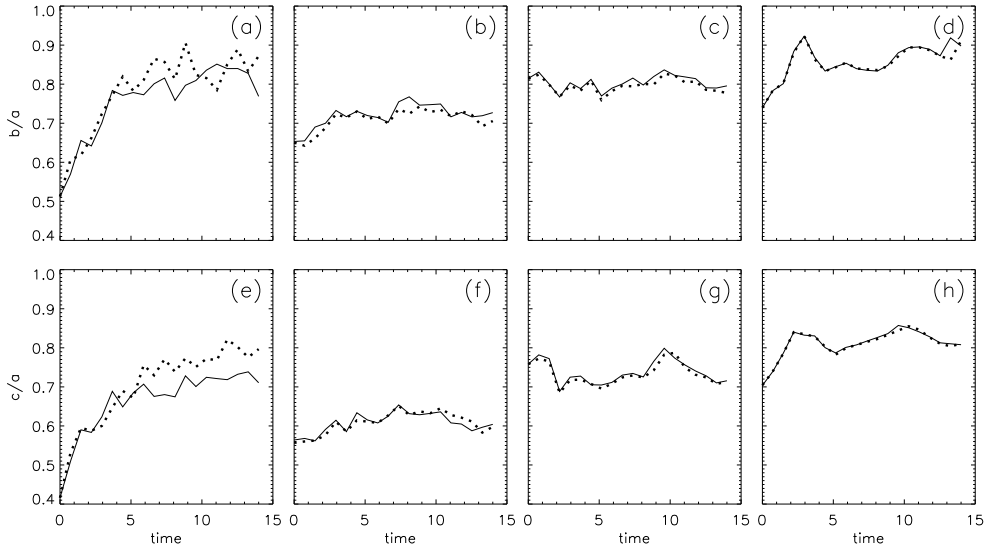

Figure A-7. Top panels: evolution of the axes ratio b/a of two dissipational systems, one with $\epsilon = 2.4$ (dotted line) and one with $\epsilon = 0.6$ (solid line) for different distances from the center. (a) $r = 14.9kpc$, (b) $r = 163.4kpc$, (c) $r = 311.9kpc$, (d) $r = 460.4kpc$. Bottom panels: same as top but for axes ratio c/a. (e) $r = 14.9kpc$, (f) $r = 163.4kpc$, (g) $r = 311.9kpc$, (h) $r = 460.4kpc$.

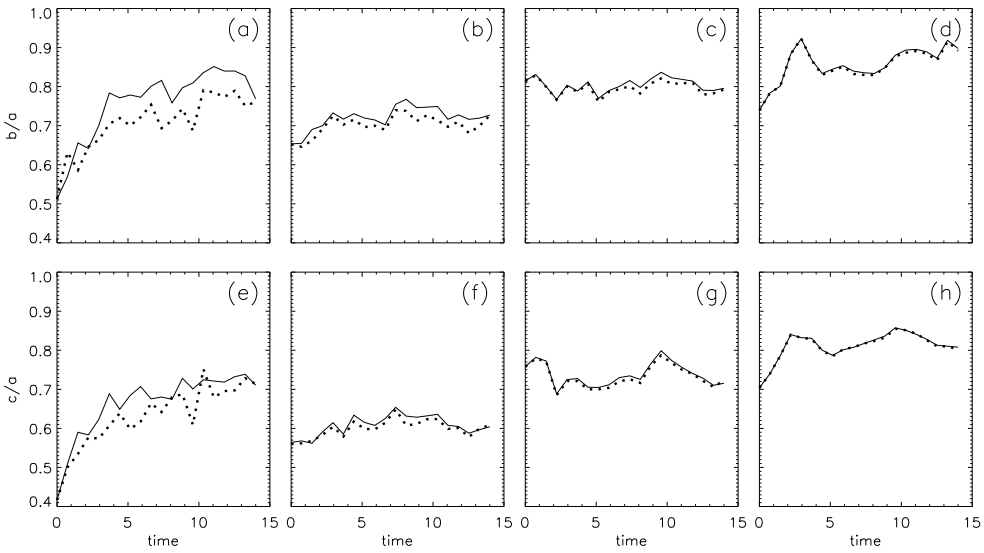

Figure A-8. Top panels: evolution of the axes ratio b/a of two dissipational systems, one with 500 central masses (dotted line) and one with one central mass (solid line) for different distances from the center. (a) $r = 14.9kpc$, (b) $r = 163.4kpc$, (c) $r = 311.9kpc$, (d) $r = 460.4kpc$. Bottom panels: same as top but for axes ratio c/a. (e) $r = 14.9kpc$, (f) $r = 163.4kpc$, (g) $r = 311.9kpc$, (h) $r = 460.4kpc$.

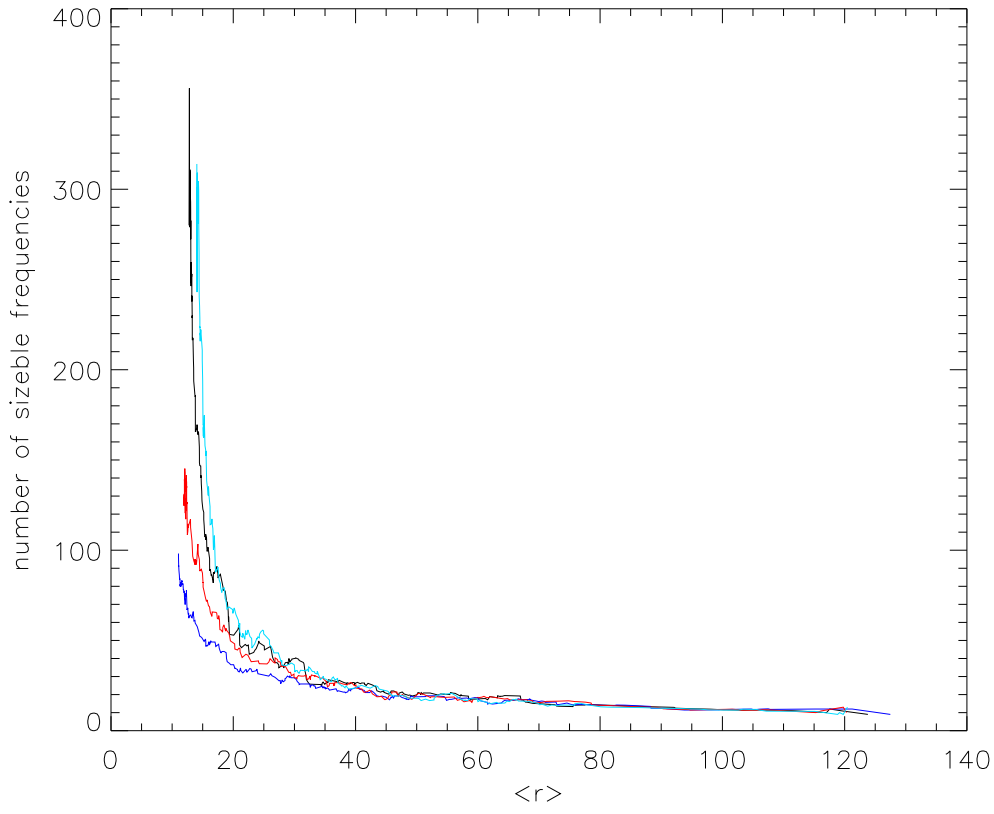

Figure A-9. Boxcar averaged complexities (number of important frequencies of motion) computed for 300 orbits versus mean radial distance from the center. Dark line: dissipational system with only one baryonic mass at the center ($\epsilon = 0.6$). Red line: dissipational system with 500 baryonic masses at the center ($\epsilon = 0.6$). Blue line: dissipationless system ($\epsilon = 0.6$). Cyan line: dissipational system with $\epsilon = 2.4$.

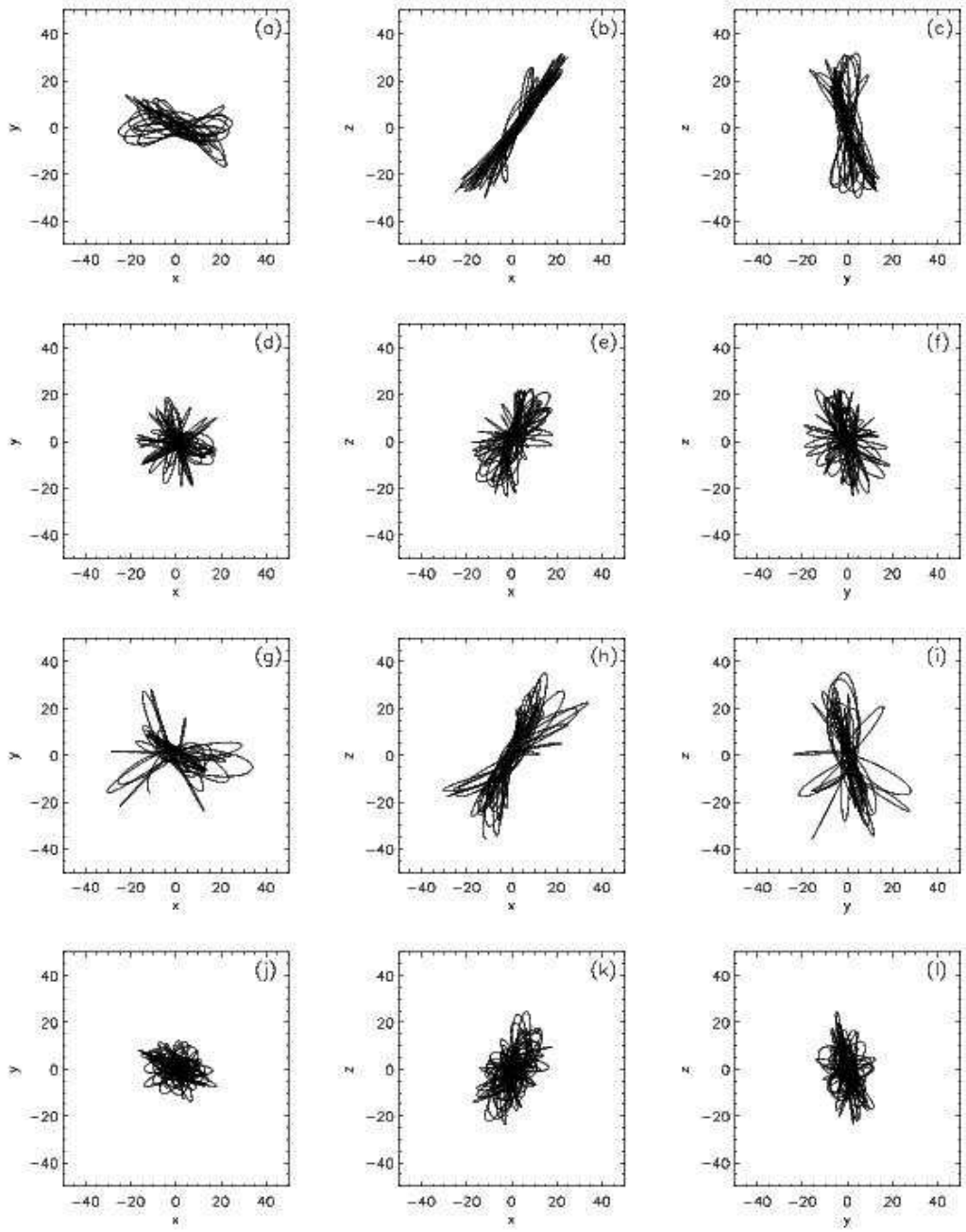

Figure A-10. Projections of the same orbit for 4 cases: (a)-(c)dissipationless system ($\epsilon = 0.6$). (d)-(f)dissipational system with one central baryonic mass ($\epsilon = 0.6$). (g)-(i)dissipational system with one central baryonic mass and softening $\epsilon = 2.4$, (j)-(l)dissipational system with 500 central baryonic masses ($\epsilon = 0.6$).

References

[1] S. Perlmutter et al. (1999), Astrophys. J. **517** 565
[2] V. Trimble (1987), Annu. Rev. Astron. Astrophys. **25** 425
[3] F. Zwicky (1933), Helv. Phys. Acta **6** 110
[4] P. Schneider, J. Ehlers and E. E. Falco (1992), *Gravitational Lensing*. (Springer Verlag, Berlin 1992)
[5] S. Refsdal and J. Surdej (1994), *Gravitational lenses*. Rep. Prog. Phys. **56** 117
[6] R. Narayan and M. Bartelmann (1996), *Lectures on Gravitational Lensing*. astro-ph 9606001
[7] N. Straumann, Ph. Jetzer and J. Kaplan (1998), *Topics on Gravitational Lensing*. Napoli Series on Physics and Astrophysics (Bibliopolis, Naples)
[8] F. W. Dyson, A. S. Eddington and C. R. Davidson (1920), Mem. Royal Astronomical Society **62** 291
[9] A. Einstein (1936), Science **84** 506
[10] J. Renn, T. Sauer and J. Stachel (1997), Science **275** 184
[11] F. Zwicky (1937), Phys. Rev. **51** 290; (1937), Phys. Rev. **51** 679
[12] K. Chang and S. Refsdal (1979), Nature **282** 561
[13] R. J. Gott (1981), Astrophys. J. **243** 140
[14] B. Paczyński (1986), Astrophys. J. **301** 503
[15] R. Schmidt and J. Wambsganss (1998), Astron. and Astrophys. **335** 379
[16] J. Wambsganss (2000), astro-ph 0008419
[17] B. Paczyński (1986), Astrophys. J. **304** 1
[18] A. De Rújula, Ph. Jetzer and E. Massó (1991), Mont. Not. R. Astr. Soc. **250** 348
[19] A. De Rújula, Ph. Jetzer and E. Massó (1992), Astron. and Astrophys. **254** 99
[20] K. Griest (1991), Astrophys. J. **366** 412
[21] R. J. Nemiroff (1991), Astron. and Astrophys. **247** 73
[22] B. Paczyński (1996), Annu. Rev. Astron. Astrophys. **34** 419
[23] E. Roulet and S. Mollerach (1997), Phys. Rept. **279** 67
[24] A.F. Zakharov and M.V. Sazhin (1998), Physics Uspekhi **41** 945
[25] Ph. Jetzer (1999), Naturwissenschaften **86** 201
[26] B. Carr (1994), Annu. Rev. Astron. Astrophys. **32** 531
[27] J. Bahcall, C. Flynn, A. Gould and S. Kirhakos (1994), Astrophys. J. **435** L51
[28] E. J. Kerins (1997), Astron. and Astrophys. **322** 709
[29] G. Gilmore and M. Unavane (1998), Mont. Not. R. Astr. Soc. **301** 813
[30] C.M. Tamanaha, J. Silk, M.A. Wood and D.E. Winget (1990), Astrophys. J. **358** 164
[31] S.D. Kawaler (1996), Astrophys. J. **467** L61
[32] F. De Paolis, G. Ingrosso, Ph. Jetzer and M. Roncadelli (1995), Phys. Rev. Lett. **74** 14
[33] F. De Paolis, G. Ingrosso, Ph. Jetzer and M. Roncadelli (1995), Astron. and Astrophys. **295** 567
[34] F. De Paolis, G. Ingrosso, Ph. Jetzer and M. Roncadelli (1999), Astrophys. J. **510** L103
[35] B. Paczyński (1991), Astrophys. J. **371** L63
[36] K. Griest et al. (1991), Astrophys. J. **372** L79
[37] E. Aubourg et al. (1993), Nature **365** 623
[38] C. Alcock et al. (1993). Nature **365** 621; (1995), Astrophys. J. **445** 133
[39] C. Alcock et al. (2000), astro-ph 0001272
[40] C. Renault et al. (1997), Astron. and Astrophys. **324** L69
[41] C. Alcock et al. (1997), Astrophys. J. **491** L11
[42] N. Palanque-Delabrouille et al. (1999), Astron. and Astrophys. **332** 1
[43] C. Alcock et al. (1997), Astrophys. J. **479** 119
[44] A. Udalski et al. (1994), Acta Astron. **44** 165
[45] L. Grenacher, Ph. Jetzer, M. Strässle and F. De Paolis (1999), Astron. and Astrophys. **351** 775
[46] A.P. Crotts (1992), Astrophys. J. **399** L43
[47] P. Baillon, A. Bouquet, Y. Giraud-Héraud and J. Kaplan (1993), Astron. and Astrophys. **277** 1
[48] Ph. Jetzer (1994), Astron. and Astrophys. **286** 426

[49] R. Ansari et al. (1997), Astron. and Astrophys. **324** 843.
[50] R. Ansari et al. (1999), Astron. and Astrophys. **344** L49
[51] A.P.S. Crotts and A.B. Tomaney (1996), Astrophys. J. **473** L87,
[52] A. Crotts and R. Uglesich (2000), astro-ph 0006282
[53] S. Mao and B. Paczyński (1991), Astrophys. J. **374** L37
[54] A. Gould and A. Loeb (1992), Astrophys. J. **396** 104
[55] D. Bennett and S.H. Rhie (1996), Astrophys. J. **472** 660
[56] N. Straumann (1999), *Lectures on Gravitational Lensing*. Troisième Cycle de la Physique en Suisse Romande
[57] R.K. Sachs (1961), Proc. Roy. Soc. London **A264** 309
[58] C.C. Dyer and R.C. Roeder (1973), Astrophys. J. **180** L31
[59] S. Refsdal (1966), Mont. Not. R. Astr. Soc. **134** 315
[60] T. Kundić et al. (1997), Astrophys. J. **482** 648
[61] M. Bartelmann (1996), Astron. and Astrophys. **313** 697
[62] N. Kaiser and G. Squires (1993), Astrophys. J. **404** 441
[63] Y. Mellier (1999), Annu. Rev. Astron. Astrophys. **37** 127
[64] M. Bartelmann and P. Schneider (1999), *Weak Gravitational Lensing*. astro-ph 9912508
[65] N. Straumann (1997), Helv. Phys. Acta **70** 894
[66] G. Squires et al. (1997), Astrophys. J. **482** 648
[67] L. Van Waerbeke et al. (2000), astro-ph 0002500
[68] D.M. Wittman et al. (2000), astro-ph 0003014
[69] Mellier, Y. 1999, ARAA, 37, 127
[70] Benjamin, J., et al. 2007, ArXiv Astrophysics e-prints, arXiv:astro-ph/0703570
[71] Massey, R., et al. 2007, ArXiv Astrophysics e-prints, arXiv:astro-ph/0701480
[72] Sereno, M. 2007, MNRAS, 377, 229
[73] Adelman-McCarthy, J., Agueros, M. A., Allam, S. S., et al. 2006, ApJS, 162, 38
[74] Bartelmann, M., & Loeb, A. 1998, ApJ, 503 48
[75] Browne, I. W. A., Wilkinson, P. N., Jackson, N.J.F., et al. 2003, MNRAS, 341, 13
[76] Clénet, Y., et al. 2006, in Proc. SPIE Vol. 6272, Advances in Adaptive Optics II, ed. Brent L. Ellerbroek, & Domenico Bonaccini Calia, 62723T
[77] Falomo, R., Kotilainen, J. K., Scarpa, R. & Treves, A. 2005, A&A, 434, 469
[78] Huchra, J., Gorenstein M., Kent, S., et al. 1985, AJ, 90, 691
[79] Iovino, A., Clowes, R. & Shaver, P. 1996, A&AS, 119, 265
[80] Jackson, N., de Bruyn, A. G., Myers, S., et al. 1995, MNRAS, 274, L25
[81] Kassiola, A., & Kovner, I. 1993, ApJ, 417, 450
Keeton, C. R. 2001, ApJ submitted, astro-ph/0102340
[82] Keeton, C. R., & Kochanek, C. S. 1998, ApJ, 495, 157
[83] Keeton, C. R., Kuhlen, M. & Haiman, Z. 2005, ApJ, 621, 559
[84] Kochanek, C. S., Schneider, P. & Wambsganss, J. 2004, Part 2 of Gravitational Lensing: Strong, Weak & Micro, Proceedings of the 33rd Saas-Fee Advanced Course, ed. G. Meylan, P. Jetzer & P. North (Springer-Verlag: Berlin)
[85] Kormann, R., Schneider, P. & Bartelmann, M. 1994, A&A, 284, 285
[86] Le Brun, V., Smette, A., Surdej, J. & Claeskens, J.-F. 2000, A&A, 363, L837
[87] Myers, S. T., Jackson, N. J., Browne, I. W. A., et al. 2003, MNRAS, 341, 1
[88] Narayan, R., & Schneider, P. 1990, MNRAS, 243, 192
[89] Patnaik, A. R., Browne, I. W. A., King, L. J., et al. 1993, MNRAS, 261, 435
[90] Peng, C. Y., Ho, L. C., Impey, C. D. & Rix, H.-W. 2002, AJ, 124, 266
[91] Perna, R., Loeb, A., & Bartelmann, M. 1997, ApJ, 488, 550
[92] Pierini, D., & Tuffs, R. J. 1999, A&A, 343, 751
[93] Pramesh Rao, A., & Subrahmanyan, R. 1988, MNRAS, 231, 229
[94] Richards, G. T., Croom, S. M., Anderson, S. F., et al. 2005, MNRAS, 360, 839
[95] Saha, P., & Williams, L. L. R. 2003, AJ, 125, 2769
[96] Schramm, T. 1990, A&A, 231, 19
[97] Véron-Cetty, M. P., & Véron, P. 2001, A&A, 374, 92
[98] Winn, J. N., Hall, P. B., & Schechter, P. L. 2003, ApJ, 597, 672
[99] White, R. L., Becker, R. H., Helfand, D. J., et al. 1997, ApJ, 475, 479
[100] York, D. G., Adelman, J., Anderson, J. E., et al. 2000, AJ, 120, 1579
[101] Chieregato, M., Miranda, M., & Jetzer, P. 2007, ArXiv e-prints, 707, arXiv:0707.2675
[102] Amara, A., Metcalf, R.B., Cox, T.J., & Ostriker, J.P. 2006, MNRAS, 367, 1367
[103] Barkana R., 1997, ApJ, 489, 21
[104] Bekki, K., & Chiba, M. 2005, ApJL, 625, L107
[105] Biggs A.D. et al., 2004, MNRAS, 350, 949

[106] Bradač M. et al., 2002, A&A, 388, 373
[107] Bullock, J. S., Kravtsov, A. V., & Weinberg, D. H. 2000, ApJ, 539, 517
[108] Chang K., Refsdal S., 1979, Nature, 282, 561
[109] Chiba M., 2002, ApJ, 565, 71
[110] Chiba, M., Minezaki, T., Kashikawa, N., Kataza, H., Inoue, K.T., 2005, ApJ, 627, 53
[111] Chen J., Kravtsov A.V., Keeton C.R., 2003, ApJ, 592, 24
[112] Congdon, A. B., & V Keeton, C. R. 2005, MNRAS, 364, 1459
[113] Courbin F. et al., 1997, A&A, 324, 1
[114] Dalal N., Kochanek C.S, 2002, ApJ, 572, 25
[115] Diemand J., Moore B., Stadel J., 2004, MNRAS, 352, 535
[116] Dobler G, Keeton, C.R., 2006, MNRAS, 365, 1243
[117] Evans, N. W., & Witt, V H. J. 2003, MNRAS, 345, 1351
[118] Hege E. K., Hubbard E. N., Strittmatter P. A., Worden S. P., 1981, ApJ, 248, 1
[119] Impey C.D. et al., 1998, ApJ, 509, 551
[120] Inoue K.T., Chiba M., 2005, ApJ, 634, 77
[121] Kayser, R., Surdej, J., Condon, J. J., Kellermann, K. I., Magain, P., Remy, M., & Smette, A. 1990, ApJ, 364, 15
[122] Keeton C.R., 2001, astro-ph/0102340
[123] Keeton C. R., Kochanek C. S., 1997, ApJ, 487, 42
[124] Keeton C.R., 2003, ApJ, 584, 664
[125] Keeton C.R., Scott Gaudi B., Petters A.O., 2005 ApJ, 635, 35
[126] Klypin A., Kravtsov A.V., Valenzuela O., Prada F., 1999, ApJ, 522, 82
[127] Kochanek C.S., 2006, Saas-Fee Advanced Course 33: Gravitational Lensing: Strong, Weak and Micro, 91, astro-ph/0407232
[128] Macciò, A. V., Moore, B., Stadel, J., & Diemand, J. 2006, MNRAS, 366, 1529
[129] Macciò A.V., Miranda M., 2006, MNRAS, 368, 599
[130] Mao S., Schneider P., 1998, MNRAS, 295, 587
[131] Marlow D.R. et al., 1999, AJ, 118, 654
[132] Metcalf R.B., Madau P., 2001, ApJ, 563, 9
[133] Metcalf R.B., Zhao H., 2002, ApJ, 567, L5
[134] Metcalf, R. B., Moustakas, L. A., Bunker, A. J., & Parry, I. R. 2004, ApJ, 607, 43
[135] Metcalf R.B., 2005a, ApJ, 622, 72
[136] Minezaki T. et al., 2004, ApJ, 600, L35
[137] Moore B., Quinn T., Governato F., Stadel J., Lake G. 1999, MNRAS, 310, 1147
[138] Mortonson, M. J., Schechter, P. L., & Wambsganss, J. 2005, ApJ, 628, 594
[139] Narayan R., Schneider P. 1990, MNRAS, 243, 192
[140] Ostriker, J. & Steinhardt, P. J. 1995, arXiv:astro-ph/9505066v1
[141] Phillips P.M. et al., 2000, MNRAS, 319, L7
[142] Pooley, D., Blackburne, J.A., Rappaport, S., Schechter, P.L., & Fong, W.-f. 2006, ApJ, 648, 67
[143] Rauch, K. P., & Blandford, R. D. 1991, ApJ, 381, L39
[144] Schechter P.L. et al., 1997, ApJ, 475, 85
[145] Schneider P., Ehlers J., Falco, E.E., 1992, Gravitational Lenses (Springer-Verlag) (SEF)
[146] Spergel, D. N., et al. 2003, ApJ, 148, 175
[147] Spergel, D. N., et al. 2006, arXiv:astro-ph/0603449
[148] Wambsganss, J., Schneider, P., & Paczyński, B. 1990, ApJ, 358, L33
[149] Wambsganss J., Paczyński B., 1994, AJ, 108, 1156
[150] Weymann R.J. et al., 1980, Nature, 285, 641
[151] Williams K. A., Momcheva I., Keeton, C.R., Zabludoff A.I., Lehar J., 2005, astro-ph/0511594
[152] Witt Hans J., Mao Shude, 1997, MNRAS, 291, 211
[153] Wyithe, J. S. B., Webster, R. L., Turner, E. L., & Mortlock, D. J. 2000, MNRAS, 315, 62
[154] Young P. et al., 1981 ApJ, 244, 723
[155] Yoo J. et al., 2005, ApJ, 626, 51
[156] Mao S., 1992, ApJ, 389, 63
[157] Mao S., Jing Y., Ostriker J. P., Weller J., 2004, ApJ, 604, L5
[158] Zentner A. R., Bullock J. S., 2003, ApJ, 598, 49
[159] Spergel D. N., Steinhardt P. J., 2000, PhRvL, 84, 3760
[160] Kochanek C.S., Dalal N., 2004, ApJ, 610, 69
[161] Bradač M. et al., 2004, A&A, 423, 797
[162] Treu, T., & Koopmans, L. V. E. 2004, ApJ, 611, 739
[163] Gerhard O., Kronawitter A., Saglia R. P., Bender R., 2001, AJ, 121, 1936
[164] Kochanek C. S., 1995, ApJ, 453, 545
[165] Maoz D., Rix H., 1993, ApJ, 416, 425

[166] Gao L., De Lucia G., White S. D. M., Jenkins A., 2004, MNRAS, 352, L1
[167] Reed D., Governato F., Quinn T., Gardner J., Stadel J., Lake G., 2005, MNRAS, 359, 1537
[168] Grogin, N. A., & Narayan, R. 1996, ApJ, 473, 570
[169] Keeton, C. R., Christlein, D., & Zabludoff, A. I. 2000, ApJ, 545, 129
[170] Oguri M., 2005, MNRAS, 361, L38
[171] Rozo, E., Zentner, A. R., Bertone, G., & Chen, J. 2006, ApJ, 639, 573
[172] Miranda M., Jetzer P. 2007 submitted
[173] Miranda M., Macció 2007, astro/ph 0706.0896
[174] Abazajian K., 2006, PhRvD, 73, 063506
[175] Asaka T., Blanchet S., Shaposhnikov M., 2005, Phys.Lett. B631, 151
[176] Asaka T., Shaposhnikov M., Laine M., 2007, JHEP, 1, 91
[177] Avila-Reese, V., Colín, P., Valenzuela, O., D'Onghia, E., & Firmani, C. 2001, ApJ, 559, 516
[178] Barkana R., Haiman Z., Ostriker J. P., 2001, ApJ, 558, 482
[179] Blandford, R., & Narayan, R. 1986, ApJ, 310, 568
[180] Bode, P., Ostriker, J. P., & Turok, N. 2001, ApJ, 556, 93
[181] Dodelson S., Widrow L. M., 1994, PhRvL, 72, 17
[182] Dolgov A. D., Hansen S. H., 2002, APh, 16, 339
[183] Hansen, S. H., Lesgourgues, J., Pastor, S., & Silk, J. 2002, MNRAS, 333, 544
[184] Colín, P., Avila-Reese, V., & Valenzuela, O. 2000, ApJ, 542, 622
[185] Stoehr, F., White, S. D. M., Tormen, G., & Springel, V. 2002, MNRAS, 335, L84
[186] Hayashi, E., Navarro, J. F., Taylor, J. E., Stadel, J., & Quinn, T. 2003, ApJ, 584, 541
[187] Hogg D., 1999 astro-ph/9905116
[188] Jackson, N., Nair, S., Browne, I. W. A., Wilkinson, P. N., Muxlow, T. W. B., de Bruyn, A. G., Koopmans, L., Bremer, M., et al., 1998, MNRAS, 296, 483
[189] Keeton C. R., Kochanek C. S., Falco E. E., 1998, ApJ, 509, 561
[190] Keeton C.R., Scott Gaudi B., Petters A.O., 2005 ApJ, 598, 138
[191] Koopmans, L. V. E., Biggs, A., Blandford, R. D., Browne, I. W. A., Jackson, N. J., Mao, S., Wilkinson, P. N., de Bruyn, A. G., et al., 2003, ApJ, 595, 712
[192] Kormann R., Schneider P., Bartelmann M., 1994, A&A, 284, 285
[193] Moore, B. 1994, Nature, 370, 629
[194] Metcalf, R. B. 2005b, ApJ, 629, 673
[195] Navarro J. F., Frenk C. S., White S. D. M., 1996, ApJ, 462, 563
[196] Patnaik, A. R., & Narasimha, D. 2001, MNRAS, 326, 1403
[197] Peebles, P. J. E. 2001, ApJ, 557, 495
[198] Raychaudhury S., Saha P., Williams L. L. R., 2003, AJ, 126, 29
[199] Saha, P., Williams, L.L.R. & Ferreras I. 2007, ApJ in press, preprint astro-ph/0703477 (Springer-Verlag) (SEF)
[200] Schneider, P., & Weiss, A. 1992, A&A, 260, 1
[201] Schechter, P. L., & Wambsganss, J. 2002, ApJ, 580, 685
[202] Sheth, R. K., & Tormen, G. 2002, MNRAS, 329, 61
[203] Seljak, U., & Zaldarriaga, M. 1996, ApJ, 469, 437
[204] Seljak, U., Makarov, A., McDonald, P., & Trac, H. 2006, Physical Review Letters, 97, 191303
[205] Sluse, D., Surdej, J., Claeskens, J.-F., Hutsemékers, D., Jean, C., Courbin, F., Nakos, T., Billeres, M., et al., 2003, A&A, 406, L43
[206] Tonry, J.L., 1998, AJ, 115, 1
[207] de Blok, W. J. G., & Bosma, A. 2002, AAP, 385, 816
[208] Kravtsov, A. V., Klypin, A. A., Bullock, J. S., & Primack, J. R. 1998, ApJ, 502, 48
[209] Swaters, R. A., Madore, B. F., & Trewhella, M. 2000, ApJL, 531, L107
[210] van den Bosch, F. C., & Swaters, R. A. 2001, MNRAS, 325, 1017
[211] Treu, T., & Koopmans, L. V. E. 2002, ApJ, 575, 87
[212] Viel, M., Lesgourgues, J., Haehnelt, M. G., Matarrese, S., & Riotto, A. 2005, PhRvD., 71, 063534
[213] Viel, M., Lesgourgues, J., Haehnelt, M. G., Matarrese, S., & Riotto, A. 2006, Physical Review Letters, 97, 071301
[214] Zakharov, A. F. 1995, A&A, 293, 1
[215] Allen, S. W., & Fabian, A. C. 1997, MNRAS, 286, 583
[216] Allen, S. W., Schmidt, R. W., & Fabian, A. C. 2002, MNRAS, 335, 256
[217] Bradač, M., et al. 2005, A&A, 437, 49
[218] Cappellari, M., & Copin, Y. 2003, MNRAS, 342, 345
[219] Cohen, J. G., & Kneib, J.-P. 2002, ApJ, 573, 524
[220] David, L. P., Jones, C., Forman, W., & Daines, S. 1994, ApJ, 428, 544
[221] Dickey, J. M., & Lockman, F. J. 1990, ARAA, 28, 215
[222] Diehl, S., & Statler, T. S. 2006, MNRAS, 368, 497

[223] Fabian, A. C., Sanders, J. S., Ettori, S., Taylor, G. B., Allen, S. W., Crawford, C. S., Iwasawa, K., & Johnstone, R. M. 2001, MNRAS, 321, L33
[224] De Filippis, E., Bautz, M. W., Sereno, M., & Garmire, G. P. 2004, ApJ, 611, 164
[225] De Filippis, E., Sereno, M., Bautz, M. W., & Longo, G. 2005, ApJ, 625, 108
[226] Fischer, P., & Tyson, J. A. 1997, AJ, 114, 14
[227] Gitti, M., & Schindler, S. 2004, A&A, 427, L9
[228] Kaastra, J. S., & Mewe, R. 1993, A&As, 97, 443
[229] Kitayama, T., Komatsu, E., Ota, N., Kuwabara, T., Suto, Y., Yoshikawa, K., Hattori, M., & Matsuo, H. 2004, PASJ, 56, 17
[230] Kling, T. P., Dell'Antonio, I., Wittman, D., & Tyson, J. A. 2005, ApJ, 625, 643
[231] Kneib, J.-P., Ellis, R. S., Smail, I., Couch, W. J., & Sharples, R. M. 1996, ApJ, 471, 643
[232] Kochanek, C. S. 1991, ApJ, 373, 354
[233] Komatsu, E., et al. 2001, PASJ, 53, 57
[234] Liedahl, D. A., Osterheld, A. L., & Goldstein, W. H. 1995, ApJl, 438, L115
[235] Paolillo, M., Fabbiano, G., Peres, G., & Kim, D.-W. 2002, ApJ, 565, 883
[236] Ricker, P. M., & Sarazin, C. L. 2001, ApJ, 561, 621
[237] Ritchie, B. W., & Thomas, P. A. 2002, MNRAS, 329, 675
[238] Sahu, K. C., et al. 1998, ApJl, 492, L125
[239] Sanders, J. S. 2006, MNRAS, 371, 829
[240] Sarazin, C. L. 1988, Cambridge Astrophysics Series, Cambridge: Cambridge University Press, 1988
[241] Schindler, S., et al. 1995, A&A, 299, L9
[242] Schindler, S., Hattori, M., Neumann, D. M., & Boehringer, H. 1997, A&A, 317, 646
[243] Sereno, M., De Filippis, E., Longo, G., & Bautz, M. W. 2006, ApJ, 645, 170
[244] Fabian, A. C., Hu, E. M., Cowie, L. L., & Grindlay, J. 1981, ApJ, 248, 47
[245] Liddle, A. R. 2004, MNRAS, 351, L49
[246] Xue, Y.-J. & Wu. X.-P. 2000, MNRAS 318, 715
[247] Allgood, B., Flores, R. A., Primack, J. R., Kravtsov, A. V., Wechsler, R. H., Faltenbacher, A., & Bullock, J. S. 2006, MNRAS, 367, 1781
[248] Barnes, J. & Efstathiou, G. 1987, ApJ, 319, 575
[249] Barnes, J. E., & Hernquist, L. 1996, ApJ, 471, 115
[250] Contopoulos, G. Order and Chaos in Dynamical Astronomy (Springer-Verlag, Berlin, 2002).
[251] Dubinski, J. 1994, ApJ, 431, 617
[252] Dubinski, J. & Carlberg, R. G. 1991, ApJ, 378, 496
[253] Gerhard, O. E., & Binney, J. 1985, MNRAS, 216, 467
[254] Efthymiopoulos, C., Contopoulos, G. Voglis,N., and Dvorak, R. 1997, Journal of Physics A 30, 8167.
[255] Jesseit, R., Naab, T., & Burkert, A. 2005, MNRAS, 360, 1185
[256] Jing, Y. P. & Suto, Y. 2002, ApJ, 574, 538
[257] Kandrup, H. E., Eckstein, B. L., & Bradley, B. O. 1997, A&A, 320, 65
[258] Kandrup, H. E., Vass, I. M., & Sideris, I. V. 2003, MNRAS, 341, 927
[259] Kazantzidis, S., Kravtsov, A. V., Zentner, A. R., Allgood, B., Nagai, D., & Moore, B. 2004, ApJl, 611, L73
[260] Lichtenberg, A. J. and Lieberman, M. A., Regular and Chaotic Dynamics (Springer-Verlag, New York, 1992).
[261] Ibata, R., Lewis, G. F., Irwin, M., Totten, E., & Quinn, T. 2001, ApJ, 551, 294
[262] Macciò, A. V., Dutton, A. A., van den Bosch, F. C., Moore, B., Potter, D., & Stadel, J. 2007, MNRAS in press, astro-ph/0608157
[263] Majewski, S. R., Skrutskie, M. F., Weinberg, M. D., & Ostheimer, J. C. 2003, ApJ, 599, 1082
[264] Mayer, L., Moore, B., Quinn, T., Governato, F., & Stadel, J. 2002, MNRAS, 336, 119
[265] Merritt, D., & Quinlan, G. D. 1998, ApJ, 498, 625
[266] Moore, B., Kazantzidis, S., Diemand, J., & Stadel, J. 2004, MNRAS, 354, 522
[267] Naab, T., & Burkert, A. 2003, ApJ, 597, 893
[268] Naab, T., Jesseit, R., & Burkert, A. 2006, MNRAS, 372, 839
[269] Navarro, J. F., Frenk, C. S., & White, S. D. M. 1997, ApJ, 490, 493
[270] Norman, C. A., May, A., & van Albada, T. S. 1985, ApJ, 296, 20
[271] Press W. H, Teukolsky S. A., Vetterling W. T. & Flannery B. P., Numerical Recipes in C, Cambridge University Press, New York (1993).
[272] Sideris, I. V. 2006 Phys Rev. E, 73: 066217.
[273] Stadel, J. G. 2001, Ph.D. Thesis, Univ. of Washington
[274] Valluri, M., & Merritt, D. 1998, ApJ, 506, 686
[275] Valluri, M., Vass, I. M., Kazantzidis, S., Kravtsov, A. V., & Bohn, C. L. 2007, ApJ in press, astro-ph/0609612
[276] Warren, M. S., Quinn, P. J., Salmon, J. K., & Zurek, W. H. 1992, ApJ, 399, 405

[277] Benson, A. J., Ellis, R. S., & Menanteau, F. 2002, MNRAS, 336, 564
[278] Somerville, R. S. 2002, ApJL, 572, L23
[279] Springel, V., & Hernquist, L. 2003, MNRAS, 339, 312
[280] Gaudi, B. S., & Petters, A. O. 2002, ApJ, 580, 468
[281] Blandford, R. D. 1990, QJRAS, 31, 305
[282] Metcalf, R. B. 2002, Bulletin of the American Astronomical Society, 34, 1236
[283] Woźniak, P. R., Alard, C., Udalski, A., Szymański, M., Kubiak, M., Pietrzyński, G., & Zebruń, K. 2000, ApJ, 529, 88
[284] Koopmans, L. V. E., & de Bruyn, A. G. 2000, AAP, 358, 793
[285] Schechter, P. L., & Wambsganss, J. 2002, ApJ, 580, 685

Acknowledgments

I am deeply indebted to several people for various expressions of kindness, patience, support, help, care and fun I had in the last four years here in Switzerland. And now I would like to thank all of them! Professor Giuseppe Longo and Dr. Paolo Scudellaro, for encouraging me to go on and to come to Zurich: without them it would have never been possible. Professor Philippe Jetzer, for giving me the chance to be here and for letting me go the way I wanted to take. I also thank him for carefully reading my manuscripts, my thesis and for kindly teaching me hystorical and scientific features of the physics world and of all its inhabitants.
There are so many great things about our institute and University I dont even know where to start; the lack of hierarchy (isn' it, Ben?), the open doors (and windows and balconies), the never-ending conversations, the astro-ph (i.e. parties), the funny trips (thank you Suzanne) but most of all the people. First of all, although he moved, one of them has shared a very special place on the K floor with me.

- I therefore thank Andrea Valerio Maccio‘ for keeping me in a very good mood and for helping me with the first steps in the world of real and 'simulated' science. I enjoyed it a lot, even with the dangerous sledge assaults! It was also a great pleasure to meet his wife Cinzia and their splendid daughter mini-Elena (smack!). I learned a lot from him (Thank you prof!).
- Fabiana, for patiently sharing the office with me, my sport equipment, banano Pippo (thank you, withouth you it would have died!), my music and my tales.
- Mauro for helping me in a 'cluster' of works (specially one!), for his teachings, for his calm, for our hystorical/polician discussions.
- Tobias and Cristian for beers, parties, holydays/summer-schools and above all for patiently traslating the whole english Summary in german!
- Pierpaolo for sharing logical/grammatical games, dinners and 'wins'.
- Claudio and Raffaele for our launchs, laughs, G-chewing gums and football matches (with and without the great Asini team!).
- Riccardo and Natalie for letting me play the piano for the first time in a real Group.
- The guitar player Rocco, The guitar/bass player Ben, the multi-intruments and sax player Justin and the hit-hard drummer Henry: without whom we could not have had the fantastic ZurichJam sessions and billion of concerts we enjoyed in the most important bar (and venues) in Zurich (...mmm).
- Anna, Katia, Manuela, Sandra S. and Sandra R., Sara, Carolina, Mandy, Mattias, Wagner, Veruska and many others have convinced me that Zurich (and Switzerland) is a very nice place to live!
- Special thanks to my heart-team ASINI, with which we partecipated in all the University tournaments without ever getting into a final position but winning a lot of unofficial (3) and extra-official (1) competitions (the Boltzmann cup!!).
- Kind thank-yous for FaBBio and Sergio, the first for surviving with me in Zurich, from the beginning to now. For our discussions about everything and nothing, for our first ski and canoa experiences, for our quarrels, for our travels and our doing-nothing. The second for its capability to move quickly in Zurich: without Sergio I would certainly have lost dates, time and money.
- And the people, althought not directly involved in my work or at the institute enviroment, helped me to face several hard moments. They came here to visit me for fun and/or for love: Daniela, my darling, who patiently endured and helped me during the first real difficult months. Carolina,

who offered me hospitality and tried to teach me German. I'm sorry, my friend, I was a real bad pupil! Gaetano, my 'scugnizzo' friend living in Lausanne:unforgettable the first amazing street parade we enjoyed together.
Carmine, for coming here more then seven times (of course, I invited him, I paid for him...) who shares with me almost all is part of my life (rooms, travels, money and...); Ralph and Ig, my german and spanish brothers, Roberto, the first who saw the swiss sun with me; Emiliano, Lorenzo, Nicola and Claudio who brought me the first 'pacco del terrone' by using the Lorenzo car, the same as the Zurich Post has. Yellow. Claudia and Annalisa, my special links with Naples, always part of of my heart; Valentina and Patrizia, those with Rome, with whom I spent the best part of the year 2005. Alessia and Manuela, my loving friends who came here to see where I was living and verify I was really fine. Ketty, 'la contessina', who finally reached me, actually for 'the party that you do not go home to sleep', to support me in one of the most important moment of my life. Gaetano 'Picchio' for his wonderful mood and for his deep sense of fun. Carlo, who came with me from Istanbul to Zurich by car and ship, crossing the Adriatico sea for 34 hours, to help me to set my new room in Zurich. Giovanna and GaetanoZeno, for looking at life with smiles and intelligence. Francesco and Ainara, for teaching me that all is always possible in this life.

- Marina and Oscar who came here by bus more then ten times, facing hard trips, to bring me smiles, love, quitness: to encourage me at any moments. Dario, for his sense of life, his deep awareness of being, for his bright music.

- And then there is someone special. Thank you Marisa, for supporting me in many aspects of my life, for our laughs, our travels, our growing up together, for teaching me about the world and nature, people and things, your philosophy of life and the secret of dreams. Finally, again my parents and my brother who never failed in their support. Together with all people I know, (most of them now around the world) I still think that one of the best place will for me always be the one where I was born.